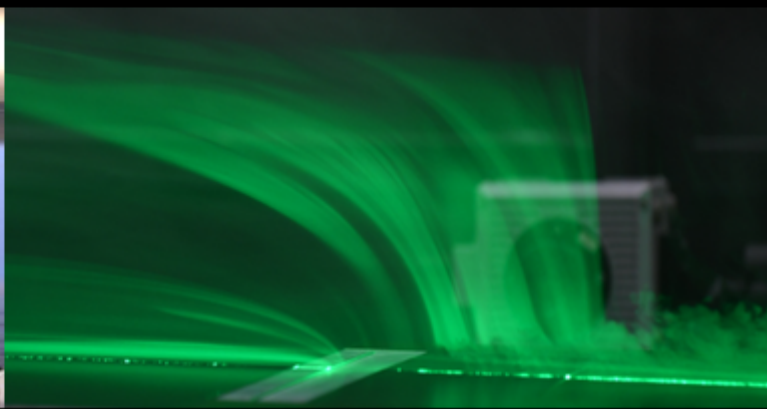
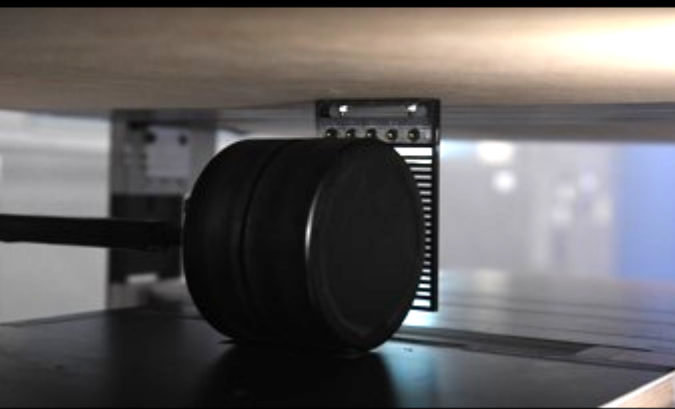




Experimental Investigation of the Effects of Mudflaps on Wheel Aerodynamics by Means of a Simulated Moving Ground

Siddharth Ghosh



Experimental investigation of the effects of mudflaps on wheel aerodynamics by means of a simulated moving ground

by

Siddharth Ghosh

to obtain the degree of Master of Science

at the Delft University of Technology,

to be defended publicly on Wednesday October 19, 2022 at 10:00 AM.

Student number: 5309263
Project duration: January 12, 2022 – October 19, 2022
Thesis committee: Dr. Andrea Sciacchitano, TU Delft, Thesis supervisor
Ir. Roy Veldhuizen, WABCO, Thesis supervisor
Prof. Dr. Fulvio Scarano, TU Delft, Committee Chair
Dr. Gerrit Elsinga, TU Delft, Committee member

An electronic version of this thesis is available at <http://repository.tudelft.nl/>.

Preface

"We truly progress when we are slightly outside our comfort zone"

–Andrea Sciacchitano, my supervisor

With mixed feelings of joy to finally finish my master's thesis and sorrow to end this beautiful journey, I would like to heartily acknowledge and thank all the people who have helped me achieve this feat.

First, I would like to thank my daily supervisor, Dr. Andrea Sciacchitano, from TU Delft. I feel fortunate to have had the chance to work under his caring and expert guidance throughout. Not only is he a good supervisor but also a great human being for helping me secure an internship and personally assisting me in the course of the experiments during these pandemic times. Second, I would like to thank my internship and thesis co-supervisor, Mr. Roy Veldhuizen, from WABCO. I am grateful to have learnt professional skills such as etiquette, confidence, and critical thinking and developed a better personal outlook by doing our bit towards being 'Eco-friendly'. I will surely not forget the wonderful time I had during my internship.

The project would be incomplete without the successful execution of the experimental campaigns, for this I would like to thank Mr. Frits Donker Duyvis, Mr. Peter Duyndam and Mr. Dennis Bruikman for providing me with the required models, helping set up the apparatus and learning the importance of time management and planning. I would also like to especially thank Tom and Luuk for providing helping hands and worthwhile discussions during the experiments. They and Kaj made my rather 'irregular' visits to the basement MSc room of the HSL and lunch sessions fun.

Next, I would like to thank my friends who have created an everlasting impression and cherishable memories during this journey. Amongst them, I would like to mention Pratik for being an amazing roommate and the tech support guy with a commendable work ethic. Srijit for having insightful conversations about aerodynamics and other topics and highlighting the importance of a good work study-life balance. Aravind, without whom gaming nights and the south-Indian food experience would not be fulfilling. Julio for sharing his invaluable experiences regarding academia. Revanth, Kavin, and Shubham, without whom, cricket and my experience in Delft would have been mundane. Further, I would extend my appreciation to Maitreya and Pramod, who helped me settle during the initial stages and made me feel not too far from home.

Lastly, and most importantly, I would like to thank my loved ones, without whom every achievement would seem meaningless. I feel blessed to have received constant support, and they truly define my '*comfort zone*'. Primarily, my parents, Mr. Gautam Ghosh and Mrs. Mona Ghosh, for having faith and believing in my dreams. My sister, Mandira for cheering and brightening my day without fail. My girlfriend, Swathi for encouraging me and providing unconditional love despite being miles apart.

Siddharth Ghosh
Delft, October 2022

Abstract

In recent times, employing drag reduction in heavy-duty vehicles has become a popular method to reduce emissions. Add-ons are aerodynamically optimised to provide drag reduction. However, the most common add-ons, such as mudflaps, are seldom studied. A literature survey suggested limited information on mudflaps to aerodynamically optimise them. Further, the need for a realistic setup was considered mandatory to conduct research on these mudflaps. Due to the expensive conveyor belts, a need for devising a cheaper alternative was also identified. Hence the objective of this thesis was to experimentally investigate the effects of mudflaps on wheel aerodynamics by employing particle image velocimetry on different designs under the influence of a simulated moving ground.

The simulated moving ground combined a leading edge, a roller setup, and a novel tangential blowing system. Two initial blowing slot designs were tested using the streamwise PROCAP device, where a step-blowing slot was compared with a flushed design. The results showed similar blowing velocity profiles with asymmetric velocity peaks caused by the one-sided pressure line input. However, the flushed design had a fuller profile on average due to smaller and more rounded support walls inside the blowing slot. Therefore, based on these observations, the final design was made with rounded, smaller walls and three pressure line inputs to produce a fuller and symmetric blowing profile.

A boundary layer analysis using planar PIV was conducted to quantify the effectiveness of the leading edge and the tangential blowing system. With blowing switched off, it was observed that the boundary layer present on the ground was about 80% smaller than the anticipated boundary layer height, partly indicating the effectiveness of the leading edge. Subsequently, switching the blower on led to removing the upstream boundary layer and introducing a fresh boundary, thereby reducing its effects drastically. Next, to assess the roller system and the simulated moving ground as a whole, planar PIV measurements of an isolated wheel were carried out and compared with existing literature. Features like downwash, separation points, wake convection and overall velocity fields were considered prime indicators of a good setup. The results demonstrated the setup's ability to simulate reality by producing similar flow features behind the stationary and rotating wheel. The tests confirmed that blowing also helps convect the wake behind the wheel and increases velocities near the jetting area. Due to experimental limitations, the Reynolds number was fixed to 0.23 million, i.e. in the sub-critical regime. The tests showed no major differences in the wake patterns compared to the previous experiments conducted in the post-critical regime in literature. Therefore, the results from the current study can give some indication of what is expected at higher Reynolds numbers.

The wheel-mudflap setup was assembled using a modular approach to quantify the effects of each component and ultimately help understand the complex flow field around mudflaps better. The assessment was done using stereoscopic PIV measurements at downstream wake planes ($z/D = 1, 1.5, 2, 3$). First, the vortex structures behind the isolated and the double wheel were studied. It was observed that the vortex structures of the double wheel were larger but quite similar for the stationary case. However, unlike the isolated wheel, the double wheel under rotation allowed the shoulder vortex and nearby ground vortex to combine into a single vortex entity at the near wake planes. The addition of an underbody led to slight increments in the local free stream velocities and interaction between the underside boundary layer and the wheel wake. Finally, the effect of mudflaps was analysed by considering the effects of the mudflap holder, followed by five mudflap designs with different solidities and solidity locations. The results illustrated the differences between the mudflap designs via variations in the counter-rotating vortices formed on the upper region of the wake and head-on collisions between the mudflap and wheel vortex structures. A PIV drag estimation analysis concluded that having lesser solidity reduces drag and wake skewing, and the location of solidity is a crucial factor, i.e. having lesser solidity on the top provided a 15% reduction in drag when compared to lesser solidity on the bottom of a mudflap. Hence, setting foundations for future mudflap designs.

Contents

Contents	vii
Nomenclature	xi
List of Figures	xv
List of Tables	xxv
1 Introduction	1
2 Background on wheel aerodynamics	3
2.1 Literature survey	3
2.1.1 Wheel and moving ground aerodynamics	3
2.1.1.1 Bluff body analogy	4
2.1.1.2 Effects of rotation	5
2.1.1.3 Ground effects	7
2.1.1.4 Comparison to stationary wheel	8
2.1.1.5 Effect of Reynolds number	9
2.1.1.6 Coherent structures	11
2.1.2 Wheel peripherals aerodynamics	13
2.1.2.1 Effects of axle	13
2.1.2.2 Effect of mudflaps	14
2.1.3 Experimental Setups	15
2.1.3.1 Conveyor belt	15
2.1.3.2 Tangential blowing and suction	16
2.1.3.3 Rollers	19
2.1.4 Concluding Remarks for literature survey	19
2.2 Research objectives and questions	20
2.2.1 Research Objectives	20
2.2.2 Research Questions	21

3	Experimental Techniques	22
3.1	Planar Particle Image Velocimetry	22
3.1.1	Imaging system	23
3.1.2	Tracer particles	24
3.1.3	Illumination	25
3.1.4	Velocity determination	26
3.2	Stereoscopic Particle Image Velocimetry	27
3.3	Drag estimation from PIV	28
3.3.1	Pressure field reconstruction	30
4	Experimental setup and procedure	31
4.1	Experimental Facilities	31
4.1.1	W-Tunnel	31
4.1.2	Open Jet Facility	32
4.2	Models	33
4.2.1	Moving Ground	33
4.2.1.1	Leading Edge	33
4.2.1.2	Roller Setup	34
4.2.1.3	Tangential Blowing System	35
4.2.1.4	Attaching plates	36
4.2.1.5	Simulated Moving Ground	36
4.2.2	Wheel and Mudflap Assembly	37
4.2.2.1	Wheel support structure	37
4.2.2.2	Isolated Wheel	39
4.2.2.3	Double Wheel	39
4.2.2.4	Underbody and mudflap holder	39
4.2.2.5	Mudflaps	40
4.3	Preliminary analysis of tangential blowing slot	41
4.4	Planar PIV measurements	41
4.4.1	Boundary layer planar measurements	42
4.4.2	Isolated wheel planar measurements	44
4.5	Stereoscopic PIV measurements	45
4.5.1	Isolated and double wheel stereoscopic measurements	46
4.5.2	Underbody and mudflap stereoscopic measurements	46

5	Processing and Data Reduction	47
5.1	Velocity fields	47
5.1.1	Boundary layer - Planar analysis	47
5.1.2	Isolated wheel - Planar analysis	48
5.1.3	Wheels and mudflap configurations - Stereoscopic analysis	49
5.2	Drag estimation	49
5.2.1	Vector field pre-processing	49
5.2.2	Wake contouring	50
5.2.3	Momentum term	51
5.2.4	Fluctuation term	53
5.2.5	Pressure term	54
6	Results and Discussion	57
6.1	Simulated moving ground	57
6.1.1	Preliminary analysis of the tangential blowing slot	57
6.1.2	Boundary layer analysis	59
6.2	Isolated Wheel	63
6.2.1	Planar results	63
6.2.2	Stereoscopic results	67
6.3	Double Wheel	71
6.4	Underbody	75
6.5	Mudflaps	77
6.5.1	Mudflap holder	77
6.5.2	Solid mudflap	78
6.5.3	Semi-solid mudflaps	79
6.5.4	Louvered mudflaps	81
6.6	Coefficient of drag	83
6.7	Answers to the research questions	86
7	Conclusion and Recommendations	88
7.1	Conclusion	88
7.2	Recommendations and future outlook	90
A	Patented mudflap designs	94
B	CAD geometries	97

C	Velocity and Vorticity plots	103
1	Isolated wheel - Planar	103
2	Isolated wheel - Stereoscopic	104
3	Double wheel - Stereoscopic	109
4	Underbody - Stereoscopic	115
5	Mudflap holder - Stereoscopic	120
6	Solid mudflap - Stereoscopic	121
7	Bottom hollow mudflap - Stereoscopic	123
8	Hollow top mudflap - Stereoscopic	124
9	2.8mm mudflap - Stereoscopic	126
10	1mm mudflap - Stereoscopic	127
11	Drag analysis	129

Nomenclature

Abbreviations

ANOVA	Analysis of Variance
AR	Aspect Ratio
B.L	Boundary Layer
CAD	Computer Aided Drawing
CO_2	Carbon Dioxide
CCD	Charged Coupled Device
C.F.D	Computational Fluid Dynamics
DC	Direct Current
DES	Detached Eddy Simulation
D.N.S	Direct Numerical Simulations
EEA	European Environment Agency
F1	Formula One
FT	Fourier transform
FOV	Field of View
GCM	Generic Conventional Model
IDDES	Improved Delayed Detached Eddy Simulation
LES	Large Eddy Simulation
M.V.T.S	Mesilla Valley Transportation Solutions
Nd:YAG	Neodymium-doped Yttrium Aluminium Garnet
Nd:YLF	Neodymium-doped Yttrium Lithium Fluoride
OJF	Open Jet Facility
PLA	Polylactic Acid
PIV	Particle Image Velocimetry
RANS	Reynolds Averaged Navier Stokes
RMS	Root Mean Square
RPM	Revolutions Per Minute
sCMOS	scientific Complementary Metal Oxide Semiconductor
SST	Shear Stress Transport
2-C	Two component
3-C	Three component
2-D	Two Dimensional
3-D	Three Dimensional
TBS	Tangential Blowing System
T.I	Turbulence Intensity
TKE	Turbulent Kinetic Energy
TU	Technical University

Greek Symbols

α	Ratio of rotational to free stream velocity
δ	Boundary layer height
δ^*	Displacement thickness
δt	Pulse duration
δz	Depth of field
Δt	Pulse separation time
θ	Angle about the wheel along the rotational axis, Momentum thickness
λ	Wavelength of light
μ	Dynamic viscosity of fluid
ρ, ρ_f	Density of fluid
ρ_p	Particle density
σ	Standard deviation
τ_p	Particle response time
ϕ	Sweep around the wheel along the flow axis
ω	Angular momentum

Non-Greek Symbols

a	Semi-major axis
A	Frontal area
b	Semi-minor axis
C_d, C_D	Coefficient of drag (2D,3D)
C_l, C_L	Coefficient of lift (2D,3D)
C_p, c_p	Coefficient of pressure
D	Diameter of wheel
d_τ	Particle image diameter
f	Frequency of vortex shedding, focal length, Acquisition frequency
$f_\#$	F-stop
F_{drag}	Drag force
I, I'	Interrogation window
l_x	Sensor size
L_x	Object size
L	Characteristic length of the body
M	Magnification factor
n	Wall normal distance
N	Number of samples
N_{rpm}	Number of revolutions per minute
p	Pressure
p_∞	Free stream/Ambient pressure
P_{req}	Required pressure
P_s	Static pressure
P_t	Total pressure
r	Radius of wheel, Radius of roller
R	Radius of support arm
Re	Reynolds number
S	Control surface
t	Time
u	Velocity at boundary layer for a given height, Required jet velocity, Cross flow velocity
u_p	Particle velocity
u'	Cross-flow fluctuation
v	Normal velocity
v'	Normal fluctuation
U_{mean}	Mean/Average free stream velocity
U, U_0, V_∞	Free stream velocity
U_θ	Induced velocity
V	Control volume
w	Width of wheel, Streamwise velocity
W	Laser sheet thickness
w'	Streamwise fluctuation
x/D	Normalized cross-flow distance with respect to wheel diameter
y	Normal distance
y_∞	Height at which velocity at B.L is equal to free stream velocity
y/D	Normalized normal distance with respect to wheel diameter
z	Cross-flow distance
z_0	Image distance
z/D	Normalized streamwise distance with respect to wheel diameter
Z_0	Object distance

List of Figures

1.1	Green houses emissions sector wise contributions in Europe. In particular, giving the break down of transport emissions, EEA, 2020.	1
1.2	Mudflaps (in green box) attached to the under body to minimize jetting of fluid behind wheels.	2
1.3	Eco-flap tested by M.V.T.S.	2
2.1	Curved slot present below the wheel to avoid contact between the stationary ground and wheel, used by Morelli, 1969	4
2.2	Representation of wheel flow physics using simpler geometry (cylinder) and boundary conditions: Left–Stationary cylinder with vortex structures symmetrically shedding from both the top and bottom ends. Middle–Rotating cylinder with vortices closer on the top end. Right–Rotating cylinder with moving ground, showing large bottom vortices shifted laterally away and upwards.	4
2.3	General flow separation mechanism and various phenomena around a non-rotating cylinder (bluff body), Mudimeli, 2018	5
2.4	Representation of the two boundary layer profiles over a rotating cylinder with a rotational velocity to free stream velocity of one, Swanson, 1961	6
2.5	Asymmetric wake behind a rotating cylinder due to early vortex shedding on the upper end (having higher relative velocity) and vice versa, under translational motion, Coutanceau and Menard, 1985	7
2.6	Time averaged vector plot for depicting delayed separation and small wake region behind the wheel, Mears, Dominy, et al., 2002, $Re = 0.25$ million.	8
2.7	Comparison of stream wise vorticity between stationary wheel (upper) having more lateral spread and rotating wheel (lower) having lesser lateral spread, Bearman et al., 1988. $Re = 0.55$ million.	8
2.8	Description of the Reynolds number regimes for a circular cylinder (non-rotating), J. E. Fackrell, 1974	10
2.9	Variation of C_L and C_D in various Reynolds number regimes for a stationary wheel, depicting the pre-critical region (shaded) and post-critical region (unshaded),Rajaratnam et al., 2019	11
2.10	Representation of vortex structures by different authors: Cogotti, 1983–Large upper vortices, hub vortices present and small lower vortices. Mercker and Berneburg, 1992–Large upper vortices, hub vortices present and medium sized lower vortices. McManus and Zhang, 2006–Arc vortex, hub vortices absent and large lower vortices. Saddington et al., 2007–Small upper vortices, hub vortices absent and large lower vortices.	12

2.11	Proposed vortex structures behind the wheel: At a distance $z/D < y$ – Small upper vortices, hub vortices present (only if there are hollow hubs), Medium sized lower vortices. At a distance $z/D > y$ – Arc vortex, hub vortices engulfed by large lower vortices. At a distance $z/D \gg y$ – Arc vortex engulfed by a larger set of lower vortices.	13
2.12	Vector plot depicting vortex core locations and cross flow in the rear side of the wheel, Axerio-Cilies et al., 2012	14
2.13	Various mudflaps designs tested by Hyams et al., 2011 namely: full mudflaps (upper), half slats (middle) and half mudflaps (lower)	15
2.14	Comparison of drag coefficients for the different mudflap designs with respect to Generic Conventional Model (GCM) as baseline, tested by Hyams et al., 2011. $Re = 1.15$ million.	15
2.15	Conveyor belt (moving belt) setup used by Hackett and Boles, 1979	16
2.16	Comparison of frontal and rear stagnation point location for various ground simulation techniques Mercker and Wiedemann, 1990	17
2.17	Moving ground (upper) setup used by Mercker and Berneburg, 1992 with tangential blowing (lower) setup designed by Berndtsson et al., 1988	18
2.18	Conveyor belt (upper) and Tangential blowing (lower) setup used by Kwon et al., 2001	18
2.19	Roller setup with 3-D printed coverings (in pink) used by Rajaratnam et al., 2019	19
3.1	Schematic of a planar PIV configuration showing different components: Laser illumination source, optics, camera, measurement plane, and a PC for image acquisition and processing, reproduced from Scarano, 2013.	23
3.2	Imaging system of a PIV setup depicting the image and object plane along with the required parameters for finding M, reproduced from Sciacchitano, 2014.	24
3.3	Light scattering intensity from laser light with wavelength of 532 [nm] as a function of scattering angle by 1 [μm] oil particle showing higher forward (FW) scatter in comparison to backward (BW) and side scatter, reproduced from Scarano, 2013.	25
3.4	Schematic for an illumination signal as function of time showing pulse width and pulse separation, reproduced from Sciacchitano, 2014.	26
3.5	PIV cross correlation map of two windows between two images (I and I'), reproduced from Scarano, 2013.	27
3.6	Schematic of a stereoscopic PIV configuration showing components similar to the planar configuration but with an additional camera, reproduced from McKeon et al., 2007.	27
3.7	Camera configuration for stereoscopic PIV using angular method where the angle between the image and lens plane is variable, reproduced from McKeon et al., 2007.	28
3.8	Perspective deformation for both the cameras used in stereoscopic PIV, reproduced from McKeon et al., 2007.	28
3.9	Schematic of the control volume showing the axis system, free stream velocity, and a given control surface.	29
4.1	W-tunnel in operation, equipped with 0.40×0.40 [m^2] exit cross section used during campaign 1 along with the defined coordinate axis system.	32
4.2	Open Jet facility test section area, with 2.8×2.8 [m^2] exit cross section area used for campaign 2 along with the defined coordinate axis system.	33

4.3	Elliptical leading design used by Schrader et al., 2010.	33
4.4	Roller setup showing the different components used by Jux, 2021.	34
4.5	Tangential blowing slot cross section: Left - Design from Berndtsson et al., 1988, Right top - Flushed model, Right bottom - Step model.	35
4.6	Finalised tangential blowing slot design with support walls spread uniformly across the slot, along with three pressure inlet ports present at the underside.	36
4.7	Representation of a cross-section of the simulated moving ground (not to actual scale).	37
4.8	Simulated moving ground - A combination of leading edge, roller setup and TBS.	37
4.9	Top view of setup depicting the required length of axle rod using potential flow theory.	38
4.10	Wheel configurations: Left - Isolated wheel along with its components, Right - Double wheel.	39
4.11	Mudflap - Underbody configuration showing the mudflap holder and mudflap mounting location.	40
4.12	Mudflap designs along with their coordinate orientation: Upper left - Solid mudflap, Upper middle - Mudflap with hollow top, Upper right - Mudflap with hollow bottom, Bottom left - Mudflap with 2.8 [mm] horizontal louvers, Bottom right - Mudflap with 1[mm] horizontal louvers	40
4.13	Measurement plane (in green) perpendicular to the floor, for the preliminary analysis of the blowing slot design.	41
4.14	Planar PIV measurement planes for the boundary layer analysis: Left - Simulated moving ground with tangential blowing slot, Right - Tangential blowing slot with the three measurement planes (zoomed-in) which are perpendicular to the floor.	42
4.15	Planar PIV measurement planes for the isolated wheel: Left - Side view showing FOV dimensions, Right - Rear view showing the three measurement planes (in green).	44
4.16	Stereoscopic PIV measurement planes (in green) for all wheel-mudflap configurations, along with FOV dimensions and distance with respect to the wheel centreline.	45
5.1	Image pre-processing in DaVis: Left - Raw image, Middle - Cropped image, Right - Removal of reflection from blower surface using subtract time filter.	47
5.2	Masking of the isolated wheel case in DaVis	48
5.3	Masking of the wheel-mudflap case (camera 2 view) in DaVis showing the masking and inverse masking of the regions of interest.	49
5.4	Raw normalised vector field of the wake of double wheel rotating configuration at $z/D = 2$, in the presence of the underbody with the mudflap holder attached. Viewed in the X-Y plane. Here velocity is normalised with respect to the free stream velocity and distance with respect to wheel diameter.	50
5.5	Interpolated normalised vector field of the wake of double wheel rotating configuration at $z/D = 2$, in the presence of the underbody with the mudflap holder attached. Viewed in the X-Y plane. Here velocity is normalised with respect to the free stream velocity and distance with respect to wheel diameter.	50
5.6	Normalised vector field with quiver showing the u-v components of the wake of double wheel rotating configuration at $z/D = 2$, in the presence of the underbody with the mudflap holder attached, represented by black lines. Viewed in the X-Y plane.	50

5.7	Wake contouring for the vector field of double wheel rotating configuration at $z/D = 2$, in the presence of the underbody with the mudflap holder attached.	51
5.8	Right half wake of the double wheel rotating configuration at $z/D = 2$, in the presence of the underbody with the mudflap holder attached. Viewed in the X-Y plane.	51
5.9	Average free stream velocity region (shown in white box) for the normalised vector field of double wheel stationary configuration at $z/D = 1.5$. Viewed in the X-Y plane.	52
5.10	Average free stream velocity region (shown in white box) for the normalised vector field of double wheel rotating configuration at $z/D = 2$, in the presence of the underbody with the mudflap holder attached. Viewed in the X-Y plane.	52
5.11	Wake streamwise velocity profile at different heights present on the wake centreline ($x/D = 0$), for the double wheel rotating configuration at $z/D = 1, 1.5, 2$ and 3	53
5.12	Streamwise turbulent kinetic energy distribution of the double wheel rotating configuration at $z/D = 2$, in the presence of the underbody with the mudflap holder attached. Viewed in the X-Y plane.	54
5.13	Type 1 - Boundary conditions for double wheel stationary configuration at $z/D = 1.5$. Viewed in the X-Y plane.	55
5.14	Type 2 - Boundary conditions for the double wheel rotating configuration at $z/D = 2$, in the presence of the underbody with the mudflap holder attached. Viewed in the X-Y plane.	55
6.1	Measurement plane (in green) perpendicular to the slot.	57
6.2	Normalised velocity field (X-Y plane) for a cross flow plane present 20 [mm] downstream of the step slot, for the step blowing slot (represented by the rectangle).	58
6.3	Normalised velocity profile along the height of the step blower at the different spanwise locations (X-direction) from the pressure line blower input present at the side.	58
6.4	Location of support wall (in red circle) for two initial designs: Top - Longer/spread out wall base for step blowing slot, Bottom - Rounded and smaller wall base for flat blowing slot	59
6.5	Normalised velocity field (X-Y plane) for a cross flow plane present 20 [mm] downstream of the flushed slot.	59
6.6	Normalised velocity profile along the height of the flushed blower at the different spanwise locations (X-direction) from the pressure line blower input present at the side.	59
6.7	Cropped measurement planes (in green) perpendicular to the slot.	59
6.8	Vector fields (Y-Z plane) showing boundary layer present on the mid-plane of the blower slot (in light grey) and ground (in dark grey). Boundary layer profiles represented (thin black lines) at intervals of $0.05D$	60
6.9	Vector fields (Y-Z plane) showing boundary layer present on the left-plane of the blower slot (in light grey) and ground (in dark grey). Boundary layer profiles represented (thin black lines) at intervals of $0.05D$	61
6.10	Vector fields (Y-Z plane) showing boundary layer present on the right-plane of the blower slot (in light grey) and ground (in dark grey). Boundary layer profiles represented (thin black lines) at intervals of $0.05D$	61

6.11	Average streamwise velocity taken from streamwise location of $0 z/D$ to $0.165 z/D$ (0 [mm] - 22.5 [mm]) profile along the height (Y-axis), for the three different measurement planes. For blower switched on, with 0.015 [MPa] supply pressure.	62
6.12	Measurement planes (in green) for the planar measurements of the isolated wheel.	63
6.13	Measurement planes (in green) for the stereoscopic measurements of the isolated wheel.	63
6.14	Normalised streamwise velocity field (Y-Z plane) at the mid-plane for the isolated wheel. Wheel represented as grey circle and blower represented as grey rectangle.	64
6.15	Normalised streamwise velocity field at an $Re = 0.72$ million : Left - Stationary wheel, Right - Rotating wheel, by Rajaratnam et al., 2019.	64
6.16	Velocity field difference between the rotating and stationary isolated wheel. Wheel represented as grey circle and blower represented as grey rectangle.	65
6.17	Normalised streamwise velocity field (Y-Z plane) at the mid-plane for the rotating isolated wheel with blowing. Wheel represented as grey circle and blower represented as grey rectangle.	66
6.18	Velocity field difference between the rotating with blowing and rotating without blowing isolated wheel. Wheel represented as grey circle and blower represented as grey rectangle.	66
6.19	Zoomed-in normalised streamwise velocity field (Y-Z plane) at the mid-plane for the rotating isolated wheel. Wheel represented as grey circle, blower represented as grey rectangle. Note: Red circle highlights wake convection.	66
6.20	Normalised streamwise velocity field (Y-Z plane) at for the rotating isolated wheel with blowing. Wheel represented as grey circle and blower represented as grey rectangle.	67
6.21	Normalised streamwise velocity field (X-Y plane) for the isolated wheel, at $z/D = 1$	68
6.22	Vorticity field (X-Y plane) for the isolated wheel, at $z/D = 1$. Green circles show rotational fields.	69
6.23	Vortex structures (in green circles) using quiver plot, for a rotating wheel at $z/D = 1.11$, for an $Re = 0.5$ million, seen in work by Axerio-Cilies et al., 2012. Note: The legend shows the vortex core locations.	70
6.24	Vortex structures (in red and blue), using Γ_2 criterion, for a rotating wheel at $z/D = 1$, for an $Re = 0.415$ million, seen in work by Parfett et al., 2022. The left ground (LG) and right ground (RG) vortex are labelled.	70
6.25	Normalised streamwise velocity field (X-Y plane) for the rotating isolated wheel with blowing, at $z/D = 3$	71
6.26	Normalised streamwise velocity field (X-Y plane) for the rotating double wheel, at $z/D = 1$	72
6.27	Vorticity field (X-Y plane) for the double wheel, at $z/D = 1$. Green circles show rotational fields.	73
6.28	Vorticity field (X-Y plane) for the rotating with blowing double wheel at different wake planes.	74
6.29	Normalised streamwise velocity field (X-Y plane) for the double wheel in the presence of underbody, at $z/D = 2$	76
6.30	Normalised streamwise velocity field (X-Y plane) for the rotating double wheel with blowing in the presence of mudflap holder, at $z/D = 1$	77

6.31	Vorticity field (X-Y plane) for the rotating double wheel with blowing in the presence of mudflap holder, at $z/D = 3$	78
6.32	Normalised streamwise velocity field (X-Y plane) for the rotating double wheel with blowing in the presence of solid mudflap, at $z/D = 1.5$	79
6.33	Vorticity field (X-Y plane) for the rotating double wheel with blowing in the presence of solid mudflap, at $z/D = 3$. With skewing direction shown in green.	79
6.34	Normalised streamwise velocity field (X-Y plane) for the rotating double wheel with blowing in the presence of hollow bottom mudflap, at $z/D = 1.5$	80
6.35	Vorticity field (X-Y plane) for the rotating double wheel with blowing in the presence of hollow bottom mudflap, at $z/D = 3$	80
6.36	Normalised streamwise velocity field (X-Y plane) for the rotating double wheel with blowing in the presence of hollow top mudflap, at $z/D = 1.5$	81
6.37	Vorticity field (X-Y plane) for the rotating double wheel with blowing in the presence of hollow top mudflap, at $z/D = 3$	81
6.38	Normalised streamwise velocity field (X-Y plane) for the rotating double wheel with blowing in the presence of 2.8mm louvered mudflap, at $z/D = 1.5$	82
6.39	Normalised streamwise velocity field (X-Y plane) for the rotating double wheel with blowing in the presence of 1mm louvered mudflap, at $z/D = 1.5$	82
6.40	Vorticity field (X-Y plane) for the rotating double wheel with blowing in the presence of 2.8mm louvered mudflap, at $z/D = 3$	83
6.41	Vorticity field (X-Y plane) for the rotating double wheel with blowing in the presence of 1mm louvered mudflap, at $z/D = 3$	83
6.42	Coefficient of drag for various configurations at different wake planes (z/D).	84
6.43	Drag coefficient for various configurations with their respective uncertainties, based on the different wake planes.	85
6.44	ANOVA analysis for the various designs, in particular, showing the difference between the hollow top design being statistically different from the hollow bottom design. The greyed out lines indicate the designs that are not statistically different from the hollow top design.	86
A.1	Mudflap design by Fleet Engineers, Inc., Muskegon, MI (US)	94
A.2	Mudflap design by Tarun Natwarlal Surti, Nashville, TN	95
A.3	Mudflap design by Globetech Manufacturing, Dayton, OH (US)	95
A.4	Mudflap design by COMPAGNIE GENERALE DES ETABLISSEMENTS MICHELIN	96
B.1	Isolated wheel CAD used by Jakhar, 2021	97
B.2	Final blower design CAD.	98
B.3	Attaching plate 1 CAD.	98
B.4	Attaching plate 2 CAD.	99
B.5	Mudflap holder CAD.	99

B.6	Solid mudflap CAD.	100
B.7	Hollow bottom mudflap CAD.	100
B.8	Hollow top mudflap CAD.	101
B.9	Mudflap with 1 [mm] louvers CAD.	101
B.10	Mudflap with 2.8 [mm] louvers CAD.	102
C.1	Normalised streamwise velocity field (Y-Z plane) at the right-plane for the stationary isolated wheel. Wheel represented as grey circle and blower represented as grey rectangle.	103
C.2	Normalised streamwise velocity field (Y-Z plane) at the right-plane for the rotating isolated wheel. Wheel represented as grey circle and blower represented as grey rectangle.	103
C.3	Normalised streamwise velocity field (Y-Z plane) at the left-plane for the stationary isolated wheel. Wheel represented as grey circle and blower represented as grey rectangle.	104
C.4	Normalised streamwise velocity field (Y-Z plane) at the left-plane for the rotating isolated wheel. Wheel represented as grey circle and blower represented as grey rectangle.	104
C.5	Normalised streamwise velocity field (X-Y plane) for the rotating isolated wheel with blowing, at $z/D = 1$	104
C.6	Normalised streamwise velocity field (X-Y plane) for the stationary isolated wheel at $z/D = 1.5$	105
C.7	Normalised streamwise velocity field (X-Y plane) for the rotating isolated wheel at $z/D = 1.5$	105
C.8	Normalised streamwise velocity field (X-Y plane) for the rotating isolated wheel with blowing, at $z/D = 1.5$	106
C.9	Normalised streamwise velocity field (X-Y plane) for the stationary isolated wheel at $z/D = 2$	106
C.10	Normalised streamwise velocity field (X-Y plane) for the rotating isolated wheel at $z/D = 2$	107
C.11	Normalised streamwise velocity field (X-Y plane) for the rotating isolated wheel with blowing, at $z/D = 2$	107
C.12	Normalised streamwise velocity field (X-Y plane) for the stationary isolated wheel at $z/D = 3$	108
C.13	Normalised streamwise velocity field (X-Y plane) for the rotating isolated wheel at $z/D = 3$	108
C.14	Normalised streamwise velocity field (X-Y plane) for the stationary double wheel, at $z/D = 1.5$	109
C.15	Normalised streamwise velocity field (X-Y plane) for the rotating double wheel, at $z/D = 1.5$	109
C.16	Normalised streamwise velocity field (X-Y plane) for the rotating double wheel with blowing, at $z/D = 1.5$	110
C.17	Normalised streamwise velocity field (X-Y plane) for the stationary double wheel, at $z/D = 2$	110

C.18 Normalised streamwise velocity field (X-Y plane) for the rotating double wheel, at $z/D = 2$	111
C.19 Normalised streamwise velocity field (X-Y plane) for the rotating double wheel with blowing, at $z/D = 2$	111
C.20 Normalised streamwise velocity field (X-Y plane) for the stationary double wheel, at $z/D = 2$	112
C.21 Normalised streamwise velocity field (X-Y plane) for the rotating double wheel, at $z/D = 2$	112
C.22 Normalised streamwise velocity field (X-Y plane) for the rotating double wheel with blowing, at $z/D = 2$	113
C.23 Vorticity field (X-Y plane) for the stationary double wheel, at $z/D = 1.5$	113
C.24 Vorticity field (X-Y plane) for the rotating double wheel, at $z/D = 1.5$	113
C.25 Vorticity field (X-Y plane) for the rotating with blowing double wheel, at $z/D = 1.5$	114
C.26 Vorticity field (X-Y plane) for the stationary double wheel, at $z/D = 2$	114
C.27 Vorticity field (X-Y plane) for the rotating double wheel, at $z/D = 2$	114
C.28 Vorticity field (X-Y plane) for the stationary double wheel, at $z/D = 3$	115
C.29 Vorticity field (X-Y plane) for the rotating double wheel, at $z/D = 3$	115
C.30 Normalised streamwise velocity field (X-Y plane) for the stationary double wheel in the presence of underbody, at $z/D = 1$	116
C.31 Normalised streamwise velocity field (X-Y plane) for the rotating double wheel in the presence of underbody, at $z/D = 1$	116
C.32 Normalised streamwise velocity field (X-Y plane) for the rotating double wheel with blowing in the presence of underbody, at $z/D = 1$	117
C.33 Normalised streamwise velocity field (X-Y plane) for the stationary double wheel in the presence of underbody, at $z/D = 1.5$	117
C.34 Normalised streamwise velocity field (X-Y plane) for the rotating double wheel in the presence of underbody, at $z/D = 1.5$	118
C.35 Normalised streamwise velocity field (X-Y plane) for the rotating double wheel with blowing in the presence of underbody, at $z/D = 1.5$	118
C.36 Normalised streamwise velocity field (X-Y plane) for the stationary double wheel in the presence of underbody, at $z/D = 3$	119
C.37 Normalised streamwise velocity field (X-Y plane) for the rotating double wheel in the presence of underbody, at $z/D = 3$	119
C.38 Normalised streamwise velocity field (X-Y plane) for the rotating double wheel with blowing in the presence of underbody, at $z/D = 3$	120
C.39 Normalised streamwise velocity field (X-Y plane) for the rotating double wheel with blowing in the presence of mudflap holder, at $z/D = 1.5$	120
C.40 Normalised streamwise velocity field (X-Y plane) for the rotating double wheel with blowing in the presence of mudflap holder, at $z/D = 2$	121

C.41 Normalised streamwise velocity field (X-Y plane) for the rotating double wheel with blowing in the presence of mudflap holder, at $z/D = 3$	121
C.42 Normalised streamwise velocity field (X-Y plane) for the rotating double wheel with blowing in the presence of solid mudflap, at $z/D = 1$	122
C.43 Normalised streamwise velocity field (X-Y plane) for the rotating double wheel with blowing in the presence of solid mudflap, at $z/D = 2$	122
C.44 Normalised streamwise velocity field (X-Y plane) for the rotating double wheel with blowing in the presence of solid mudflap, at $z/D = 3$	123
C.45 Normalised streamwise velocity field (X-Y plane) for the rotating double wheel with blowing in the presence of hollow bottom mudflap, at $z/D = 1$	123
C.46 Normalised streamwise velocity field (X-Y plane) for the rotating double wheel with blowing in the presence of hollow bottom mudflap, at $z/D = 2$	124
C.47 Normalised streamwise velocity field (X-Y plane) for the rotating double wheel with blowing in the presence of hollow bottom mudflap, at $z/D = 3$	124
C.48 Normalised streamwise velocity field (X-Y plane) for the rotating double wheel with blowing in the presence of hollow top mudflap, at $z/D = 1$	125
C.49 Normalised streamwise velocity field (X-Y plane) for the rotating double wheel with blowing in the presence of hollow top mudflap, at $z/D = 2$	125
C.50 Normalised streamwise velocity field (X-Y plane) for the rotating double wheel with blowing in the presence of hollow top mudflap, at $z/D = 3$	126
C.51 Normalised streamwise velocity field (X-Y plane) for the rotating double wheel with blowing in the presence of 2.8mm louvered mudflap, at $z/D = 1$	126
C.52 Normalised streamwise velocity field (X-Y plane) for the rotating double wheel with blowing in the presence of 2.8mm louvered mudflap, at $z/D = 2$	127
C.53 Normalised streamwise velocity field (X-Y plane) for the rotating double wheel with blowing in the presence of 2.8mm louvered mudflap, at $z/D = 3$	127
C.54 Normalised streamwise velocity field (X-Y plane) for the rotating double wheel with blowing in the presence of 1mm louvered mudflap, at $z/D = 1$	128
C.55 Normalised streamwise velocity field (X-Y plane) for the rotating double wheel with blowing in the presence of 1mm louvered mudflap, at $z/D = 2$	128
C.56 Normalised streamwise velocity field (X-Y plane) for the rotating double wheel with blowing in the presence of 1mm louvered mudflap, at $z/D = 3$	129
C.57 Breakdown of the drag coefficient in terms of momentum, pressure and fluctuation terms for the various configurations at different wake planes (z/D).	129
C.58 ANOVA results for different designs with their respective P-values.	130

List of Tables

4.1	Planar PIV settings for boundary layer analysis	43
4.2	Planar PIV settings for isolated wheel	45
4.3	Stereoscopic PIV settings for wheel-mudflap analysis	46
5.1	Boundary conditions for type 1 measurements.	55
5.2	Boundary conditions for type 2 measurements.	55
6.1	Average boundary layer parameters for streamwise location of $0 z/D$ to $0.165 z/D$ (0 [mm] - 22.5 [mm]).	62

Introduction

The transportation of goods has been an essential requirement for economic growth and sustenance. A primary transportation method via land includes the use of heavy-duty vehicles. A heavy-duty vehicle is identified as a vehicle with a minimum of 2.6 tonnes of load; the most common types include trucks with trailers. However, using such vehicles leads to emissions of greenhouse gases such as carbon dioxide (CO₂). The work by EEA, 2020 illustrates the break up of emissions contributed by the transport sector in Europe; in particular, heavy-duty vehicles and buses contribute up to 5.6%, as seen in fig. 1.1. These emissions eventually lead to rising global temperatures, causing detrimental effects like climate change, melting of ice caps, etc. Hence, in recent times, the need to reduce emissions has been of high priority. One method to decrease emissions is to employ drag reduction.

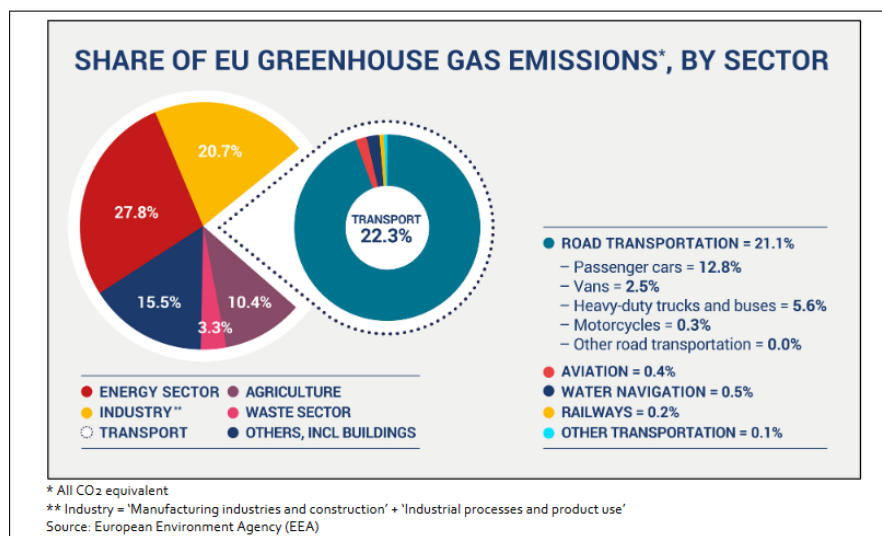


Figure 1.1: Green houses emissions sector wise contributions in Europe. In particular, giving the break down of transport emissions, EEA, 2020.

In heavy-duty vehicles, the use of aerodynamically efficient add-ons has become a popular technique to achieve drag reduction. Add-ons are devices/parts installed in the heavy-duty vehicle to perform certain functions or provide benefits. Although there exists a vast amount of literature on add-ons such as bow-tails, skirts, and wheel covers located around the wheels, there lacks a detailed aerodynamic analysis of the most commonly used add-on called mudflaps. Mudflaps are primarily used to reduce the spread and splash of the jetting fluid behind the wheels, as seen in fig. 1.2¹. However, they also increase the overall

¹https://media.istockphoto.com/photos/moving-transport-truck-on-a-wet-highway-picture-id1156164780?k=20&m=1156164780&s=612x612&w=0&h=9X_4uxMOM3czBp2SUcnI75fOW0W0rjf0LbqpejNaJl8=

drag of the heavy-duty vehicle. Mudflaps alone contribute up to 2.1% (i.e. roughly 0.118% overall carbon emissions in EU) of the total drag produced by a heavy-duty vehicle equipped with dry freight trailers, Hyams et al., 2011. Therefore, drag reductions in mudflaps could prove to reduce emissions and be economical. For instance, the patented mudflap design ‘Eco Flap’ shown in fig. 1.3² provides fuel savings up to 0.77%, according to Mesilla Valley Transportation Solutions (M.V.T.S)³. However, these patented designs lack sufficient scientific evidence and explanation to back these claims. As a result, it is necessary to analyze the design of these add-ons and reduce the drag by aerodynamically optimizing them. A significant challenge in creating such an efficient design is the complex flow field behind the wheels. Consequently, the complex interaction between the add-on and wheel itself leads to various phenomena such as changes in wake and vortex structures, the shift of separation points, and mainly chaotic flow fields, sometimes called ‘dirty air’.



Figure 1.2: Mudflaps (in green box) attached to the underbody to minimize jetting of fluid behind wheels.



Figure 1.3: Eco-flap tested by M.V.T.S.

Most wheel experiments involve the use of conveyor belts; these belts help simulate wheel rotation and remove the ground boundary layer. However, the expensive nature of this device makes it less desirable for testing. The expense includes ensuring the smooth translation of the rolling to translating motion at high speeds (such as 25 [m/s]), which requires precision machining, seamless belts, and powerful motors. Therefore in this thesis, firstly, a cheaper alternative to the conveyor belt is devised. Next, an attempt to understand the flow physics and determine the drag-sensitive zones of a mudflap is provided. This ultimately helps set a benchmark for designing aerodynamic mudflaps using a realistic setup for a greener future.

The structure of this report is made such that it firstly provides a theoretical background in chapter 2. It deals with various topics such as the wheel, moving ground and wheel peripheral aerodynamics, required to understand and systematically define the scope of the thesis. Next, chapter 3 gives an overview of the experimental technique: Particle image velocimetry, used in this work. Subsequently, the experimental setups and procedures are explained in chapter 4. Having obtained the raw data, the processing and data reduction techniques are described in chapter 5. Chapter 6 provides a detailed discussion of the results obtained. Finally, the chapter 7 outlines this study’s main conclusions and a few recommendations for future work.

²<https://images.squarespace-cdn.com/content/v1/581a0884ff7c5021847b42ae/1482519359740-B9C3RLUALV7T04R7HGAL/mud-flaps-wind-no-blue.png>

³<https://m-v-t-s.com/wp-content/uploads/2018/09/Eco-Flaps-MVTS-Certified-Test-V5.pdf>

2

Background on wheel aerodynamics

This chapter presents an overview of the theoretical background based on which the research goals of the thesis were set. Section 2.1 reviews the literature available on the wheel and moving ground aerodynamics, followed by wheel peripherals: axle and mudflap. Additionally, different experimental setups used for their study are also summarised. Finally, section 2.2 provides the research objective, and research questions to be able to quantify and set the scope of this work. Note that the experimental technique used in this work is reviewed in separately chapter 3.

2.1. Literature survey

The primary research goal of this study is to gain insights into designing an aerodynamic mudflap using a realistic setup. Hence, this section presents a brief summary of the extensive literature review conducted. First in section 2.1.1, wheel aerodynamics was understood by recognizing the primary flow patterns, coherent vortex structures, and the effect of Reynolds number that characterize such a flow. Second in section 2.1.2, the effect of wheel peripherals such as the axle and mudflaps are reviewed. Finally, having understood the flow physics, experimental setups in the past were assessed to choose the suitable methods that simulate the required conditions in section 2.1.3.

2.1.1. Wheel and moving ground aerodynamics

The mid 20th century is marked as the first significant period where attempts to understand wheel physics were initiated. Morelli, 1969 made primary attempts to study the stationary wheel and rotating wheels without the use of moving ground. A curved slot was made on the stationary floor to achieve free rotation of the wheel without any inference, as seen in fig. 2.1. However, this led to a gap between the wheel and the stationary floor, which gave rise to low pressure zones at the base of the wheel. Consequently, efforts by Stapleford and Carr, 1969 and Cogotti, 1983 were made to close the gaps using different materials such as foam rubber and paper strips. These works provided the required correction of the previously present negative lift to a positive lift value present at the base of the wheel.

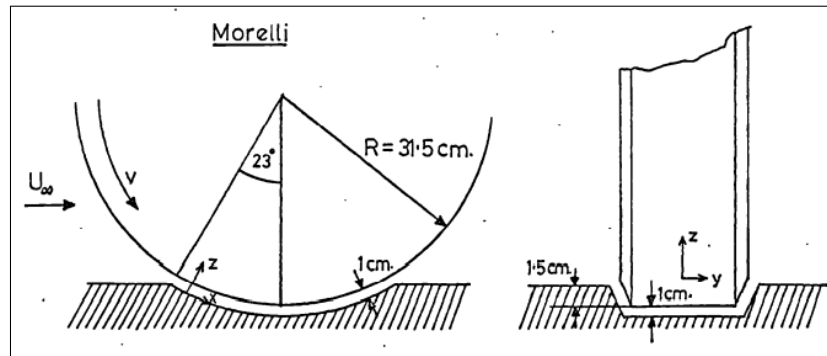


Figure 2.1: Curved slot present below the wheel to avoid contact between the stationary ground and wheel, used by Morelli, 1969

The work by J. Fackrell and Harvey, 1975; J. E. Fackrell, 1974 remains one of the most impactful in the field wheel aerodynamics. This work, in many ways, stands as a foundation for describing the flow around wheels. The work describes the flow using simpler geometries that closely resemble a wheel and then gradually includes the different boundary conditions applicable to it as represented in fig. 2.2. It provides a theoretical background on bluff bodies such as cylinders and spheres (of low aspect ratios) under the influence of rotation. This is followed by an analysis of ground effects on such bodies, which closely resemble a rotating wheel over a moving ground. Consequently, a vast amount of literature has been mentioned in the latter sub-sections, confirming most claims made by Fackrell and a few additional insights.

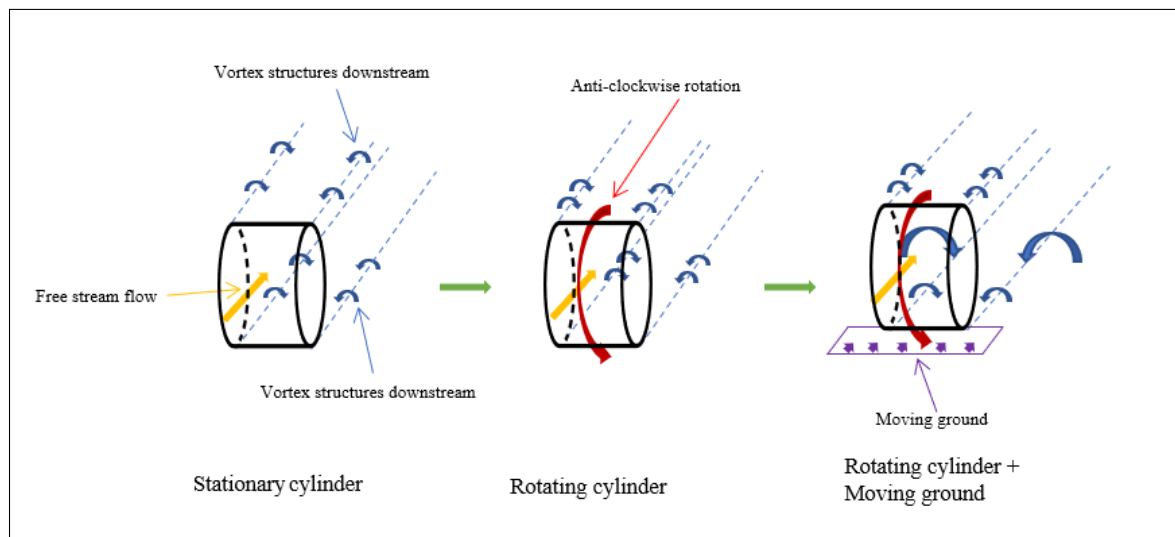


Figure 2.2: Representation of wheel flow physics using simpler geometry (cylinder) and boundary conditions: Left–Stationary cylinder with vortex structures symmetrically shedding from both the top and bottom ends. Middle–Rotating cylinder with vortices closer on the top end. Right–Rotating cylinder with moving ground, showing large bottom vortices shifted laterally away and upwards.

Bluff body analogy

A significant feature of any bluff body can be described by its ability to produce a separation region beyond the max thickness location. This phenomenon is characterized by the boundary layer separation caused by large adverse pressure gradients that occur due to the geometric shape of the body, as seen in fig. 2.3. These pressure gradients slow down the oncoming fluid particles and eventually reverse their direction. The reversal leads to fluid particles' inward movement, which further rolls up into vortices. Consequently, the vortices shed periodically, leading to low-pressure regions behind the bluff body. It must be noted that this mechanism of vortex shedding is highly dependent on the Reynolds number of the flow, and a more detailed discussion of the same is provided in section 2.1.1.5. Further, bluff bodies such as cylinders and spheres are characterized by a considerable pressure drag in the separation

regions. In contrast, skin friction provides minimal contributions to the overall drag of the body.

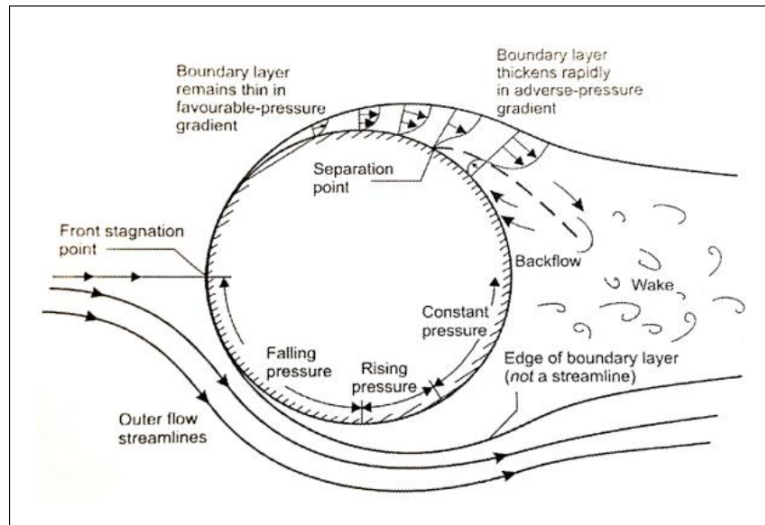


Figure 2.3: General flow separation mechanism and various phenomena around a non-rotating cylinder (bluff body), Mudimeli, 2018

Since the closest bluff body representing a wheel is a circular cylinder with a low aspect ratio, the study of flow patterns around cylinders is useful. Starting with the aspects of two-dimensional flow around a cylinder, there are numerous regions of interest like stagnation points, shear layers, and separation zones. One common trait in all bluff bodies is the location of the stagnation region present at the front of the body; this aspect also holds for wheels. Next, the upper and lower regions of the body encounter fast-moving fluid particles, which lead to low-pressure zones. Generally, in terms of pressure, the boundary layer transits in the upper/lower regions of the cylinder and comes across deceleration due to the adverse pressure gradients. This phenomenon creates a flow reversal effect. Separation occurs once these reversed zones gain enough thickness, making a void/bubble downstream. The bubble again creates a low-pressure zone that evokes re-circulation and vortices into the wake region of the cylinder, Doolan, 2010.

The studies related to the influence of aspect ratios in circular cylinders were better reviewed by Zdravkovich, 2003. The general trend observed was the drag coefficient reduction with the reduction of aspect ratio (bearing the same frontal area). This trend was explained using the larger base pressures generated on the rear side of the cylinders, which tend to reduce the pressure drag. However, considering the effects of skin friction drag, an increasing trend was observed for decreasing aspect ratios (below unity). This is because relatively larger sharp ends of the cylinder induce separation, creating shear layers and re-circulation zones at the sides. Further, these re-circulation zones were characterized by visibly large longitudinal vortices along the sides. Therefore, to avoid the increment of drag due to skin friction, it was concluded that having smoother edges was beneficial for cylinders. This claim was in good agreement with the findings of Fackrell.

Effects of rotation

Considering the effects of rotation alone, one noticeable difference that can be observed is the location of zero shear force denoted by eq. (2.1).

$$\frac{\partial u}{\partial n} = \Big|_{\text{separation}} 0 \quad (2.1)$$

where:

$$u = \text{Velocity at a given height [m/s]}$$

$$n = \text{Wall normal distance [m]}$$

Separation occurs downstream of this point for stationary bodies in the adverse pressure regions. Whereas, in the case of rotational bodies, this sometimes occurs in favorable pressure regions. This change is accounted for because a small layer of fluid remains attached to the rotating body irrespective of the free stream fluid. Further, such a motion against the incoming free stream induces transition, leading to a turbulent boundary layer prior to separation. Consequently, the early onset of separation also leads to lower base pressures, suggesting the relocation of the lower stagnation point to a more rearward position.

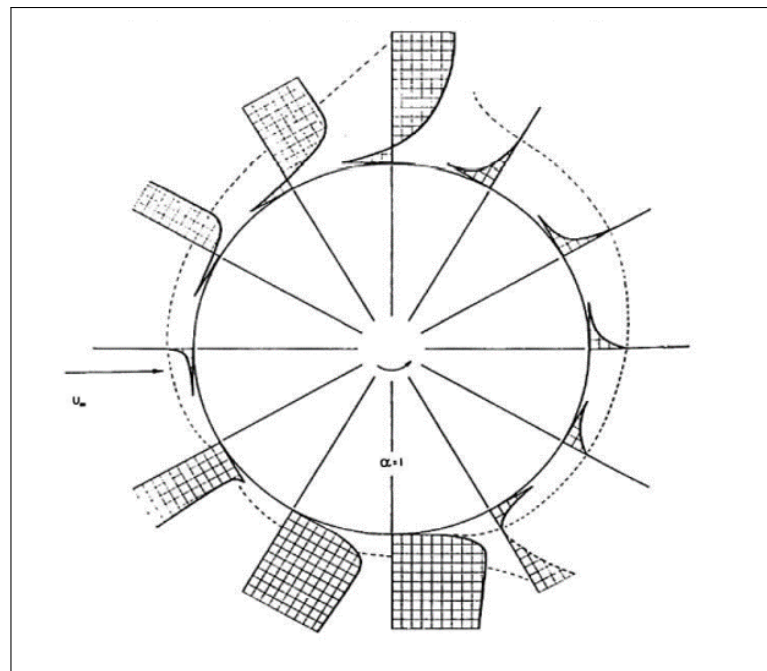


Figure 2.4: Representation of the two boundary layer profiles over a rotating cylinder with a rotational velocity to free stream velocity of one, Swanson, 1961

Studies based on rotating cylinders give insights into the boundary layer development, separation points, vortex structures, and phenomena such as the Magnus effect. These features are also be found partially around wheels; the Magnus effect, in particular, contributes a down force due to the difference in velocities between the upper and lower part of the wheel as seen previously by Morelli, 1969. A review of the Magnus effect on rotating cylinders was carried out by Swanson, 1961. The work presents boundary layer development on such bodies at different velocity ratios ($\alpha = \text{rotational velocity/free stream velocity}$). In the case of wheels, this ratio is unity; hence the boundary layer development in such a case is worth looking into. Two boundary layers developed starting from a point translated away from the stagnation point, i.e., in the direction of rotation. These boundary layers spanned equal lengths over the cylinder. However, the one present on the slower side (in terms of relative velocity) of the cylinder was thicker, as seen in fig. 2.4.

The work of Coutanceau and Menard, 1985 shows the time evolution of the vortex structures behind a rotating cylinder in combination with translation. It was suggested that the first vortex structure sheds from the side with the higher relative velocity, followed by the side with the lower velocity. Further, similar to Fackrell's findings, the separation point on the side with higher relative velocity (upper side of the wheel) was seen to move ahead compared to the stationary counterpart. Due to this delay in shedding on one side, the flow field becomes asymmetric and experiences a downwash, as seen in fig. 2.5.

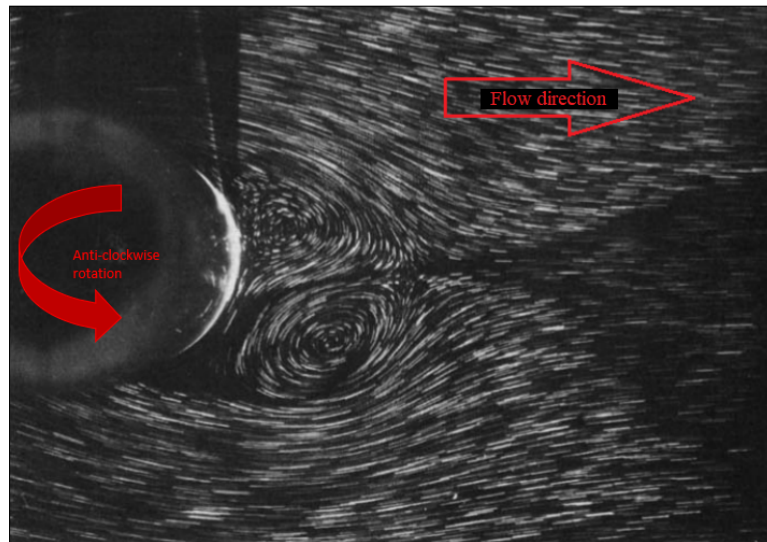


Figure 2.5: Asymmetric wake behind a rotating cylinder due to early vortex shedding on the upper end (having higher relative velocity) and vice versa, under translational motion, Coutanceau and Menard, 1985

Ground effects

One of the major features that make wheels inherently different from the rotating cylinders is the presence of a moving ground. The ground in contact with the wheel affects the flow field around the wheel quite drastically, especially on its lower portion. Therefore, to simulate ground effects, various ideas were tried. Since simulating a moving ground would require a complex setup, initially, wheels with a different clearance in combination with a stationary ground were investigated by Morelli, 1969. This clearance led to the venturi effects, i.e., local acceleration of fluid particles due to a contracting area creating a negative lift at the base of the wheel. Furthermore, the value becomes more negative as the clearance is reduced. However, this trend reversed after one point, leading to a positive lift until the clearance was finally brought to zero. The reversal was accounted for by a thick boundary layer on the stationary floor seen at such low clearances, which influenced the oncoming fluid particles by slowing them down.

On a more theoretical note, one could propose the usage of potential flow solutions for simpler geometries like cylinders. However, a significant flaw remains the inability to include the viscous contributions and wake effects. This leads to non-physical conclusions, such as the presence of negative pressure values at the base of the wheel. Hence, the contact patch between the wheel and floor was sifted through to understand the viscous effects better. Contrasting to what one might expect, it was found that the viscous effects were much more prevalent in the contact region. The jetting motion of the fluid occurring at the base of the wheel confirms this. The effect by itself is pretty local to the region.

Although J. E. Fackrell, 1974 predicted the presence of a strong positive peak due to the noticeable jetting, the experiments lacked enough evidence to confirm this change in pressure. Studies by Axon et al., 1998 later confirmed this apparent change in pressure peak and Mears et al., 2004 experimentally verified the association of pressure peak with jetting. Another aspect that is interesting to discuss is the strength of jetting, which partially depends on the contact patch size of the wheel. Wickern et al., 1997 suggests that the effects of the contact patch on the overall drag coefficient are quite small, ranging between ± 0.001 . Thereby claiming that the variation in the strength jetting fluid is also rather minimal. Further the work of Mears, Dominy, et al., 2002 and Mears, Dominy, et al., 2002, not only confirms the drag and pressure readings stated by Fackrell, but also found a subsequent negative pressure peak present right after the contact patch. The fig. 2.6 shows the effects of rotation, and a moving ground on wheel flow, the larger wake present behind the rotating wheel is accounted by the effect of jetting and early separation that occurs at the upper part of the wheel.

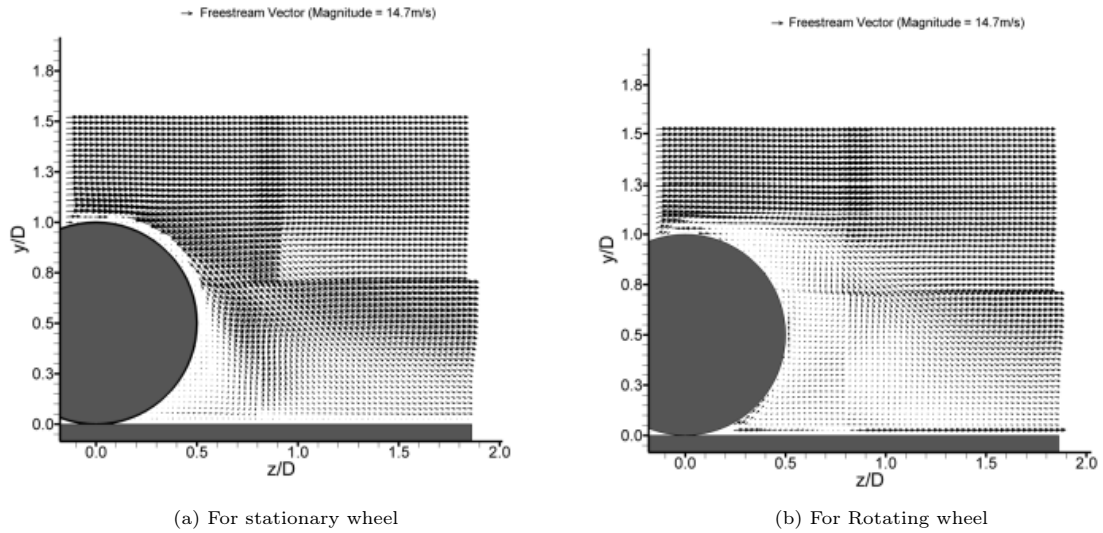


Figure 2.6: Time averaged vector plot for depicting delayed separation and small wake region behind the wheel, Mears, Dominy, et al., 2002, $Re = 0.25$ million.

Additionally, the tests were carried out using a pneumatic tire, which has a different contact patch size compared to that used by Fackrell. However, this change in contact patch size hardly influenced the over lift and drag values, indicating its low significance.

Comparison to stationary wheel

Understanding the stationary wheel in contact with the ground is also crucial to fully understanding the moving ground and rotation effects. In contrast to the rotating wheel, the stationary wheel behaves very similarly to a cylinder of low aspect ratio, with separation points present further down in the adverse pressure region of the wheel. This not only affects the evolution of the wake region but also leads to higher drag and lift values. Further, when in contact with the stationary ground, the wheel now produces a much lower yet positive pressure peak close to unity. This behavior is attributed to the lack of jetting phenomenon in stationary wheels.

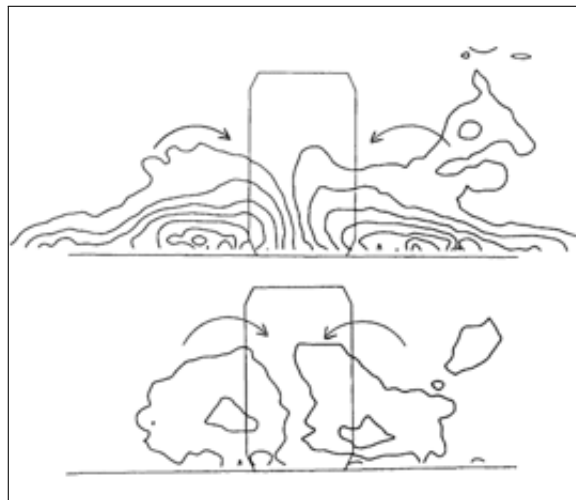


Figure 2.7: Comparison of stream wise vorticity between stationary wheel (upper) having more lateral spread and rotating wheel (lower) having lesser lateral spread, Bearman et al., 1988. $Re = 0.55$ million.

The lateral wake spread behind and around the wheel is much larger for the stationary wheel, Bearman et al., 1988 as seen in fig. 2.7. The lack of jetting and rotation around the wheel reduces the kinetic energy imparted into the flow. The downwash effects behind the wheel also differ considerably for the

stationary and moving case. For the former, the wake region is comparatively shorter in height and induces much higher downwash behind the wheel. In contrast, the moving wheel has a higher wake region with lesser downwash, as stated by McManus and Zhang, 2006.

Effect of Reynolds number

In general, non-dimensional numbers help decrease the number of variables required to replicate a system and its behavior. This saves time and supports better correlations of physical phenomena to scalable systems. In the case of wheel aerodynamics, one of the more prominent non-dimensional number is identified as the Reynolds number.

The Reynolds number is defined as the ratio of the inertial forces over viscous forces given in eq. (2.2).

$$Re = \frac{\rho V D}{\mu} \quad (2.2)$$

where:

$\rho = \text{Density of the fluid [kg/m}^3\text{]}$

$V = \text{Free stream velocity [m/s]}$

$D = \text{Diameter of the wheel [m]}$

$\mu = \text{Dynamic viscosity of the fluid [kg/(m.s)]}$

Based on the understanding provided in the previous section, most inferences were drawn from geometries such as cylinders, specifically in terms of the location of separation points. Hence, the effect of the Reynolds number will play a significant role in determining the nature of the flow field around the wheel. In general, flow fields over cylinders can be characterized based on their Reynolds number as seen in fig. 2.8. At lower Reynolds numbers ranging from unity to about 90, the flow remains fairly laminar with small instabilities that die down due to the high viscous effects. Next, values from roughly 100 to 10,000 translate to the ‘sub-critical’ range. The beginning of this range is marked by the periodic shedding of Karman vortices, followed by an increase in turbulence which accentuates 3-D effects due to crossflow components. However, the range 10,000 to 3,500,000, called the ‘Critical and Post-critical’ range, is identified by chaotic features that are less periodic. These features include quick thinning of the wake region associated with the alternating separation and attachment of the flow at the upper part of the cylinder. Last, the range above the 3,500,000 mark is the ‘trans-critical’ range. This range surprisingly recovers the width of the wake region and brings back the periodic shedding of wake structures. However, it must be noted that these structures are much more turbulent than the previous structures. Further, numerous factors like turbulence intensity of the free stream, surface roughness, and cylinder profile affect the wake size and strength.

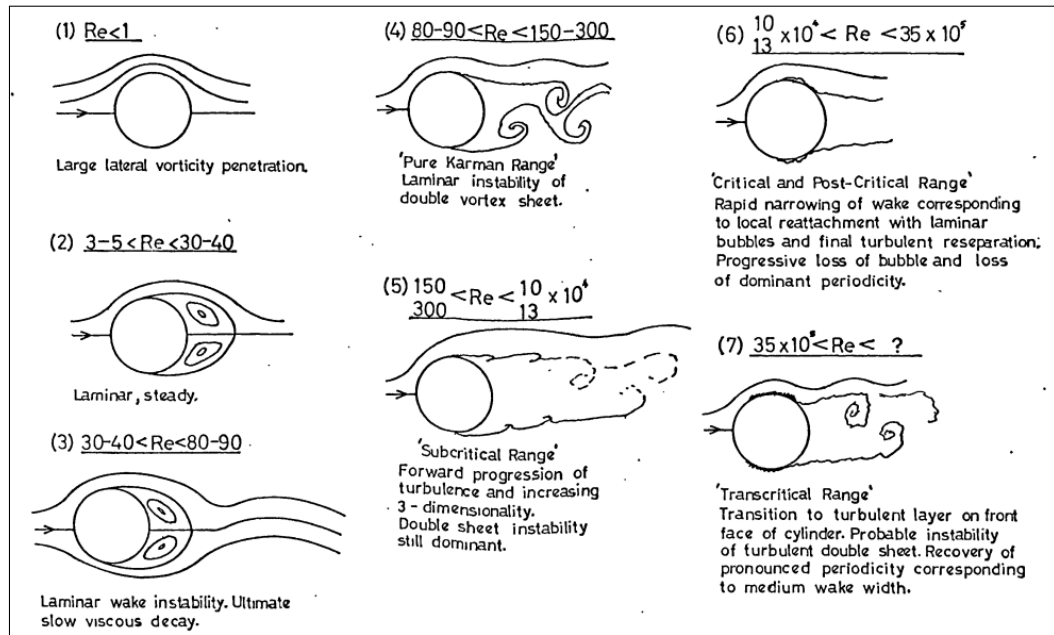


Figure 2.8: Description of the Reynolds number regimes for a circular cylinder (non-rotating), J. E. Fackrell, 1974

The more recent experimental studies of Rajaratnam et al., 2019, show the effect of Reynolds number on a stationary wheel. The work depicts the variation of the lift and drag coefficients in the three previously discussed regions, the pre-critical region ranging to a Reynolds number of 380,000, followed by the transition region roughly from 380,000 to 490,000, and finally, the post-critical range from 500,000 onwards as seen in fig. 2.9. Since the cases related to Formula one and heavy-duty vehicles have high wheel Reynolds numbers which correspond to the post-critical regime, most of the literature reviewed in this study has a Reynolds number of roughly 0.5 million.

For rotating wheels, although limited by factors such as aspect ratio, a similar analogy can be drawn with regards to the variety of Reynolds number ranges. The focus of the literature survey is mainly on the higher Reynolds numbers ranging from roughly 1000 to 1,000,000 (Refer section 2.1.1.6 for Reynolds numbers of the different cases). Such a broad range of Reynolds numbers is being considered to help account for different phenomena associated with heavy-duty vehicles since they move at different speeds and come in different wheel sizes.

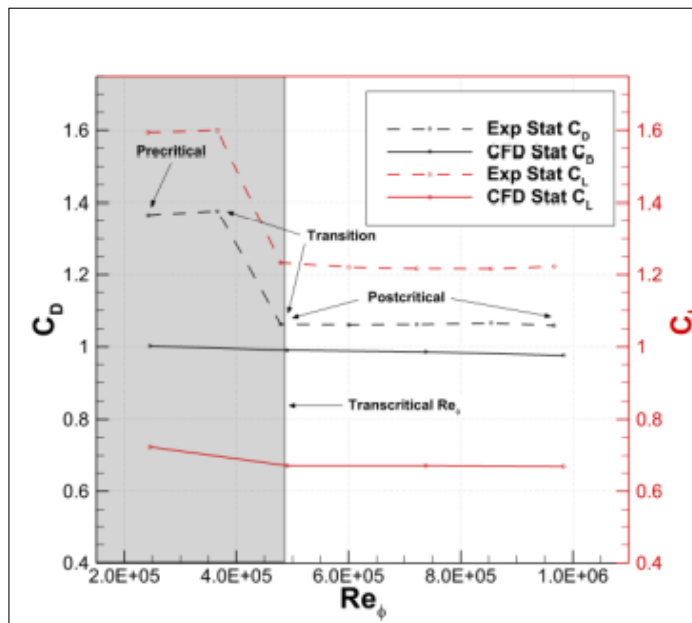


Figure 2.9: Variation of C_L and C_D in various Reynolds number regimes for a stationary wheel, depicting the pre-critical region (shaded) and post-critical region (unshaded), Rajaratnam et al., 2019

Coherent structures

There have been a number of efforts to explain the vortex structures around the wheel. As mentioned previously, the first attempts Bearman and Zdravkovich, 1978 ($Re = 0.55$ million) and J. E. Fackrell, 1974 ($Re = 0.53$ million), were based on bodies such as cylinders close to the ground. These are mainly proposed based on theoretical solutions like the potential flow theory and boundary layer theory. Although these gave a fair estimate of lift and drag values over these bodies, they lack to provide conclusive evidence for some of the phenomena that were later deemed as the effect of viscosity. Initially, the vortex structures were represented using a schematic diagram by Mercker and Berneburg, 1992. The diagram consisted of two counter-rotating vortices. One is a weak central pair present at the wheel's upper rear side and the other is a stronger pair present at the bottom rear side of the wheel. These were a result of the separation and jetting, respectively.

However, these structures were not always visible, and some works such as Knowles et al., 2002 ($Re = 0.369$ million) suggest that the upper vortices quickly die down and are not necessarily coherent. Consequently, Saddington et al., 2007 ($Re = 0.68$ million) investigated to understand the anomaly better and came up suggesting that the visibility and relative strength of the upper vortices were a function of ' z/D ' (normalized distance concerning the diameter of the wheel). For values below z/D of unity, the upper vortices were noticeable. In contrast, for values above unity, the vortices tend to die down and combine with the more extensive set of vortices emanating from the wheel's base, sometimes also known as root vortices. Further, the work also suggests that these vortex structures keep their shape intact and have a low spread until one diameter length away from the wheel.

With rising advancements in computational fluid dynamics, a few more insights have been added to what Saddington et al., 2007 stated. The work of McManus and Zhang, 2006 ($Re = 0.53$ million), in particular, claims that the two upper vortices behave like a single arc-shaped vortex instead of two separate entities. On a similar note, Wäschle, 2007 suggests that the upper vortices are one single ring vortex such that the vortex core aligns along with the flow instead of being perpendicular to it. It also claims that the lower pair of ground vortices structurally resemble a horseshoe vortex which pulls the weaker upper vortices into forming the ring vortex. Unlike the previous computational studies, which were based on Reynolds averaged Navier stokes models (RANS), Pirozzoli et al., 2012 ($Re = 1000$) used low speed direct numerical simulations (D.N.S) using which an additional pair of weak vortices were found between the upper and lower pairs.

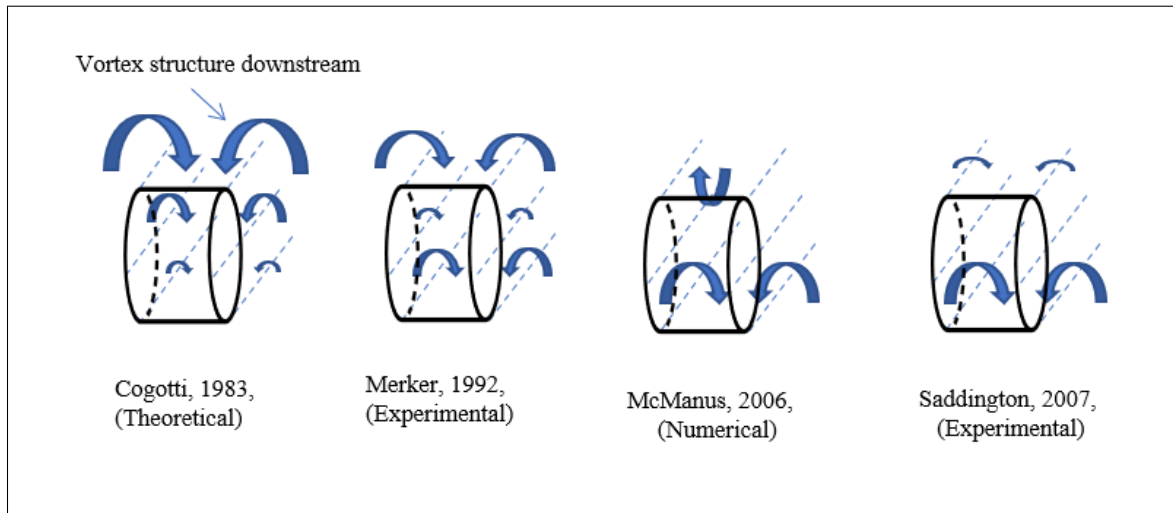


Figure 2.10: Representation of vortex structures by different authors: Cogotti, 1983–Large upper vortices, hub vortices present and small lower vortices. Merker and Berneburg, 1992–Large upper vortices, hub vortices present and medium sized lower vortices. McManus and Zhang, 2006–Arc vortex, hub vortices absent and large lower vortices. Saddington et al., 2007–Small upper vortices, hub vortices absent and large lower vortices.

Further, Axerio-Cilies et al., 2012 ($Re = 0.50$ million) too claimed the presence of the third pair of counter-rotating vortices present at the central height of the wheel, which in particular, were not a product of the hub geometry. Having seen the pretty different opinions, Croner et al., 2013 ($Re = 0.91$ million) revisited these topics to come up with a different approach based on saddle point topology that involves the finding separation points. The method did not rely on the location of suction peaks which previously were known to be the leading indicators of separation. The conclusions of this new method were similar to that stated by Mcmanus, confirming the presence of an arc-shaped vortex at the upper rear end of the wheel.

The most recent works, such as the work by Parfett et al., 2022 ($Re = 0.415$ million), involve the study of the time-resolved vortex structures shed behind an isolated Formula one wheel. This work used single-pass particle image velocimetry to study the wake pattern behind the wheels. The study found and confirmed the presence of the ground vortex pair and suggested that the instantaneous fields were sometimes dominated by the left vortex or the right vortex or even shed symmetrically. Additionally, whenever the ground vortex pair was shed asymmetrically, the dominant vortex was almost twice as strong as the non-dominant vortex. An interesting finding in this study was the origin of the ground vortex pair. Unlike the claims of J. E. Fackrell, 1974, Sprot et al., 2012, which suggest that the ground vortex was caused mainly due to the jetting phenomenon, this work claimed that the flow ahead of the contact patch was the reason instead. The flow ahead of the contact patch encounters the front of the wheel, which moves downwards. Here, the boundary layer generates shedding vortices that move around the wheel's sides and roll up to form the counter-rotating ground vortex pair.

All in all, various authors have reported several claims regarding the coherent structures around the wheel, as shown in fig. 2.10. However, there lacks a consensus about these structures. There can be many reasons for this, such as different boundary conditions, Reynolds number effects and slight changes in the setup/wheel model. The strength, size and general location of the vortex heavily depend on the Reynolds regime considered, as already indicated by section 2.1.1.5. Further, the reason behind the formation of the ground vortex pair is also not certain. Some earlier authors state jetting as the primary reason and in the contrary the recent ones state, the frontal flow to be the cause. Therefore based on the conclusions, a hypothesis regarding the Reynolds number is proposed. At low Reynolds numbers ranging from 1,000 to 10,000, there are three noticeable counter-rotating vortex pairs along with the wheel's height. This includes the top and bottom counter-rotating pair, along with a small pair of vortices along the hub region which only occurs if there is a hollow hub region in the wheel as seen in fig. 2.11. As the Reynolds number range increases from 10,000-100,000 or more, the upper vortices tend to combine themselves, forming an arc-shaped vortex. Consequently, the lower vortex gradually engulfs the middle and upper vortices further downstream. Also note that the reason behind

the formation of these vortices is not commented upon as this is beyond the scope of this study.

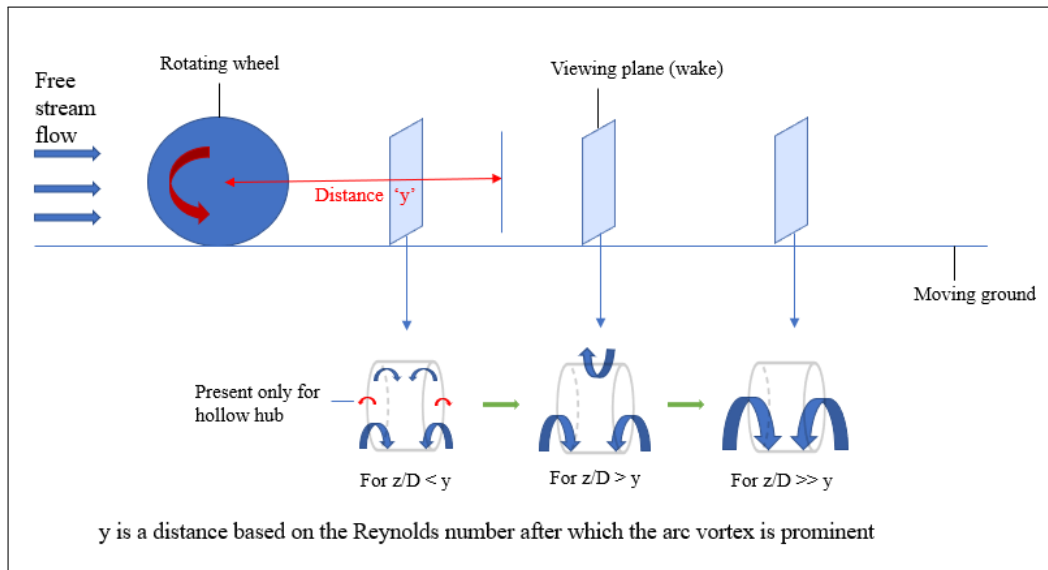


Figure 2.11: Proposed vortex structures behind the wheel: At a distance $z/D < y$ – Small upper vortices, hub vortices present (only if there are hollow hubs), Medium sized lower vortices. At a distance $z/D > y$ – Arc vortex, hub vortices engulfed by large lower vortices. At a distance $z/D \gg y$ – Arc vortex engulfed by a larger set of lower vortices.

2.1.2. Wheel peripherals aerodynamics

The majority of literature on wheels is mainly based on Formula One (F1) wheels, which includes the early works of J. E. Fackrell, 1974, and Cogotti, 1983 to the more recent works like the one by Parfett et al., 2022. Since heavy-duty vehicles operate at similar Reynolds numbers by compensating for the lower speeds with larger wheel diameters, this literature review is heavily inclined towards insights from Formula one wheel studies. Although majority flow physics has been discussed in earlier sections, this section, in particular, will deal with the more nuanced topics that include the effects of axles and mudflaps.

Effects of axle

Since most wheels are connected using axles, it is necessary to quantify the effects of this connecting member on wheel aerodynamics. The work of Nigbur, 1999 was one of the first studies where such an effect was considered. The study showed that such geometry affects the flowfield around the wheel. It stated that the wake structures around the wheel were visibly asymmetric due to possible regions of high turbulence intensity.

Later Axerio-Cilies et al., 2012 provided a detailed analysis of the flowfield around the connecting member along with the effects of brake discs. The work claimed that there was a presence of solid cross flow starting from the outboard side (with wheel hub) to the inboard side (with the brake discs), as seen in fig. 2.12. This led to a strong low-pressure region around the brake discs and hence the asymmetric behavior. It must be noted that the flow structures were asymmetric and downwash at the rear side of the wheel. The inboard side experienced a weaker downwash due to brake assembly and cross flow. Consequently, the reversed flow behind the wheel was now less prominent, making the re-circulation bubble appear smaller. However, the axle and wheel camber remained the main reason for the asymmetric flow field. It increased the turbulence on the inward side and vice versa. Therefore, stabilizing the wake structure on the outboard side. Subsequently, it was stated that the inboard vortex is stronger and more influential in terms of drag contributions. Considering the standard turbulent kinetic energy (TKE), the axle helped sustain the value to a longer distance downstream of the wheel. At the same time, the highest velocity fluctuations died down rather quickly, within a distance of 6 [cm] (for a wheel diameter of 0.395 [m]). Further, using $v'w'$, it stated that normal and stream-wise

fluctuations were positively correlated in the lower side of the wheel wake fluctuations and negatively correlated on the upper side of the wheel wake. It reasoned this change using the presence of the hard ground beneath, which tends to reduce the normal fluctuations more effectively.

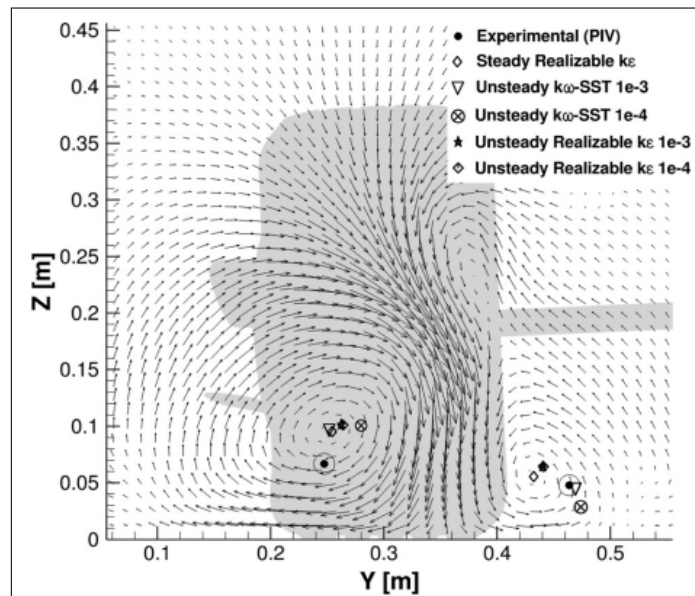


Figure 2.12: Vector plot depicting vortex core locations and cross flow in the rear side of the wheel, Axerio-Cilies et al., 2012

Effect of mudflaps

Mudflaps, in general, are add-ons used to reduce splash and spray effects behind the wheel due to the fluid jetting that occurs behind the wheel. Although there are some patents claiming improved aerodynamic performance, there hardly exists any literature which aerodynamically analyses mudflaps (Please refer to figure A.1 to A.4 in the appendix for the mudflap patented designs). However, Hyams et al., 2011 conducted a study on various drag reduction devices present on a heavy-duty vehicle. A few mudflaps designs, in particular, were tested. Although the work does not provide a strong motivation for design choices, the designs seemed to perform well. Three models were tested, namely full flaps extending from the trailer underbody to the base of the wheel, half flaps extending only over the wheel, and half slats which were half mudflaps with vertically slanted slats that point the oncoming fluid inwards of the underbody region as seen in fig. 2.13. Results show that the slatted design performed the best since it produced the slightest drag, which is even lower than the base model (without mudflaps), as seen in fig. 2.14. Note that although the full flaps produce a much higher drag (8.6%), it is usually only used for ‘pup’ trailers. The more common trucks use the half-slat version, which produces 2.1% drag of the overall body. A hypothesis for the improved performance using slats could be the pressure recovery they provide in the underbody region, reducing the overall pressure drag on the vehicle.

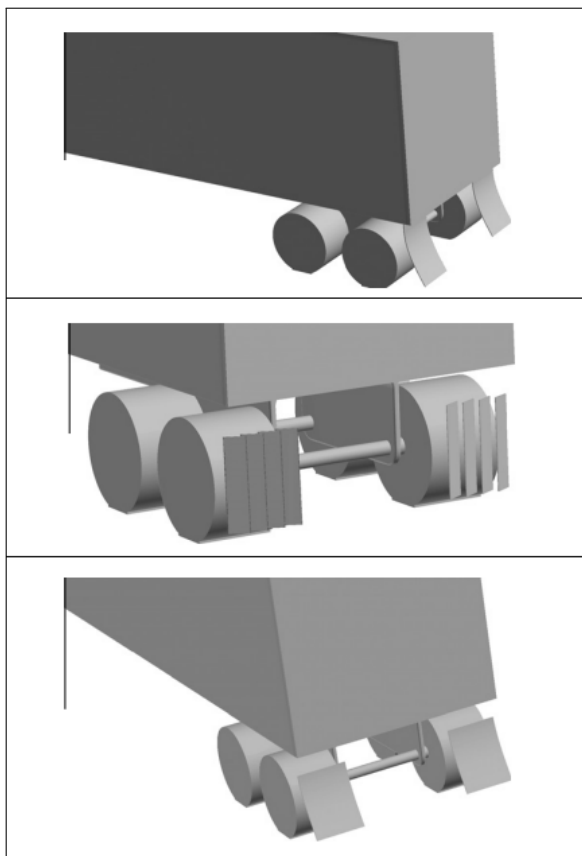


Figure 2.13: Various mudflaps designs tested by Hyams et al., 2011 namely: full mudflaps (upper), half slats (middle) and half mudflaps (lower)

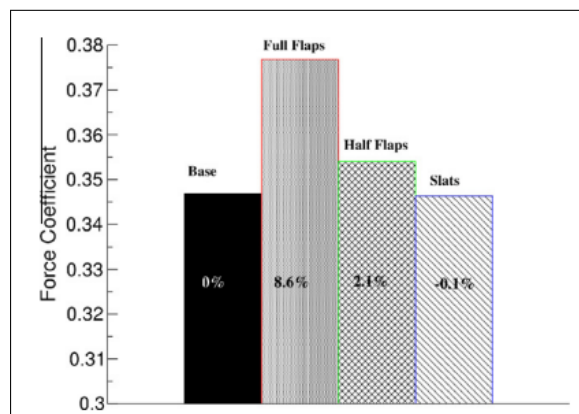


Figure 2.14: Comparison of drag coefficients for the different mudflap designs with respect to Generic Conventional Model (GCM) as baseline, tested by Hyams et al., 2011. $Re = 1.15$ million.

2.1.3. Experimental Setups

Unlike aeroplanes, vehicles whose primary locomotion is via ground require a special requirement to simulate the effects of the moving ground. Therefore, this section deals with different experimental setups used in the past for simulating the effects of moving ground along with limitations. Subsection 2.1.3.1 explains the conveyor belt that is the most widely used method to simulate moving ground. The following subsection 2.1.3.2 reviews methods such as tangential blowing and suction, which do not explicitly require a moving ground. Finally, subsection 2.1.3.3 reviews the use of rollers which is a cheaper alternative to the conveyor belt method for simulating rotation.

Conveyor belt

Since the moving ground is a significant factor in deciding the flow physics around the wheel, whose effects were previously discussed in section 2.1.1.3, there have been a variety of methods that were tried to simulate such effects. The conveyor belt remains as the most widely used setup to simulate the moving ground, primary due its ability to both induce wheel rotation and have no boundary layer over it. The system consists of a belt that translates at a speed that matches the free stream velocity, this translation is usually achieved with the help of rollers that are enclosed within the belt. One of the earliest is Hackett and Boles, 1979, here the moving ground effects were simulated using a belt conveyor system as seen in fig. 2.15.

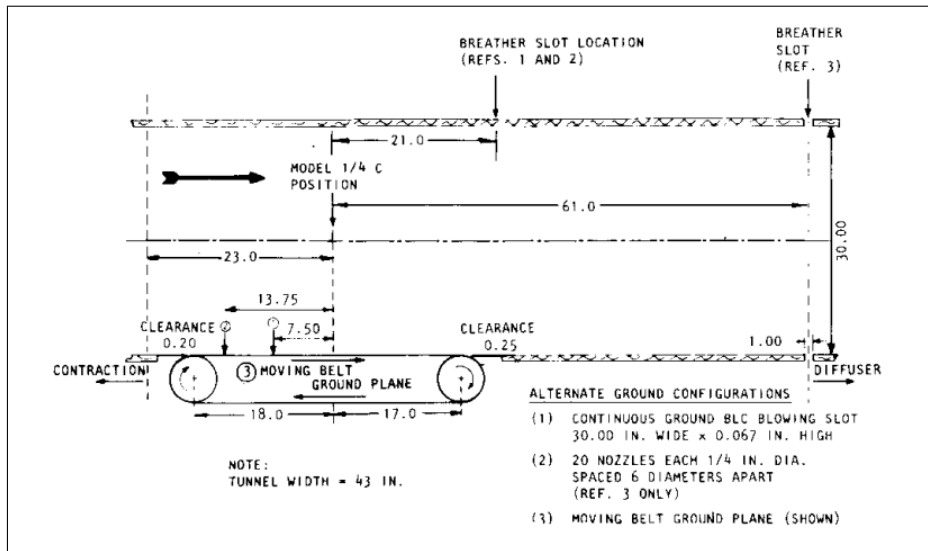


Figure 2.15: Conveyor belt (moving belt) setup used by Hackett and Boles, 1979

Tangential blowing and suction

In the same work by Hackett and Boles, 1979, they provided a cheaper method. It was tested in conditions where despite having a stationary ground, the effects of the oncoming boundary layer were tackled using a tangential blower. A tangential blower is a device that blows pressurized air along a thin pipe/outlet to add extra fluid with higher momentum to either re-energize the flow or remove the already present layer over a body. In this work, the outlet velocity at the tangential blower was determined by trial and error. The idea was to monitor the ground skin friction values over the floor using static probes that indicated the flow direction and velocity. Typically, these probes would indicate the presence of a reversed flow along a specific section of the ground due to boundary layer separation. When the tangential blower was used at an optimal outlet velocity, these regions were successfully removed, and the probes gave positive readings corresponding to the attached flow. Unlike most of the papers presented in this survey, this work, in particular, included testing an aeroplane model. Hence, it was seen that separation points on the ground changed at higher altitudes and the angle of attacks of the model. Accordingly, the tangential blower was required to blow at higher velocities. This led to a large spread of the blown air far downstream, making it less effective. Therefore, to avoid this issue, an array of multiple nozzles were used instead of the continuous blowing slot. These nozzles helped increase the momentum of the fluid at regular intervals, but on the hind side led to thicker boundary layers which would increase the apparent lift on the body, especially at the lower angles of attacks. Hence, it would be best suitable only at a higher angle of attack.

Next, Mercker and Wiedemann, 1990 compared techniques such as distributed suction, tangential blowing, belt conveyor system and the stationary ground itself to quantify the pros and cons of each technique for an automobile model. The distributed suction method involved an array of suction holes along the length of the test section, which were used to suck in the oncoming boundary layer. Similarly, the tangential blowing system was placed ahead of the model at a distance of 3.75 [m] upstream of the model. Although theoretically, the outlet velocity was about four times the free stream velocity, the actual outlet used was about 5.85 times the velocity. The required outlet velocity was estimated using the equivalent velocity needed to reduce the displacement thickness of the already present boundary layer to zero. The discrepancy between the theoretical and the actual value was assumed due to different streamwise evolutions of the boundary layer. The conveyor belt system and the stationary ground method remained similar to the ones used in the past.

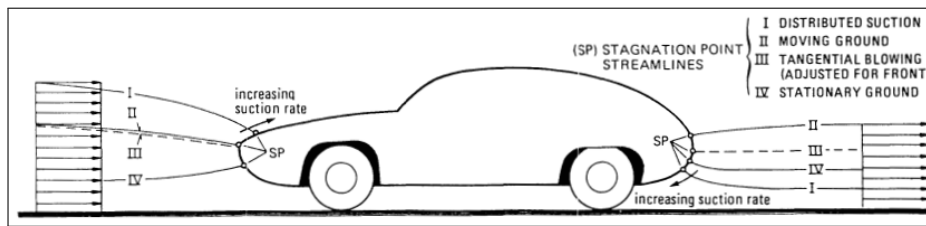


Figure 2.16: Comparison of frontal and rear stagnation point location for various ground simulation techniques Mercker and Wiedemann, 1990

Consequently, the comparison of the results was mainly based on the location of stagnation points around the model, as seen in fig. 2.16. As the conveyor belt system is the closest to the actual moving ground case, it was considered the reference. In general, the tangential blowing system produced stagnation points closest to the conveyor belt case, followed by the distributed suction and stationary ground case. The stagnation points at the frontal part of the model for the tangential and conveyor belt case were almost identical; they differed only at the rear stagnation point. It was assumed that this deviation was majorly due to the inefficiency of the tangential blower downstream of the flow. The distribution suction was mainly flawed by the presence of local suction zones that produced a non-uniform flow and was seen to affect the mass balance of the oncoming flow by reducing it via suction. In terms of flow angularity, it was seen that the suction method induced angular perturbations an order larger than that of the tangential blowing, which was quite negligible. The perturbations produced by the suction method decayed slower than the tangential blower method.

Furthermore, the flow quality further downstream of the model was compared with flow conditions in Couette flow since the wind tunnel walls, and the moving ground simulated a similar case. Hence based on Couette flow assumptions, the effects of each method on downstream flow were compared. Similar to the previous results, the conveyor belt produced most similar conditions followed by tangential blowing, suction method and stationary ground. In conclusion, the work deemed tangential blowing a good alternative for the conveyor belt system.

Fago et al., 1991 tested the effects of a moving ground on ground clearance. The work was based on an automotive model (without wheels) with low ground clearance. The moving ground effects were quantified using a comparison between the stationary ground and a conveyor belt system. The results showed that the stationary ground led to large drag values, becoming less prominent at higher clearances. It suggests that local effects are naturally more effective when closer to the ground. Similarly, the lift values were also higher for the stationary ground at low clearances and gradually reduced for higher clearances. Furthermore, when the length of the model was increased, it was seen that the drag values changed very slightly, whereas the lift values were comparatively higher. The reason for such a difference between the stationary and moving ground was the increasing skin friction under the model, which was prominent for the stationary case, altering the flow structures beneath and downstream of the model.

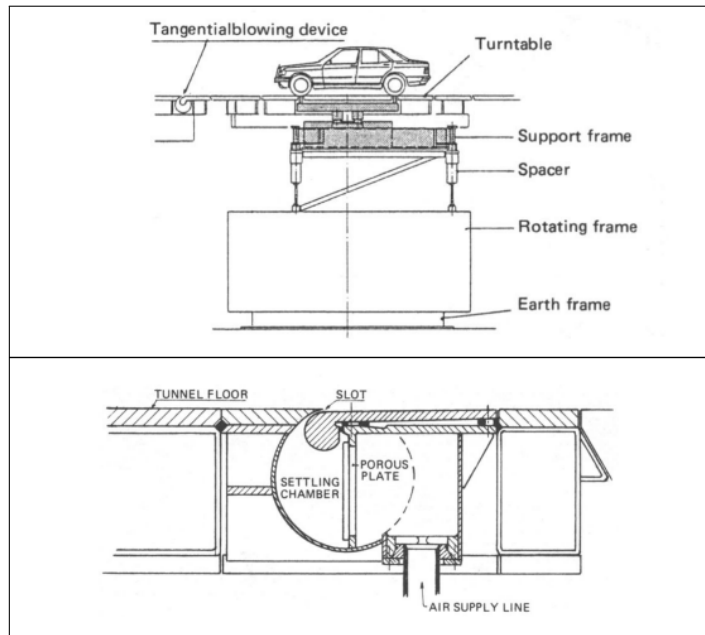


Figure 2.17: Moving ground (upper) setup used by Mercker and Berneburg, 1992 with tangential blowing (lower) setup designed by Berndtsson et al., 1988

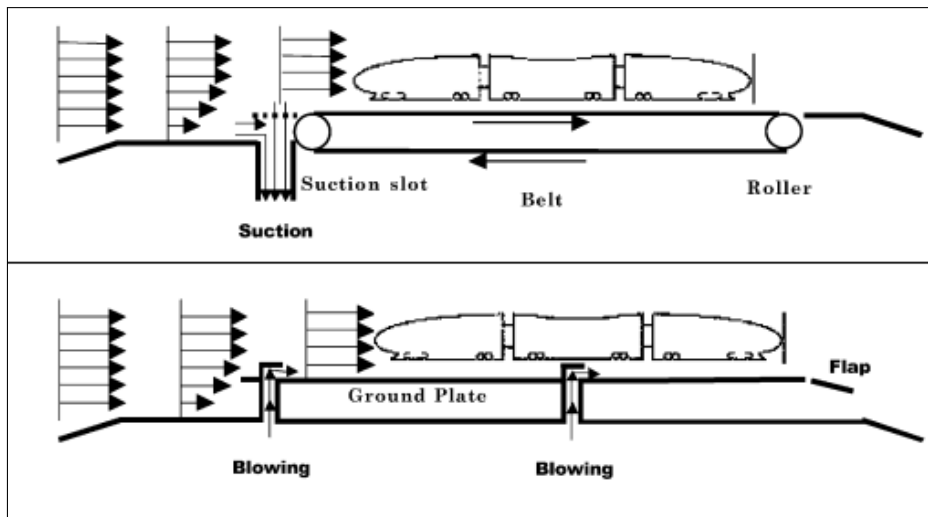


Figure 2.18: Conveyor belt (upper) and Tangential blowing (lower) setup used by Kwon et al., 2001

Sometime later, Kwon et al., 2001 investigated a combination of ground simulation techniques to simulate floor over high-speed trains. The work mainly compared two methods, the first being a slightly elevated conveyor belt where a suction slot was introduced right before the elevation. The combination of the suction slot and slight elevation to the conveyor belt ensures that the oncoming boundary layer and its effects upstream of the model are almost negligible. The second method comprises a tangential blowing system, where multiple slots are used along the length of the model downstream, as seen in fig. 2.18. Similar to that of Berndtsson et al., 1988 and Mercker and Wiedemann, 1990 as seen in fig. 2.17, the outlet velocity was determined using the displacement thickness as seen in eq. (2.3).

$$\delta^* = \int_0^{\infty} \left(1 - \frac{u}{U_0}\right) dy \quad (2.3)$$

where:

$$U_0 = \text{Free stream velocity [m/s]}$$

$$u = \text{Required jet velocity [m/s]}$$

One interesting outcome the work suggested was the difference in the strength of the vortical structures at the base of the model for these two methods. The tangential blowing method led to a stronger set of vortical structures, which is assumed to be the slightly higher base drag values. Although there were slight differences in the overall drag values for the more extended models, the work stated that the tangential blowing system could be an excellent alternative to the conveyor belt when displacement thickness is zero.

Rollers

Recent studies, such as the work of Rajaratnam et al., 2019, demonstrate the effectiveness of rollers instead of using the conveyor belt. The work reviews the roller setup using experiments and numerical simulations using the Detached Eddy model (DES), and K-Omega SST Improved Delayed Detached Eddy model (IDDES). The experimental setup included a wheel mounted on a roller, with 3-D printed coverings that diminish suction effects due to the gaps around the contact patch as seen in fig. 2.19. Nevertheless, the results did indicate an increase in the overall lift coefficient at the wheel's base due to the inevitable suction, which reduces the pressure around the contact patch leading to a higher pressure difference between the bottom and top part of the wheel. However, this effect was also stated by previous works by Stapleford and Carr, 1969, Cogotti, 1983 and Mears et al., 2004. Hence, considering the marginal differences in the results, the work fairly demonstrated the setup's effectiveness and agreed with the previous stationary and rotating wheels studies.

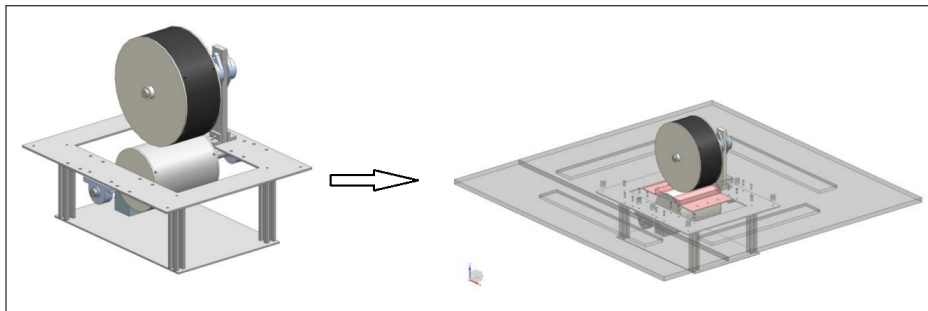


Figure 2.19: Roller setup with 3-D printed coverings (in pink) used by Rajaratnam et al., 2019

2.1.4. Concluding Remarks for literature survey

The literature survey aimed to give an overview of the major efforts made by various authors to understand wheel aerodynamics, the effects of wheel peripherals, and the different experimental setups used for simulating wheel flow.

First, the theoretical foundations were laid down using the most prevalent theories. It was found that Fackrell's work was the most influential, and the latter findings were in good accordance with it. All in all, it was seen that the rotating wheels exhibited jetting phenomena, along with a set of counter-rotating vortex pairs behind the wheel. More specifically, the lower rotating vortex pair was more prominent than the upper set due to the ground effects. However, there lacks an accurate consensus on the other vortex structures behind the wheel. The more critical dimensionless parameter was identified as the Reynolds. Consequently, most wheels were tested at a Reynolds number of 0.5 million, signifying the importance of the post-critical Reynolds regime.

Second, the influence of wheel peripherals was understood to gain insights in designing an efficient mudflap. The presence of bodies, such as axle and wheel camber, induces asymmetries in the flow mainly due to the difference in pressure fields caused by the geometries. Second, for mudflaps, there

was limited literature available. It suggested that vertical slats slanted inwards toward the axle/underbody of the vehicle reduce the drag considerably. However, it lacks a detailed aerodynamic analysis, requiring further investigation.

Third, having understood what to expect, the different experimental setups were explored. The significant challenges of setting up such a test environment included the commonly found ground boundary layer absent in real-time situations and the need to mimic wheel jetting. Therefore, the conveyor belt setup was the most effective and vastly used as it directly addresses the problems mentioned earlier. However, many alternatives were used in the past due to the highly expensive monetary nature of the conveyor setup. These include the tangential blower and suction systems that partially remove the boundary layer and the roller system that simulates jetting. Hence a suitable alternative could be to use a combination of these setups to simulate moving ground at a relatively lower expense.

Finally, the literature survey suggested that a potential alternative to the conveyor belt is possible. In principle, the alternative should simulate the primary aspects of the moving ground, i.e. no boundary layer on the ground along with wheel rotation. Therefore, in the master's thesis, the aim would be first to create such a setup and then try different mudflap designs based on the wake and vortex structures behind the wheel.

2.2. Research objectives and questions

This section consists of two parts: the research objective in section 2.2.1 and the research questions of the thesis in section 2.2.2.

2.2.1. Research Objectives

In the previous section, it was seen that there exists limited literature on mudflap aerodynamics, which lacked a detailed analysis of its design. This motivates us to investigate mudflaps using a realistic setup and contribute towards reducing the drag they offer. Hence the research objective of this project is:

“To experimentally investigate the effects of mudflaps on wheel aerodynamics by employing particle image velocimetry on different designs, under the influence of a simulated moving ground. ”

To further simplify the main goal stated above, it is divided into three sub-goals:

The first is to reproduce a simulated moving ground using a combination of previous setups (mentioned in the literature); these include the simultaneous use of a leading-edge, a roller and a tangential blower. Additionally, the tangential blower used in this setup, in particular, needs to be designed from scratch. Hence a major part of the sub-goal would be to design an efficient tangential blower.

The second is to assess the effectiveness of the simulated ground on an isolated wheel by verifying the results from the literature. This will include comparing flow parameters such as velocity and vorticity obtained particle image velocimetry.

Finally, the last sub-goal is to test different mudflap designs of varying solidity ratios⁴ and its location, placed behind a double wheel setup (isolated wheel alongside another wheel) using stereoscopic particle image velocimetry. Additionally, the underbody effects of a heavy-duty vehicle will be simulated using a flat plate over the wheel-mudflap assembly.

⁴Solidity ratio: Ratio of frontal area of the mudflap to the frontal area of the fully solid mudflap

2.2.2. Research Questions

1. What are the geometric design considerations for the tangential blowing slot?
 - (a) What is the mean velocity profile obtained from the tangential blowing prototypes?
 - (b) What design choices concerning the blowing slot effectively provide uniform tangential blowing?
2. Can the simulated moving ground be a good alternative to the conveyor belt?
 - (a) What is the boundary layer profile (boundary layer thickness and mean velocity) in the presence of the leading edge with tangential blowing switched off?
 - (b) What is the boundary layer profile (boundary layer thickness and mean velocity) in the presence of the leading edge with tangential blowing switched on?
 - (c) How does the wake in terms of velocity fields and vortex structures behind an isolated wheel compare with literature (stationary and rotating cases)? What differences does tangential blowing bring to the rotating case?
 - (d) Are there any drawbacks of using the simulated moving ground?
3. Which portion of the mudflap design (considering a rectangular frontal area) is responsible for higher drag contributions?
 - (a) What differences do the double wheel and the underbody bring on the velocity fields and vortex structures of the wheel-mudflap setup?
 - (b) What is the effect of solidity and solidity location in mudflaps? How does it influence the drag, velocity fields and vortex structures behind the wheel?

3

Experimental Techniques

This chapter gives an overview of the experimental techniques used in this project. It comprises of two experimental campaigns, the first uses planar particle image velocimetry and the second uses stereoscopic particle image velocimetry. A brief of their working principle and methodology is provided. Further, the method of estimating drag from PIV data is explained.

In this chapter, section 3.1 explains about the PIV in general, and provides its working principle, details about the imaging system, tracer particles and illumination system. section 3.2 focuses mainly on the working principle of Stereoscopic PIV and the extra steps taken compared to the planar measurements. Finally, section 3.3 briefly explains how to estimate drag from PIV data using a control volume approach, particularly pressure field reconstruction.

3.1. Planar Particle Image Velocimetry

Particle image velocimetry is an experimental technique that involves the determination of fluid velocity using two subsequent images of certain fluid particles. The particles are called tracer particles, which are first injected into the free stream fluid (air). Next, the particles are illuminated using a laser light source at two different instances. The time between the two instances is called the pulse separation time (Δt). When illuminated, the images are obtained using digital cameras that use the frame straddling technique to store the data. Finally, having obtained the images, a cross-correlation analysis is done between the two images to identify the individual particles in each image. Using this information, the corresponding displacement of the particles and hence the equivalent velocity can be known. Planar PIV is a sub-category of PIV measurement types. In this method, velocity fields of a given plane are measured using one camera as shown in fig. 3.1. These measurements provide two velocity components in the two-dimensional measurement plane (2D-2C). The individual components of a PIV system are further explained below.

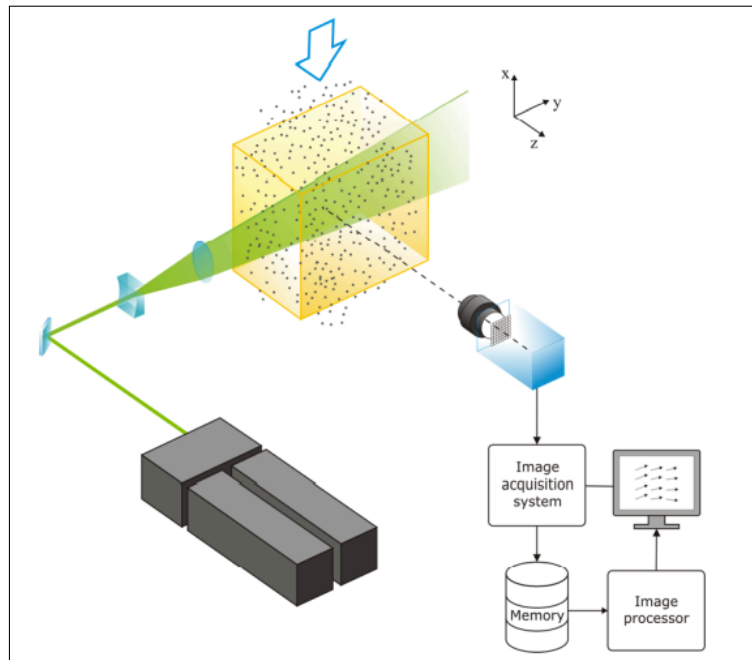


Figure 3.1: Schematic of a planar PIV configuration showing different components: Laser illumination source, optics, camera, measurement plane, and a PC for image acquisition and processing, reproduced from Scarano, 2013.

3.1.1. Imaging system

The imaging system mainly consists of the charge coupled device (CCD) cameras, which have optical lenses of a pre-defined focal length that helps achieve the field of view for a given measurement. The field of view is tuned using the magnification factor (M) expressed by eq. (3.1), such that a particular region (object plane) shown in fig. 3.2 can be focused.

$$M = \frac{z_0}{Z_0} = \frac{l_x}{L_x} \quad (3.1)$$

where:

M = Magnification factor [-]

z_0 = Image distance [m]

Z_0 = Object distance [m]

l_x = Sensor size [m]

L_x = Object size [m]

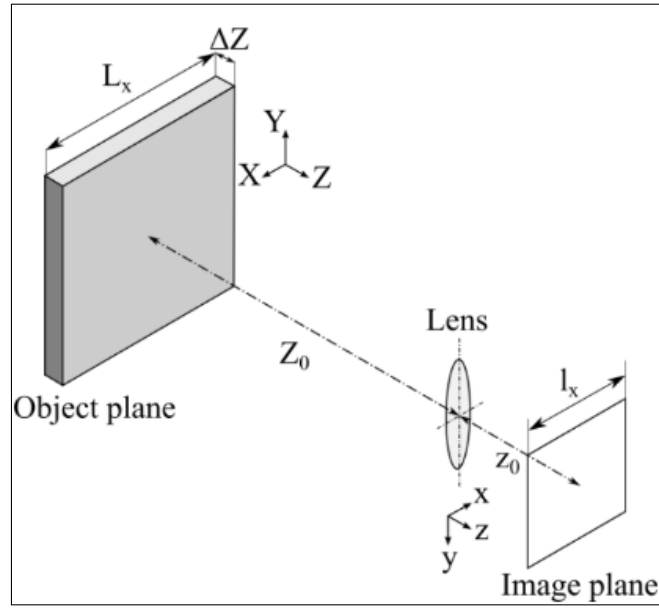


Figure 3.2: Imaging system of a PIV setup depicting the image and object plane along with the required parameters for finding M , reproduced from Sciacchitano, 2014.

Further, assuming the lens used is a thin lens (lens with thickness \ll focal length), the focal length can be described using the optical distances (z_0 and Z_0) as shown in eq. (3.2).

$$\frac{1}{f} = \frac{1}{Z_0} + \frac{1}{z_0} \quad (3.2)$$

Finally, the depth of field will be determined using eq. (3.3). This parameter is important since it provides the thickness of the region in focus. It must be noted that the depth of field must be larger or equal to the laser sheet thickness to avoid noise. Hence, the depth of field is varied using the camera's aperture, which is related to the $f_{\#}$. The $f_{\#}$ is the ratio of the camera's focal length to the lens's aperture.

$$\delta z = 4.88 \left(\frac{1+M}{M} \right)^2 f_{\#}^2 \lambda \quad (3.3)$$

where:

$$\begin{aligned} \delta z &= \text{Depth of field [m]} \\ M &= \text{Magnification factor [-]} \\ f_{\#} &= \text{F stop [-]} \\ \lambda &= \text{Laser light wavelength [m]} \end{aligned}$$

3.1.2. Tracer particles

The next component of the system is the tracer particles. The particles, in general, should be small enough to create negligible changes in the flow properties and yet follow the flow. However, they should also be large enough to be able to scatter light and hence be detected by the camera. The particles used usually oil-based or water-based (for free stream fluid as air), which is non-toxic and easier to evaporate.

To be able to follow the flow accurately, the particle response time will be evaluated using the eq. (3.4)

from Raffel et al., 1998, assuming the particles operate in Stokes flow regime⁵. Using the particle response time, the particle's ability to react to the sudden change in fluid velocity can be measured. A lower particle response equates to a better representation of fluid flow velocity. Therefore, a smaller particle diameter seems preferable for representing fluid flow better.

$$\tau_p = \frac{d_p^2(\rho_p - \rho_f)}{18\mu} \quad (3.4)$$

where:

$$\begin{aligned} \tau_p &= \text{Particle response time [s]} \\ d_p &= \text{Particle diameter [m]} \\ \rho_p &= \text{Particle density [kg/m}^3\text{]} \\ \rho_f &= \text{Fluid density [kg/m}^3\text{]} \\ \mu &= \text{Fluid dynamic viscosity [kg/(m.s)]} \end{aligned}$$

The ability to scatter light is an important feature of the particles since it allows them to be easily identified. The scattered light depends on parameters such as the ratio of the particle's refractive index to fluid, particle size, orientation, shape and polarization, Raffel et al., 1998. Using Mie's scattering theory, it can be concluded that for particles with diameters larger than the wavelength of the illuminating light, there will be maximum forward light scattering and much lower sideward and backward scattering (several orders lower). Figure 3.3 shows the light scattering intensity of an oil particle using a polar distribution depicting the dominance of forward scattering.

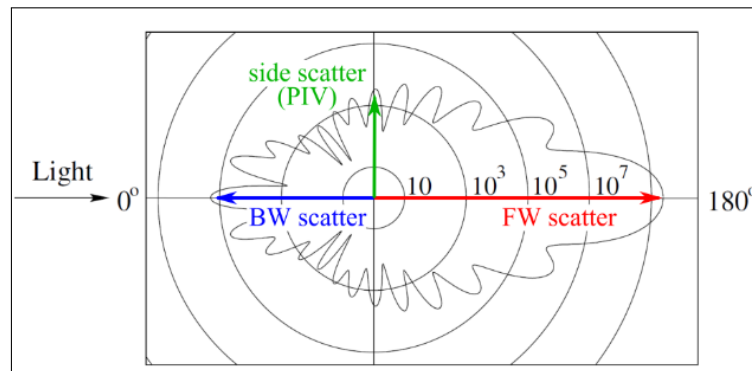


Figure 3.3: Light scattering intensity from laser light with wavelength of 532 [nm] as a function of scattering angle by 1 [μm] oil particle showing higher forward (FW) scatter in comparison to backward (BW) and side scatter, reproduced from Scarano, 2013.

3.1.3. Illumination

The illumination is provided using a laser light source. The Nd:YAG (neodymium-doped yttrium aluminium garnet) solid-state lasers are usually preferred since they provide highly energy-dense, monochromatic light at short pulse durations. The laser sheet's dimensions are controlled using a combination of optical lenses. These are placed to produce a well-aligned set of laser sheets that appear at two different time instances separated by Δt .

⁵Stokes flow: Flow which is dominated by viscous forces, with Reynolds number based on particle diameter $\ll 1$

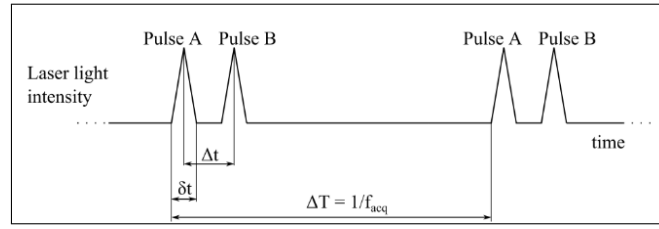


Figure 3.4: Schematic for an illumination signal as function of time showing pulse width and pulse separation, reproduced from Sciacchitano, 2014.

The pulse duration (δt) is the duration of illumination of the particles as shown in fig. 3.4. It determines whether the particles are visualised as streaks or dots. Ideally, the particles should be identified as dots to distinguish between two different particles easily. Hence, shorter pulse duration is preferred as longer ones produce streaks. Therefore, an upper limit for the pulse separation width can be estimated using eq. (3.5).

$$\delta t \ll \frac{d_\tau}{M|u_p|} \quad (3.5)$$

where:

$\delta t =$ Pulse duration [s]

$d_\tau =$ Particle image diameter [m]

$M =$ Magnification factor [–]

$u_p =$ Particle velocity [m/s]

3.1.4. Velocity determination

The final component of the system includes velocity determination. The steps are as follows.

Firstly, the obtained image frames are partitioned into small cells called interrogation cells or windows that contain a statistically significant number of tracer particles as shown in fig. 3.5. To acquire the displacement of a tracer particle, identifying that particle at the two instances is required. This is done using a cross-correlation function shown in eq. (3.6). Here, I and I' are the two images with corresponding cell intensities; m and n relate to the difference in the row and column cell number of the image window between the two images.

$$\Phi(m, n) = \frac{\sum_{i,j=1}^{I,J} I(i, j) \cdot I'(i + m, j + n)}{\sqrt{\sigma(I) \cdot \sigma(I')}} \quad (3.6)$$

where:

$\Phi(m, n) =$ Cross correlation value

$I =$ Interrogation window of image 1

$I' =$ Interrogation window of image 2

$m, n =$ Row and column number

$\sigma =$ Standard deviation

The cross-correlation function produces the largest peak only when the two windows correspond to the same set of tracer particles with similar orientations. Now that the particle is tracked in two images, the position difference provides the displacement. Hence, the velocity of the tracer particle in terms of image scale can be calculated using the distance travelled and the pulse separation time between the two images. Further, this value can be divided by the magnification factor to obtain the real-time velocity of the particle.

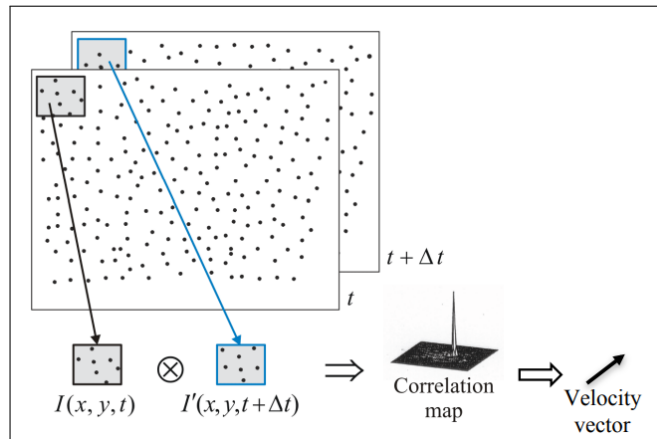


Figure 3.5: PIV cross correlation map of two windows between two images (I and I'), reproduced from Scarano, 2013.

Although eq. (3.6) can be used to determine the cross-correlation in physical space, the calculations get less computationally intensive when done in the spectral space (numerical cross correlation). Here the cross-correlation is found using the Fourier Transform (FT) based on the Wiener-Khinchine theorem as seen in eq. (3.7).

$$I \otimes I' = FT^{-1}[FT(I) \times FT(I')] \quad (3.7)$$

where:

I = Interrogation window of image 1

I' = Interrogation window of image 2

$FT(x)$ = Fourier transform

3.2. Stereoscopic Particle Image Velocimetry

Stereoscopic PIV is a sub-category of PIV measurement types which involves the usage of two cameras. These measurements provide the in-plane and out-of-plane velocity components for a two-dimensional measurement plane (2D-3C). Furthermore, having two cameras allows for correcting errors caused by the out-of-plane velocity components, which can be mistaken as in-plane displacements by a single camera.

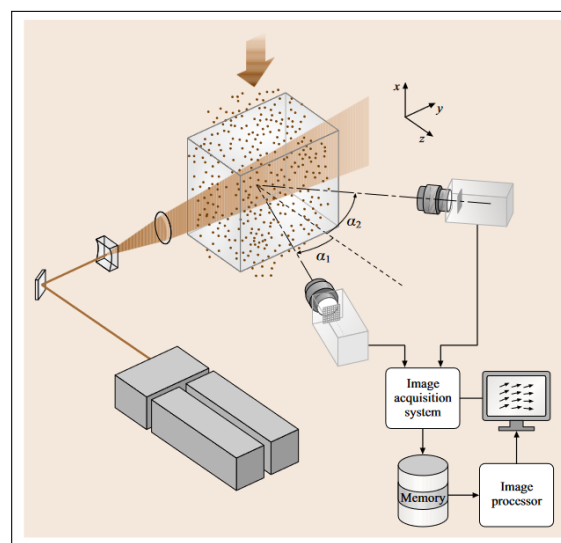


Figure 3.6: Schematic of a stereoscopic PIV configuration showing components similar to the planar configuration but with an additional camera, reproduced from McKeon et al., 2007.

Stereoscopic PIV involves a Scheimflug configuration, where the cameras are placed such that the image planes are at an angle to the optical axis of the camera lens. Consequently, the image planes will become non-parallel to the object in focus. There will also be a slight misalignment between the image planes, leading to different magnification factors and perspectives. Therefore, a correction is applied using a polynomial mapping function, Prasad, 2000, also known as geometrical calibration. Here the functions map the object and image coordinates using a reference, usually a calibration plate. Additionally, coinciding the calibration plate with the laser sheet is necessary for calibration. This helps reduce errors in the mapping process. However, a self-calibration procedure is applied to further remove smaller misalignment(s), where a stereo-cross-correlation is used to identify the individual particles between images from the two cameras. More information about stereoscopic PIV can be found in the work by McKeon et al., 2007.

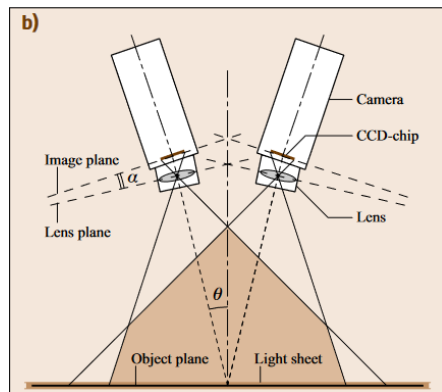


Figure 3.7: Camera configuration for stereoscopic PIV using angular method where the angle between the image and lens plane is variable, reproduced from McKeon et al., 2007.

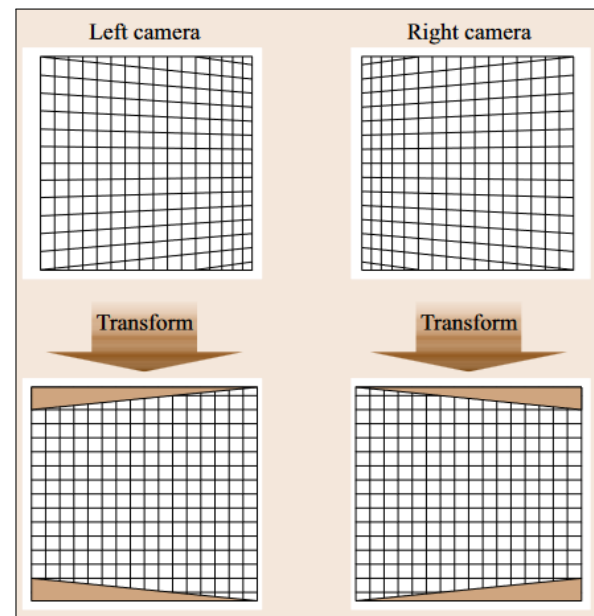


Figure 3.8: Perspective deformation for both the cameras used in stereoscopic PIV, reproduced from McKeon et al., 2007.

3.3. Drag estimation from PIV

Drag estimation from PIV can be done using the wake integral method, sometimes called the momentum defect principle. The principle uses the conservation law of momentum to apply within a control volume, as shown in fig. 3.9. The boundaries of this control volume are defined such that planes present around the model (whose drag is to be found) are sufficiently far enough to have a pressure equal to the free stream pressure, and the planes present both upstream and downstream are aligned to the free stream flow direction. The steps to estimate drag are explained below.

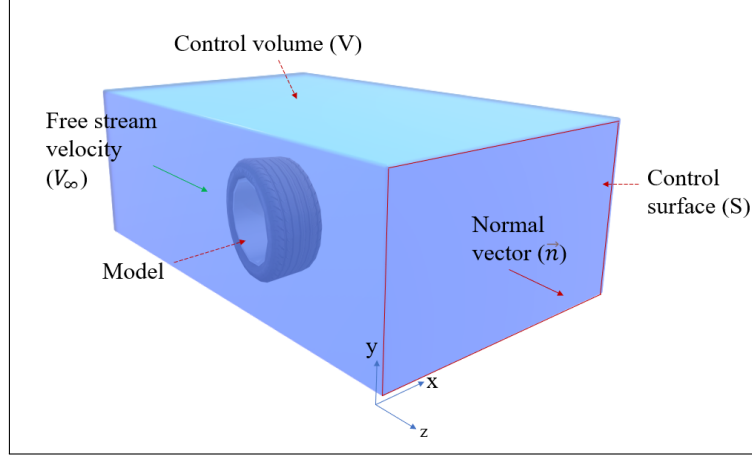


Figure 3.9: Schematic of the control volume showing the axis system, free stream velocity, and a given control surface.

First, consider the momentum equation in the streamwise direction. Since the drag force acts along this direction, it can be substituted as the force term as seen in eq. (3.8).

$$F_{drag}(t) = -\rho \iiint_V \frac{\partial w}{\partial t} dV - \rho \iint_S (\vec{v} \cdot \vec{n}) w dS - \rho \iint_S ((p\vec{n} - \vec{\tau} \cdot \vec{n}) dS)_z \quad (3.8)$$

Here, $F_{drag}(t)$ represents the drag force at a given time instant t , V is the control volume, S is a control surface, \vec{n} is outward normal vector from the control surface. The free stream air density is given by ρ , $\vec{\tau}$ is the shear stress tensor, p is the static pressure, V_∞ is free stream velocity and w is velocity component in the free stream direction.

Since the control volume boundaries are sufficiently far enough from the body, the viscous contributions can be neglected, Kurtulus et al., 2007 and non-streamwise surface contributions from the $\iint p dS$ and $\vec{v} \cdot \vec{n}$ term is zero. This simplifies the equation to eq. (3.9).

$$F_{drag}(t) = -\rho \iiint_V \frac{\partial w}{\partial t} dV + \rho \left(\iint_{upstream} V_\infty^2 dS - \iint_{downstream} w^2 dS \right) + \left(\iint_{upstream} p_\infty dS - \iint_{downstream} p dS \right) \quad (3.9)$$

Next using the mass conservation equation that states mass entering the control volume upstream is equal to the mass exiting downstream downstream in the wake, the equation becomes eq. (3.10).

$$F_{drag}(t) = -\rho \iiint_V \frac{\partial w}{\partial t} dV + \rho \iint_{wake} (V_\infty - w) w dS + \iint_{wake} (p_\infty - p) dS \quad (3.10)$$

Finally applying the Reynolds averaging replacing the quantities such as pressure and velocity as a sum of their mean and fluctuation components ($x = \bar{x} + x'$). The temporal term and fluctuation terms in the equation drops to zero. This gives the final drag equation as eq. (3.11).

$$\bar{F}_{drag} = \rho \iint_{wake} (V_\infty - \bar{w}) \bar{w} dS - \rho \iint_{wake} \overline{w'^2} dS + \iint_{wake} (p_\infty - \bar{p}) dS \quad (3.11)$$

Alternatively, the equation can also be written in terms of drag coefficient shown by Talezade and Manshadi, 2020, where A is the frontal area of the model, as shown in eq. (3.12). The first term of equation represents the

$$C_d = \underbrace{\frac{2}{\rho V_\infty^2 A} \iint_S (p_\infty - \bar{p}) dS}_{\text{Pressure term}} + \underbrace{\frac{2}{A} \iint_S \frac{\bar{w}}{V_\infty} \left(1 - \frac{\bar{w}}{V_\infty}\right) dS}_{\text{Momentum term}} - \underbrace{\frac{4}{AV_\infty^2} \iint_S \frac{\overline{w'^2}}{2} dS}_{\text{Fluctuation term}}. \quad (3.12)$$

From, eq. (3.12), it can be seen that the drag coefficient of the object can be calculated using the mean velocity, streamwise fluctuation velocity and the mean pressure field data. However, from PIV, only the velocity and its fluctuation data can be retrieved, and pressure data is not readily available. Hence the pressure field data is reconstructed using the methodology demonstrated by Van Oudheusden, 2013; Van Oudheusden et al., 2007. The details are explained in the subsection below.

3.3.1. Pressure field reconstruction

The conservation of momentum equation is again considered under the assumption that the flow is incompressible and having no body force as shown in eq. (3.13).

$$\nabla p = -\rho \frac{D\vec{v}}{Dt} + \mu \nabla^2 \vec{v} \quad (3.13)$$

Expanding the total derivative term in terms of the temporal and spatial terms, the equation becomes eq. (3.14),

$$\nabla p = -\rho \left(\frac{\partial \vec{v}}{\partial t} + (\vec{v} \cdot \nabla) \vec{v} \right) + \mu \nabla^2 \vec{v} \quad (3.14)$$

Further, applying the Reynolds averaging the equation can be written as eq. (3.15)

$$\nabla \bar{p} = -\rho (\bar{\vec{v}} \cdot \nabla) \bar{\vec{v}} - \rho \nabla \cdot (\overline{\vec{v}' \cdot \vec{v}'}) + \mu \nabla^2 \bar{\vec{v}} \quad (3.15)$$

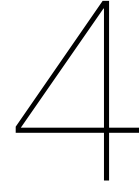
Since the PIV wake planes are considered at distances where the contributions of viscous terms are negligible, the corresponding viscous terms in eq. (3.15) can be ignored. Next taking the divergence of the eq. (3.15), results in eq. (3.16).

$$\nabla^2 \bar{p} = -\rho (\bar{\vec{v}} \cdot \nabla) \bar{\vec{v}} - \rho \nabla \cdot (\overline{\vec{v}' \cdot \vec{v}'}) \quad (3.16)$$

Equation (3.16) is commonly known as the Pressure Poisson Equation (PPE). Mathematically by nature, this equation is a second-order partial differential equation. Hence will require boundary conditions to produce the exact solution. In this particular case, the equation can be solved numerically by applying the boundary conditions to the boundaries of the PIV measurement plane represented on a grid, Hoffman and Frankel, 2018. The grid contains points that represent the velocity values of the PIV plane. Using these values, the terms on the right-hand side of the eq. (3.16) can be evaluated using finite difference schemes, i.e. forward/backward differences for the boundary points and central difference for the inner points. Also, the laplacian operator can be represented using a sparse matrix that relates all the points present in the grid. This leads the numerical system to follow eq. (3.17).

$$\bar{p}_{xx} + \bar{p}_{yy} = F(x, y) \text{ or } \underbrace{\underline{A}}_{\text{Laplacian}} \cdot \underbrace{\underline{P}}_{\text{Unknown pressure}} = \underbrace{\underline{F}}_{\text{Source term}} \quad (3.17)$$

Therefore, solving eq. (3.17) by inverting the matrix A and multiplying it by matrix F will provide the unknown pressure values throughout the grid. The drag estimation used in the thesis is discussed in detail in section 5.2, where both the application of boundary conditions and the evaluation of pressure are provided.



Experimental setup and procedure

This chapter summarizes the experimental facilities, models and procedures used throughout this thesis. Section 4.1 briefs the different wind tunnel facilities used. Section 4.2 briefs the different models used during the campaigns with the rationale behind their designs. Section 4.3 describes the setup used for assessing the tangential blowing slot. Section 4.4 provides the summary of the planar PIV measurements conducted for the simulated moving ground and the isolated wheel. Finally, section 4.5 gives details about the stereoscopic PIV measurements used for capturing the wake of the wheels and mudflap assembly.

4.1. Experimental Facilities

The project as a whole involved two experimental campaigns. The first campaign was aimed at quantifying the effectiveness of the tangential blowing system and the effectiveness of simulated ground for the case of an isolated wheel using planar PIV measurements. This campaign was carried out in the W-tunnel facility, whose details are given in subsection 4.1.1.

The second campaign was carried out in the open jet facility (OJF), whose details are provided in subsection 4.1.2. This campaign dealt with acquiring Stereoscopic PIV measurements at different sections of the wake behind the wheel-mudflap setup. Note that the usage of two different tunnel facilities was purely based on their availability.

4.1.1. W-Tunnel

The W-tunnel is an open-jet, low-speed wind tunnel located at the High-Speed Laboratory of the TU Delft, as shown in fig. 4.1. The W tunnel has a test section with an inlet that consists of a plenum with dimensions $2.0 \times 1.5 \times 2.0$ [m^3] (Height \times Length \times Width). The drive system of the wind tunnel consists of a centrifugal fan driven by an electric motor with a power rating of 16.5 [kW] located after the inlet. The flow passes through a diffuser where it decelerates and then passes through a settling chamber where the flow is straightened to reduce turbulence intensity. Next, the flow contracts via a nozzle with an exit cross-section of 0.40×0.40 [m^2]. The least turbulence intensity of this wind tunnel is of the order of 0.5%⁶.

⁶<https://www.tudelft.nl/lr/organisatie/afdelingen/aerodynamics-wind-energy-flight-performance-and-propulsion/facilities/low-speed-wind-tunnels/w-tunnel>

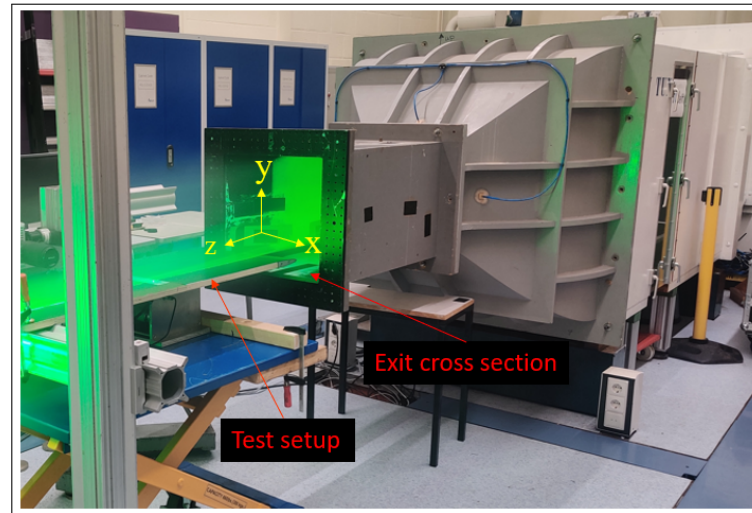


Figure 4.1: W-tunnel in operation, equipped with $0.40 \times 0.40 \text{ [m}^2\text{]}$ exit cross section used during campaign 1 along with the defined coordinate axis system.

The maximum velocity achieved in the wind tunnel is about 35 [m/s] . The velocity of the wind tunnel is determined using a Pitot tube. The pitot tube mainly consists of two openings, one that is usually placed normal to the flow for acquiring the total pressure (P_t) such that the flow stagnates at that point and the other that is placed parallel to the incoming flow to measure static pressure (P_s). Now with the help of these pressure readings using Bernoulli's principle, Anderson, 2011, the velocity of the incoming flow at that point can be calculated as seen in equation 4.1.

$$V = \sqrt{\frac{2(P_t - P_s)}{\rho}} \quad (4.1)$$

where:

$V = \text{Exit velocity [m/s]}$

$P_t = \text{Total pressure [Pa]}$

$P_s = \text{Static pressure [Pa]}$

$\rho = \text{Density of fluid [kg/m}^3\text{]}$

4.1.2. Open Jet Facility

The OJF facility houses an open test section closed return subsonic wind tunnel located at the High-speed facility of TU Delft as shown in fig. 4.2. The OJF has an octagonal exit test section area of $2.8 \times 2.8 \text{ [m}^2\text{]}$. Similar to the W-tunnel, the OJF is driven by a centrifugal fan. An electric motor runs this fan with a power rating of 500 [kW] . Additionally, the flow is passed through a contraction area of 3:1 to allow further acceleration to reach a max speed of 35 [m/s] . The turbulence intensity of this wind tunnel is reported to be 0.5% , Lignarolo et al., 2014. The facility is also equipped with cooling mesh; however, it was not used during the campaign. As a result, the tests were carried out at temperatures ranging from $25\text{-}28 \text{ [}^\circ\text{C]}$.

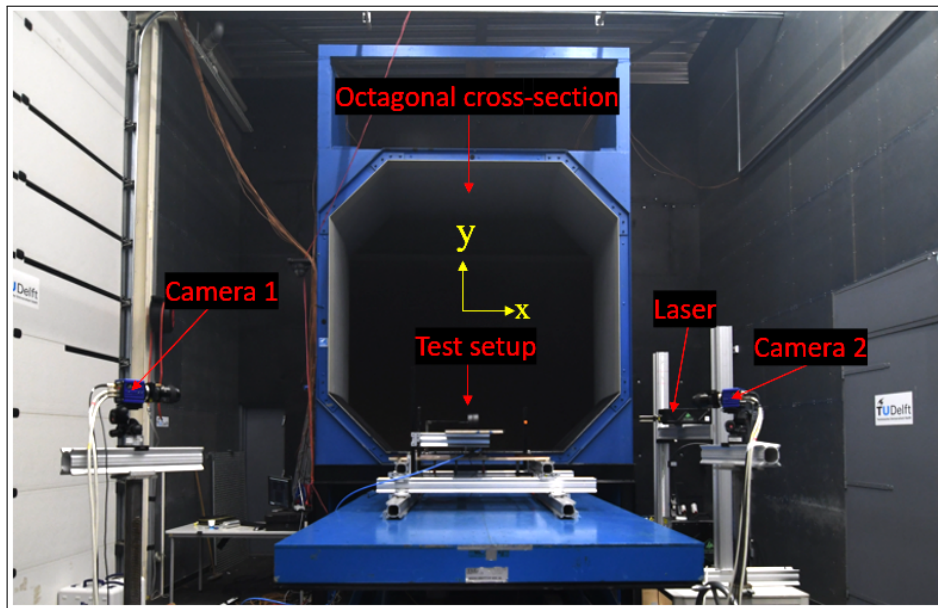


Figure 4.2: Open Jet facility test section area, with $2.8 \times 2.8 \text{ [m}^2\text{]}$ exit cross section area used for campaign 2 along with the defined coordinate axis system.

4.2. Models

This section describes the different models required to emulate a realistic wheel-mudflap assembly. Section 4.2.1 contains the motivation for the simulated moving ground's requirements and an outline for producing its corresponding components. Similarly, section 4.2.2 contains the rationale for selecting wheel and mudflap geometries along with a brief of their production.

4.2.1. Moving Ground

As highlighted in subsection 2.1.4, a moving ground is necessary for emulating wheel flow. However, the expensive nature of the conveyor belt calls for the demand for a cheaper alternative. Hence, in this subsection, a cheaper alternative is provided. This alternative consists of a combination of modified ground simulating devices/systems used in the past. The combination mainly includes a leading edge, roller setup, the tangential blowing system and additional plates to fasten them together. Since the combination is aimed to replicate the different aspects of moving ground, it will be mentioned as the 'simulated moving ground' hereafter.

Leading Edge

A modified super-elliptic leading edge design was used in this thesis shown in fig. 4.3 and also labelled in fig. 4.8. This design was proposed by Lin et al., 1992, whose results were also reported by Schrader et al., 2010.

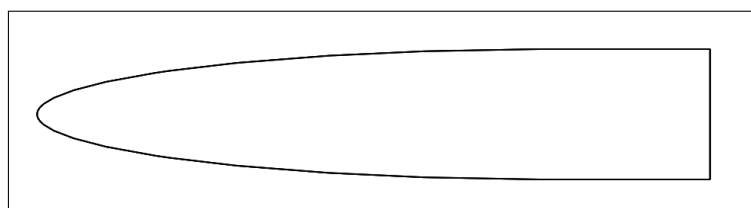


Figure 4.3: Elliptical leading design used by Schrader et al., 2010.

The work investigated the effect of various leading edge shapes on the boundary layer receptivity, where receptivity represented the creation of boundary layer instabilities due to ambient disturbances

like vorticity and sound waves. In terms of geometry, the super ellipse was defined using eq. (4.2). The value of the exponent on the right hand side of eq. (4.2) increases gradually from 2 to 3 from the start of the leading edge to the flat end joint, such that it maintains zero curvature at the joint. The results suggested that the boundary layer was less receptive to sharper leading edge shapes (i.e. ellipses with higher aspect ratios) with continuous curvatures. An aspect ratio ($AR \equiv a/b$) of 6 led to streamwise perturbations of the order of 10^{-4} times the free stream velocity, and a continuous curvature helped reduce the receptivity by almost 50%. Hence, the elliptic design was chosen to represent the leading edge section of the simulated moving ground to avoid any major disturbances that are of the order of the free stream velocity.

$$\left(\frac{y}{b}\right)^2 = 1 - \left(\frac{a-x}{a}\right)^{2+\left(\frac{x}{a}\right)^2} \quad (4.2)$$

where:

$$\begin{aligned} x &= \text{Axial coordinate} \\ y &= \text{Vertical coordinate} \\ a &= \text{Semi - major axis} \\ b &= \text{Semi - minor axis} \end{aligned}$$

Roller Setup

The roller setup consisted of a roller, direct current (DC) motor, side plates, ground plates and a support arm for the wheel support structures. The setup was previously used by Jux, 2021 as shown in fig. 4.4, however slight modifications were made. These included removing the auxiliary roller (non-driven) and placing the support arm further away from the roller. To avoid any aerodynamic influences, the distance was calculated based on eq. (4.4), which is further explained in section 4.2.2.1. Although the auxiliary roller supports the process of wheel rotation and provides stability, the air gap between the two rollers could affect the wheel vortex structures near the ground. Hence it was removed from the roller setup and then the roller setup was accommodated in the simulated moving ground shown in fig. 4.8.

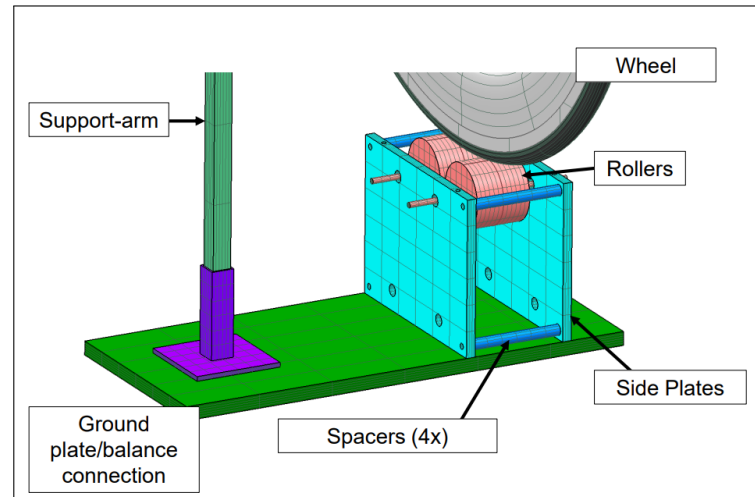


Figure 4.4: Roller setup showing the different components used by Jux, 2021.

The roller surface was knurled to avoid losses due to slippage. Since the free stream velocity for the experiments was set to 25 [m/s], the equivalent roller angular velocity was evaluated using eq. (4.3) approximately equal to 3410 revolutions per minute (RPM) for a roller diameter of 70 [mm].

$$N_{rpm} = \frac{60V_{\infty}}{2\pi r} \quad (4.3)$$

where:

$$N_{rpm} = \text{RPM no. [rev/min]}$$

$$V_{\infty} = \text{Free stream velocity [m/s]}$$

$$r = \text{Radius of the roller [m]}$$

Tangential Blowing System

The tangential blowing system (TBS) was primarily used for locally removing the boundary layer present on the stationary floor. Hence it was placed behind the roller system, i.e. behind the wheel, to remove any immediate boundary layer effects on the wake of the wheel as seen in fig. 4.8. The system consists of a tangential blowing slot, connecting tubes that provide pressurized air, and a pressure regulating valve to indicate and control the supply pressure.

Initially, two blowing slot designs were made. These designs were inspired from the design made by Berndtsson et al., 1988 as shown in fig. 4.5. The first design consists of a step-like outlet (3 [mm] high) to allow the exiting air to be tangential to the floor. The second design consists of a gradual outlet flushed into the floor. The slot design in itself was made such that curve remains smooth and contracts gradually until the outlet. Further, to provide structural strength when exposed high pressure air, these slots were designed with 1.5 [mm] thick support walls placed uniformly across their cross section shown in fig. 4.6. The motivation behind these designs was to finalize an appropriate tangential blowing slot that solely removes the downstream boundary layer without causing any major flow angularity effects downstream. Hence, by comparing the two designs, the final design was made as shown in fig. 4.6, which is further explained in detail in section 6.1.1. For detailed CAD geometry refer appendix fig. B.2.

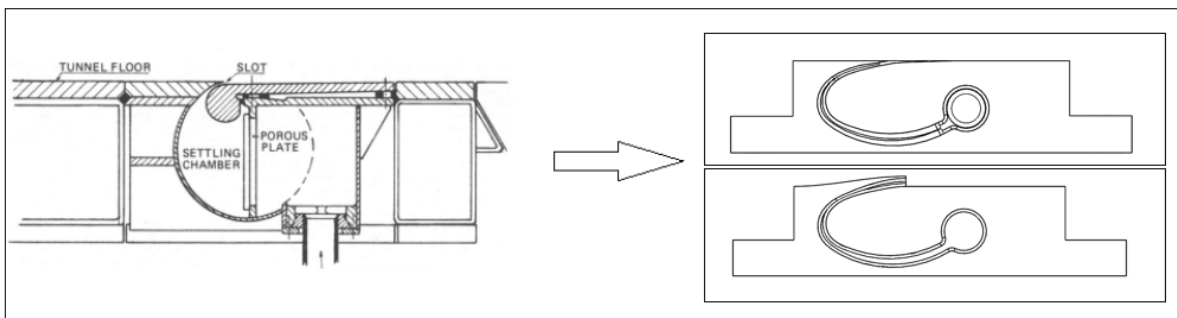


Figure 4.5: Tangential blowing slot cross section: Left - Design from Berndtsson et al., 1988, Right top - Flushed model, Right bottom - Step model.

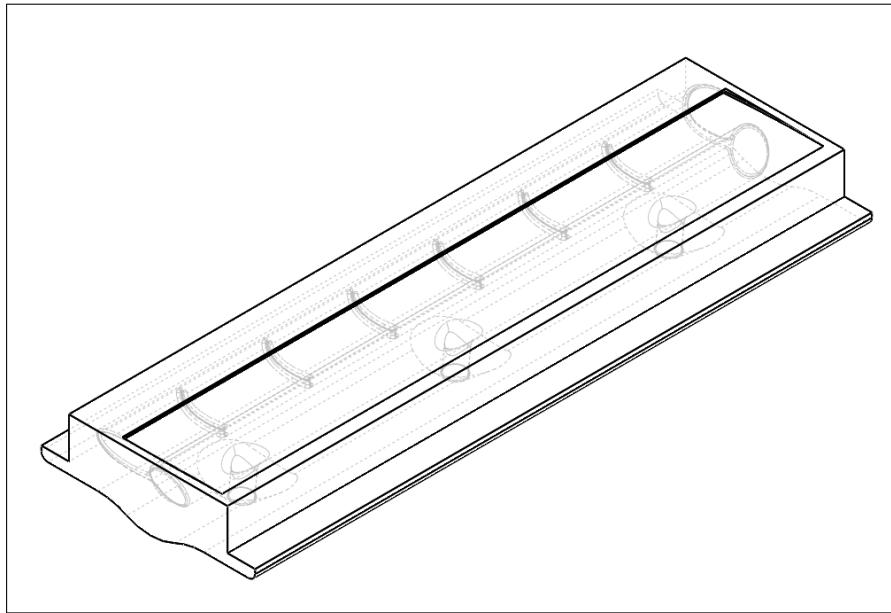


Figure 4.6: Finalised tangential blowing slot design with support walls spread uniformly across the slot, along with three pressure inlet ports present at the underside.

In terms of manufacturing, the blowing slots were 3-D printed via the *Ultimaker(S5)* which used polylactic acid (PLA) as a base material (for further information, refer Ultimaker, 2022). The connecting tubes were ready-made polyvinyl chloride (PVC) tubes. The pressure regulating valves was ready-made and had a gauge with a least count of 0.01 [MPa].

Attaching plates

An integral part of the simulated moving ground was the attaching wooden plates. These plates (For plate geometry CAD refer appendix appendix B) were rectangular cut-outs that act as the floor/ground over which the wheel setup was placed. The width of the plates was estimated to be sufficient to accommodate the wheels' wake and provide enough distance between the wheel and supporting L-rod to avoid any aerodynamic influences. These wooden pieces were cut and produced using a combination of lathe, saw and milling machines. The plates had a flat frontal section on which the leading edge was glued, with two open cut-outs. These hollow cuts allowed the roller and the tangential blower to be consolidated as one. Additionally, an anti-reflective sheet was glued to these plates to avoid/reduce the number of reflections from the surface when exposed to high-intensity light. For detailed CAD geometries of the attaching plates refer appendix fig. B.3 and fig. B.4.

Simulated Moving Ground

The simulated moving ground was made as an alternative to the conveyor belt. As mentioned earlier in section 4.2.1, it comprises the leading edge, roller setup and the attaching plates (floor/ground). 5 [mm] bolts were used to fasten the roller setup and the blower slot to the wooden plates. The fig. 4.7 shows a representative cross section the simulated moving ground and fig. 4.8 shows the simulated moving ground with its respective components, used during experimental campaigns. Note that the blowing slot was 3-D printed in black for the OJF campaign to avoid reflections during the stereoscopic measurements explained later in section 4.5.

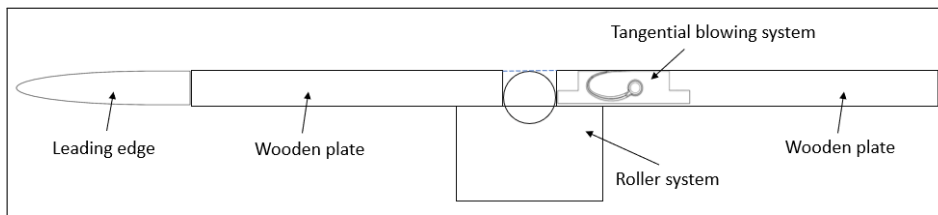


Figure 4.7: Representation of a cross-section of the simulated moving ground (not to actual scale).

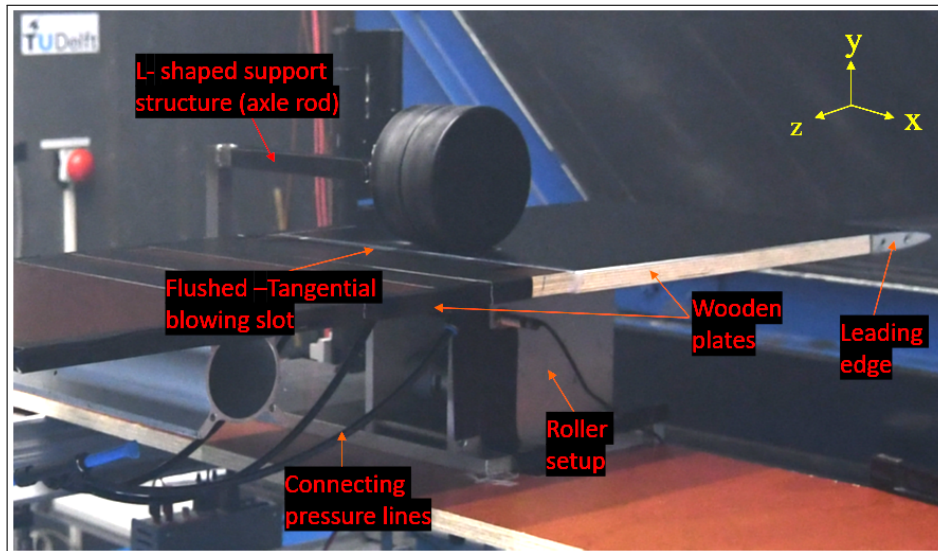


Figure 4.8: Simulated moving ground - A combination of leading edge, roller setup and TBS.

4.2.2. Wheel and Mudflap Assembly

After assembling the moving ground, the next task was to obtain the isolated wheel assembly. The wheel assembly consists of a representative wheel skeleton, hub caps/covers, bearing plates, bearings and a support structure. The subsections 4.2.2.1, 4.2.2.2, 4.2.2.3, 4.2.2.4, and 4.2.2.5 provide the descriptions of the wheel support structure, isolated wheel, double wheel, underbody and the different mudflap designs, respectively.

Wheel support structure

The wheel support structure consists of an axle rod attached to support arm (forming an L-shaped structure) fixed to the support plate, as shown in fig. 4.8. The components are made of stainless steel to provide sturdy support to the wheel, especially under rotation as it is subjected to high loads (normal and bending loads).

The axle rod was designed such that the length of the rod was sufficient to avoid any aerodynamic influences of the support arm to the wheel, and the diameter of the axle rod was scaled to the diameter of a real-time axle found in heavy-duty vehicles. The required length of the axle rod was estimated using potential flow theory, where the cross-section of the support arm was assumed as a two-dimensional circular cylinder as shown in fig. 4.9.

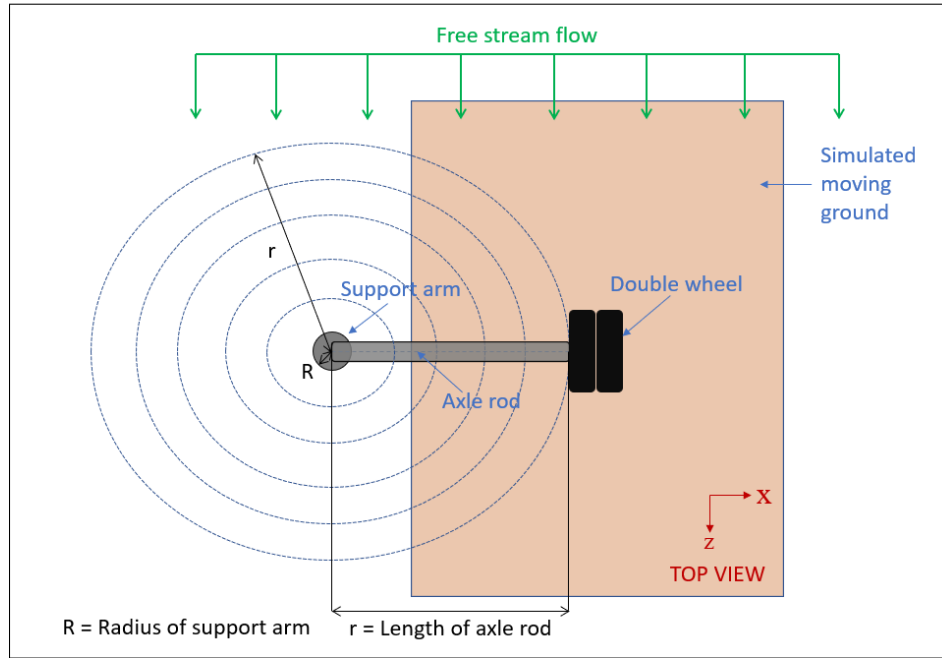


Figure 4.9: Top view of setup depicting the required length of axle rod using potential flow theory.

The velocity induced (U_θ) by the cylindrical structure, i.e. support arm can be estimated using eq. (4.4), Anderson, 2011.

$$U_\theta = U \sin \theta \left(1 + \frac{R^2}{r^2} \right) \quad (4.4)$$

where:

- U_θ = Velocity induced by cylinder [m/s]
- θ = Angle between free stream and reference point [°]
- U = Free stream velocity [m/s]
- R = Radius of the cylinder/support arm [m]
- r = Length for 1% of perturbation velocity [m]

Since the idea was to find largest perturbation velocity induced by the 2-D cylinder, angle was assumed as $\theta = 90$ [°]. Therefore the required radius/length at which the perturbation was 1% of the free stream velocity (i.e. induced velocity = 1.01 times the free stream velocity) can be written as eq. (4.5),

$$1.01U = U \left(1 + \frac{R^2}{r^2} \right) \quad (4.5)$$

$$0.01 = \frac{R^2}{r^2} \quad (4.6)$$

$$r = 10R \quad (4.7)$$

Hence, from eq. (4.7), it was seen that a minimum distance of 10 times the radius of the support arm was required for perturbations of 1% or lower. As a result, the axle rod length was set to 13.5 [cm] for a support arm radius of 1 [cm].

In terms of manufacturing, the components of the support structure were all machined using a combination of lathe and milling machines.

Isolated Wheel

The isolated wheel (for wheel geometry CAD refer appendix fig. B.1) is a single wheel configuration as shown in fig. 4.10. Such a configuration was necessary for comparing and validating the results of an isolated found in the literature. Since the wheel skeletal was ready-made as it was previously used by Jakhar, 2021, and the dimensions were scaled according to actual truck wheel dimensions, no attempts were made to modify the wheel diameter. However, a separate bearing hub was made to accommodate the axle rod. The wheel dimensions were 136 [mm] in diameter and 42 [mm] in width. Further, for the rotating wheel case, the wheel was rotated at 1755 [rev/min] to match the free stream velocity.

In terms of manufacturing, the hubs covers were 3-D printed, the bearing plate was machined, and the bearings were ready-made.

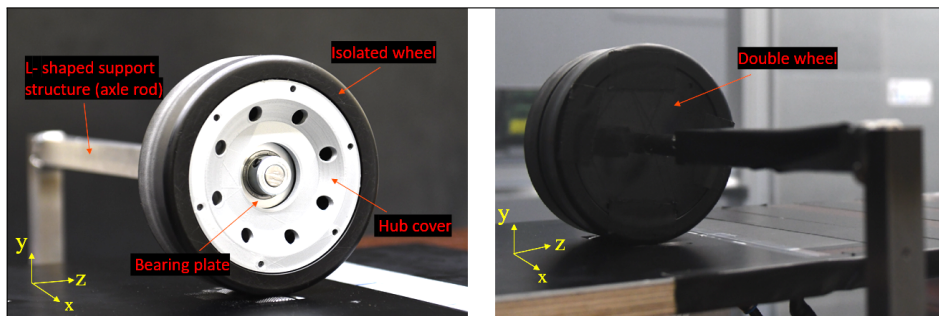


Figure 4.10: Wheel configurations: Left - Isolated wheel along with its components, Right - Double wheel.

Double Wheel

The double wheel configuration is very similar to the single wheel configuration in components, as shown in the fig. 4.10. Instead of a single wheel, two wheels are placed adjacent. Hence, the width of the double wheel setup is equal to 84 [mm], and the diameter remains 136 [mm]. This configuration mimics the double wheel configuration found in real-time for heavy-duty vehicles.

Underbody and mudflap holder

The underbody was a flat piece of wood mounted above the wheel-floor setup. This structure's purpose was to mimic the underbody of a truck and provide a platform from which the different mudflaps could be attached underneath, as shown in figure fig. 4.11. Additionally, similar to the simulated moving ground, a leading edge was glued to the front of the underbody to avoid large perturbations and affect the wheel flow. The underbody was essential for capturing the exact flow physics. Without the underbody, the air downstream of the wheel would insufficiently interact with the mudflap. Further, a mudflap holder was designed to help mount the different mudflaps while testing; it contains a hollow section to reduce the effects of blockage. The holder was designed to mount the mudflaps at a slanted angle of 86 [°] with respect to the underbody surface; this angle was based on the mean inclination of curved mudflaps found commonly in heavy-duty vehicles. The length of the mudflap holder in the Y-direction was of 31 [mm]. The vertical distance (Y-direction) between the wheel centre and the underbody was 100 [mm], and the horizontal distance (Z-direction) between the wheel centre and mudflap holder was 76 [mm], these values were scaled according to real-time heavy-duty vehicles. Refer appendix fig. B.5 for CAD.

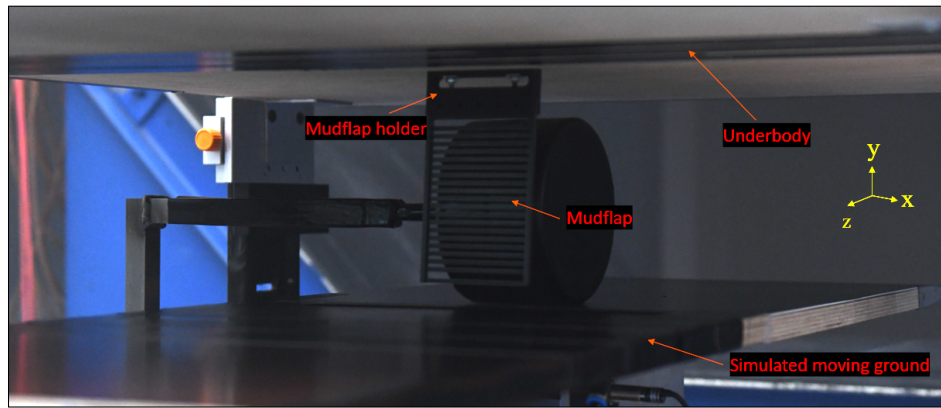


Figure 4.11: Mudflap - Underbody configuration showing the mudflap holder and mudflap mounting location.

In manufacturing, the underbody was sawed and milled, and an additional leading edge was glued to the frontal face to avoid any major downstream influences.

Mudflaps

Since one of the primary goals of this work was to study the effects of mudflap design on its aerodynamics, various mudflaps were tested. The motivation behind their design was to check the effects of solidity, solidity location, and how they influence the vortex structures behind the wheel. The width of the mudflap was the same as the width of the double wheel (84 [mm]), and the height of the mudflap was 121 [mm], scaled according to the real-time mudflaps.

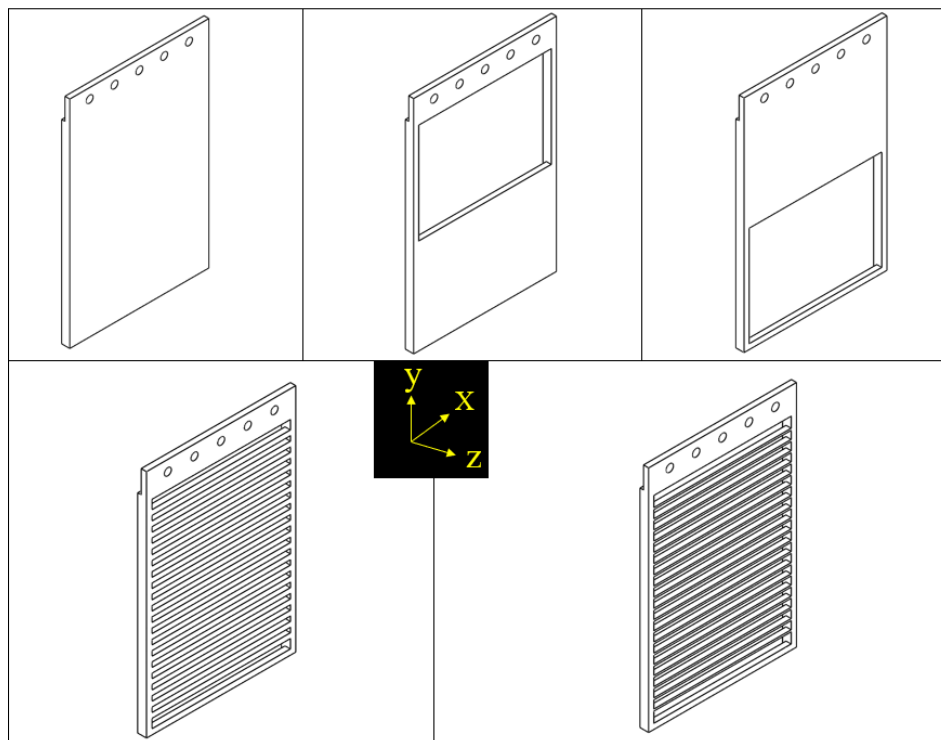


Figure 4.12: Mudflap designs along with their coordinate orientation: Upper left - Solid mudflap, Upper middle - Mudflap with hollow top, Upper right - Mudflap with hollow bottom, Bottom left - Mudflap with 2.8 [mm] horizontal louvers, Bottom right - Mudflap with 1[mm] horizontal louvers

Five different designs (For mudflap geometries CAD refer appendix fig. B.6 to fig. B.10) were tested as shown in fig. 4.12. The first design was a simple solid mudflap with a solidity ratio of 1, which was a reference design for the rest of the mudflaps. Next, two semi-solid mudflaps were made, where either

top or bottom half was made to be hollow, such that the solidity of the mudflaps would be 0.52 (i.e. approximately half of the solid one). Finally, two more designs were made using horizontal louvers to investigate the effects of louvers. The louvered mudflap designs had a solidity ratio of 0.26 (with 1 [mm] louver each), and 0.52 (with 2.8 [mm] louver each) to both compare the effects of horizontal louvers (commonly found in heavy duty vehicle mudflap designs) and the distribution of solidity.

4.3. Preliminary analysis of tangential blowing slot

Before installing the tangential blowing system into the simulated moving ground, a preliminary analysis of the initial blowing slot designs was done using an in-house setup at the high speed facility, TU Delft. The in-house setup consisted of a solid steel breadboard on which the tangential blowing slots were mounted. The tangential blowing slots were given a pressure supply from pressure pipelines present at high-speed facility, TU Delft. The pressure regulating valve was used to control exit velocity from the blowing slots.

The effectiveness of the blowing slots was quantified using the flow angularity and flow uniformity present at the outlet. Hence the "PROCAP - streamwise" device (for more information, refer Streamwise, 2016) was used. In short, this device acquires pressure data using a pitot tube and generates a 3-D vector field using the help of cameras that recognise the location of the pitot tube in space at a given time. Therefore, for the tangential blowing slot, the idea was to acquire the velocity data at a distance of 20 [mm] from the exit section of the slot shown in fig. 4.13.

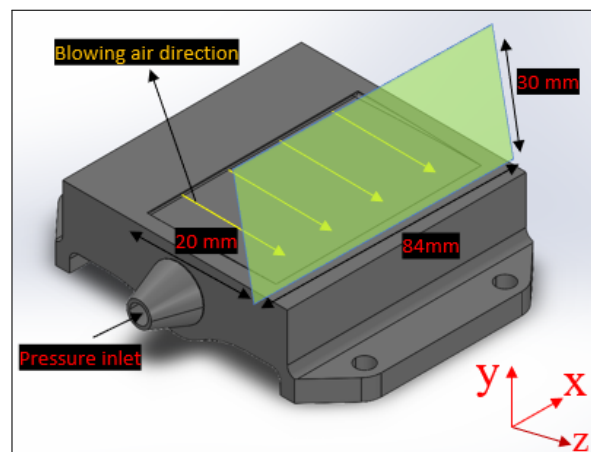


Figure 4.13: Measurement plane (in green) perpendicular to the floor, for the preliminary analysis of the blowing slot design.

It must be noted that the data generated is relatively coarse, i.e., the voxel size was limited to $4 \times 4 \times 4$ [mm³], and the PROCAP device could only measure velocities up to 15 [m/s]. Hence the data generated from this setup was only used for initial estimates of the blowing slot design to avoid any major structural/flow discrepancies. The results are discussed in section 6.1.1.

4.4. Planar PIV measurements

One major hypothesis that this thesis involved was that the simulated moving ground was a good alternative to the conveyor belt. Hence, the simulated ground was assessed using planar PIV measurements to validate the hypothesis. These measurements were further divided into types. The first type involves acquiring data for assessing the leading edge's effectiveness and the tangential blowing system explained in subsection 4.4.1. The second type involves acquiring data for assessing the effectiveness of the roller and the simulated ground as a whole by comparing the results of an isolated wheel explained in subsection 4.4.2.

The planar PIV setup comprised a digital scientific Complementary Metal-Oxide-Semiconductor (sCMOS) camera (Photron) with appropriate lenses (Micro Nikkor f 200mm,50mm), a Neodymium-doped yttrium lithium fluoride (Nd:YLF) laser (Quantronix), a fog generator (SAFEX Fog 2010+) to provide seeding particles, a programmable timing unit and a computer equipped DaVis software (for further information refer LaVision, 2016) for the data acquisition and controlling the timing/action of the respective components. The wind tunnel operating conditions were such that the free stream velocity was 25 [m/s] with an ambient temperature of 24 [°C]. Additionally, the wheel-based Reynolds number was fixed to 0.23 million for readings related to the isolated wheel.

4.4.1. Boundary layer planar measurements

A boundary layer analysis was determined to be a suitable method for assessing the effectiveness of the leading edge and tangential blowing slot. Hence planar PIV analysis was conducted on three different Y-Z planes: Mid-plane present at the central position of the blowing slot, i.e. at 0 [mm], left plane present -85 [mm] away left from the mid-plane and right plane present +85 [mm] away right from the mid-plane as shown in fig. 4.14. At each of these planes, two separate runs were conducted, one with the tangential blower switched off to get the boundary layer profile on the floor/ground and the second with the tangential blower switched on to see the effects of blowing on the boundary layer. Also, the motivation behind choosing the three planes was to get a sense of the mean flow at the tangential blower outlet.

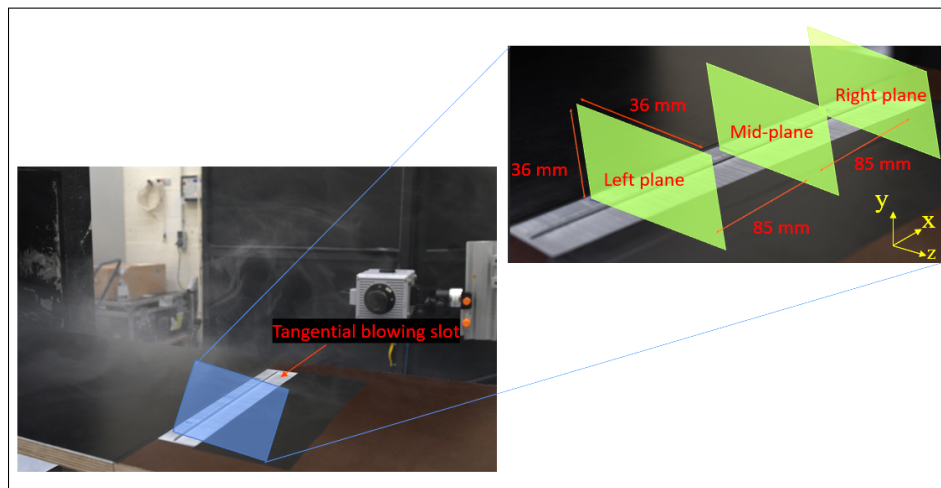


Figure 4.14: Planar PIV measurement planes for the boundary layer analysis: Left - Simulated moving ground with tangential blowing slot, Right - Tangential blowing slot with the three measurement planes (zoomed-in) which are perpendicular to the floor.

The required pressure for the tangential blower was estimated using the combination of the Bernoulli equation, shown in eq. (4.8) and the simplified form of the continuity equation for pipe flow, shown in eq. (4.9). First, using the Bernoulli equation, the required pressure for a given velocity is determined. Next, since the blowing slot acts like a nozzle, the continuity equation was used to determine the outlet velocity at the blower using the inlet velocity determined from the Bernoulli equation. Using the estimated required pressure value, the blowing velocity was further tuned by trial and error, i.e., by processing a few PIV images and determining the blowing velocity to match the free stream velocity. Hence, the required pressure was found to be 0.015 [MPa] for the free stream velocity of 25 [m/s].

$$P_{req} = P_s + \frac{\rho V_1^2}{2} \quad (4.8)$$

where:

$$\begin{aligned}
 P_{req} &= \text{Required pressure [Pa]} \\
 P_s &= \text{Static pressure [Pa]} \\
 \rho &= \text{Density of air [kg/m}^3\text{]} \\
 V_1 &= \text{Velocity of pressurized air [m/s]}
 \end{aligned}$$

$$A_1 V_1 = A_2 V_2 \quad (4.9)$$

where:

$$\begin{aligned}
 A_1 &= \text{Blowing slot inlet area [m}^2\text{]} \\
 A_2 &= \text{Blowing slot outlet area [m}^2\text{]} \\
 V_1 &= \text{Velocity of inlet air [m/s]} \\
 V_2 &= \text{Velocity of outlet air [m/s]}
 \end{aligned}$$

The field of view was based on the height of the estimated boundary layer. The boundary layer height was estimated using the Blasius solution for flat plate; it uses eq. (4.10) for the laminar boundary layer thickness and eq. (4.11) for the turbulent boundary layer thickness.

$$\delta(x) \approx \frac{5x}{\sqrt{Re_x}} \quad (4.10)$$

$$\delta(x) \approx \frac{0.37x}{Re_x^{1/5}} \quad (4.11)$$

where:

$$\begin{aligned}
 \delta(x) &= \text{Boundary layer height [m]} \\
 Re_x &= \text{Reynolds number [-]} \\
 x &= \text{Streamwise distance from L.E [m]}
 \end{aligned}$$

Parameter	Value
Field of view (FOV)	36 × 36 [mm ²]
Sensor field of view	1024 × 1024 [px ²]
Lens focal length (f)	200 [mm]
Pulse width (Δt)	18 [μ s]
Pixel size	20 [μ m]
Particle diameter (d_p)	1 [μ m]
Magnification factor (M)	0.56 [-]
F-stop ($f_\#$)	5.6 [-]
Laser sheet thickness (W)	2.5 [mm]
No. of images (N)	500 [-]
Acquisition frequency (f)	250 [Hz]

Table 4.1: Planar PIV settings for boundary layer analysis

It was estimated that the maximum boundary layer height would be approximately 12.45 [mm] at distance 520 [mm] from the leading edge, where the blowing slot was located; hence a field of view of 36×36 [mm²] was chosen to fully capture both the boundary layer and the free stream flow present above the boundary layer. Consequently, after having fixed the required field of view, the pulse width was determined to be 18 [μ s] based on the free stream velocity and FOV. About 500 uncorrelated images were recorded at an acquisition frequency of 250 [Hz]. After having acquired the raw images, they are

processed using DaVis and MATLAB (refer MathWorks, 2019 for more information), whose details are explained in section 5.1.1. The planar PIV setup settings values are summarized in table 4.1.

4.4.2. Isolated wheel planar measurements

To quantify the effectiveness of the simulated moving ground, the isolated wheel case was studied in detail. The aim was to validate the results of an isolated wheel (both stationary and rotating), by identifying the flow patterns of flow separation and wake behind the wheel.

The isolated wheel was placed above the center line of the roller and support structure was placed such that it remains outside the free stream flow. The isolated wheel setup mainly had three configurations. The first being a stationary wheel, the second being the rotating wheel and the third being the rotating wheel with the tangential blowing system being switched on. The blowing slot was operated at 0.015 [MPa] as determined in section 4.4.1. The wheel rotation was maintained such that the linear velocity of the wheel was 25 [m/s], i.e, the wheel was rotated approximately at an RPM of 1755 using the roller system. There were three measurement planes for each of the configurations namely: At the mid plane of the wheel, which is coincident with the central position of the blowing slot. The next planes were located at the right and left edge of the wheel were about 18 [mm] away from central axis on either side as shown in fig. 4.15. These measurements were chosen to get a sense of the mean wake structures behind the wheel and possibly visualise any asymmetries around the wheel.

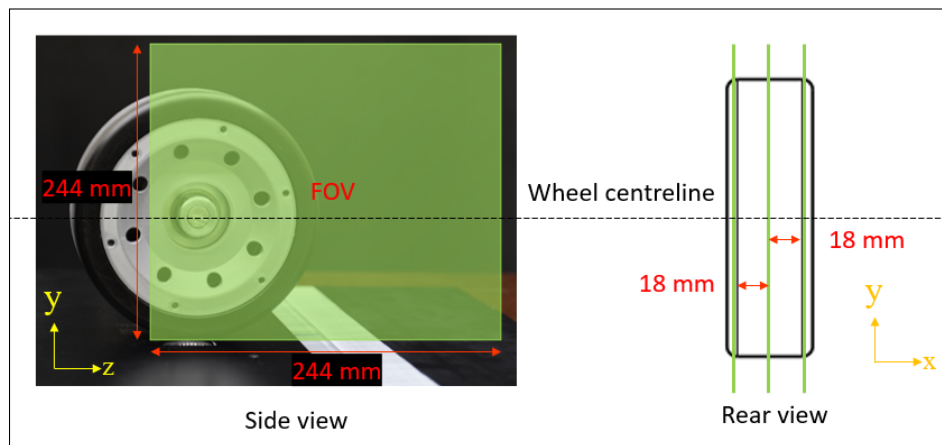


Figure 4.15: Planar PIV measurement planes for the isolated wheel: Left - Side view showing FOV dimensions, Right - Rear view showing the three measurement planes (in green).

The field of view for the isolated wheel case was 244×244 [mm²], which means dimensions were about 1.8 times the diameter of the wheel. Such a dimension was chosen to capture the local features around the wheel (such as separation points) and a fair amount of the wake behind the wheel to observe any immediate vortex structures. Hence, a pulse width of 80 [μm] was selected based on the free stream velocity and FOV. Similar to the boundary layer analysis, 500 uncorrelated samples were taken at an acquisition frequency of 250 [Hz]. The images' processing details are further explained in section 5.1.2. The planar PIV setup settings are summarized in table 4.2.

Parameter	Value
Field of View (FOV)	244×244 [mm ²]
Lens focal length (f)	50 [mm]
Pulse width (Δt)	80 [μ s]
Pixel size	20 [μ m]
Particle diameter (d_p)	1 [μ m]
Magnification factor (M)	0.084 [-]
F-stop ($f_{\#}$)	5.6 [-]
Laser sheet thickness (W)	2.5 [mm]
No. of images (N)	500 [-]
Acquisition frequency (f)	250 [Hz]

Table 4.2: Planar PIV settings for isolated wheel

4.5. Stereoscopic PIV measurements

Stereoscopic PIV measurements were performed on wheel-mudflap configurations to assess the wake structures and evaluate the drag offered. A modular approach was taken to assess the effects of each of the components. The approach involved adding one component at a time to help differentiate their effects; the order of their addition was as follows: Isolated wheel, double wheel, underbody, mudflap holder, and finally, different mudflaps. The measurements, on the whole, had the same PIV setup. However only differed in the way the images were post-processed based on the presence of the underbody. This is further explained in section 5.1.3.

The stereoscopic PIV setup comprised of two digital sCMOS cameras (LaVision) with appropriate lenses (Micro Nikkor f 105mm), an Nd:YAG laser (Quantel Evergreen 200 I), a fog generator (SAFEX Fog 2010+) to provide seeding particles, a programmable timing unit and a computer with DaVis software installed for the data acquisition and controlling the timing/action of the respective components. The wind tunnel operating conditions were such that the free stream velocity was 25 [m/s] with an ambient temperature of 25-28 [°C], fixing the wheel-based Reynolds number to 0.23 million. Additionally, the cameras were placed such that they remained outside the flow, as shown previously in fig. 4.2. The angle between the optical axis of the cameras was roughly 85 [°], configured using the Scheimflug attachments.

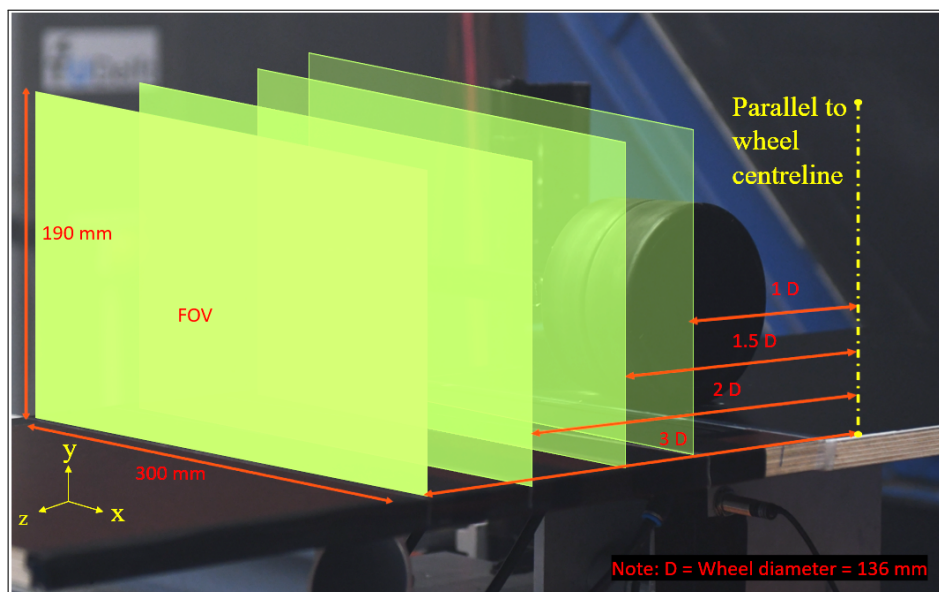


Figure 4.16: Stereoscopic PIV measurement planes (in green) for all wheel-mudflap configurations, along with FOV dimensions and distance with respect to the wheel centreline.

4.5.1. Isolated and double wheel stereoscopic measurements

Before quantifying the effects of the wheel-mudflap assembly, it was first necessary to determine the wake structure behind the wheels. The three type of measurements were done at four (X-Y) planes present behind wheels as shown in fig. 4.16. The three types were the stationary wheel, rotating wheel, and rotating wheel with tangential blowing. The four planes were located at $z/D = 1, 1.5, 2$ and 3 , where 'z' is the distance from the wheel centre to the measurement plane and 'D' is the diameter of the wheel. Planes below $z/D = 1$ were not chosen since they were highly susceptible to reflections from the wheel. The field of view was determined such that whole of the wake behind is captured, essential for drag calculations. Based on results from Leniewicz et al., 2014, the FOV was set to 190×300 [mm^2] (Height \times Width). The pulse width was determined to be 25 [μs] based on the free stream velocity and FOV. About 250 uncorrelated images were recorded at an acquisition frequency of 15 [Hz]. After acquiring the raw images, they are processed using DaVis and MATLAB, whose details are explained in section 5.1.3. The planar PIV setup settings values are summarized in table 4.3.

Parameter	Value
Field of view (FOV)	190×300 [mm^2]
Sensor field of view	2560×2160 [px^2]
Lens focal length (f)	105 [mm]
Pulse width (Δt)	25 [μs]
Pixel size	6.5 [μm]
Particle diameter (d_p)	1 [μm]
Magnification factor (M) (for cameras 1 & 2)	0.047 [-]
F-stop ($f_{\#}$) (for cameras 1 & 2)	11 & 16 [-]
Laser sheet width (W)	2.5 [mm]
No. of images (N)	250 [-]
Acquisition frequency (f)	15 [Hz]

Table 4.3: Stereoscopic PIV settings for wheel-mudflap analysis

4.5.2. Underbody and mudflap stereoscopic measurements

After acquiring the images for the wheels, the next step was to quantify the effects of the underbody, mudflap holder and the different mudflaps. Here only the rotating wheel with tangential blowing measurements were carried out, at the same planes as mentioned in section 4.5.1. This was done by first mounting the underbody over the double wheel and capturing the wake. Next, the mudflap holder was attached and measurements were carried out to see it's effects. Finally, the different mudflaps were attached to the mudflap holder to study the effects of each mudflap design. It must be noted that the series of measurements were randomized to avoid the errors due effects like temperature drift, Barlow et al., 1999.

The PIV settings and FOV remained the same as seen in table 4.3. However, the part of the image above the underbody was cropped during the post-processing of the images. This is further explained in section 5.1.3.

5

Processing and Data Reduction

This chapter presents the steps taken to process the acquired raw PIV data. The data is processed to produce the respective velocity fields and estimate the drag offered. Section 5.1 explains the sequence of the steps taken to process the raw images using DaVis, giving details about removing background noise, masking area, correct window size, and so on. Finally, section 5.2 provides the steps taken to obtain drag values and pressure fields of the various configurations tested.

5.1. Velocity fields

This section provides a brief about the procedures taken in DaVis to produce the velocity fields.

5.1.1. Boundary layer - Planar analysis

The boundary layer analysis involved generating velocity fields; this was done using image pre-processing, as shown in fig. 5.1 and PIV vector calculation. The first step included cropping the raw images to 1018×284 [pix²]. This was decided by first processing a single image to help determine the field of view showing the blowing slot and the boundary layer. Next, a subtract time filter was applied to all the images, where the minimum intensity of the image was subtracted from the raw image to provide output without background noise.

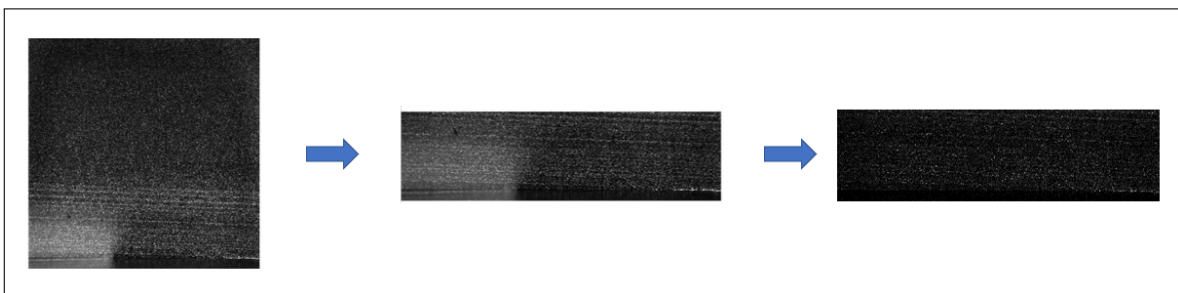


Figure 5.1: Image pre-processing in DaVis: Left - Raw image, Middle - Cropped image, Right - Removal of reflection from blower surface using subtract time filter.

Finally, PIV sum of correlation was applied to find the averaged vector field. This method is usually preferred for steady micro-scale experiments (such as studying boundary layers). The method involves taking a cross-correlation between two instantaneous images and then repeating the operation on multiple image pairs to determine the average correlation function as expressed in eq. (5.1) to determine the corresponding velocity field. Such an operation helps increase the signal-to-noise ratio (SNR). Note

that a low SNR reduces the ability to recognise individual particles giving erroneous velocity fields, Meinhart et al., 2000.

$$\overline{R}_{AB}(s) = \overline{\iint A(X)B(X+s)d^2X} = \iint \overline{A(X)B(X+s)}d^2X \quad (5.1)$$

where:

$$\begin{aligned} \overline{R}_{AB}(s) &= \text{Averaged instantaneous correlation function} \\ A &= \text{Instantaneous image 1} \\ B &= \text{Instantaneous image 2} \\ X &= \text{Spatial coordinate in image plane} \\ s &= \text{Spatial coordinate in correlation plane} \end{aligned}$$

The vector calculation parameters involved using the multi-pass iteration method, where the initial interrogation window size was taken to be 64×64 , with an elliptical gaussian weighting function of 4:1 and overlap of 75% for two passes. The final interrogation window was 16×16 with the same type of interrogation window and overlap, with three passes. The window sizes were chosen such that the vector fields displayed the mean flow characteristics and had less noise; the elliptical function was chosen since it better suited the rectangular FOV.

5.1.2. Isolated wheel - Planar analysis

Similar to the boundary layer analysis, the pre-processing of the raw images involved using the subtract time filter. However, it did not involve the PIV sum of correlation and instead had the usual correlation method. To avoid any faulty vectors from the reflections of the ground and the isolated wheel, the images were masked using a combination of the mask (to allow) and inverse mask (to remove) prior to the vector calculation, as shown in fig. 5.2.

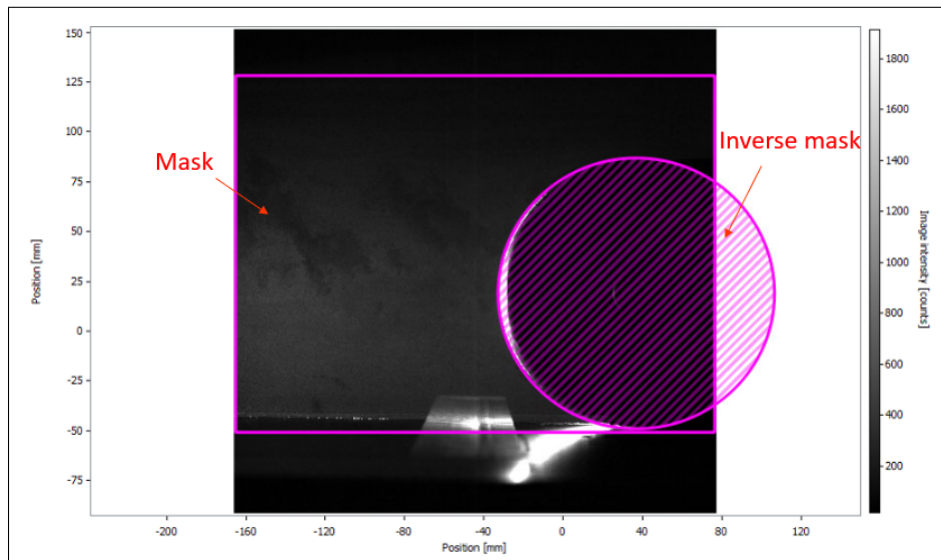


Figure 5.2: Masking of the isolated wheel case in DaVis

The vector calculation involved using the multi-pass iteration method, the initial interrogation window size of 64×64 , with a circular gaussian weighting function of 1:1 and an overlap of 75% for two passes. The final interrogation window was 24×24 with the same type of interrogation window and overlap, with three passes. These were for the same reasons as mentioned previously in section 5.1.1. Further, the averaged vector field was taken such that velocities fall within the 3σ (standard deviation) of the mean of all the images; this was done to remove any remaining outliers in the data.

5.1.3. Wheels and mudflap configurations - Stereoscopic analysis

The stereoscopic analysis of the wheel-mudflap involves processing raw images from two cameras. Since camera two, shown in fig. 4.2 was close to free stream air from the octagonal exit section, it was prone to minute vibrations. Consequently, resulting in the shift of instantaneous raw images. Hence, the images were pre-processed using the shift/vibration correction, which helps correct the shift by manually setting a reference point found in two images at a given instant. Next, the subtract time filter was applied to remove the background noise. For the underbody cases, the raw images were further cropped using the masking function such that only the image only contained data below the underbody, as shown in fig. 5.3. This was to avoid reflections from the underbody, and the region above the underbody was not of interest.

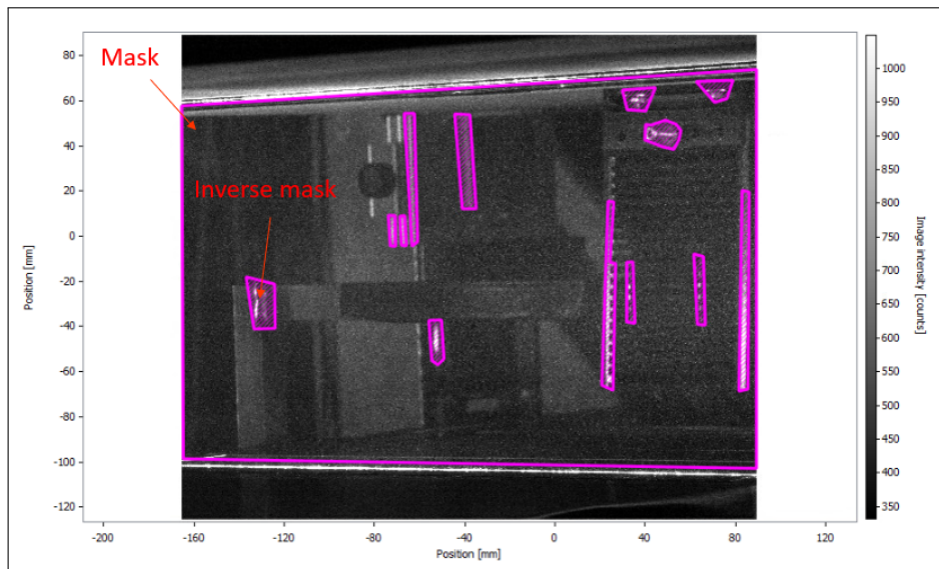


Figure 5.3: Masking of the wheel-mudflap case (camera 2 view) in DaVis showing the masking and inverse masking of the regions of interest.

Similar to the settings mentioned in section 5.1.2, a stereoscopic PIV analysis was carried out, where the regions with reflections were first masked, and the vector calculation was done using the multi-pass iteration method. The initial window size was 96×96 , and the final size was 64×64 with a round window of 1:1 size and overlap of 75%.

5.2. Drag estimation

This section explains the steps taken to estimate drag from the velocity fields obtained from the stereoscopic PIV measurements.

5.2.1. Vector field pre-processing

Since the images obtained from the section 5.1 contain white spaces due to inevitable reflections in the raw images, it was necessary to fill these gaps before processing them. Hence the ‘scatteredInterpolant’ function in MATLAB was used to interpolate the values in the white spaces. This function uses the natural neighbour interpolation to provide smooth approximations of the actual value. For more information regarding the natural neighbour interpolation, refer to Sibson, 1981. An example of the stream-wise velocity component’s raw and interpolated vector field is shown in fig. 5.4 and fig. 5.5 respectively. It must be noted that the interpolation and the next steps are also done for the other parameters, such as the X and Y velocity components and the fluctuations components.

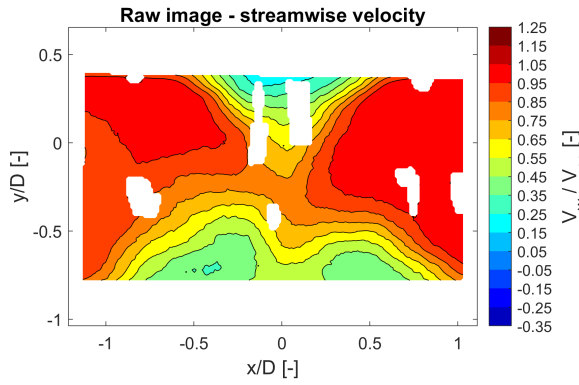


Figure 5.4: Raw normalised vector field of the wake of double wheel rotating configuration at $z/D = 2$, in the presence of the underbody with the mudflap holder attached. Viewed in the X-Y plane. Here velocity is normalised with respect to the free stream velocity and distance with respect to wheel diameter.

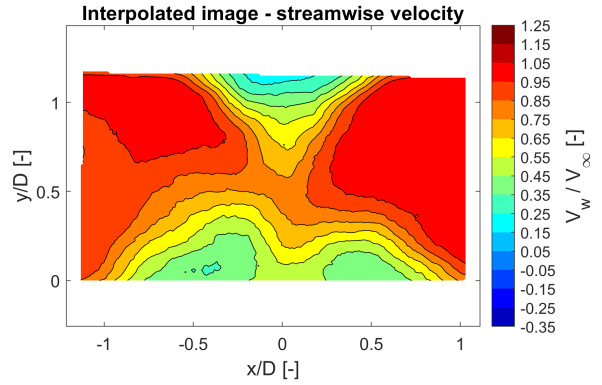


Figure 5.5: Interpolated normalised vector field of the wake of double wheel rotating configuration at $z/D = 2$, in the presence of the underbody with the mudflap holder attached. Viewed in the X-Y plane. Here velocity is normalised with respect to the free stream velocity and distance with respect to wheel diameter.

Next, the interpolated image was cropped to a rectangular image to minimise the effects of the erroneous boundary layer (due to reflections) on the floor and the underbody. This was done by recognising the corner points and excluding the excess field. Finally, the model outline was drawn for reference. The cropped image example is shown in fig. 5.6.

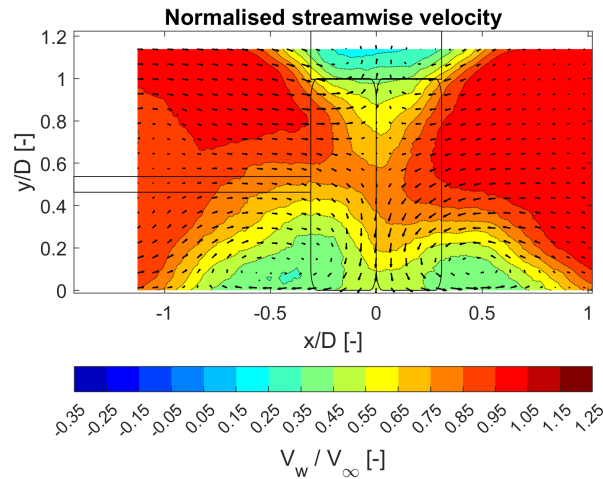


Figure 5.6: Normalised vector field with quiver showing the u-v components of the wake of double wheel rotating configuration at $z/D = 2$, in the presence of the underbody with the mudflap holder attached, represented by black lines. Viewed in the X-Y plane.

5.2.2. Wake contouring

Wake contouring isolates the wake of the body of interest from the rest of the field. This process was done to help evaluate the drag more accurately by avoiding the noise/other velocity deficits that are not due to the body. Although there exists no universal method of wake contouring, the simplest way was to filter the data based on a threshold velocity. Using trial and error, it was found that a threshold of 0.90 times the free stream velocity gives the wake of the model, separating it from the free stream. Additionally, small islands/regions of velocity deficits (like the one present on the left corner of the fig. 5.6 at the height of 0.4 - 0.86 y/D) were present further away from the wake of the body were omitted. The omission was done by comparing the area of these islands and choosing the largest island as the body's wake. The example case of wake contouring is shown in fig. 5.7.

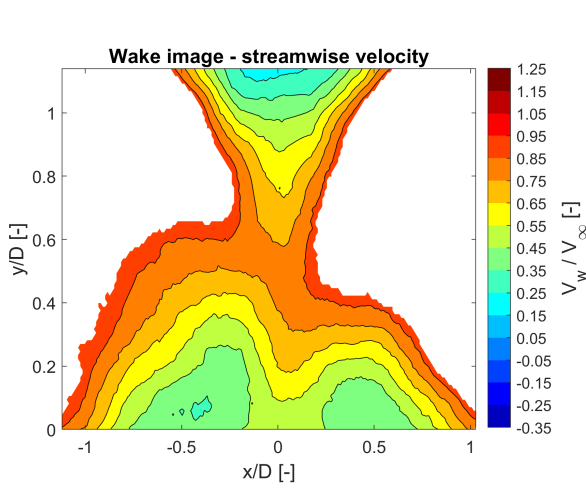


Figure 5.7: Wake contouring for the vector field of double wheel rotating configuration at $z/D = 2$, in the presence of the underbody with the mudflap holder attached.

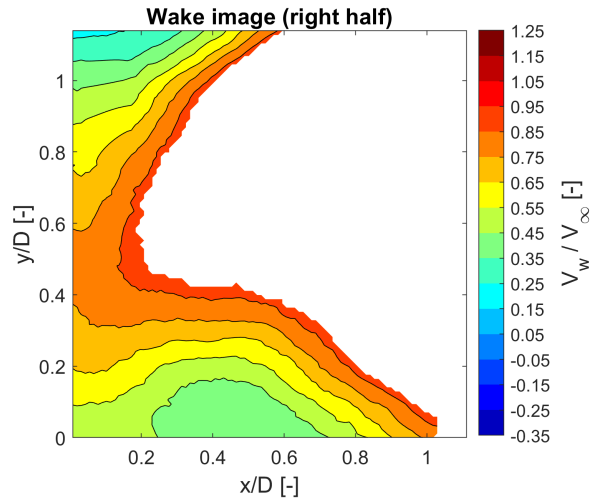


Figure 5.8: Right half wake of the double wheel rotating configuration at $z/D = 2$, in the presence of the underbody with the mudflap holder attached. Viewed in the X-Y plane.

One noticeable effect seen in all the wake contoured images was that the wake of the axle and wheel were indistinguishable. Hence, the right half of the wake was considered for drag estimation to isolate the wake of the wheel and mudflap from the axle and its interference effects. This was a suitable assumption since the geometries were axis-symmetric about the Y-axis (height). The image centreline was based on comparing the wheel centre found in the raw images with the one found in respective wake images. The example case of the half wake is shown in fig. 5.8.

5.2.3. Momentum term

After acquiring the contoured wake and its corresponding values, the next step was to estimate drag. As shown earlier, in eq. (3.12), the estimation required evaluations of three terms: momentum, pressure, and fluctuation. In this subsection, the steps for obtaining the momentum are described.

$$\text{Momentum term} = \frac{2}{A} \iint_S \frac{|\bar{w}|}{V_\infty} \left(1 - \frac{\bar{w}}{V_\infty}\right) dS \quad (5.2)$$

The momentum term provides the amount of momentum deficit in the wake in the streamwise direction compared to the momentum upstream of the body. The momentum term requires the values of the model's frontal area, free stream velocity and averaged streamwise velocity component of the wake. For its evaluation, the slightly modified eq. (5.2) is used, whose motivation is provided at the end of this subsection.

Ideally, the free stream velocity is the velocity set at the wind tunnel (V_{tunnel}); it is seldom seen that this value remains constant or is the same as the free stream velocity that the model experiences. This can be explained using the following reasons.

First, during the experimental campaign, it was seen that the wind tunnel velocity measured from the pitot system varied up to ± 0.2 [m/s] around the set point (25 [m/s]). This behaviour was mainly accounted for by the slight variations in the RPM of large centrifugal fans. Second, several configurations were tested during the campaign, with different frontal areas, and the location of the model changed for different z/D measurements. This meant the models experienced marginally different free stream velocities and required open jet wind tunnel corrections suggested by Mercker and Wiedemann, 1996. The work states four corrections: the jet expansion correction, the nozzle blockage correction, the collector blockage correction and the empty tunnel pressure gradient correction. The collector blockage correction was considered negligible due to the build of the OJF, which has a sufficient distance between the collector and the test setup. Next, the blockages of the whole setup concerning the wind tunnel's

cross-section area were at max 1.45%. Hence, making the nozzle blockage corrections negligible and the remaining corrections quite complex, especially when the mudflap-underbody system was involved. Fortunately, using PIV diminishes the need for such corrections since it provides the velocity field around the model (with sufficiently large FOV). Hence, a more straightforward approach was taken to estimate the free stream velocity; this involved identifying the location of a uniform field present away from the wake of the model and taking an average velocity of such a section as shown in fig. 5.9 and fig. 5.10.

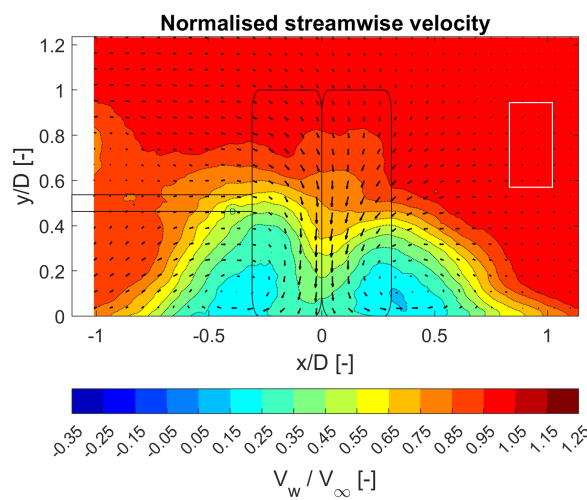


Figure 5.9: Average free stream velocity region (shown in white box) for the normalised vector field of double wheel stationary configuration at $z/D = 1.5$. Viewed in the X-Y plane.

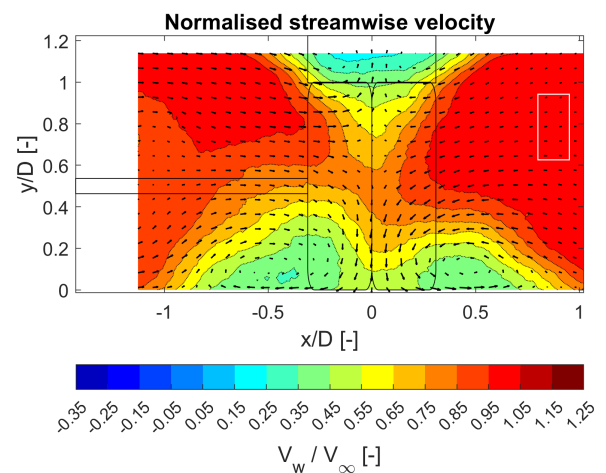


Figure 5.10: Average free stream velocity region (shown in white box) for the normalised vector field of double wheel rotating configuration at $z/D = 2$, in the presence of the underbody with the mudflap holder attached. Viewed in the X-Y plane.

Although the averaged streamwise velocity component of the wake value was retrieved from PIV data, it must be noted that this value was sometimes negative due to flow reversals close to the model. The fig. 5.11 shows the velocity profiles at different z/D locations of the rotating double wheel case, where the negative wake velocities were prominent for the $z/D=1$ case, at the lower part of the wake (below the 30 [mm] mark). The flow reversal was due to the separated flow that occurred behind the wheel, creating a local negative pressure zone. However, the negative pressure zone was not seen in the planes further downstream (e.g. $z/D = 1.5, 2, 3$), as it slowly faded due to the pressure recovery downstream. Consequently, these negative values underpredict the momentum term contribution for the total drag. Therefore, to correct the underprediction, the absolute value of the average wake velocities was taken for the term outside the brackets in eq. (5.2). However, the term inside the bracket corresponds to the relative velocity of the wake. Hence such a correction was not required.

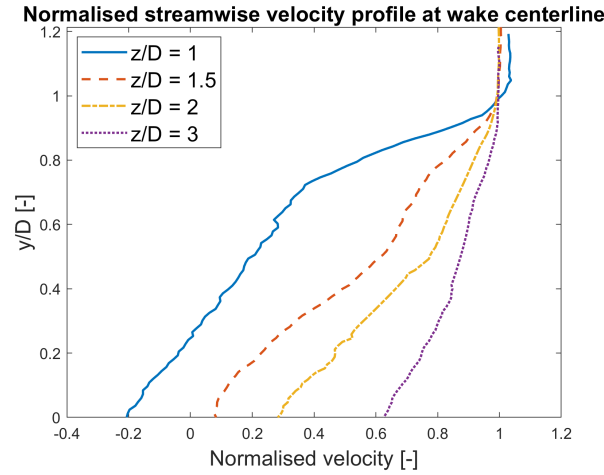


Figure 5.11: Wake streamwise velocity profile at different heights present on the wake centreline ($x/D = 0$), for the double wheel rotating configuration at $z/D = 1, 1.5, 2$ and 3 .

5.2.4. Fluctuation term

The fluctuation term measures the streamwise turbulent kinetic energy (TKE) present in the wake. It is assumed that flow has isotropic turbulence, and the contribution of the viscous stress term is equal to the TKE. The streamwise TKE was found using eq. (5.4), stated by Wilcox et al., 1998. Further, the fluctuation term is evaluated from the relation between the standard deviation in streamwise velocity (σ_w') and Reynolds stress in eq. (5.3). Since the standard deviation of the streamwise velocity was readily available, the streamwise TKE could be easily calculated. The example case is shown in fig. 5.12, where the most intense turbulent structures are found on either side of the double wheel.

$$\sigma_w = \sqrt{\overline{w'^2}} \quad (5.3)$$

$$k_s = \frac{1}{2} \overline{w'^2} \quad (5.4)$$

where,

$$\begin{aligned} \sigma_w &= \text{Std dev. of streamwise wake velocity [m/s]} \\ k_s &= \text{Streamwise turbulent kinetic energy [m}^2/\text{s}^2] \\ w' &= \text{Streamwise wake fluctuation [m/s]} \end{aligned}$$

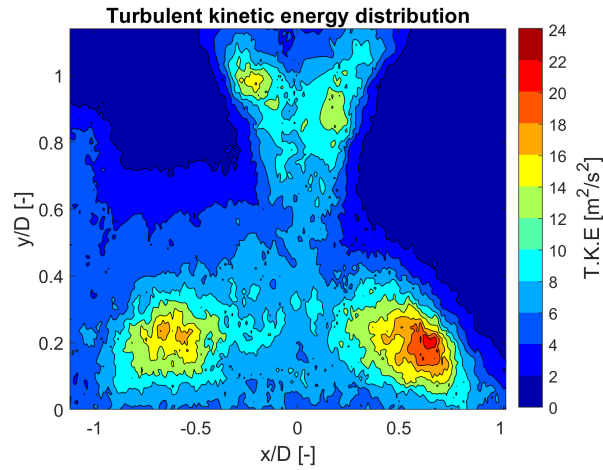


Figure 5.12: Streamwise turbulent kinetic energy distribution of the double wheel rotating configuration at $z/D = 2$, in the presence of the underbody with the mudflap holder attached. Viewed in the X-Y plane.

Finally, the fluctuation term was evaluated using the values of the TKE, the model's frontal area and the free stream velocity as seen in equation eq. (5.5).

$$\text{Fluctuation term} = \frac{-4}{AV_{\infty}^2} \iint_S k_s dS \quad (5.5)$$

5.2.5. Pressure term

The pressure term is the contribution of the pressure drag that arises due to the difference between the mean pressure field and the free stream pressure. As discussed in section 3.3.1, the pressure field was reconstructed using the discretized form of the PPE shown in eq. (5.6). The respective pressure gradients are computed using eq. (5.7) and eq. (5.8). Here the velocity and velocity fluctuation gradients are found using different finite difference schemes discussed in section 3.3.1.

$$\bar{p}_{xx} + \bar{p}_{yy} = \frac{\partial}{\partial x} \frac{\partial \bar{p}}{\partial x} + \frac{\partial}{\partial y} \frac{\partial \bar{p}}{\partial y} \quad (5.6)$$

$$\frac{\partial \bar{p}}{\partial x} = -\rho \left(\bar{u} \frac{\partial \bar{u}}{\partial x} + \bar{v} \frac{\partial \bar{u}}{\partial y} + \frac{\partial \overline{u'^2}}{\partial x} + \frac{\partial \overline{u'v'}}{\partial y} \right) \quad (5.7)$$

$$\frac{\partial \bar{p}}{\partial y} = -\rho \left(\bar{u} \frac{\partial \bar{v}}{\partial x} + \bar{v} \frac{\partial \bar{v}}{\partial y} + \frac{\partial \overline{v'^2}}{\partial y} + \frac{\partial \overline{u'v'}}{\partial x} \right) \quad (5.8)$$

Based on the boundary conditions, two types of measurements were conducted during the second campaign. The first case was with the models placed without the presence of the underbody as shown in fig. 5.13, and the second case was the models placed with the presence of the underbody as shown in fig. 5.14. The boundary conditions were applied using the values of pressure/pressure gradients at each side and are summarised in table 5.1 and table 5.2.

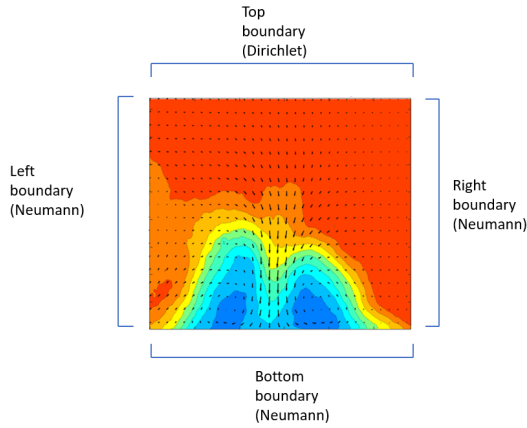


Figure 5.13: Type 1 - Boundary conditions for double wheel stationary configuration at $z/D = 1.5$. Viewed in the X-Y plane.

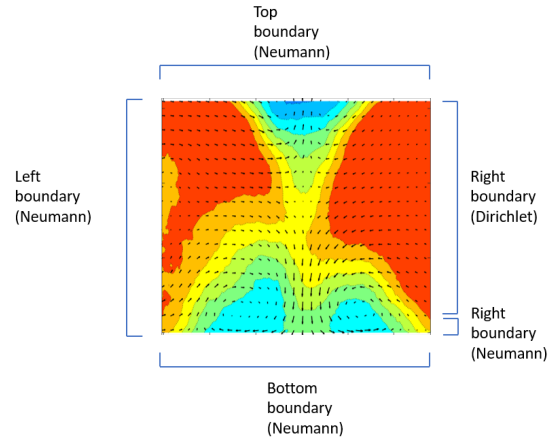


Figure 5.14: Type 2 - Boundary conditions for the double wheel rotating configuration at $z/D = 2$, in the presence of the underbody with the mudflap holder attached. Viewed in the X-Y plane.

Location	Type	Value
Top	Dirichlet	$p = \bar{p}_{Bernoulli}$
Bottom	Neumann	$\frac{dp}{dy} = 0$
Left	Neumann	$\frac{dp}{dx} = a, \frac{dp}{dy} = b$
Right	Neumann	$\frac{dp}{dx} = a, \frac{dp}{dy} = b$

Table 5.1: Boundary conditions for type 1 measurements.

Location	Type	Value
Top	Neumann	$\frac{dp}{dy} = 0$
Bottom	Neumann	$\frac{dp}{dy} = 0$
Left	Neumann	$\frac{dp}{dx} = a, \frac{dp}{dy} = b$
Right	Dirichlet, Neumann	$p = \bar{p}_{Bernoulli}, \frac{dp}{dx} = a, \frac{dp}{dy} = b$

Table 5.2: Boundary conditions for type 2 measurements.

The choices for the respective boundary conditions were based on the in-plane velocity information. Applying Neumann conditions on all sides would provide the pressure field up to an additive constant; hence with the help of the Dirichlet condition (at least one point), this constant could be determined to find the exact pressure values. For the type 1 cases, it was consistently seen that the velocity on the top remained relatively uniform. Hence this side was chosen for applying the Dirichlet condition. As a consequence, the pressure value ($\bar{p}_{Bernoulli}$) was determined using the Bernoulli equation as shown in eq. (5.9), as the flow was incompressible.

$$\bar{p}_{Bernoulli} + \overline{w^2}_{Dirichlet} = p_{\infty} + \frac{\rho}{2} V_{\infty}^2 \quad (5.9)$$

where,

$$\begin{aligned}\bar{p}_{Bernoulli} &= \text{Average pressure value at the Dirichlet boundary [Pa]} \\ \bar{w}_{Dirichlet} &= \text{Average velocity value at the Dirichlet boundary [m/s]} \\ p_{\infty} &= \text{Free stream pressure [Pa]} \\ V_{\infty} &= \text{Free stream velocity [m/s]} \\ \rho &= \text{Air density [kg/m}^3\text{]}\end{aligned}$$

Whenever the boundaries corresponded to solid surfaces such as the underbody or the floor, the pressure gradient, velocities and normal fluctuations (Y-direction) was considered zero. Additionally, the no-slip condition on these walls meant the tangential velocities were also zero. Hence leads to the simplification seen in eq. (5.10). However, for the sides which did not have either solid surfaces or a uniform field, they were determined to the respective constants (say a,b) shown in eq. (5.12) and eq. (5.11).

$$\left. \frac{dp}{dy} \right|_{\text{solid boundary}} = -\rho \left(u \frac{\partial v}{\partial x} + v \frac{\partial u}{\partial y} \right) = 0 \quad (5.10)$$

$$\left. \frac{dp}{dx} \right|_{\text{free boundary}} = -\rho \left(u \frac{\partial u}{\partial x} + v \frac{\partial u}{\partial y} \right) = a \quad (5.11)$$

$$\left. \frac{dp}{dy} \right|_{\text{free boundary}} = -\rho \left(u \frac{\partial v}{\partial x} + v \frac{\partial v}{\partial y} \right) = b \quad (5.12)$$

The pressure field was reconstructed using the methodology mentioned above. Finally, the pressure term drag contribution was evaluated using the mean pressure, free stream pressure, air density, free stream velocity and frontal area as seen in eq. (5.13).

$$\text{Pressure term} = \frac{2}{\rho V_{\infty}^2 A} \iint_S (p_{\infty} - \bar{p}) dS \quad (5.13)$$

6

Results and Discussion

This chapter presents the results and discussion of the various experiments conducted during the two campaigns. Section 6.1 presents the preliminary analysis of the tangential blowing slots, followed by a discussion on the boundary layer analysis. Section 6.2 presents the wake analysis of the isolated wheel using the planar and stereoscopic measurements. Next, the wheel-mudflap setup was analysed by discussing the effects of each component in the following sequence: The double wheel in section 6.3, the underbody in section 6.4, and the mudflap holder along with different mudflaps in section 6.5. Section 6.6 presents the drag coefficients obtained in the wheel-mudflap setup, backed with the key inferences. Finally, section 6.7 provides the answers to the research questions found from the results obtained throughout this chapter.

6.1. Simulated moving ground

This section provides an assessment of the simulated moving ground. First, in section 6.1.1, the results of the preliminary analysis of the two tangential blowing slots are given. Second, in section 6.1.2, the effectiveness of the simulated moving ground in producing a uniform velocity over its surface was analysed using the boundary layer analysis.

6.1.1. Preliminary analysis of the tangential blowing slot

The measurement plane is re-shown in fig. 6.1 for quick reference (Refer section 4.3 for its supporting information).

The fig. 6.2, provides the velocity field of the outlet of the step blowing slot, normalised with respect to the max detectable velocity (15 [m/s]) by the PROCAP device. First, the slot outlet had two distinct velocity peaks present approximately at a spanwise location of 15 [mm] and 60 [mm]; however, it had a lower velocity in the central region (spanwise location of 30 [mm]). This trend was due to the presence of the support wall present in the central section of the blowing slot, which restricted flow in this section. Second, the peak on the right was larger than the one on the left, and this was because of the one-sided pressure line blower input. The blower had a pressure line input on the left side of the geometry; hence the flow prefers to conserve momentum and go straight (left to right) instead of

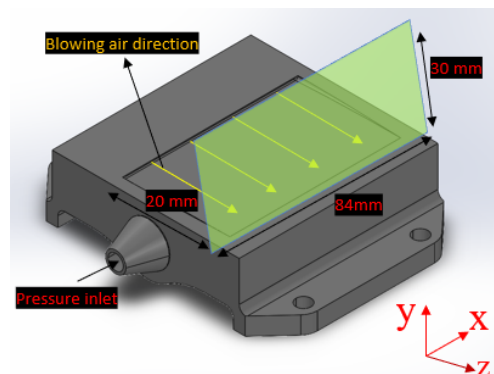


Figure 6.1: Measurement plane (in green) perpendicular to the slot.

leaving the outlet at 15 [mm] present perpendicular to it.

However, when the flow met the end of the duct, it was forced to move towards the blowing outlet, approximately at the 60 [mm] mark. Third, there were several shear layers at the blowing outlet, starting from the bottom (0 [mm]), where the jet originates to a height of 17 [mm], where there is stationary/ambient air. These shear layers were a product of the dominant viscous effects between the stationary air and moving outlet air. The velocity profiles along these shear layers are further visualised in fig. 6.3, three spanwise locations along the outlet were chosen: the approximate centre of the left, right peak, and the central position of the blowing slot, where the support walls exist. It was seen that the slot had 25% and 13% velocity reduction at the central position and left side, respectively.

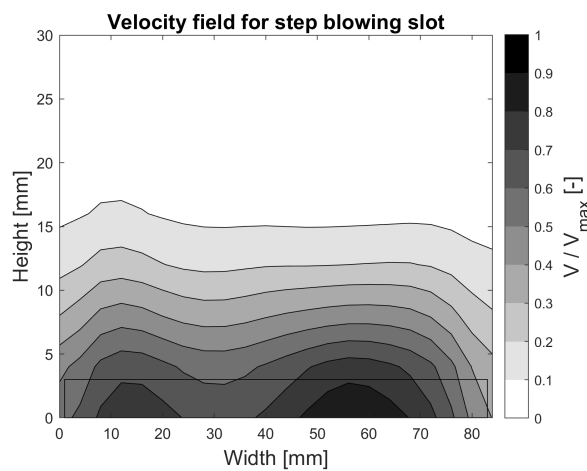


Figure 6.2: Normalised velocity field (X-Y plane) for a cross flow plane present 20 [mm] downstream of the step slot, for the step blowing slot (represented by the rectangle).

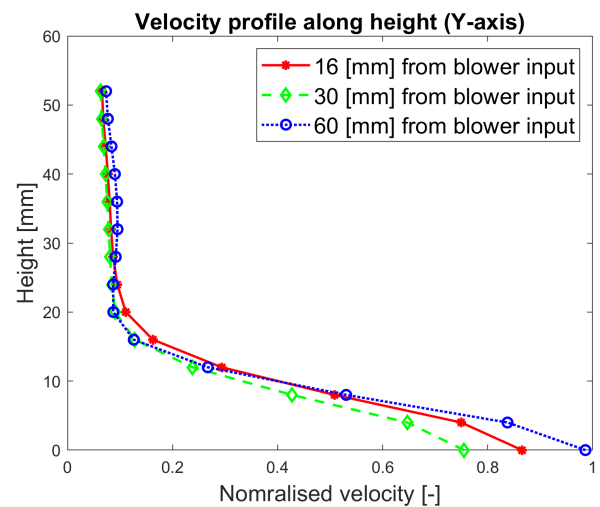


Figure 6.3: Normalised velocity profile along the height of the step blower at the different spanwise locations (X-direction) from the pressure line blower input present at the side.

The step blowing outlet was fundamentally flawed as a good tangential blower because the geometry of the step along the ground would produce flow perturbations in the free stream. Hence, in the second iteration, the flushed model was made to address the step. The model had a flushed outlet parallel to the floor and a rounded support walls at the centre. The fig. 6.5 shows the normalised velocity profile of the flushed model. First, it was seen that velocities at the central positions were now improved due to the rounding and shortening of the central support wall as shown in fig. 6.4. Second, the height of the peak velocities was slightly reduced from 2.8 [mm] to 2.5 [mm] for the right peak and from 2.7 [mm] to 2 [mm] for the left peak. This change was accounted for by the flushed outlet design that provided a smaller jet in height. Third, the shear layers were formed at approximately the same heights and were more uniform. Therefore, there were negligible flow angularity effects when comparing the step and flushed versions. Finally, fig. 6.6 shows the velocity profiles at the same locations as for the step blowing slot. The peak velocities at the relative outlet positions were around 95% or more.

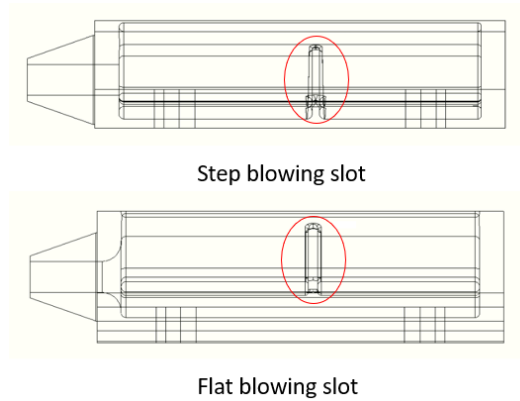


Figure 6.4: Location of support wall (in red circle) for two initial designs: Top - Longer/spread out wall base for step blowing slot, Bottom - Rounded and smaller wall base for flat blowing slot

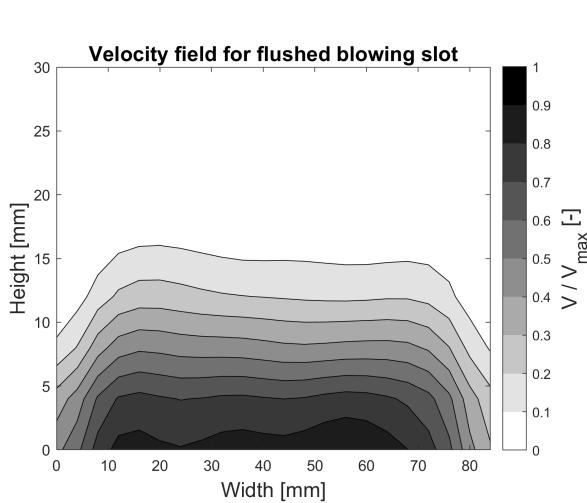


Figure 6.5: Normalised velocity field (X-Y plane) for a cross flow plane present 20 [mm] downstream of the flushed slot.

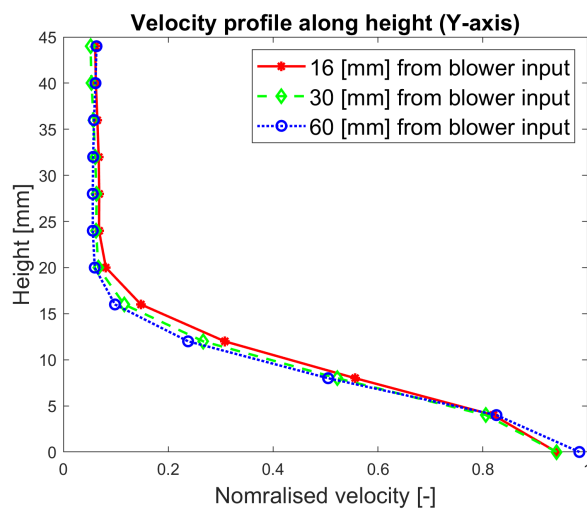


Figure 6.6: Normalised velocity profile along the height of the flushed blower at the different spanwise locations (X-direction) from the pressure line blower input present at the side.

Hence based on the above observations, the final design was concluded to have a flushed outlet along with smaller walls. Additionally, to remove the asymmetry in the peak velocities, pressure line inputs were uniformly given at the blower’s central, left, and right sides.

6.1.2. Boundary layer analysis

The mean velocity fields of the boundary layer analysis are provided in this subsection.

The FOV was cropped to an appropriate size to visualise the boundary layer better; the jet’s initiation from the blower occurs slightly upstream of the FOV as seen in fig. 6.7 (Refer section 5.1.1 for its supporting information). Here zero on the vertical axis represents the floor of the simulated ground, and the zero on the horizontal axis marks the part of the blower where it flushes with the flat ground. More specifically, the negative length values show a part of the blower with a slight inclination, and the positive length values show the flat ground. Also, note that the coordinate axes and velocity have been non-dimensionalised with

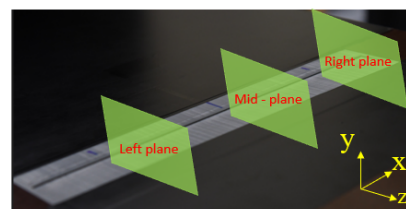


Figure 6.7: Cropped measurement planes (in green) perpendicular to the slot.

the wheel diameter and free stream velocity, respectively, to help compare with plots in the upcoming section.

The distinct shear layers of the laminar boundary layer were seen in fig. 6.8(a) that presents the velocity field over the simulated moving ground with the blower switched off. However, the growth of the boundary layer height downstream was not very apparent. Such a trend was accounted for by the geometric surface/profile of the blowing slot that slightly disrupts the upstream boundary layer (a sudden dip followed by a gradual rise to the flat floor). Hence, the average height of the boundary layer over this section was 2.82 [mm] (0.0207 y/D), which was smaller than the anticipated flat plate boundary layer of 12.45 [mm] mentioned in section 4.4.1. This signified the combined effect of the leading edge and the blower geometry (blowing off state). Further from the quivers in the plots, the flow was seen to be reasonably tangential to the floor, indicating that there were negligible flow angularity effects created by the leading edge design (at the given section of the model).

The boundary layer was removed significantly when the blower was switched on, as shown in fig. 6.8(b). However, some shear layers were still present partially above and below the blowing jet. The shear layers on the upper part vanished as the jet developed downstream. The shear layers on the lower part of the jet showed the formation of a new boundary layer due to the inherent no-slip condition present on the solid ground. Therefore tangential blower did not ‘truly’ remove the boundary layer but certainly reduced its effects by removing the upstream boundary layer and introducing a fresh boundary layer which was much smaller. Additionally, the quivers over the smooth curvature of the blowing slot demonstrate negligible flow angularities by the jet.

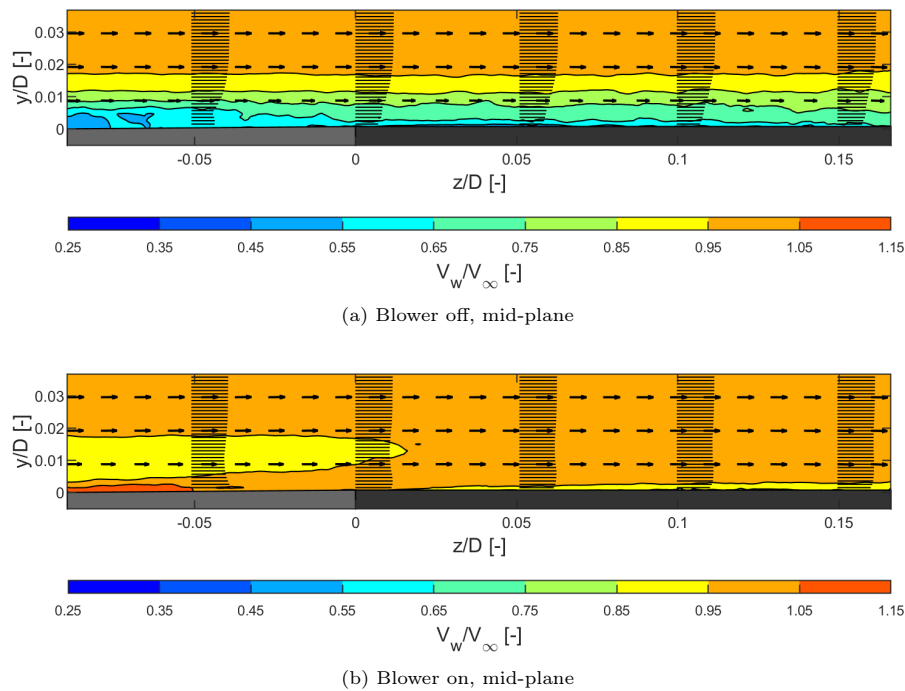


Figure 6.8: Vector fields (Y-Z plane) showing boundary layer present on the mid-plane of the blower slot (in light grey) and ground (in dark grey). Boundary layer profiles represented (thin black lines) at intervals of 0.05D.

Similar conclusions can be drawn from fig. 6.9 corresponding the left plane, where there was a shear layer present on the upper part of the jet. However, one noticeable difference seen in fig. 6.10(b) is that the blower did not completely remove the upstream boundary layer on the right plane, i.e. it still had the shear layer corresponding to 0.85-0.95 (22-24 [m/s]). This could be reasoned by either the subtle change in the input pressure input given to the blower or a manufacturing defect in the slot. The former was a more likely cause because the pressure inputs had to be manually reset to 0.015 [MPa] for every measurement plane.

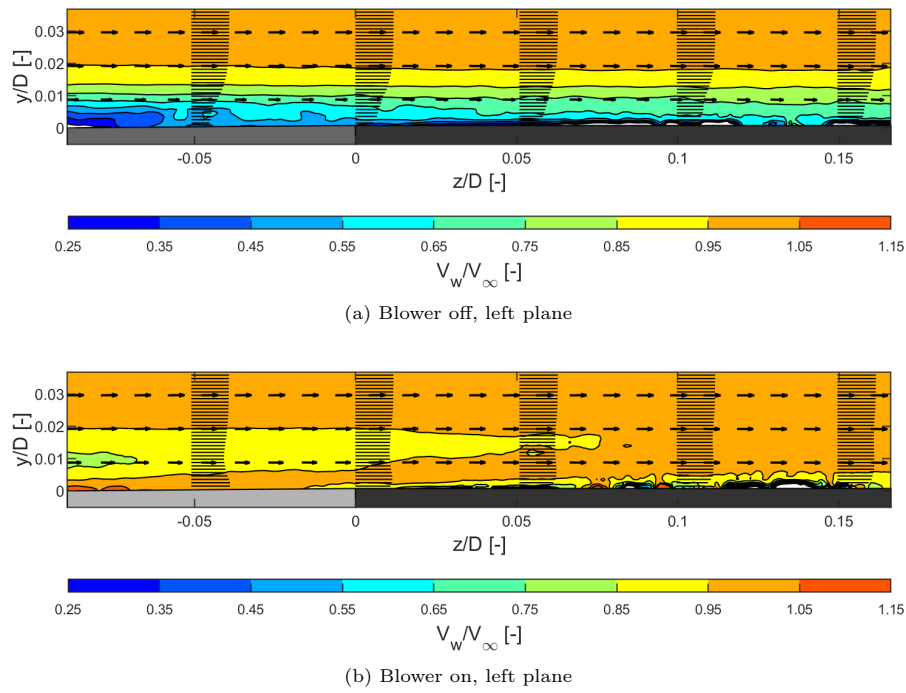


Figure 6.9: Vector fields (Y-Z plane) showing boundary layer present on the left-plane of the blower slot (in light grey) and ground (in dark grey). Boundary layer profiles represented (thin black lines) at intervals of $0.05D$.

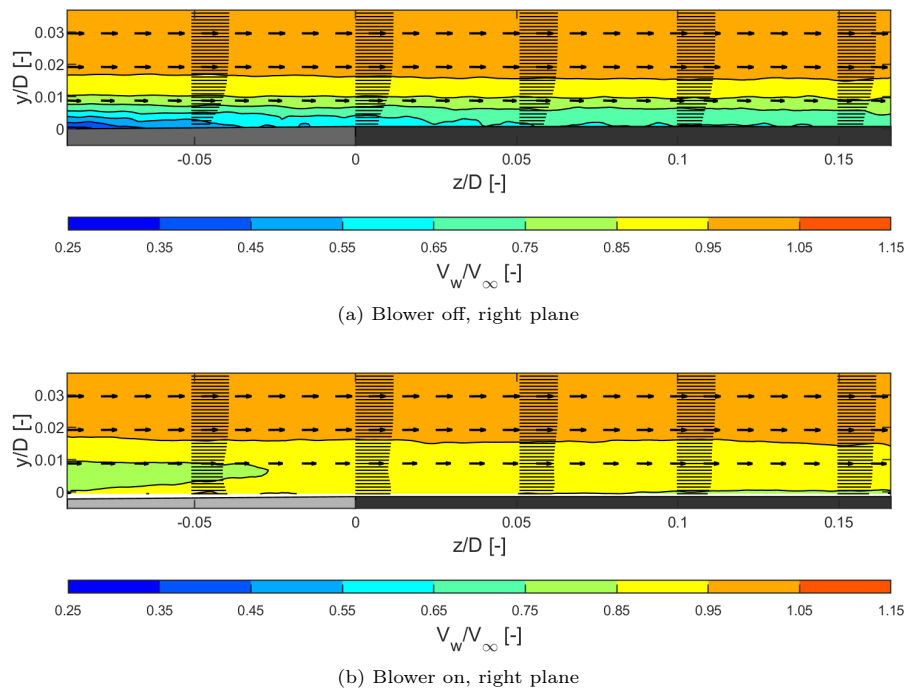


Figure 6.10: Vector fields (Y-Z plane) showing boundary layer present on the right-plane of the blower slot (in light grey) and ground (in dark grey). Boundary layer profiles represented (thin black lines) at intervals of $0.05D$.

The velocity profiles produced by the blowing slot at the different measurement planes along the flat ground are visualised using fig. 6.11, the mid-profile boundary layer is also shown for reference/comparison. The shear layer on the jet's upper region reduces the velocity; however, the blowing, on average, produces a much fuller profile compared to the boundary layer present previously.

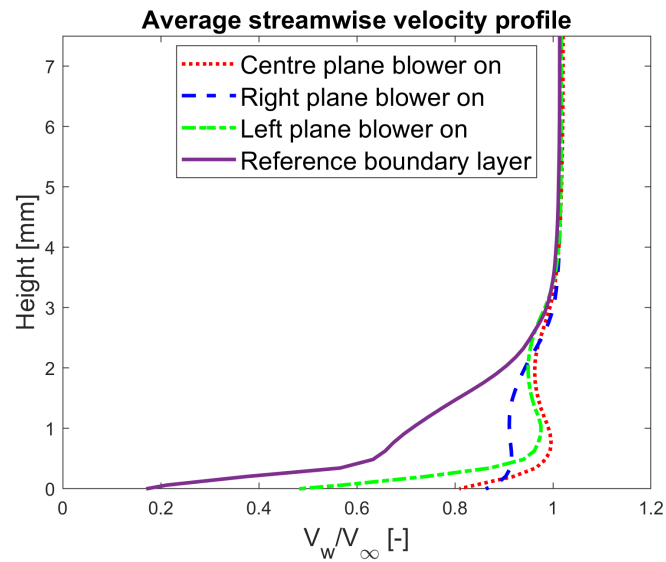


Figure 6.11: Average streamwise velocity taken from streamwise location of $0 z/D$ to $0.165 z/D$ (0 [mm] - 22.5 [mm]) profile along the height (Y-axis), for the three different measurement planes. For blower switched on, with 0.015 [MPa] supply pressure.

An average of the boundary layer parameters over flat surface ($0 z/D$ to $0.165 z/D$) of the simulated ground is shown in table 6.1. For reference, the boundary layer of the mid-plane is considered, it was seen that boundary layer thickness (δ) remained roughly 2.82 [mm]. Subsequently, switching the blower on led to fresh boundary layer with height up to 0.768 [mm] for the given section, note that the effects of shear layer present above at the initial part around $0 z/D$ mark were ignored for boundary layer height calculations. However, for the displacement thickness (δ^*) and momentum thickness (θ) the effects of the shear layer present above the fresh boundary layer were considered for a better estimate of the displacement and momentum of the flow rate. Hence helping summarise the effects of the blowing.

Case	δ [mm]	δ^* [mm]	θ [mm]
Blower off (mid)	2.820	0.831	0.473
Blower on (mid)	0.344	0.197	0.172
Blower on (right)	0.314	0.286	0.255
Blower on (left)	0.768	0.364	0.174

Table 6.1: Average boundary layer parameters for streamwise location of $0 z/D$ to $0.165 z/D$ (0 [mm] - 22.5 [mm]).

6.2. Isolated Wheel

This section provides the wake analysis present behind the isolated wheel. Section 6.2.1 discusses the wake using the Y-Z plane view as re-shown in fig. 6.12, and section 6.2.2 discusses the wake using the X-Y plane view as re-shown in fig. 6.13.

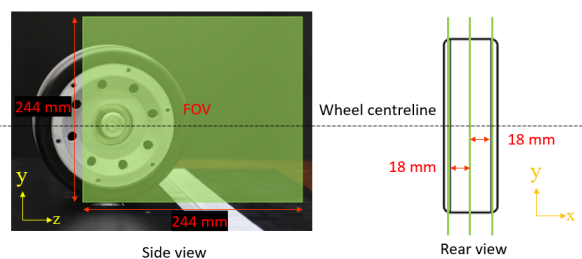


Figure 6.12: Measurement planes (in green) for the planar measurements of the isolated wheel.

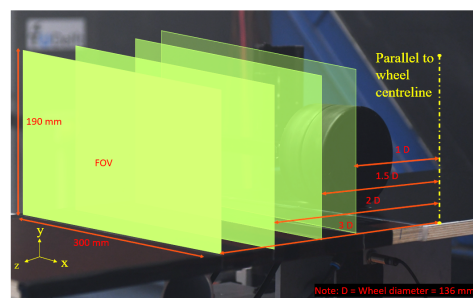


Figure 6.13: Measurement planes (in green) for the stereoscopic measurements of the isolated wheel.

6.2.1. Planar results

The velocity fields obtained in the mid-plane of the isolated wheel for the stationary and rotating are shown in fig. 6.14. The height and downstream distances are normalised using wheel diameter 'D', and the origin is placed at the centre of the wheel. Firstly, it was observed that the downwash behind the stationary wheel was higher in comparison to the rotating case. Second, the jetting phenomenon reported by various authors mentioned in the literature survey was confirmed behind the rotating wheel. This changed the wake structure present at the bottom of the wheel by slightly pushing it upwards. Third, the rotating wheel's separation point was further upstream compared to the stationary wheel. For comparison, experimental PIV results from Rajaratnam et al., 2019 are shown in fig. 6.15. The velocity fields, in general, are quite similar. However, the cases differed when comparing the separation point locations. A possible reason for this difference could be the Reynolds number at which these experiments were carried out, i.e. the Reynolds number for this thesis was fixed to 0.23 million (sub-critical regime) in comparison to 0.72 million (post-critical regime) for the ones conducted by Rajaratnam et al., 2019. In the sub-critical regime, the boundary layer over the wheel is laminar and hence encounters an early separation. In contrast, in the post-critical regime, the boundary layer becomes turbulent prior to separation and delays separation. Similar analogies were drawn for cylinders where the early separation in the sub-critical regime occurs due to the forward progression of turbulence and increasing three-dimensional flow effects, J. E. Fackrell, 1974. Nevertheless, when comparing the wake behaviour further downstream, the velocity gradients looked almost identical, suggesting that testing at a sub-critical lower Reynolds number of 0.23 million will still show similar wake characteristics behind the wheel.

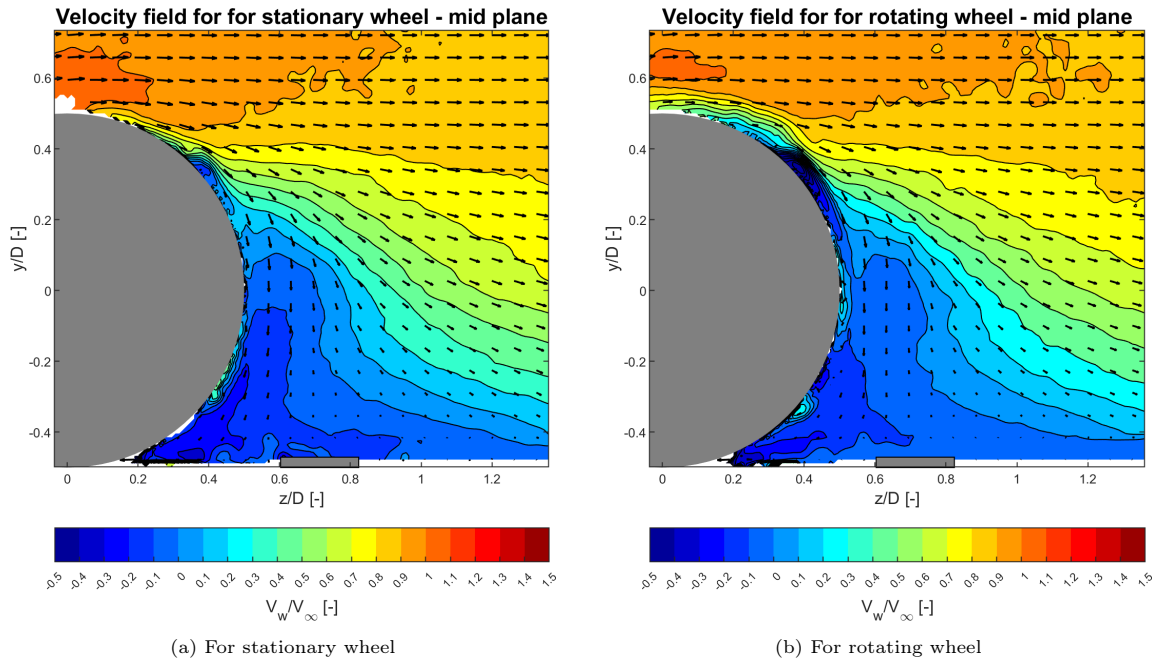


Figure 6.14: Normalised streamwise velocity field (Y-Z plane) at the mid-plane for the isolated wheel. Wheel represented as grey circle and blower represented as grey rectangle.

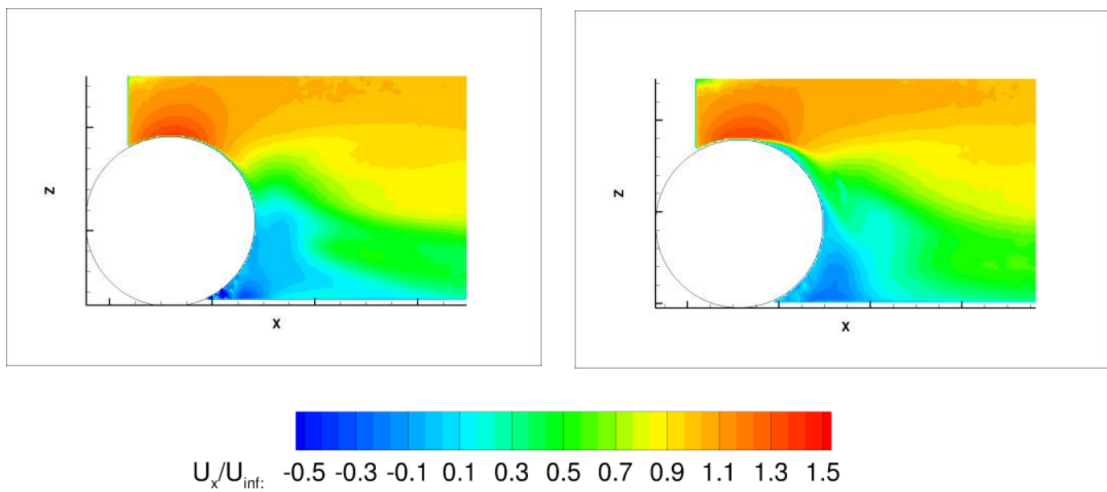


Figure 6.15: Normalised streamwise velocity field at an $Re = 0.72$ million : Left - Stationary wheel, Right - Rotating wheel, by Rajaratnam et al., 2019.

Figure 6.16 shows the difference (ΔV plot) between the velocity magnitude of the rotating and stationary wheel to investigate their differences further. First, the velocity deficit around the rotating wheel (in blue) signified the small layer of fluid that remained attached to the wheel during its rotation. This reduced the relative velocity since the wheel rotation was opposite to the free stream velocity. Second, there was an increment of velocity (in red) in the lower wake region, again highlighting the jetting behaviour behind the rotating wheel.

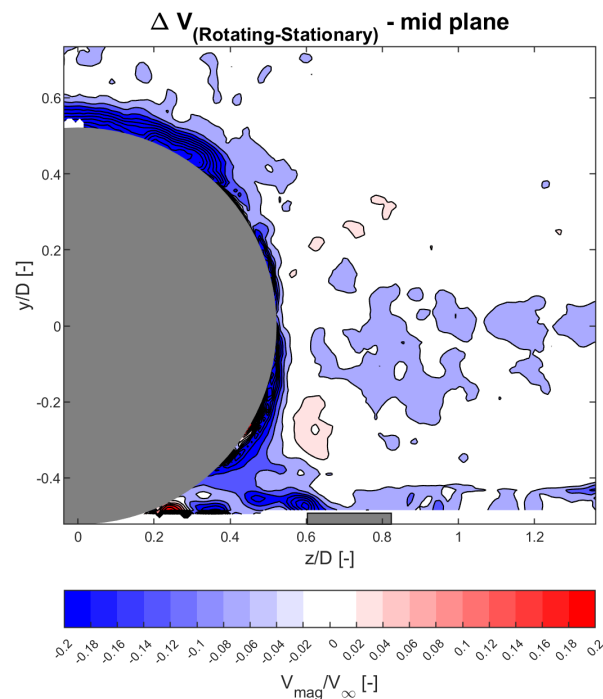


Figure 6.16: Velocity field difference between the rotating and stationary isolated wheel. Wheel represented as grey circle and blower represented as grey rectangle.

The addition of blowing to the rotating wheel had some differences in the wheel wake, as seen in fig. 6.17, primarily because of the location of the blower, which could not be installed further upstream due to geometric/manufacturing constraints in the simulated moving ground. The blower was located approximately 0.6-0.8 z/D downstream of the wheel centre. In contrast, jetting occurs immediately beneath the wheel (interface between the wheel and the simulated ground) upstream of the blower. However, the fig. 6.18 shows the difference in the velocity magnitudes of the blower on and the blower off case helps compare the two cases better. It is seen that blowing increases the strength of jetting (in red) present at the bottom part of the wheel by allowing the wake to convect downstream. Although the higher velocities in the upper part of the wheel indicate that blowing could reduce the amount of fluid sticking to the wheel during rotation, such an inference can not be made with complete confidence. This is because of the limitations of the planar PIV setup, which was prone to high reflections along the upper wheel surface. The wake convection was further visualised using fig. 6.19, which depicts the wake of the blowing case convects more downstream compared to its counterpart, mainly due to the reduction of the boundary layer effects. Further, the findings of Wäschle et al., 2004 also suggest that the rotating wheel experiences a higher vortex stretching and wake convection in the longitudinal (downstream) direction. Therefore, this signifies that blowing does help resemble reality better.

Velocity field for rotating wheel with blowing - mid plane

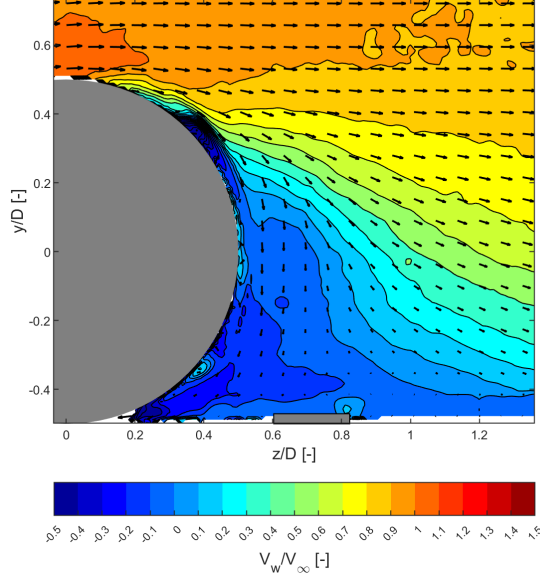


Figure 6.17: Normalised streamwise velocity field (Y-Z plane) at the mid-plane for the rotating isolated wheel with blowing. Wheel represented as grey circle and blower represented as grey rectangle.

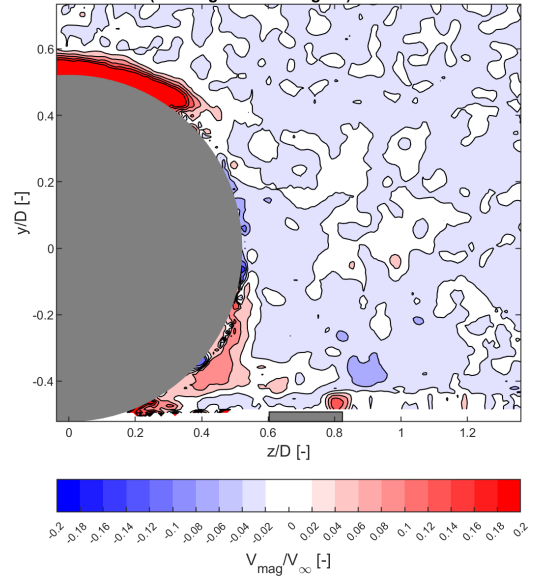
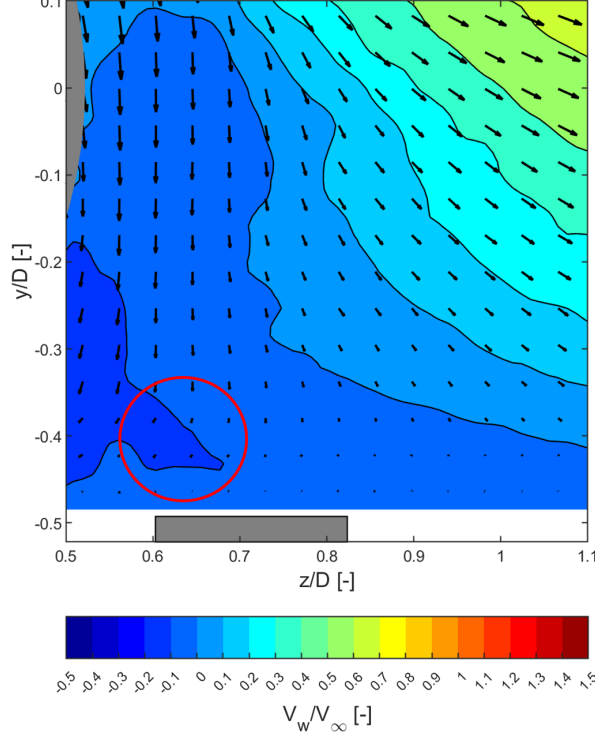
 ΔV (Blowing on - Blowing off) - mid plane

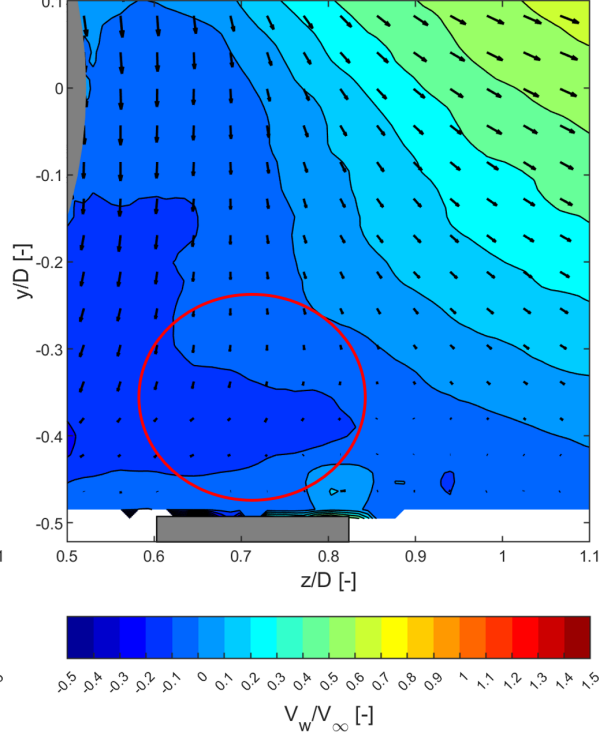
Figure 6.18: Velocity field difference between the rotating with blowing and rotating without blowing isolated wheel. Wheel represented as grey circle and blower represented as grey rectangle.

Zoomed-in velocity field without blowing - mid plane



(a) Without blowing, mid-plane

Zoomed-in velocity field with blowing - mid plane



(b) With blowing, mid-plane

Figure 6.19: Zoomed-in normalised streamwise velocity field (Y-Z plane) at the mid-plane for the rotating isolated wheel. Wheel represented as grey circle, blower represented as grey rectangle. Note: Red circle highlights wake convection.

Similar conclusions were drawn for differences between the stationary, rotating and rotating with blowing cases at the planes present on the left and right planes of the wheel (For velocity plots of the stationary and rotating case, please refer to appendix fig. C.1 to fig. C.4). However, asymmetries in the wake were due to the wheel's axle on the left side. For example, in fig. 6.20, the differences in the wake velocities

were seen. The right plane which was farthest from the axle, had a much lower downwash and a smaller wake due to better pressure recovery in that plane. However, for the left plane, the downwash and the wake were larger due to the axle, which partially restricted the pressure recovery. The pressure recovery is associated with the tendency of the free stream air to mix with the wake, i.e. the pressure difference between them allows high-pressure free stream air to mix with the low-pressure wake region.

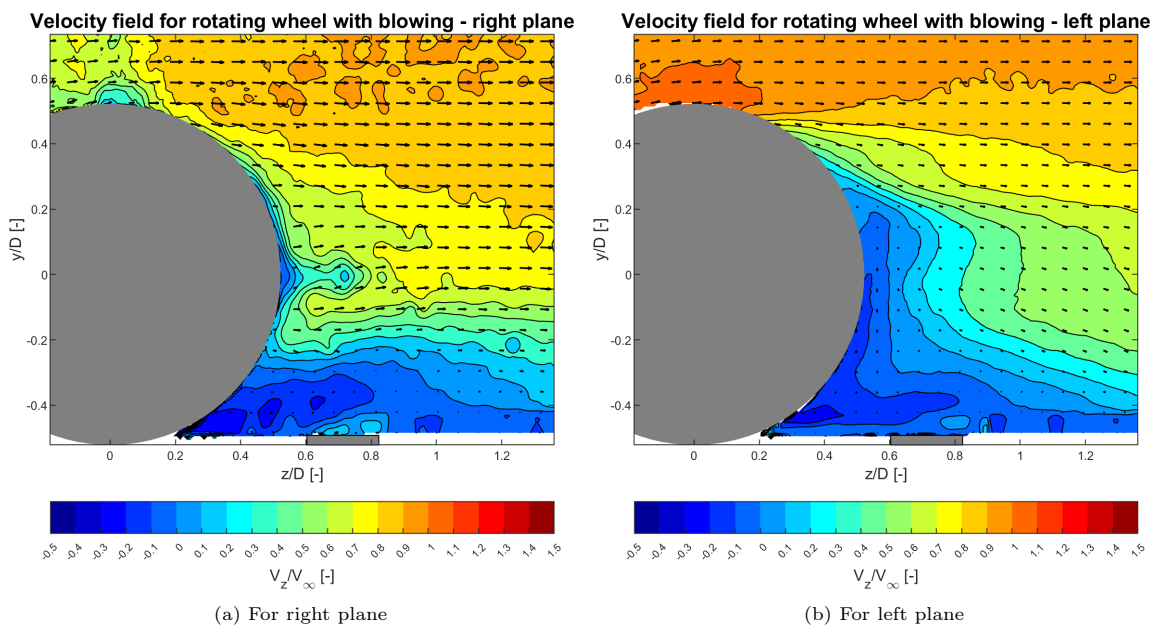


Figure 6.20: Normalised streamwise velocity field (Y-Z plane) at for the rotating isolated wheel with blowing. Wheel represented as grey circle and blower represented as grey rectangle.

6.2.2. Stereoscopic results

The evolution of the wheel's vortex structures was analysed to study further the differences between the stationary, rotating and rotating with blowing cases. For instance, the stereoscopic measurements taken at $z/D = 1$ of the stationary and rotating cases are shown in fig. 6.21. The wake height (Y-direction) was smaller for the stationary case than for the rotating case. This was because of the delayed separation in the stationary case, also seen in the planar results. Contours corresponding to the lower normalised velocities (in blue) had a noticeable difference, suggesting a variation in the ground vortex structures.

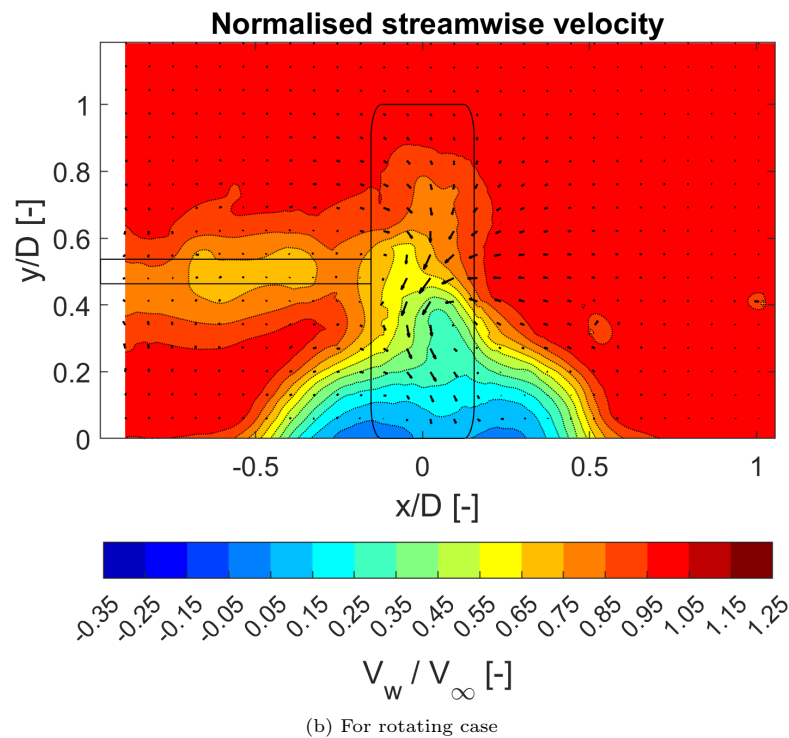
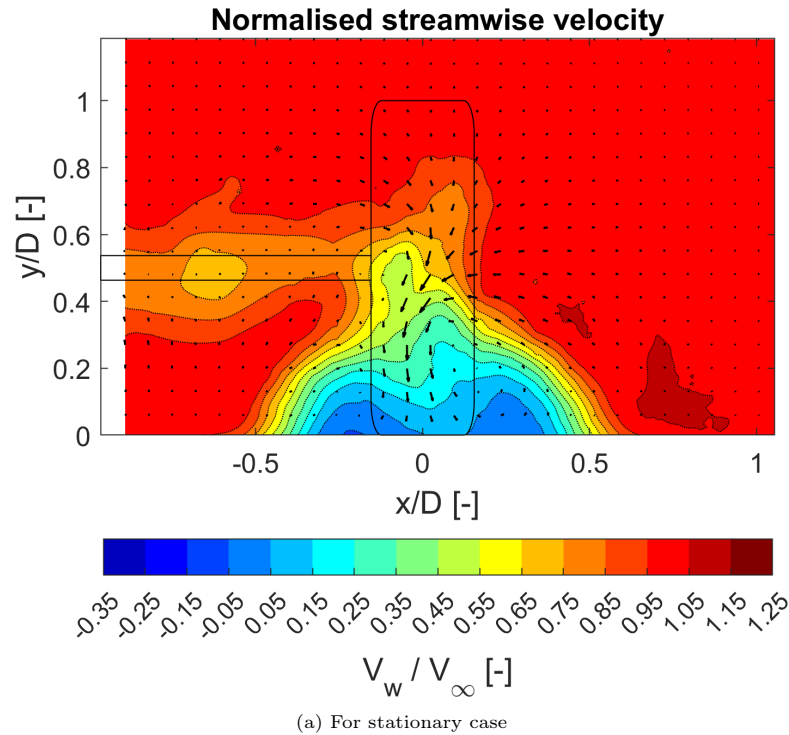


Figure 6.21: Normalised streamwise velocity field (X-Y plane) for the isolated wheel, at $z/D = 1$.

The vorticity plots were analysed to investigate the vortex structures. Notice that the quiver size was increased to identify the flow rotation patterns. Although vorticity fields do not necessarily give the location of a vortex as they cannot distinguish between shear and rotational fields, Graftieaux et al., 2001, they can be used to get a first estimate of the intensity of the vortex. Hence, it was used along with quivers better at visualising the location of the vortex/rotating fields (Refer fig. 6.23 that demonstrates the vortex core locations and quivers).

There were three large vortex structures identified in the $z/D = 1$ plane, as shown in fig. 6.22 for stationary and rotating isolated wheel case. The pair of counter-rotating ground vortices were in good accordance with the findings of previous works such as McManus and Zhang, 2006; Parfett et al., 2022; Saddington et al., 2007. Additionally, the ground vortices were relatively closer, for the rotating case. The vortex on the right (away from the axle) was larger than the one on the left (near the axle). The asymmetry was primarily because of the axle, also reported by Axerio and Iaccarino, 2009.

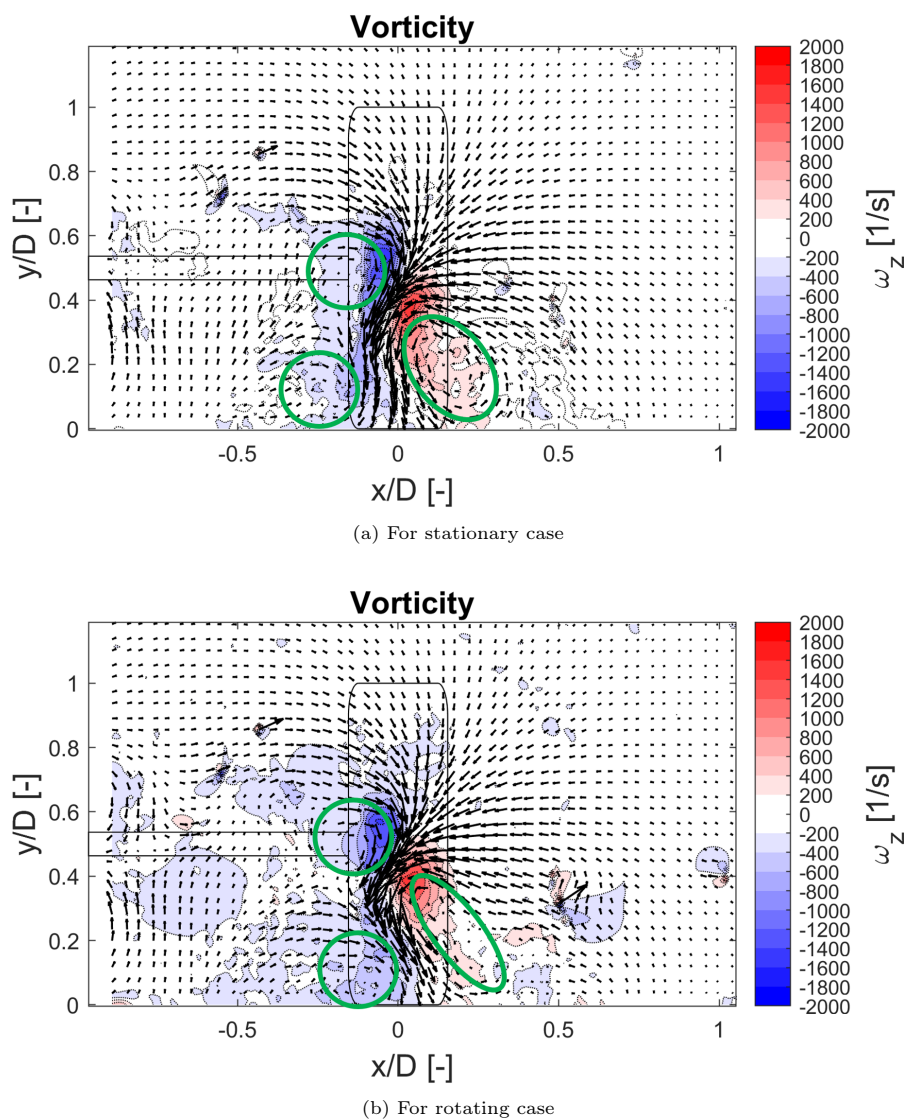


Figure 6.22: Vorticity field (X-Y plane) for the isolated wheel, at $z/D = 1$. Green circles show rotational fields.

The third vortex structure, called the shoulder vortex, was due to the interaction with the axle. The work by Axerio-Cilies et al., 2012 and Parfett et al., 2022, show the presence of similar structures when using a strut as shown in fig. 6.23 and fig. 6.24. Also, it must be noted that this structure was not found in computational studies like the one by McManus and Zhang, 2006 because it lacked the requirements of an axle for support.

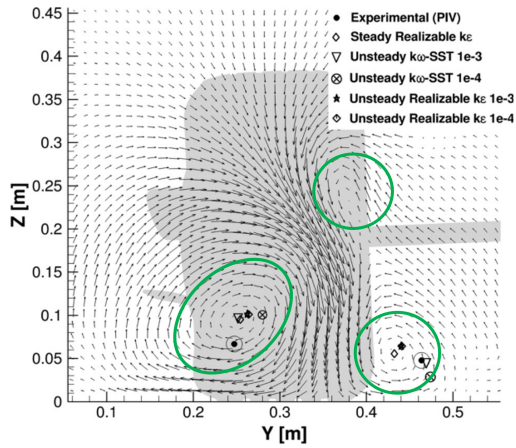


Figure 6.23: Vortex structures (in green circles) using quiver plot, for a rotating wheel at $z/D = 1.11$, for an $Re = 0.5$ million, seen in work by Axerio-Cilies et al., 2012. Note: The legend shows the vortex core locations.

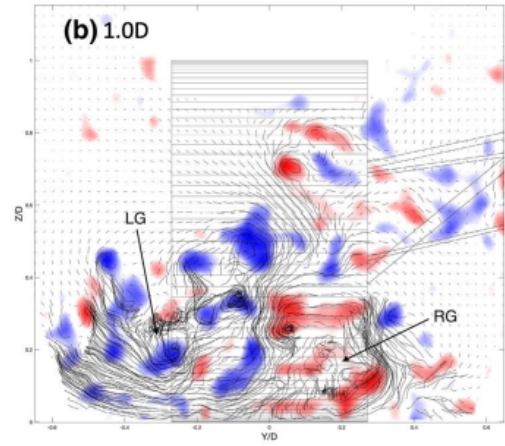


Figure 6.24: Vortex structures (in red and blue), using Γ_2 criterion, for a rotating wheel at $z/D = 1$, for an $Re = 0.415$ million, seen in work by Parfett et al., 2022. The left ground (LG) and right ground (RG) vortex are labelled.

The effects of blowing on the isolated rotating wheel had no major influence on the height or the vortex structures when seen in the X-Y plane, at $z/D = 1$. Hence, this suggests that the immediate boundary layer downstream does not drastically affect the wake of the isolated wheel width/height. However, the measurements taken in the planes corresponding to $z/D = 1.5, 2, 3$ of the rotating with blowing cases increased the height of the wake up to 3%⁷ and reduced the width of the low-velocity region up to 1%⁸ (Refer appendix figures C.5 to C.13 for the velocity plots of the remaining cases of stationary, rotating and rotating with blowing isolated wheel cases).

The nature of the evolution of wake can be understood using fig. 6.25. Going downstream made the wake expand because of the pressure recovery that occurs gradually from the surrounding free stream air. In other words, going downstream meant variations in the wake velocity occurred more gradually. Further, the vortex located away from the axle (right ground vortex) becomes more dominant, confirming the findings of Parfett et al., 2022. The work also mentions that the dominant vortex was almost twice as strong as its counterpart, signifying downstream asymmetries.

⁷Change in height (at the centre line) = Ratio of difference between the height of the layer corresponding $0.9 \frac{V_W}{V_\infty}$ between the two cases to the height of $0.9 \frac{V_W}{V_\infty}$ of stationary case.

⁸Change in width (at baseline) = Ratio of difference between the width of the layer corresponding lowest $\frac{V_W}{V_\infty}$ between the two cases to the width of lowest $\frac{V_W}{V_\infty}$ of stationary case.

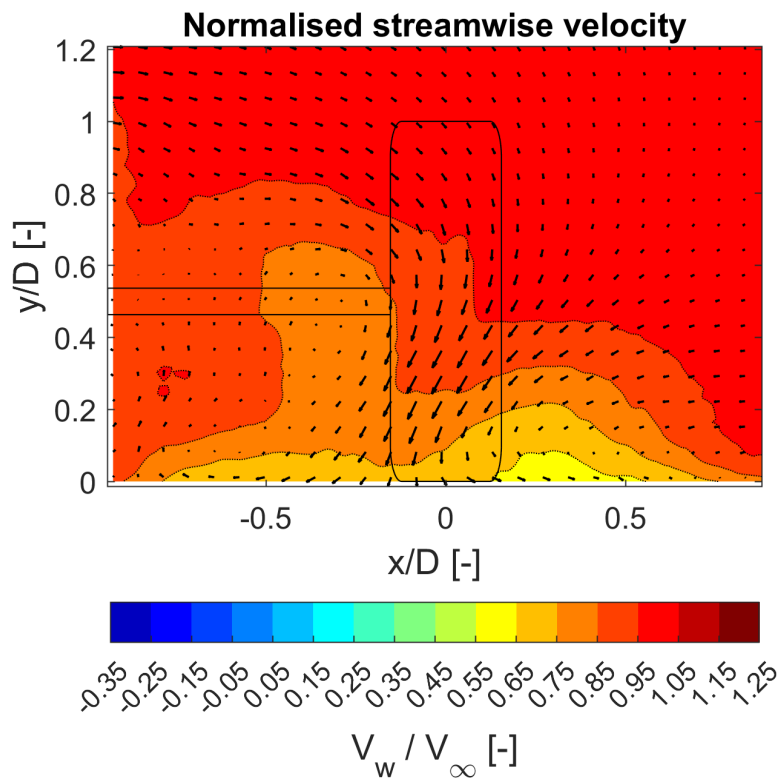
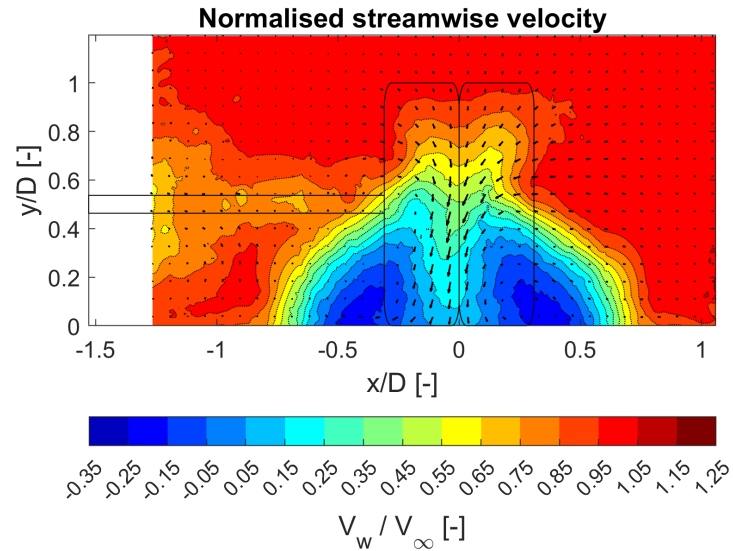


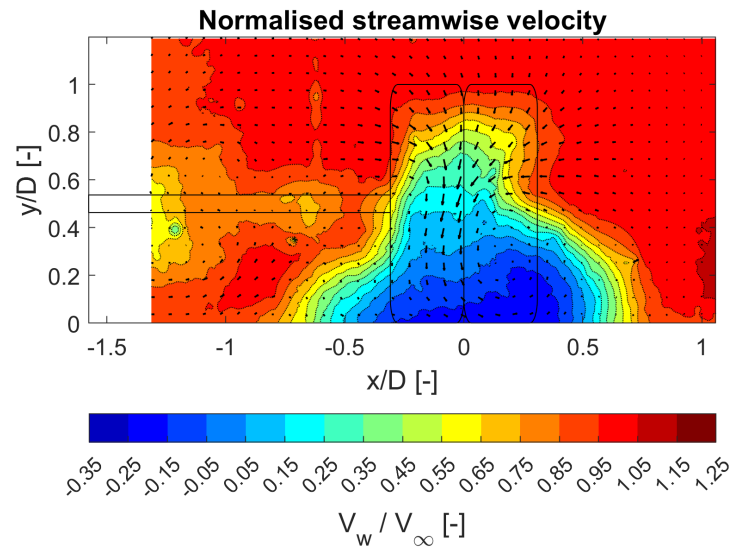
Figure 6.25: Normalised streamwise velocity field (X-Y plane) for the rotating isolated wheel with blowing, at $z/D = 3$.

6.3. Double Wheel

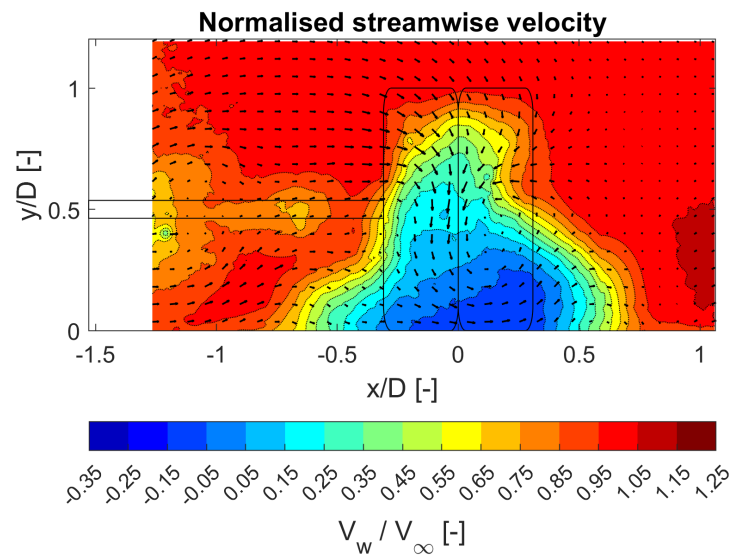
Compared to the isolated wheel, the wake structures found in the double wheel were larger. For instance, the fig. 6.26 show the wake behind the stationary, rotating double wheel and rotating double wheel with blowing, at $z/D = 1$. The stationary double wheel wake was shorter (5.20%) and wider (21.46%) compared to the rotating case, indicating the delayed separation and a larger downwash in the stationary case. Additionally, the effects of blowing were also more noticeable due to the wake of the double wheel being larger than the isolated wheel. Such behaviour was accounted primarily for the increased surface contact (adjacent wheel) that increases both the jetting area and the amount of downward facing front face of the wheel that touches the ground. More specifically, the front-facing part generates the small vortex structures in the boundary layer upstream of the contact patch that aid the ground vortex structures downstream, Parfett et al., 2022. The rotating double wheel with blowing increased the height (4.16%) and reduced the width (18.54%) of the wake compared to the rotating case, i.e. it helped convect the wake slightly upwards and downstream along the direction of jetting by reducing the boundary layer effects.



(a) For stationary case



(b) For rotating case



(c) For rotating with blowing case

Figure 6.26: Normalised streamwise velocity field (X-Y plane) for the rotating double wheel, at $z/D = 1$.

Vorticity fields in fig. 6.27 are shown to investigate the changes in the vortex structures in comparison to the isolated wheel. The counter-rotating pair was much larger, and the shoulder vortex was engulfed by the left vortex (nearer to the axle), forming a larger structure for the stationary case. For the rotating case, the vortices came closer and were located slightly higher. The left vortex and the shoulder vortex remained combined but produced rather small circular fields, unlike the isolated wheel where no such phenomenon occurs. The addition blowing, as explained earlier, shows a further reduction in the downwash and pushes vortex structures upwards along the direction of jetting.

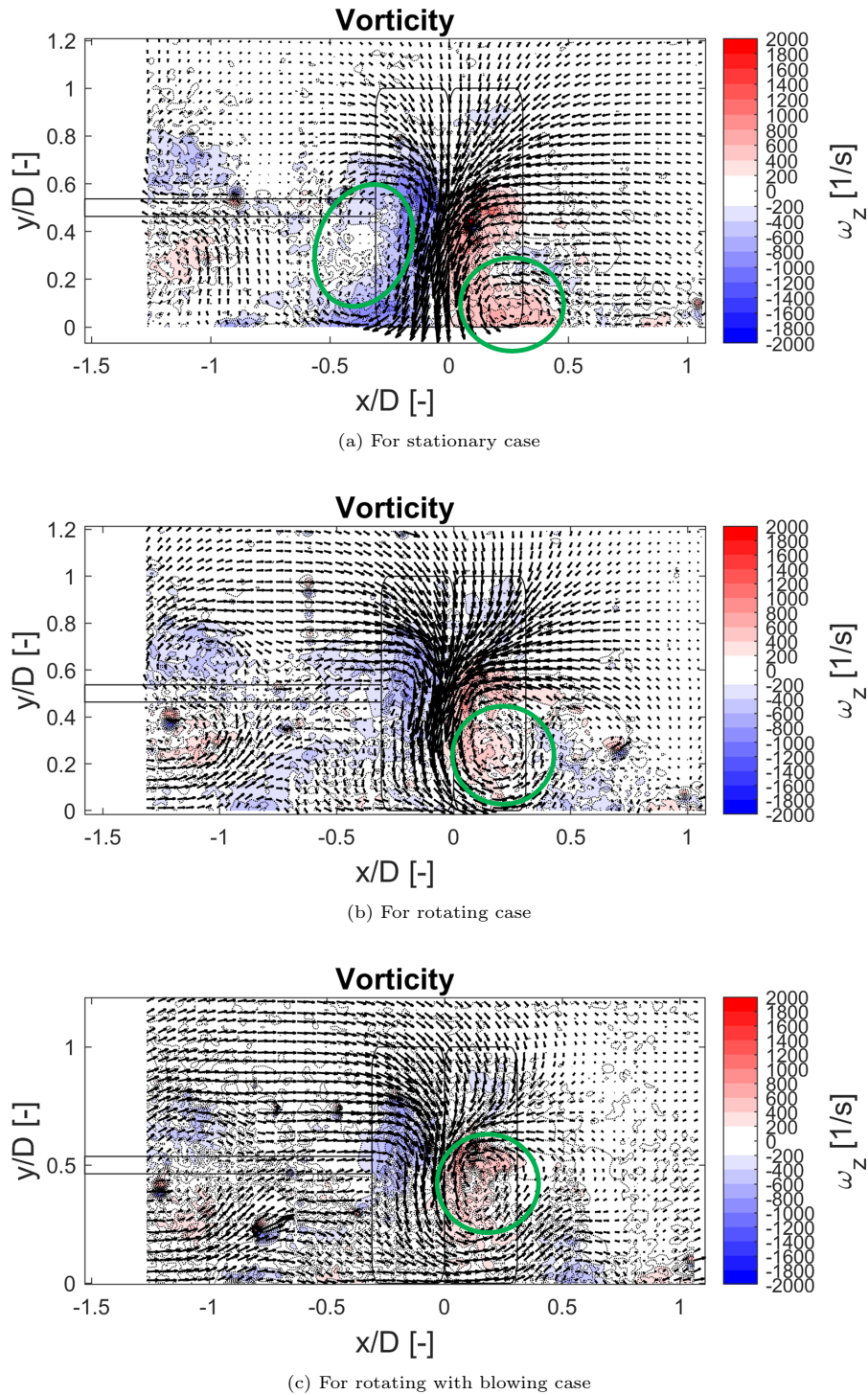


Figure 6.27: Vorticity field (X-Y plane) for the double wheel, at $z/D = 1$. Green circles show rotational fields.

The differences between the stationary double wheel, rotating double wheel and rotating double wheel

with blowing were similar in all the planes measured downstream (Refer appendix figures C.14 to C.21 for the velocity plots of the remaining cases of stationary, rotating and rotating with blowing double wheel cases). The velocity fields show the reduction of height and increment of width, similar to the isolated wheel. However, to investigate the effects of the wake evolution downstream, the vorticity fields for the rotating double wheel with blowing are considered since they will help make the inferences for the mudflap designs discussed in the latter sections. Figure 6.28 shows the vortex evolution for the planes $z/D = 2$ and 3. The ground vortex on the left becomes more apparent when going downstream, i.e. the vortex detaches itself from the shoulder vortex. Similarly, vortex structures generally tend to move outwards (diffuse into the free stream) from the wheel centre. The vorticity levels also reduce, indicating pressure recovery similar to the isolated wheel. Please refer appendix figures C.24 to C.29 for the vorticity plots of the cases of stationary double wheel and rotating double wheel cases.

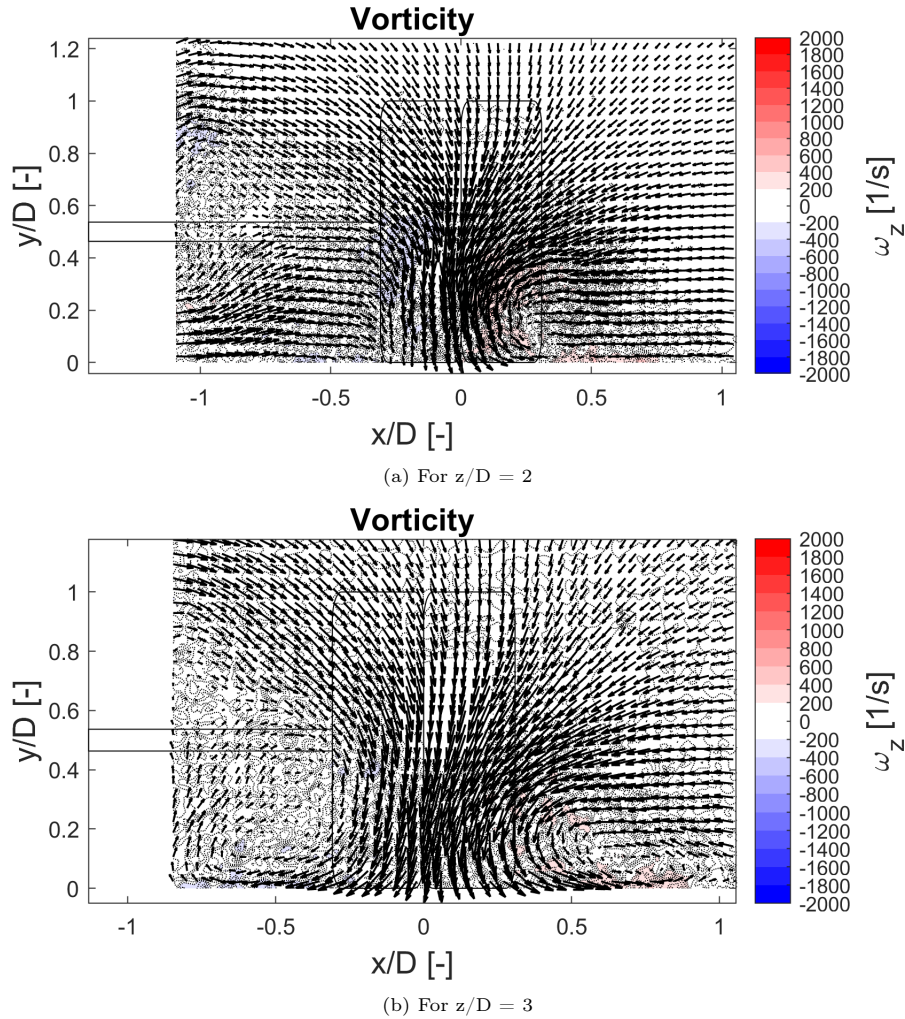
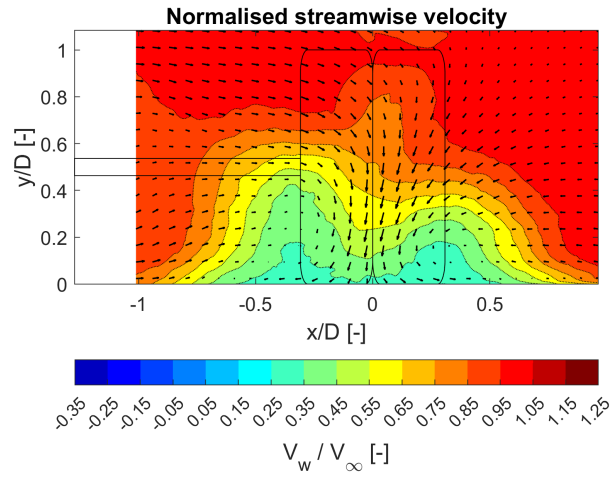


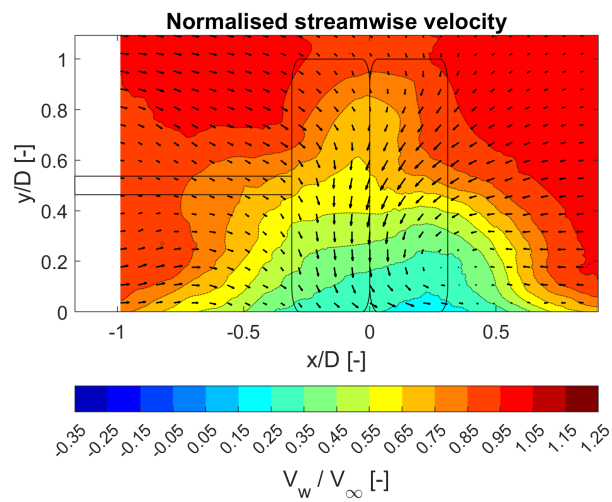
Figure 6.28: Vorticity field (X-Y plane) for the rotating with blowing double wheel at different wake planes.

6.4. Underbody

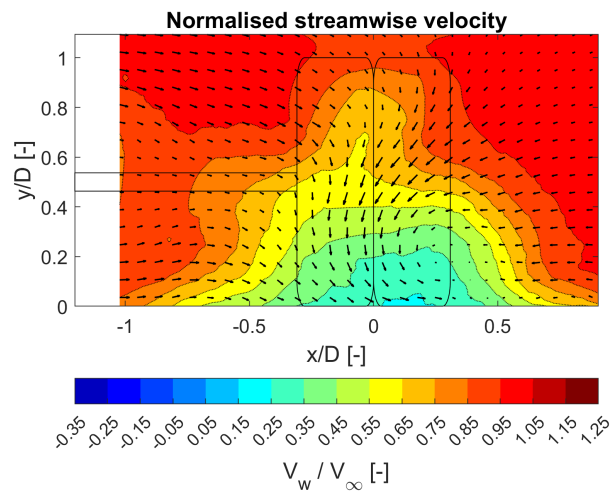
The addition of the underbody over the double wheel setup increased the mean free stream velocity by approximately 0.7-1 [m/s]. This was because of the sudden contraction of flow caused by the underbody and the simulated moving ground. The velocity fields looked quite similar to the double wheel (after normalising with the free stream velocity) for the $z/D = 1, 1.5$ planes. However, there were noticeable differences for the planes further downstream, such as $z/D = 2$ and 3. The velocity plots for the $z/D = 2$ plane of the stationary double wheel with underbody, rotating double wheel with underbody, and rotating with blowing and underbody cases are shown in fig. 6.29 (see next page). The boundary layer on the underside of the underbody grew to a point where it interacted with the wake of the double wheel. The rotating double wheel with blowing had the highest interaction with the boundary layer of the underbody amongst the three cases shown. Hence, the differences in the height of the wake mentioned in the section 6.3 were re-confirmed and show that blowing is more effective for bodies with low-ground clearance. Finally, it is worth noting that the combined effects of the wake expansion and growing boundary layer downstream create a larger velocity deficit when compared to the wake of the double wheel alone (Refer appendix fig. C.30 to fig. C.38 for the remaining cases of underbody).



(a) For stationary case



(b) For rotating case



(c) For rotating with blowing case

Figure 6.29: Normalised streamwise velocity field (X-Y plane) for the double wheel in the presence of underbody, at $z/D = 2$.

6.5. Mudflaps

It was deemed sufficient to analyse the mudflap designs using only the rotating blowing case, as a considerable amount of differences between the stationary, rotating, and rotating wheel with blowing were provided in the previous section. The measurements related to the stationary cases were non-essential because the focus was to study the mudflaps' effects when the heavy-duty vehicle is in motion.

6.5.1. Mudflap holder

Before comparing the different mudflap designs, it was necessary first to quantify the effect of the mudflap holder. From fig. 6.30, it was observed that the wake of the mudflap superimposes itself to the wake of the wheel, creating a larger velocity deficit. However, a local zone of velocity increment was seen at the central part of the wake (positioned around $x/D = 0.1$ and $y/D = 0.5$). This was due to the Venturi effect, Anderson, 2011, created between the wheel's upper part and the mudflap holder's lower portion. As a result, the ground vortices were pushed slightly downwards. Additionally, the rolling of the fluid layers around the mudflap holder induced sidewash at its edges (making fluid from both the left and right edges move inwards towards the centre line).

In the downstream planes, similar effects were observed with ground vortices moving further away from the wheel centre line. Consequently, a greater wake overlap between the mudflap holder and wheel wake along with a gradual variation of velocities in the wake (Refer appendix figures C.39 to C.41 for the velocity plots of the downstream cases of the mudflap holder-double wheel cases) were also seen. However, one noticeable difference compared to the double wheel was the presence of a new pair of counter-rotating vortices on the upper part of the mudflap seen in fig. 6.30 for the plane $z/D = 3$. These vortices were formed by the combination of the rolling fluid layers around the mudflap holder and the upwash present on the lower end of the holder due to pressure recovery from the free stream air below it.

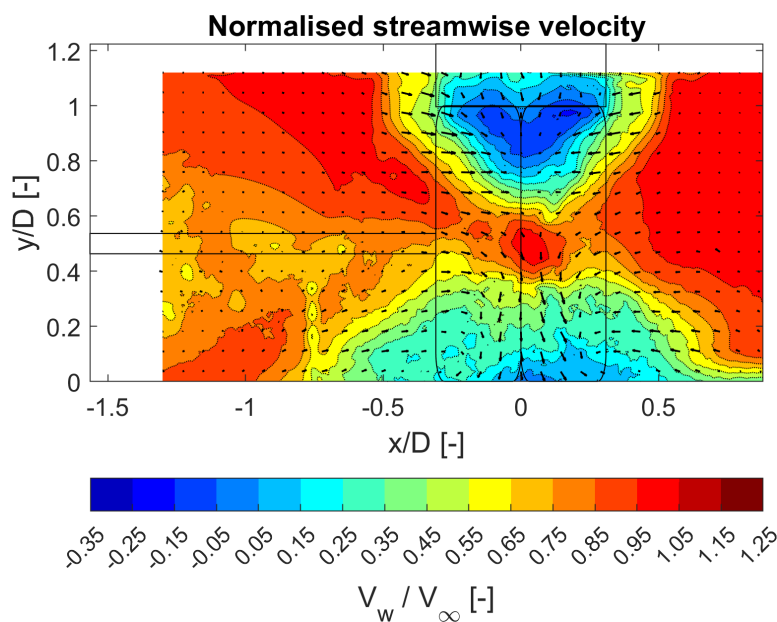


Figure 6.30: Normalised streamwise velocity field (X-Y plane) for the rotating double wheel with blowing in the presence of mudflap holder, at $z/D = 1$.

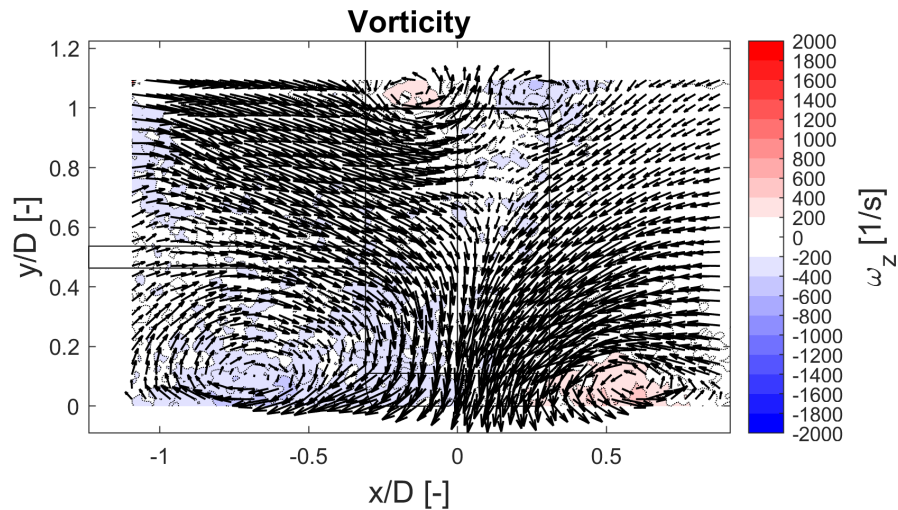


Figure 6.31: Vorticity field (X-Y plane) for the rotating double wheel with blowing in the presence of mudflap holder, at $z/D = 3$.

6.5.2. Solid mudflap

A common issue noticed for most of the mudflap measurements at the $z/D = 1$ plane were reflections from the mudflap body, due to which the estimated particle velocities were erroneous. As a result, the fluctuations and the derived pressure fields were also prone to errors. Hence they are discarded for further discussions.

The fig. 6.32 shows the velocity field of the double wheel in the presence of the solid mudflap at the $z/D = 1.5$ plane. Using a solid mudflap resulted in the largest velocity deficit out of all the cases. The counter-rotating ground vortex pair behind the double wheel were greatly affected, i.e. they were spread more laterally along with a reduction in height and rotation. Such behaviour was accounted for by a head-on collision⁹ of the ground vortices with the solid mudflap. Further, the previously present downwash was almost negligible; instead, there was upwash. This was because the newly formed upper counter-rotating vortex pair were more dominant compared to the mudflap holder case discussed previously in section 6.5.1.

Going downstream led to greater asymmetries in the field, with larger upwash and stretching of the upper right vortex. This led to skewing of the wake, shown in fig. 6.33 for the plane $z/D = 3$. A possible reason for the skewing downstream could be the dominance of the upper right vortex structure, which was hypothesized to be the asymmetries caused by the axle.

⁹Head-on collision: The process where upstream vortex structures interact with the solid geometry (mudflap) present downstream changing both structure and intensity of the vortices.

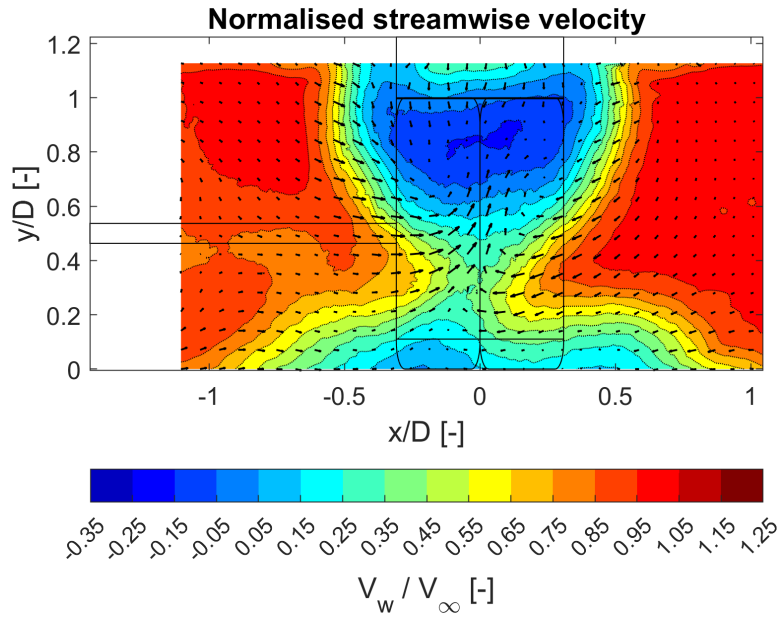


Figure 6.32: Normalised streamwise velocity field (X-Y plane) for the rotating double wheel with blowing in the presence of solid mudflap, at $z/D = 1.5$.

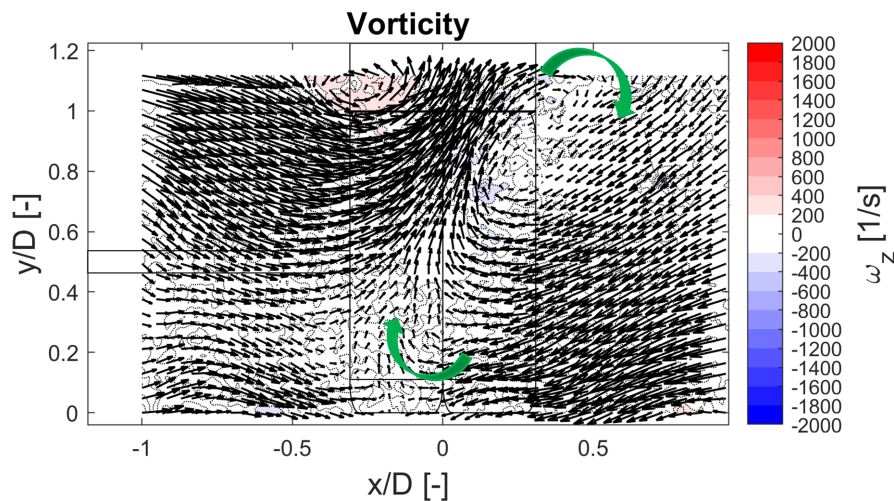


Figure 6.33: Vorticity field (X-Y plane) for the rotating double wheel with blowing in the presence of solid mudflap, at $z/D = 3$. With skewing direction shown in green.

6.5.3. Semi-solid mudflaps

The mudflap design with a solid top-hollow bottom produced similar results to the solid mudflap. Figure 6.34 shows the velocity field behind the hollow bottom mudflap. It was observed that the shape of the ground vortices was relatively better preserved to the solid mudflap, but their ability to locally rotate the flow remained similar. This was due to the lack of head-on collision at the lower portion of the mudflap. Furthermore, there were marginally higher velocities at the central part of the wake. Similarly, in the downstream planes, the wake evolution was also alike. The skewing effect was less pronounced in the lower part of the wake, i.e. the top right vortex experience lesser stretching, as shown in figure fig. 6.35. This reduction was due to the partial pressure recovery from the mudflap's hollow bottom.

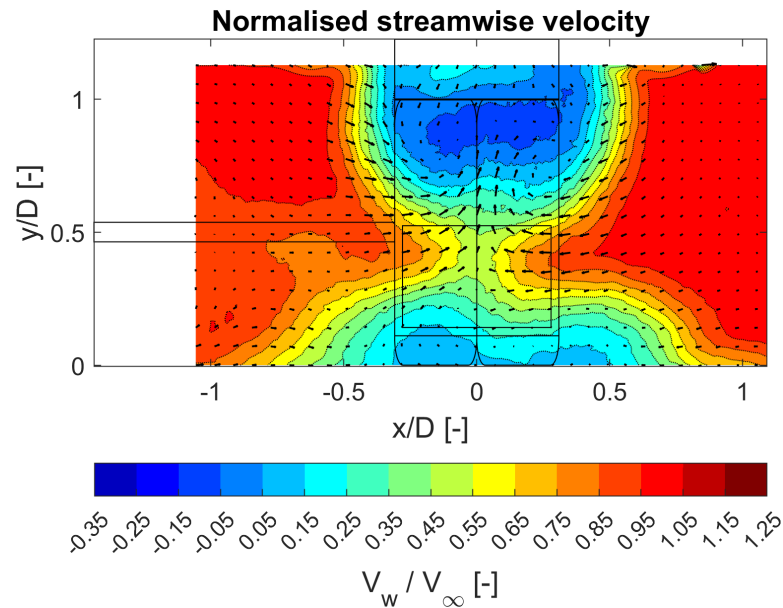


Figure 6.34: Normalised streamwise velocity field (X-Y plane) for the rotating double wheel with blowing in the presence of hollow bottom mudflap, at $z/D = 1.5$.

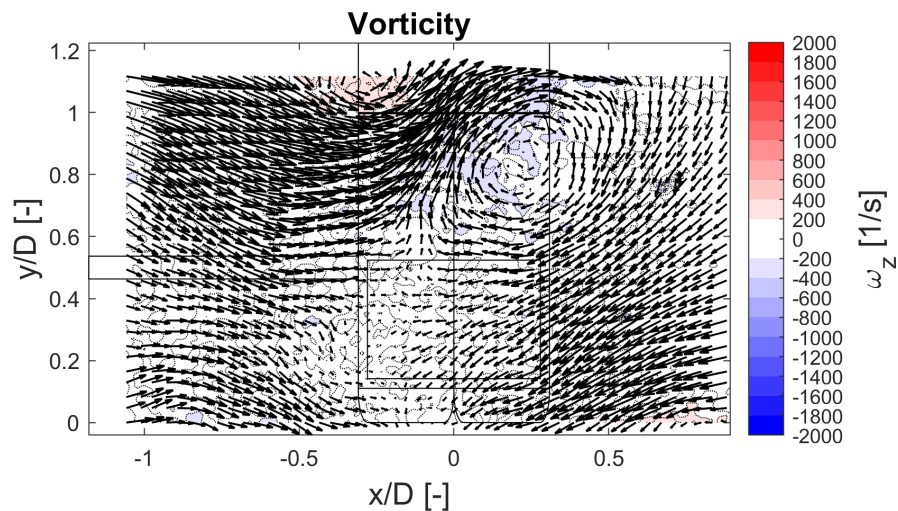


Figure 6.35: Vorticity field (X-Y plane) for the rotating double wheel with blowing in the presence of hollow bottom mudflap, at $z/D = 3$.

The mudflap design with hollow top-solid bottom produced the lowest velocity deficits among all the mudflap designs. Figure 6.36 shows the velocity field at the $z/D = 1.5$ planes; it was noticed that the ground vortex structures were affected the least when comparing all the mudflap designs. Although it was expected that the head-on collision at the solid bottom part would heavily influence the ground vortex structure, the hollow top helped regain a major portion of the downwash. Hence pushing away and partly reviving the ground vortices. Therefore the ground vortex pair's size and ability to induce a local rotation were well retained. However, when comparing the double wheel with the mudflap holder case, the wake overlap was still higher, suggesting a larger wake overlap due to solidity at the bottom of the mudflap.

The evolution of the wake was quite similar to the mudflap holder case seen in appendix fig. 6.37 for the $z/D = 3$ plane. The vortices retained their shape and evolved to move away from the wheel/mudflap centre line. Additionally, no major skewing was identified, indicating that having a hollow section at the upper of the mudflap is more effective at reducing the effects of the upper vortex pair.

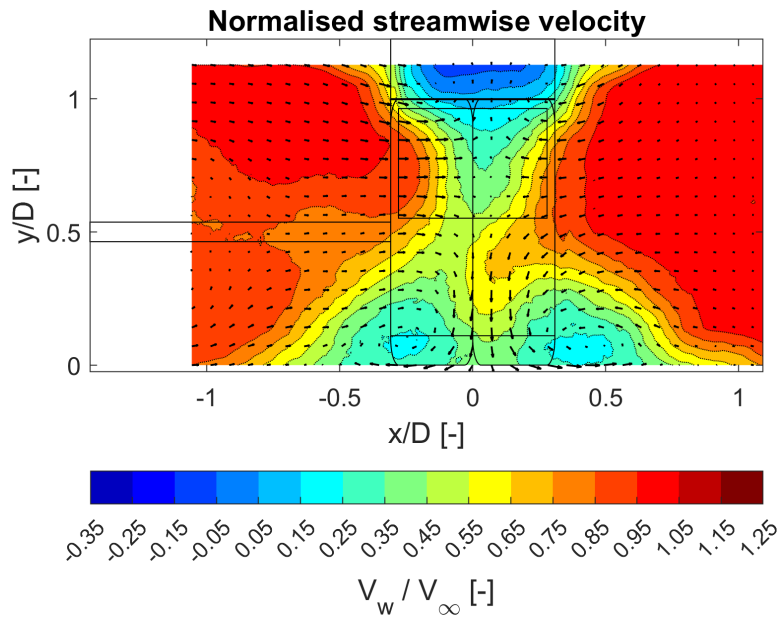


Figure 6.36: Normalised streamwise velocity field (X-Y plane) for the rotating double wheel with blowing in the presence of hollow top mudflap, at $z/D = 1.5$.

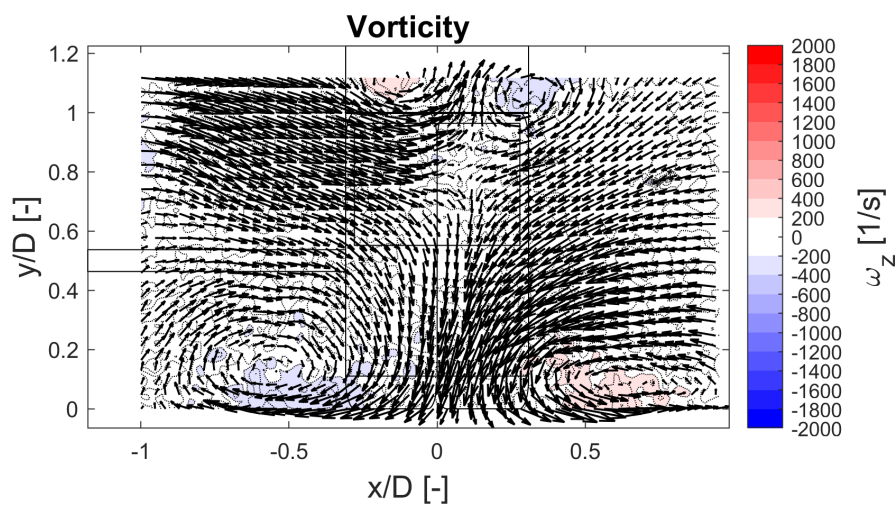


Figure 6.37: Vorticity field (X-Y plane) for the rotating double wheel with blowing in the presence of hollow top mudflap, at $z/D = 3$.

6.5.4. Louvered mudflaps

The louvered mudflap with 2.8mm louvers (solidity = 0.52) had a relatively larger velocity deficit in comparison to 1mm louvered mudflap (solidity = 0.26) as seen in fig. 6.38 and fig. 6.39. The velocity deficit was prominent in the upper region of the mudflap, suggesting that solidity in the upper region was crucial. The louvers marginally reduce the amount of downwash and affect the ground vortex pair by reducing their ability to induce rotation/skew the flow locally. However, they do not seize it completely.

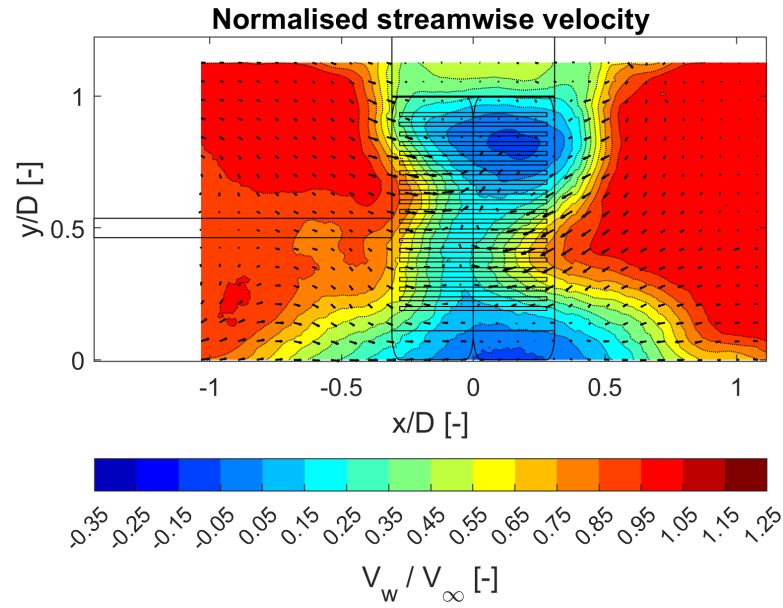


Figure 6.38: Normalised streamwise velocity field (X-Y plane) for the rotating double wheel with blowing in the presence of 2.8mm louvered mudflap, at $z/D = 1.5$.

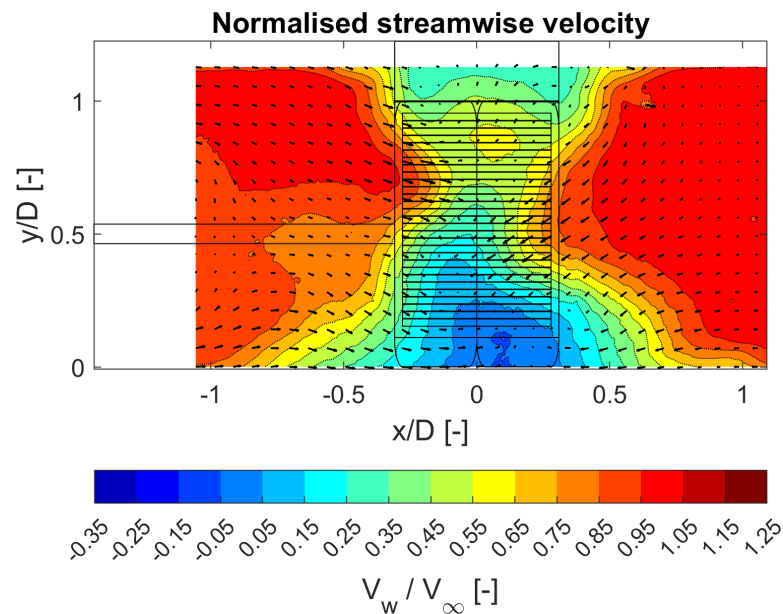


Figure 6.39: Normalised streamwise velocity field (X-Y plane) for the rotating double wheel with blowing in the presence of 1mm louvered mudflap, at $z/D = 1.5$.

The effect of the thickness of louvers can be understood by further analysing the wake structures. The 2.8mm louvers were able to reduce the local rotation effects of the ground vortex pair in comparison to the 1mm louvers due to the relative difference in the head-on collision as seen in fig. 6.40 and fig. 6.41, for $z/D = 3$ plane. On the contrary, thicker louvers, especially in the upper portion of the mudflap, meant stronger upper counter-rotating vortex pair and skewing.

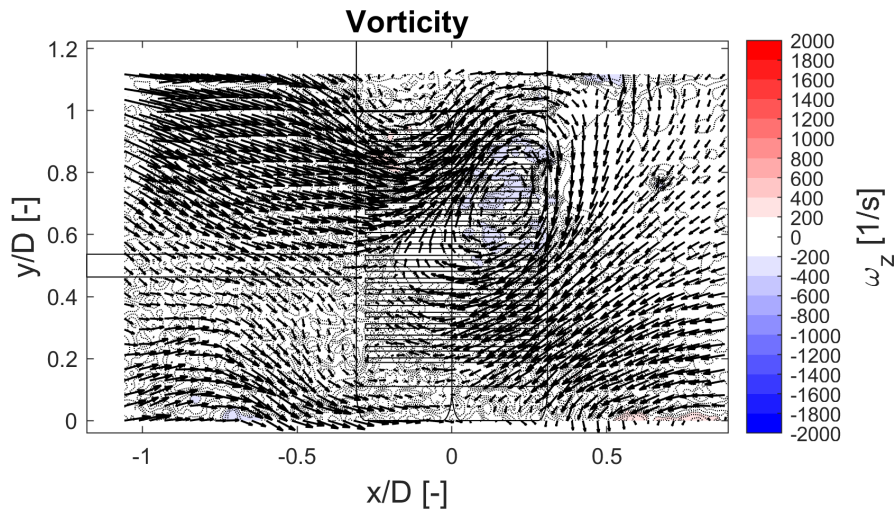


Figure 6.40: Vorticity field (X-Y plane) for the rotating double wheel with blowing in the presence of 2.8mm louvered mudflap, at $z/D = 3$.

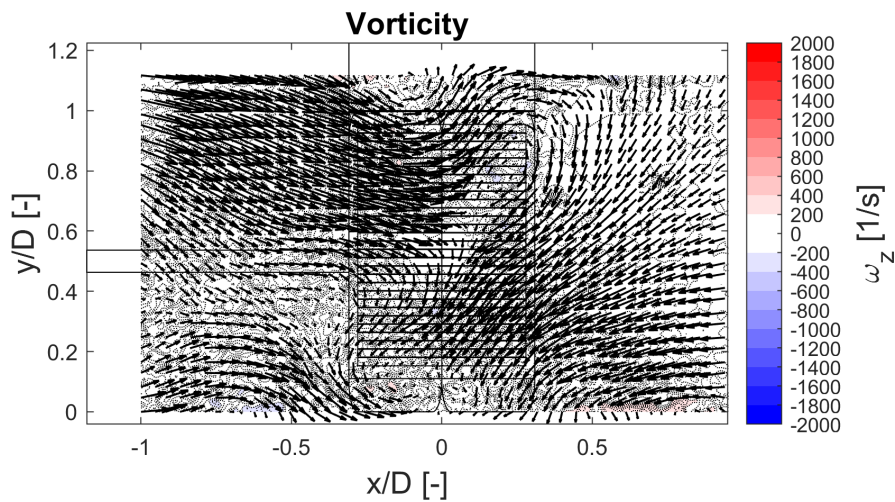


Figure 6.41: Vorticity field (X-Y plane) for the rotating double wheel with blowing in the presence of 1mm louvered mudflap, at $z/D = 3$.

There were no major differences in the wake evolution patterns when comparing the louvered flaps to the solid/hollow bottom mudflap designs (Refer appendix figures C.42 to C.47 for the velocity and vorticity plots of the remaining cases for all the mudflap configurations).

6.6. Coefficient of drag

Figure 6.42 shows the coefficient of drag for the various configurations at the wake downstream planes $z/D = 1.5, 2, 3$. Note that the drag coefficients were all based on the half frontal area of the double wheel, which was $136 \times 84/2 [mm^2]$ (The diameter times half width of the double wheel) using equation eq. (3.12) and the effects of the axle were neglected by taking the right of the wake. The drag estimates showed a clear difference between the different configurations. In general, the addition of geometries introduced more obstruction and velocity deficits, giving higher drag coefficients at each step. The momentum term was the main contributor to drag, followed by the fluctuation and pressure terms (Refer to appendix fig. C.57 for a detailed breakdown of the momentum, pressure and fluctuation terms). However, the inferences in the previous sections of this chapter can help distinguish between each case.

Firstly, the reference case, i.e. the double wheel configuration, showed the least drag with major wake

velocity deficits around the ground vortex region. Adding the underbody resulted in a jump in the drag coefficient, mainly due to the increment of the mean free stream velocity and wake interaction with the boundary on the underbody. Consequently, this meant higher contributions to the momentum term. Next, the mudflap holder introduces two more vortex structures at the top, transferring the energy from the streamwise component to the in-plane velocities, hence giving rise to higher drag. The inferences on the mudflaps suggested that the upper part of the mudflap is more crucial than the lower part for reducing the velocity deficit. Therefore, the hollow top mudflap offered the least drag of all the mudflap designs tested, followed by the louvered mudflaps (1 [mm] and 2.8 [mm]), hollow bottom mudflap and finally, the solid mudflap, respectively.

The drag coefficients of a given configuration for different wake planes downstream were expected to be the same, abiding by the conservation laws. However, it was observed that was not the case. The mudflaps with more solidity at the top exhibit more wake skewing as the wake progress downstream. As a result, dividing the wake using the centre line and finding the drag led to an overestimation¹⁰. In contrast, for the case of the double wheel and the underbody at the plane $z/D = 3$, an underestimation of the drag coefficient was noticed. Since the FOV was fixed for the stereoscopic PIV measurements, the wake expansion downstream inevitably causes the wake to spread horizontally beyond the FOV. Therefore, leading to the reduced C_D value of the double wheel and underbody.

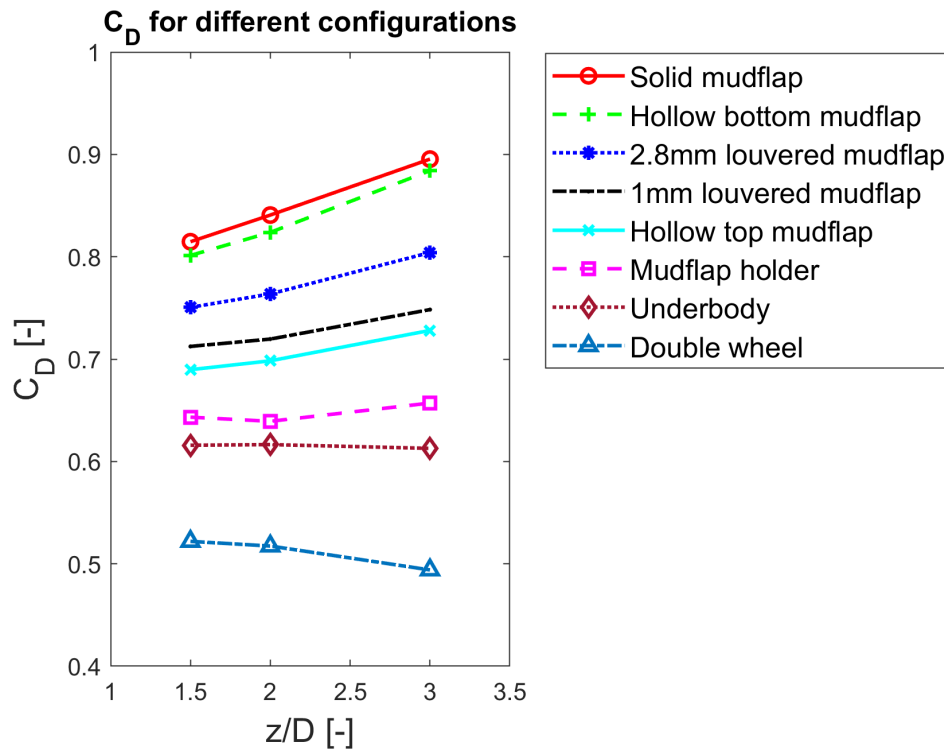


Figure 6.42: Coefficient of drag for various configurations at different wake planes (z/D).

Quantifying the amount of error/uncertainty in any given measurement is always necessary. Ideally, the values (drag coefficient) obtained would be the actual value; however, various factors such as measurement and random errors are represented using a range of values instead of a single value. The range is also known as the uncertainty bar. Generally, these uncertainties are quantified using a linear uncertainty propagation analysis (Refer Coleman and Steele, 2009; Sciacchitano and Wieneke, 2016 for more information). However, considering the set of the experiments and the procedures for drag estimation described in section 5.2, there were additional parameters like uncertainties due to deviations in the centre line, exact mean free stream velocity (average box), exact boundary conditions for the derived pressure fields (specifically for the left side of the images around the axle region) and so on. Hence, to avoid further complications, a straightforward approach was taken. The uncertainties are determined

¹⁰Note: Taking the entire image instead of the half wake, still included the effects of the axle wake and its interference leading to even higher drag coefficients, hence was not feasible even at the plane $z/D = 3$.

by the differences in the drag values obtained at the downstream planes as shown in fig. 6.43.

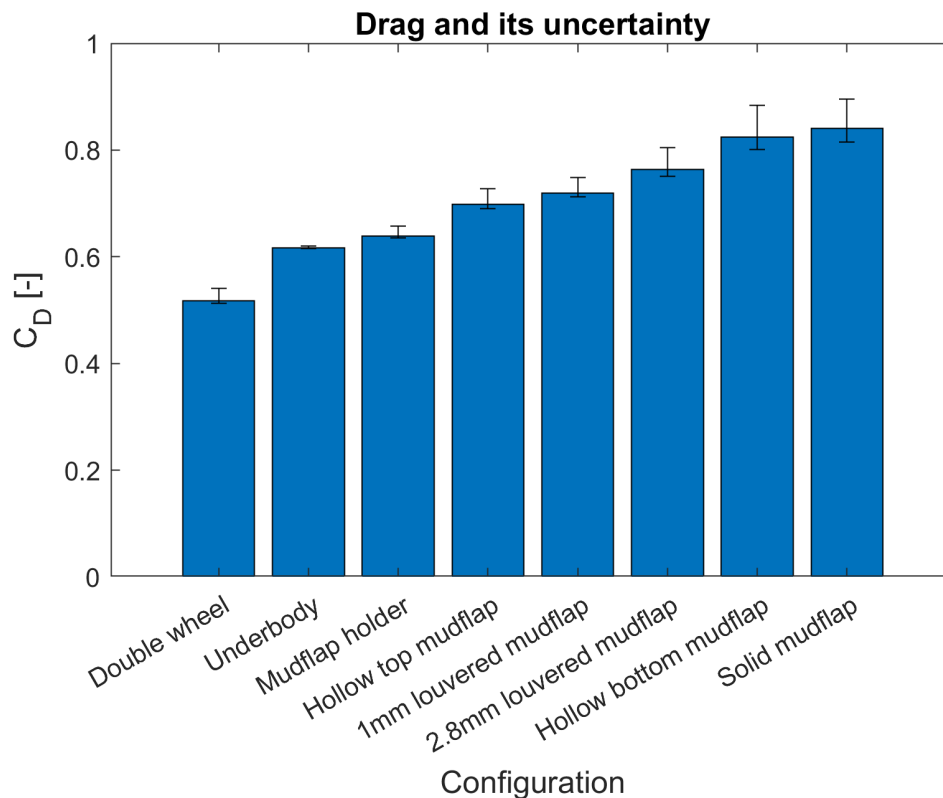


Figure 6.43: Drag coefficient for various configurations with their respective uncertainties, based on the different wake planes.

The main takeaways were that the cases corresponding to the double wheel, underbody, and mudflap holder showed a visible difference (i.e. with no overlap between the uncertainty bars) compared to any of the mudflap cases. Although there was some overlap amongst the subsequent mudflap cases, a noticeable difference was observed between the hollow top, 2.8 [mm] louvered mudflap and hollow bottom mudflaps. Therefore, providing confidence in concluding that the solidity on the mudflap's top half offers more drag than the solidity on the bottom half, i.e. about a 15% difference in the drag coefficients. Additionally, it partly supports the conclusion that for a fixed amount of solidity = 0.52, having a uniform distribution of solidity using horizontal louvers was more effective than having solidity on the top since the overlap between the uncertainty bars was 28 drag counts. In short, the study shows that solidity was one factor, but placement of solidity is another crucial factor.

Further, to determine the statistical significance of the mudflap designs an analysis of variance (ANOVA) was conducted (for more information about ANOVA refer Wold, St, et al., 1989). The fig. 6.44 clearly shows that the difference between the mean drag coefficient of the hollow top mudflap and hollow bottom mudflap were statistically significant. However, the same cannot be said for the louvered mudflaps as their drag coefficients were quite similar. Please refer appendix fig. C.58 for the full ANOVA table of all designs with their respective P-values.

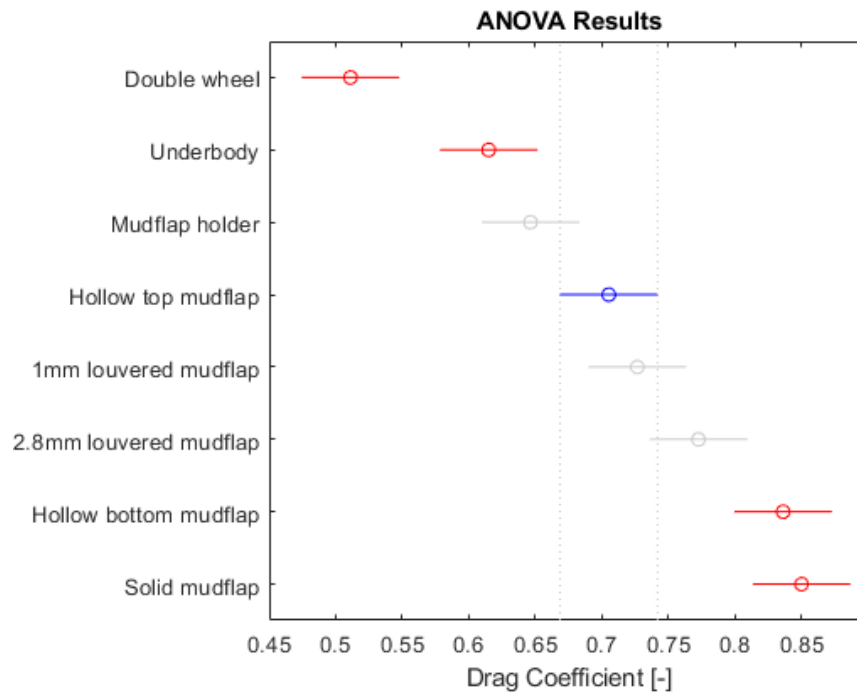


Figure 6.44: ANOVA analysis for the various designs, in particular, showing the difference between the hollow top design being statistically different from the hollow bottom design. The greyed out lines indicate the designs that are not statistically different from the hollow top design.

6.7. Answers to the research questions

This section addresses the research questions provided in section 2.2, briefly summarising the findings in this chapter.

1. What are the geometric design considerations for the tangential blowing slot?

The geometric considerations that helped devise an efficient tangential blower design were the blowing outlet type, support wall design, and pressure line inlet's location as shown in section 6.1.1. It was observed that having a flushed blowing outlet produced a similar blowing profile compared to the step profile. The flushed outlet proved to be a better choice, identical to the design made by Berndtsson et al., 1988 because the step outlet's geometric shape could produce flow perturbations. Although thicker and non-filleted support walls provided more structural integrity and were easier to manufacture, they created a noticeable obstruction to the flow. Consequently, smaller and rounded supported walls were chosen to avoid its influence. Therefore, emphasizing the need for a balance between the structural integrity and obstruction to the flow. Finally, a one-side pressure line inlet resulted in asymmetric blowing profiles, so it is suggested to provide as many equally spaced pressure line inputs to provide a more symmetric blowing profile.

2. Can the simulated moving ground be a good alternative to the conveyor belt?

The conveyor belt features that make it an excellent ground simulation technique are the ability to provide wheel rotation and have no inherent boundary layer on its surface. Hence the effectiveness of the simulated moving ground to be a good alternative was based on these parameters. The ability to remove the boundary layer was assessed using the boundary layer analysis described in section 6.1.2. The simulated moving ground removed the upstream boundary layer locally; however, it could not eliminate the no-slip boundary condition downstream, resulting in a fresh boundary layer. Nonetheless, it drastically reduced the effects of the boundary layer and provided a fuller velocity profile on its surface when compared to stationary ground. The effects of rotation and its effectiveness for experiments related to wheel aerodynamics were assessed in section 6.2

where results from literature were compared. Similar flow features were seen for both the stationary and rotating wheel. These included dominant ground vortex pair, the difference in downwash, location of separation points, wake size and convection. The effects of blowing demonstrated the ability of the simulated ground to help convect the wake behind the wheel further downstream by reducing the effects of the downstream boundary layer. Since the effect of wake convection and vortex stretching in the longitudinal direction was also mentioned by Wäschle et al., 2004, the usage of blowing demonstrates its ability to resemble reality better.

Overall, the simulated moving ground proved to be an excellent alternative to the conveyor, especially for experiments related to wheel aerodynamics. However, it was limited by the placement of the blowing slot location and its lack of ability to completely nullify the effects of its no-slip condition. Hence it is suggested to use multiple slots to address the effects of the downstream boundary layer.

3. Which portion of the mudflap design (considering a rectangular frontal area) is responsible for higher drag contributions?

To investigate the effects of a mudflap, it was first necessary to assess the effects of the others bodies around it. The double-wheel setup (found commonly in heavy-duty vehicles) generally produced larger vortex structures compared to the isolated wheel. However, when under rotation, experienced the presence of a combined vortex structure which contained the shoulder and the ground vortex in proximity in the near wake planes ($z/D = 1, 1.5$). The addition of the underbody increased the local velocities around the wheel due to flow contraction effects caused by the underbody and led to the interaction between its boundary layer and the wheel wake resulting in higher drag. Using a mudflap holder gave rise to a new counter-rotating vortex pair on the part of the wake whose strength and size varied with the change in mudflap solidity and solidity location. Finally, the effects of mudflap designs were analysed in section 4.2.2.5, highlighting two key inferences. First, having more solidity led to higher drag contributions and larger wake skewing. Second, having less solidity in the upper region of the mudflap was more beneficial than less solidity in the lower region, i.e. hollow top provided a reduction of 17% of the drag compared to the hollow bottom with only a 2% reduction. This reduction in the drag coefficient was mainly due to better pressure recovery and decreased influences of the top vortex pair.

Conclusion and Recommendations

This chapter provides the key conclusions in section 7.1, that were previously discussed in detail in chapter 6. Section 7.2 gives some recommendations and outlooks for the future research related to moving ground and mudflaps.

7.1. Conclusion

In heavy-duty vehicles, employing drag reduction to avoid emissions has become a popular method in the recent past. Add-ons are usually aerodynamically optimised to provide drag reduction. However, the most common add-ons, such as mudflaps, are seldom studied. A literature survey provided a summary of the different attempts made in the past to understand topics like the aerodynamics of wheels, moving ground, and wheel peripherals like mudflaps. It suggested that there exists limited literature on mudflaps to aerodynamically optimise them. Further, the need for a realistic setup was considered mandatory to conduct research on these mudflaps. Therefore, various experimental setups and the experimental techniques used were reviewed, which suggested devising a potential alternative to the expensive conveyor belts was possible. Hence the primary objective of this thesis was to:

“To experimentally investigate the effects of mudflaps on wheel aerodynamics by employing particle image velocimetry on different designs, under the influence of a simulated moving ground.”

First, the objective was to reproduce the moving ground using an alternative hybrid setup; this includes the simultaneous use of a leading-edge, a roller and a tangential blower. The leading edge design and roller setup were already available from the work of Schrader et al., 2010 and Jux, 2021, respectively. They required only slight modifications, such as scaling the leading edge to an appropriate size and removing additional roller in the roller setup. However, the tangential blower used in this setup was designed from scratch, taking inspiration from the work of Berndtsson et al., 1988. Initially, two blowing slots were designed: the step design and the flushed design. They were assessed using the PROCAP device. Since both the slots provided similar blowing velocity profiles, it suggested that the flushed model was a better choice due to its ability to reduce any flow perturbations caused by the geometry of the blowing slot. However, required design changes such as rounding and diminishing the size support walls in the blowing slots and removing asymmetric peaks along the blowing slot cross sections by introducing pressure line inputs uniformly along the design. Hence, the final design was made according to these design changes.

Second, the objective was to assess the effectiveness of the simulated ground. A boundary layer analysis demonstrated its ability to remove the boundary layer. The effectiveness of the leading edge was

quantified using the blower off state, which showed a reduction of the anticipated boundary layer height (estimated from Blasius theory) by 80%. Next, the effectiveness of the blowing slot was quantified by switching the blower on; it was observed that the blower did not fully remove the boundary layer due to the inherent no-slip condition present on the solid ground. However, blowing reduced its effects by introducing a fresh boundary layer which was much smaller and produced no noticeable flow angularity effects. Finally, an isolated wheel was considered to quantify the effects of the roller and the simulated ground as a whole, whose results were verified using literature. For this, planar PIV measurements were employed to study the wake behind the isolated wheel. The planar measurements showed that testing at a sub-critical Reynolds regime of 0.23 million led to the upstream movement of the separation points for the stationary and rotating cases. However, the wake patterns were similar. The differences between the stationary and rotating wheel concerning the fluid layer attachment to the wheel's surface, downwash, and separation points were found to be in good accordance with the literature such as the work of J. E. Fackrell, 1974, confirming the ability of the simulated ground to emulate the required flow conditions. Additionally, the effect of blowing was studied. It was observed that blowing helped convect the wheel's wake further downstream by reducing the effects of the ground boundary layer, thereby helping emulate reality better.

Further, stereoscopic PIV wake plane measurements of the isolated wheel were done to help bridge the gap between the wake structures found in the literature to the wake structures found in the wheel-mudflap setup (i.e. double wheel, effects of the underbody, mudflaps) that were assessed next. In short, the differences between the cases seen in the planar measurements were re-confirmed, and the wake of the stationary wheel was wider and shorter than the wake of the rotating wheel. Three main structures were identified similar to those seen by Axerio-Cilies et al., 2012; Parfett et al., 2022: a pair of ground vortices and a shoulder vortex. The addition of blowing led the ground vortices to convect slightly upwards in the direction of jetting.

Third, the wheel-mudflap setup in heavy-duty vehicles was studied using stereoscopic wake measurements. A modular approach was adopted to assess the effects of each component. Initially, the wake of the double wheel was studied. It was observed that the wake was larger than the isolated wheel and that the difference between the stationary, rotating and rotating with blowing was more evident. Although the stationary wheel had similar vortex structures, the rotating case had a peculiar effect where the shoulder vortex and ground vortex closer to the axle combined to form one bigger vortex. The addition of the underbody led to increased velocities around the wheel due to the contracting area effect. In downstream planes, the interaction between the boundary layer on the underside of the underbody interacted with the wake of the wheel resulting in larger velocity deficits. The mudflap system consisted of five different mudflaps and the mudflap holder. The mudflap holder initiated a small counter-rotating vortex pair on the upper part of the wake, which was superimposed with the wheel wake. The upper vortex pair generally grew stronger with the addition of mudflaps. The solid mudflap created the largest wake deficit and performed the worst in retaining the ground vortex structures due to the head-on collision. Further, it was also seen that in the downstream planes, the upper vortex present farther away from the axle created wake skewing effects indicating the strengthening of asymmetries. The semi-solid mudflap with a hollow bottom performed quite similar to the solid mudflap and was marginally better at retaining the ground vortices. However, the semi-solid mudflap with a hollow top performed the best in retaining the ground vortex structures and creating the least velocity deficit. This was because of the better pressure recovery behind the mudflap and the partial revival of the ground vortices via downwash. The louvered mudflaps marginally reduced the downwash and were affected by the head-on collision based on the thickness of the louvers. Thicker louvers meant larger head-on collision and a strong set of the upper vortex pair leading to more skewing.

Finally, the drag estimates obtained from the different wake planes of the wheel-mudflap setup showed that larger wake deficits led to larger drag. Although taking half of the wake for drag estimation gave rise to higher drag for skewed wakes, the method proved efficient in the planes closer to the body (i.e. $z/D = 1.5, 2$). It was able to drastically reduce the influence of the axle and its interference effects. The results showed that the location of solidity was a crucial factor along with the value of solidity for determining the drag. It was seen that placing the lesser solidity on the top led to lower drag, weaker upper vortex pair (also skewing), and better retention of the ground vortex pair. In terms of drag coefficient, having a hollow bottom led to only a 2% reduction in drag, whereas a hollow top provided

a 17% reduction in drag when compared to the fully solid mudflap.

Overall, the thesis has led to highly relevant conclusions in the field of heavy-duty vehicles and their aerodynamic testing. Devising a hybrid moving ground setup provided an excellent and cheaper alternative to the conveyor belt. Therefore, giving economical options for future testing of moving ground-related experiments. Further, determining the drag-sensitive zone in mudflaps has helped set the foundations for developing an aerodynamic mudflap that will save fuel and eventually lead to fewer emissions.

7.2. Recommendations and future outlook

Although this thesis demonstrated the simulating moving ground's ability to be a suitable alternative to the conveyor belt and provided conclusive evidence on the drag-sensitive zones of a mudflap design, there is always room for improvements to produce future research outputs. They are discussed below.

The moving ground alone might not be sufficient in terms of setup simulating reality. The wheel-mudflap system usually experiences a velocity gradient across the cross-flow plane, i.e. there are lower velocities on the inner side of the wheel due to blockages from the frontal part of the vehicle compared to higher velocities on the outer side of the wheel. This suggests that the flow inlet conditions must be modified to produce such an effect. Next, the placement of the wheel-mudflap system for this work was at the centre of the underbody. However, in reality, the system exists at the edge of the underbody, making it prone to tip effects. Hence further investigation to better analyse the asymmetries across the wheel-mudflap region is encouraged.

Albeit the mudflaps are required to be sturdy, a fluid-structure interaction study will help quantify any flapping/curvature effects of the mudflap. The max velocities achieved by heavy-duty vehicles correspond to the post-critical Reynolds regime of the wheel ($Re > 0.5 \times 10^6$); in contrast, the Reynolds number used in this study was in the sub-critical Reynolds regime ($Re = 0.23 \times 10^6$). Therefore, requiring additional research to fully quantify the effects of higher Reynolds numbers. Additionally, the use of drag estimation via PIV for setups which include multiple bodies, makes it challenging to isolate and remove the wake of support structures like the axle. Even the half wake method was limited to the planes closer to the body due to the growth of asymmetries downstream. As a result, it is suggested to use measuring devices such as balances to help isolate the effects better.

In terms of usage of the simulating moving ground, the placement of the tangential blower was seen to be crucial. Due to the physical limitations of the setup, the tangential blower could not be placed behind the wheel in close proximity. Hence, placing the tangential blower as close as possible to the test model to better emulate near-wake effects is suggested. Although the blower removed the upstream boundary layer locally, using multiple slots across the simulated moving grounds, similar to the work of Kwon et al., 2001, can help tackle this issue. Additionally, the introduction of the underbody highlighted the differences brought by the blower. Therefore, using the simulated moving ground for experiments related to near-ground effects or bodies with low ground clearances is recommended.

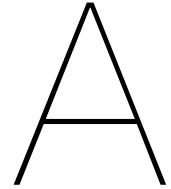
Finally, in terms of future mudflap designs, the conclusions suggest keeping the upper part of the design as hollow as possible. However, design changes such as vertical louvers/slats used in the work of Hyams et al., 2011 or even inspiration from honeycomb patterns to deal with vortex structures by straightening them, as shown by Hamzah et al., 2021, could be potential solutions to reduce drag further. Also, the asymmetric fields suggest the need for an asymmetric design to reduce drag. Hence providing ample possibilities for future designs of an aerodynamically efficient mudflap.

Bibliography

- Anderson, J. (2011). Ebook: Fundamentals of aerodynamics (si units). McGraw Hill.
- Axerio, J., & Iaccarino, G. (2009). Asymmetries in the wake structure of a formula 1 tire. Sixth International Symposium on Turbulence and Shear Flow Phenomena.
- Axerio-Cilies, J., Issakhanian, E., Jimenez, J., & Iaccarino, G. (2012). An aerodynamic investigation of an isolated stationary formula 1 wheel assembly. *Journal of fluids engineering*, 134(2).
- Axon, L., Garry, K., & Howell, J. (1998). An evaluation of cfd for modelling the flow around stationary and rotating isolated wheels. *SAE transactions*, 205–215.
- Barlow, J. B., Rae, W. H., & Pope, A. (1999). *Low-speed wind tunnel testing*. John wiley & sons.
- Bearman, P., De Beer, D., Hamidy, E., & Harvey, J. (1988). The effect of a moving floor on wind-tunnel simulation of road vehicles. *SAE Transactions*, 200–214.
- Bearman, P., & Zdravkovich, M. (1978). Flow around a circular cylinder near a plane boundary. *Journal of Fluid Mechanics*, 89(1), 33–47.
- Berndtsson, A., Eckert, W., & Mercker, E. (1988). The effect of groundplane boundary layer control on automotive testing in a wind tunnel. *SAE Transactions*, 215–230.
- Cogotti, A. (1983). Aerodynamic characteristics of car wheel. *Int. J. of Vehicle Design*.
- Coleman, H., & Steele, W. (2009). *Experimentation, validation, and uncertainty analysis for engineers*, 3rd edn wiley. Hoboken, NJ.
- Coutanceau, M., & Menard, C. (1985). Influence of rotation on the near-wake development behind an impulsively started circular cylinder. *Journal of Fluid Mechanics*, 158, 399–446.
- Croner, E., Bézard, H., Sicot, C., & Mothay, G. (2013). Aerodynamic characterization of the wake of an isolated rolling wheel. *International journal of heat and fluid flow*, 43, 233–243.
- Doolan, C. J. (2010). Computational bluff body aerodynamic noise prediction using a statistical approach. *Applied acoustics*, 71(12), 1194–1203.
- EEA. (2020). Co2 emissions from heavy-duty vehicles preliminary co2 baseline (q3-q4 2019) estimate.
- Fackrell, J., & Harvey, J. (1975). The aerodynamics of an isolated road wheel. *Proceedings of the Second AIAA Symposium of Aerodynamics of Sports and Competition Automobiles*, 16.
- Fackrell, J. E. (1974). The aerodynamics of an isolated wheel rotating in contact with the ground.
- Fago, B., Lindner, H., & Mahrenholtz, O. (1991). The effect of ground simulation on the flow around vehicles in wind tunnel testing. *Journal of Wind Engineering and Industrial Aerodynamics*, 38(1), 47–57.
- Graftieaux, L., Michard, M., & Grosjean, N. (2001). Combining piv, pod and vortex identification algorithms for the study of unsteady turbulent swirling flows. *Measurement Science and technology*, 12(9), 1422.
- Hackett, J., & Boles, R. (1979). Moving-ground simulation by tangential blowing. *Journal of Aircraft*, 16(12), 803–808.
- Hamzah, H., Jasim, L. M., Alkhabbaz, A., & Sahin, B. (2021). Role of honeycomb in improving subsonic wind tunnel flow quality: Numerical study based on orthogonal grid. *J. mechanical Engineering Research and Developments*, 44, 352–369.
- Hoffman, J. D., & Frankel, S. (2018). *Numerical methods for engineers and scientists*. CRC press.
- Hyams, D. G., Sreenivas, K., Pankajakshan, R., Nichols, D. S., Briley, W. R., & Whitfield, D. L. (2011). Computational simulation of model and full scale class 8 trucks with drag reduction devices. *Computers & Fluids*, 41(1), 27–40.
- Jakhar, R. (2021). Aerodynamics of trailer wheels in tandem: Experimental investigation into the effects of wheel rotation, trailer side-skirts, and wheel cavity covers (Master's thesis). Delft University of Technology.
- Jux, C. (2021). Digital Appendix to the PhD thesis: Development of robotic volumetric PIV - with applications in sports aerodynamics. <https://doi.org/10.4121/16871923.v1>

- Knowles, R., Saddington, A., & Knowles, K. (2002). On the near wake of rotating, 40%-scale champ car wheels. *SAE Transactions*, 2245–2253.
- Kurtulus, D., Scarano, F., & David, L. (2007). Unsteady aerodynamic forces estimation on a square cylinder by tr-piv. *Experiments in fluids*, 42(2), 185–196.
- Kwon, H.-b., Park, Y.-W., Lee, D.-h., & Kim, M.-S. (2001). Wind tunnel experiments on korean high-speed trains using various ground simulation techniques. *Journal of Wind Engineering and Industrial Aerodynamics*, 89(13), 1179–1195.
- LaVision. (2016). Davis 10.0.5. <https://www.lavision.de/en/products/davis-software/>
- Leniewicz, P., Kulak, M., & Karczewski, M. (2014). Aerodynamic analysis of an isolated vehicle wheel. *Journal of Physics: Conference Series*, 530(1), 012064.
- Lignarolo, L., Ragni, D., Krishnaswami, C., Chen, Q., Ferreira, C. S., & Van Bussel, G. (2014). Experimental analysis of the wake of a horizontal-axis wind-turbine model. *Renewable Energy*, 70, 31–46.
- Lin, N., Reed, H. L., & Saric, W. (1992). Effect of leading-edge geometry on boundary-layer receptivity to freestream sound. *Instability, transition, and turbulence* (pp. 421–440). Springer.
- MathWorks. (2019). Matlab r2019b. https://nl.mathworks.com/products/new_products/release2019b.html
- McKeon, B., Comte-Bellot, G., Foss, J., Westerweel, J., Scarano, F., Tropea, C., Meyers, J., Lee, J., Cavone, A., Schodl, R., et al. (2007). Velocity, vorticity, and mach number. *Springer handbooks* (pp. 215–471). Springer.
- McManus, J., & Zhang, X. (2006). A computational study of the flow around an isolated wheel in contact with the ground.
- Mears, A., Crossland, S., & Dominy, R. (2004). An investigation into the flow-field about an exposed racing wheel. technical paper 2004-01-0446. Society of Automotive Engineers, Warrendale, PA.
- Mears, A., Dominy, R., & Sims-Williams, D. (2002). The flow about an isolated rotating wheel effects of yaw on lift, drag and flow structure. 4th MIRA International Vehicle Aerodynamics Conference, Warwick, UK, October.
- Mears, A., Dominy, R. G., & Sims-Williams, D. (2002). The air flow about an exposed racing wheel (tech. rep.). SAE Technical Paper.
- Meinhart, C. D., Wereley, S. T., & Santiago, J. G. (2000). A piv algorithm for estimating time-averaged velocity fields. *J. Fluids Eng.*, 122(2), 285–289.
- Mercker, E., & Berneburg, H. (1992). On the simulation of road driving of a passenger car in a wind tunnel using a moving belt and rotating wheels. *Proceedings of Florence ATA Conference*, 1, 992.
- Mercker, E., & Wiedemann, J. (1990). Comparison of different ground simulation techniques for use in automotive wind tunnels. *SAE transactions*, 495–509.
- Mercker, E., & Wiedemann, J. (1996). On the correction of interference effects in open jet wind tunnels. *SAE transactions*, 795–809.
- Morelli, A. (1969). Aerodynamic effects on an automobile wheel. *ATA Rev*, 22(6), 281–288.
- Mudimeli, D. (2018). Boundary layer separation from a circular cylinder (tech. rep.). <https://doi.org/10.13140/RG.2.2.36111.84642>
- Nigbur, J. (1999). Characteristics of the wake downstream of an isolated automotive wheel.
- Parfett, A., Babinsky, H., & Harvey, J. (2022). A study of the time-resolved structure of the vortices shed into the wake of an isolated f1 car wheel. *Experiments in Fluids*, 63(7), 1–22.
- Pirozzoli, S., Orlandi, P., & Bernardini, M. (2012). The fluid dynamics of rolling wheels at low reynolds number. *Journal of fluid mechanics*, 706, 496–533.
- Prasad, A. K. (2000). Stereoscopic particle image velocimetry. *Experiments in fluids*, 29(2), 103–116.
- Raffel, M., Willert, C. E., Kompenhans, J., et al. (1998). *Particle image velocimetry: A practical guide* (Vol. 2). Springer.
- Rajaratnam, E. et al. (2019). Experimental and computational study of the flow around a stationary and rotating isolated wheel and the influence of a moving ground plane, [doi:10.4271/2019-01-0647].
- Saddington, A. J., Knowles, R., & Knowles, K. (2007). Laser doppler anemometry measurements in the near-wake of an isolated formula one wheel. *Experiments in fluids*, 42(5), 671–681.
- Scarano, F. (2013). *Experimental aerodynamics* (tech. rep.). Delft University of Technology, Delft, Netherlands.

- Schrader, L.-U., Brandt, L., Mavriplis, C., & Henningson, D. S. (2010). Receptivity to free-stream vorticity of flow past a flat plate with elliptic leading edge. *Journal of Fluid Mechanics*, 653, 245–271.
- Sciacchitano, A. (2014). Uncertainty quantification in particle image velocimetry and advances in time-resolved image and data analysis (Doctoral dissertation). Delft University of Technology.
- Sciacchitano, A., & Wieneke, B. (2016). Piv uncertainty propagation. *Measurement Science and Technology*, 27(8), 084006.
- Sibson, R. (1981). A brief description of natural neighbour interpolation. *Interpreting multivariate data*.
- Sprot, A., Sims-Williams, D., & Dominy, R. (2012). The aerodynamic characteristics of a fully deformable formula one wind tunnel tyre. *SAE International journal of passenger cars. Mechanical systems.*, 5(2), 1026–1041.
- Stapleford, W., & Carr, G. (1969). Aerodynamic characteristics of exposed rotating wheels. Motor Industry Research Association.
- Streamwise. (2016). Procap compact. <https://www.streamwise.ch/procap/>
- Swanson, W. (1961). The magnus effect: A summary of investigations to date.
- Talezade, A., Shirazi, & Manshadi, D. (2020). Streamlined bodies drag force estimation using wake integration technique. *Journal of the Brazilian Society of Mechanical Sciences and Engineering*, 42(6), 1–11.
- Ultimaker. (2022). Ultimaker s5. <https://ultimaker.com/3d-printers/ultimaker-s5>
- Van Oudheusden, B. W. (2013). Piv-based pressure measurement. *Measurement Science and Technology*, 24(3), 032001.
- Van Oudheusden, B. W., Scarano, F., Roosenboom, E. W., Casimiri, E. W., & Souverein, L. J. (2007). Evaluation of integral forces and pressure fields from planar velocimetry data for incompressible and compressible flows. *Experiments in fluids*, 43(2), 153–162.
- Wäschle, A. (2007). The influence of rotating wheels on vehicle aerodynamics-numerical and experimental investigations (tech. rep.). SAE Technical Paper.
- Wäschle, A., Cyr, S., Kuthada, T., & Wiedemann, J. (2004). Flow around an isolated wheel-experimental and numerical comparison of two cfd codes (tech. rep.). SAE Technical Paper.
- Wickern, G., Zwicker, K., & Pfadenhauer, M. (1997). Rotating wheels-their impact on wind tunnel test techniques and on vehicle drag results. *SAE transactions*, 254–270.
- Wilcox, D. C. et al. (1998). *Turbulence modeling for cfd* (Vol. 2). DCW industries La Canada, CA.
- Wold, S., St, L. et al. (1989). Analysis of variance (anova). *Chemometrics and intelligent laboratory systems*, 6(4), 259–272.
- Zdravkovich, M. (2003). *Flow around circular cylinders vol 2: Applications*, oxford university press, oxford.



Patented mudflap designs

This section provides various mudflap patented designs for heavy-duty vehicles. In general, the designs claim to provide a drag reduction when compared to fully solid mudflaps. However, they lack sufficient evidence to aerodynamically explain their designs. For instance, the designs in fig. A.1 and fig. A.2 show no major differences in the upper and lower region of the mudflap, although this study clearly shows having hollow regions in upper portion is far more beneficial.

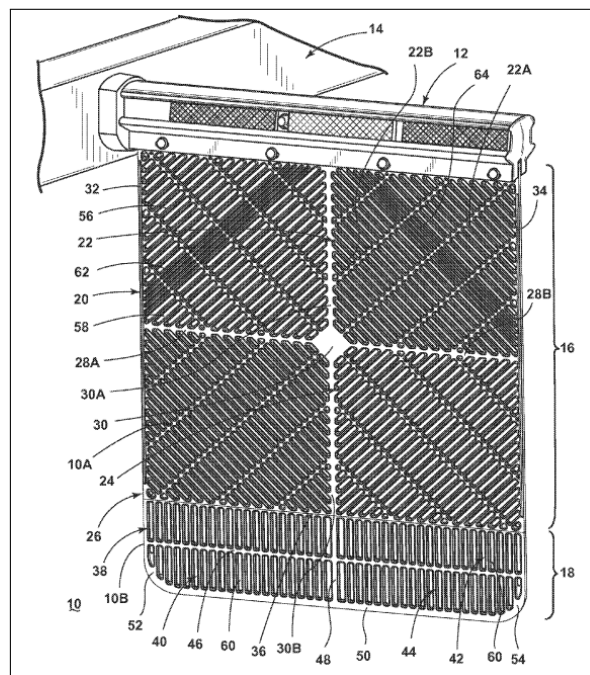


Figure A.1: Mudflap design by Fleet Engineers, Inc.,
Muskegon, MI (US)

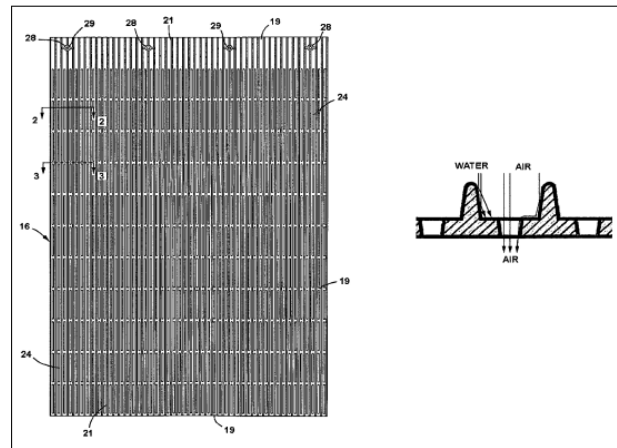


Figure A.2: Mudflap design by Tarun Natwarlal Surti, Nashville, TN

The designs fig. A.3 and fig. A.4, do seem to provide better drag reduction. However, the effects of vertical louvers are yet to be fully understood. The fig. A.4, in particular, shows a great potential in drag reduction, due to the gradual increase in spacing towards the upper region of the mudflap. The honey-comb structure can further help straighten the flow.

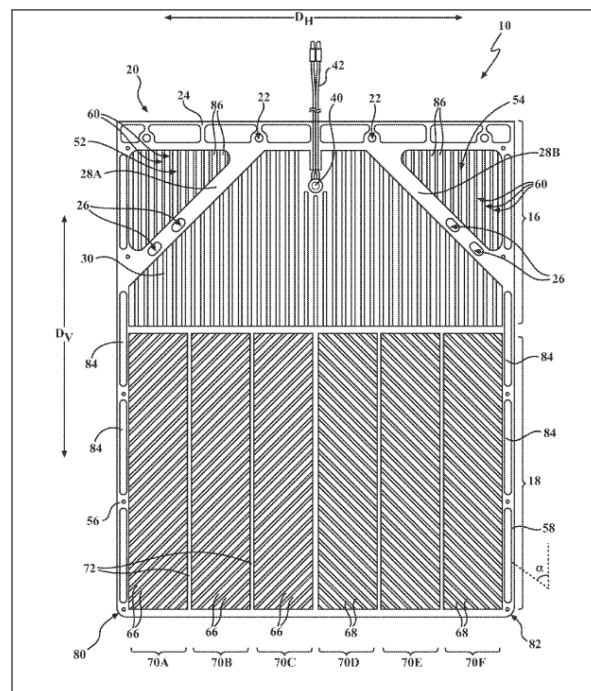


Figure A.3: Mudflap design by Globetech Manufacturing, Dayton, OH (US)

B

CAD geometries

This section provided the CAD geometries for the different models described in chapter 4.

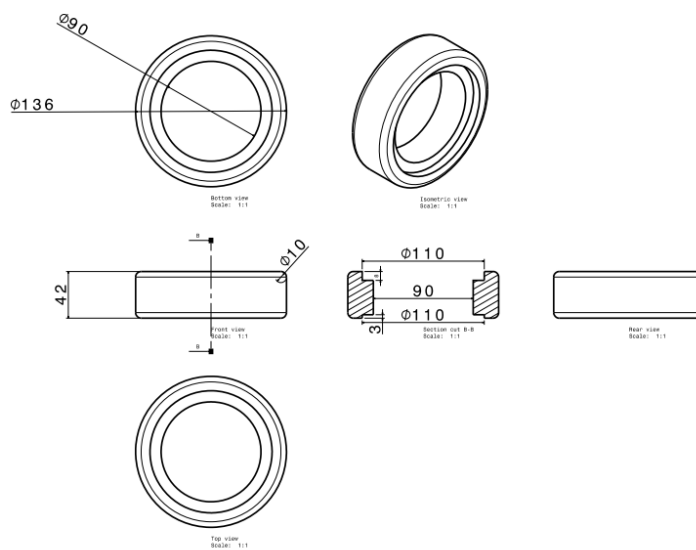


Figure B.1: Isolated wheel CAD used by Jakhar, 2021

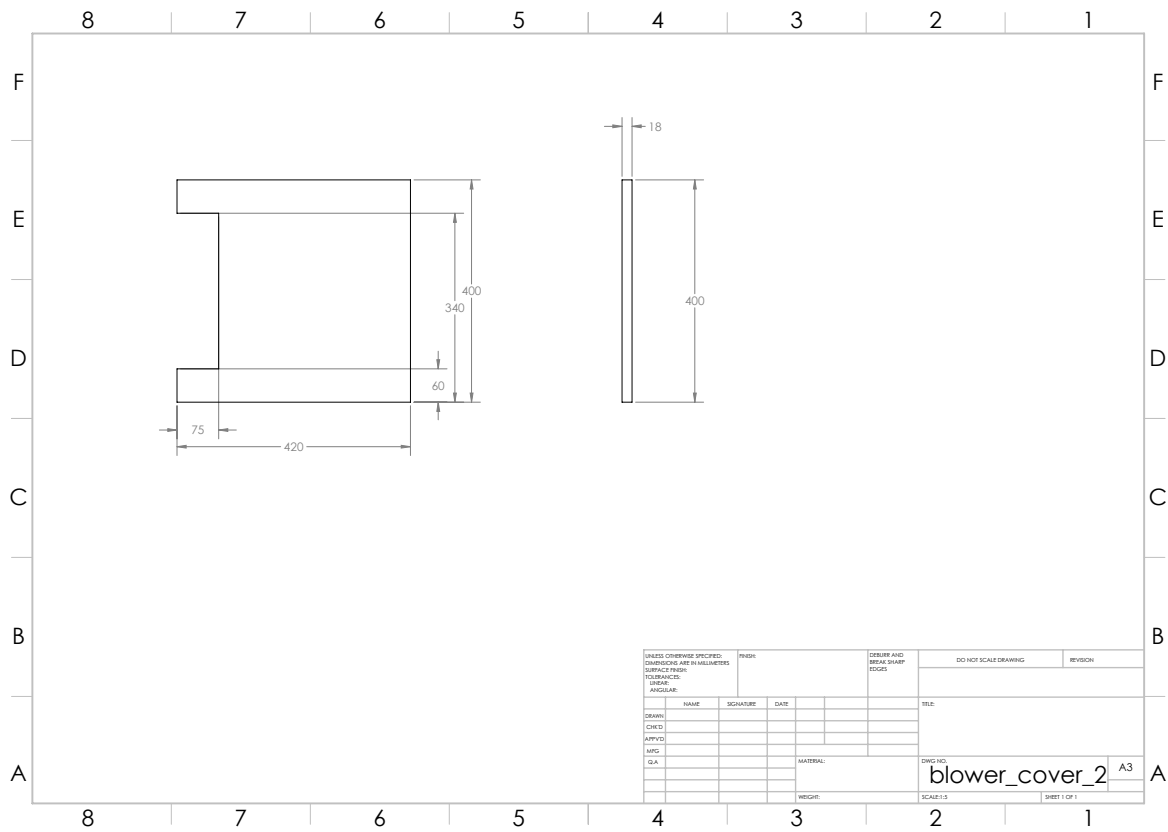


Figure B.4: Attaching plate 2 CAD.

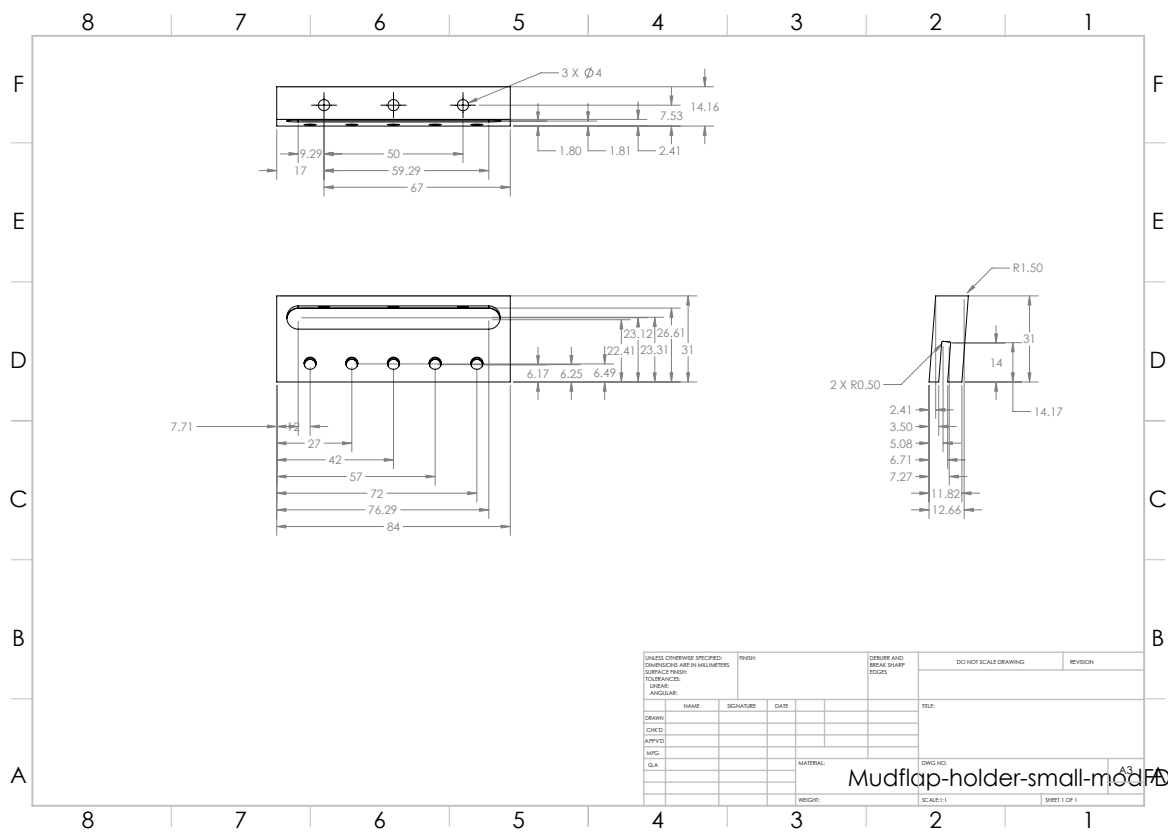


Figure B.5: Mudflap holder CAD.

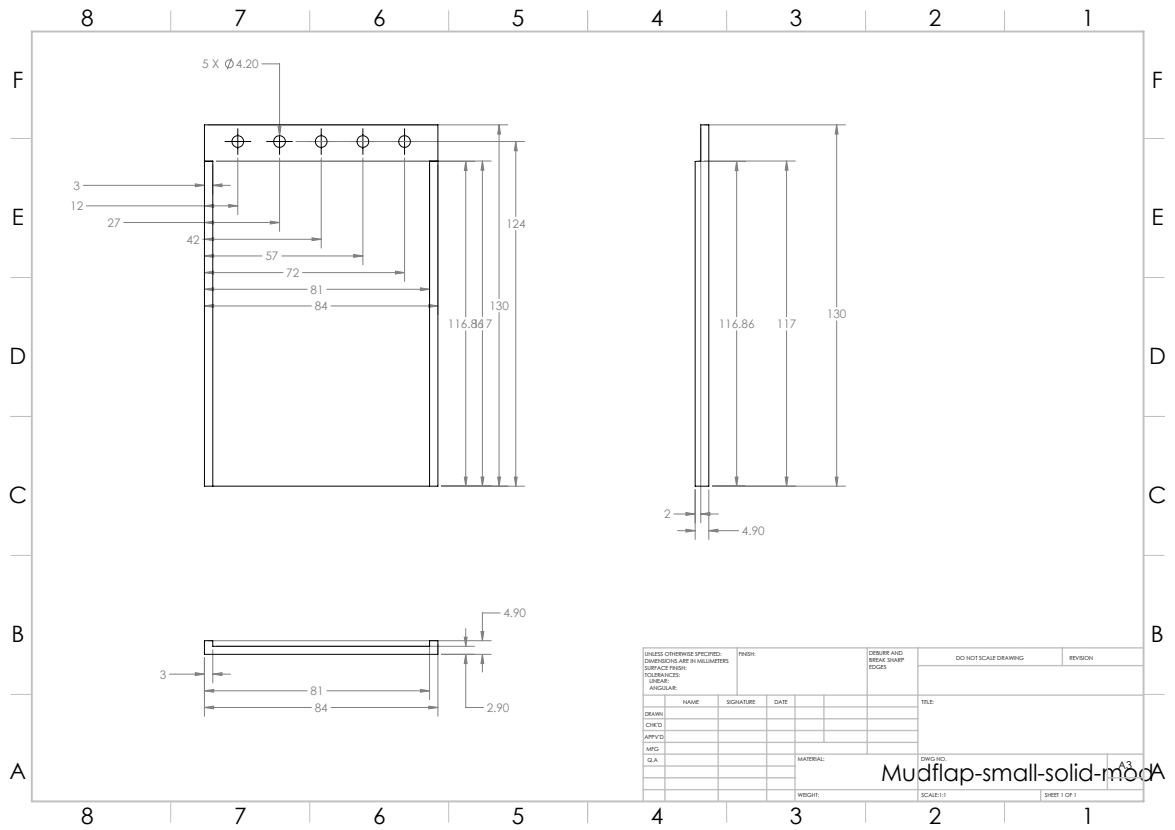


Figure B.6: Solid mudflap CAD.

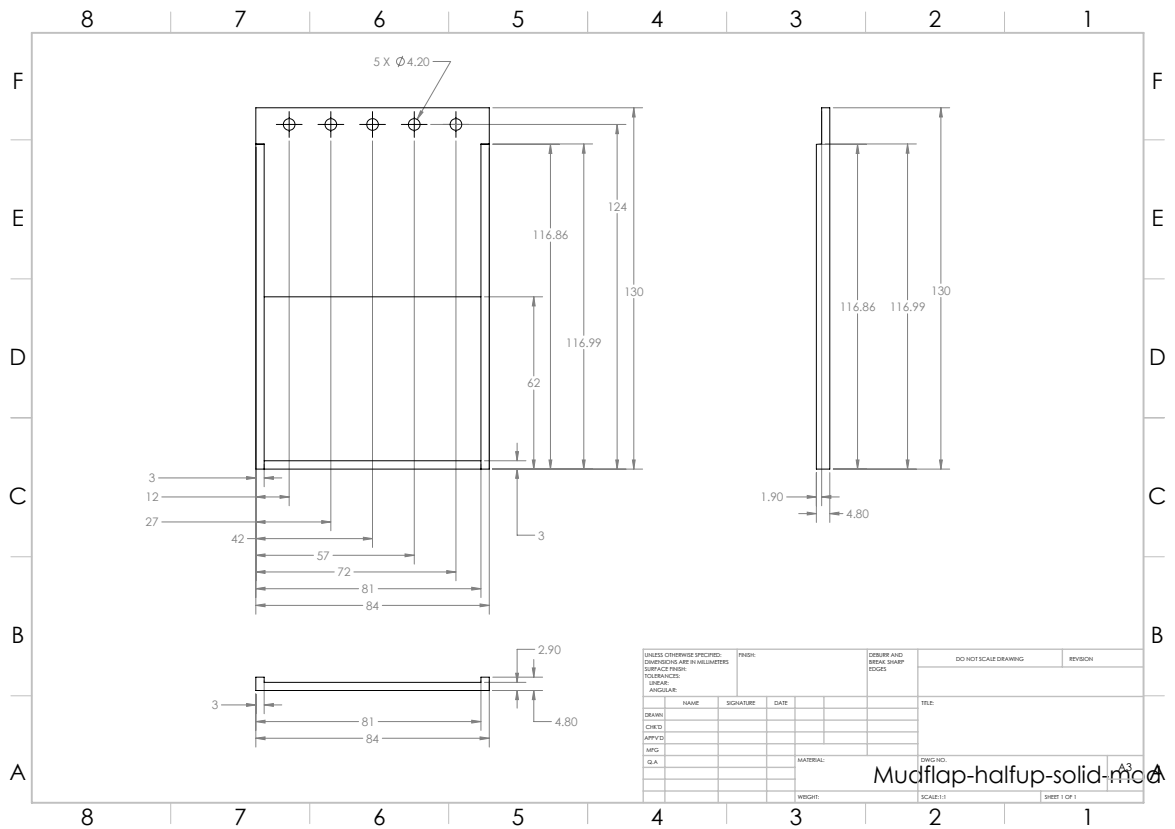


Figure B.7: Hollow bottom mudflap CAD.

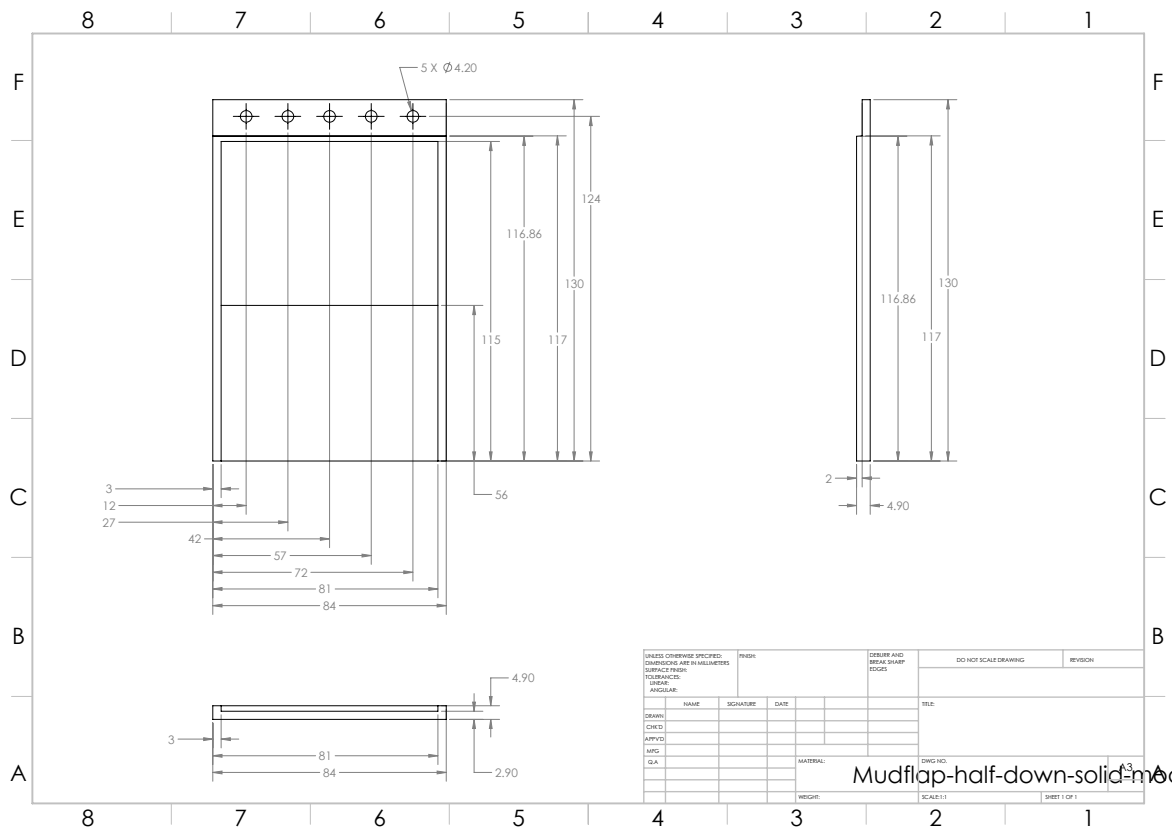


Figure B.8: Hollow top mudflap CAD.

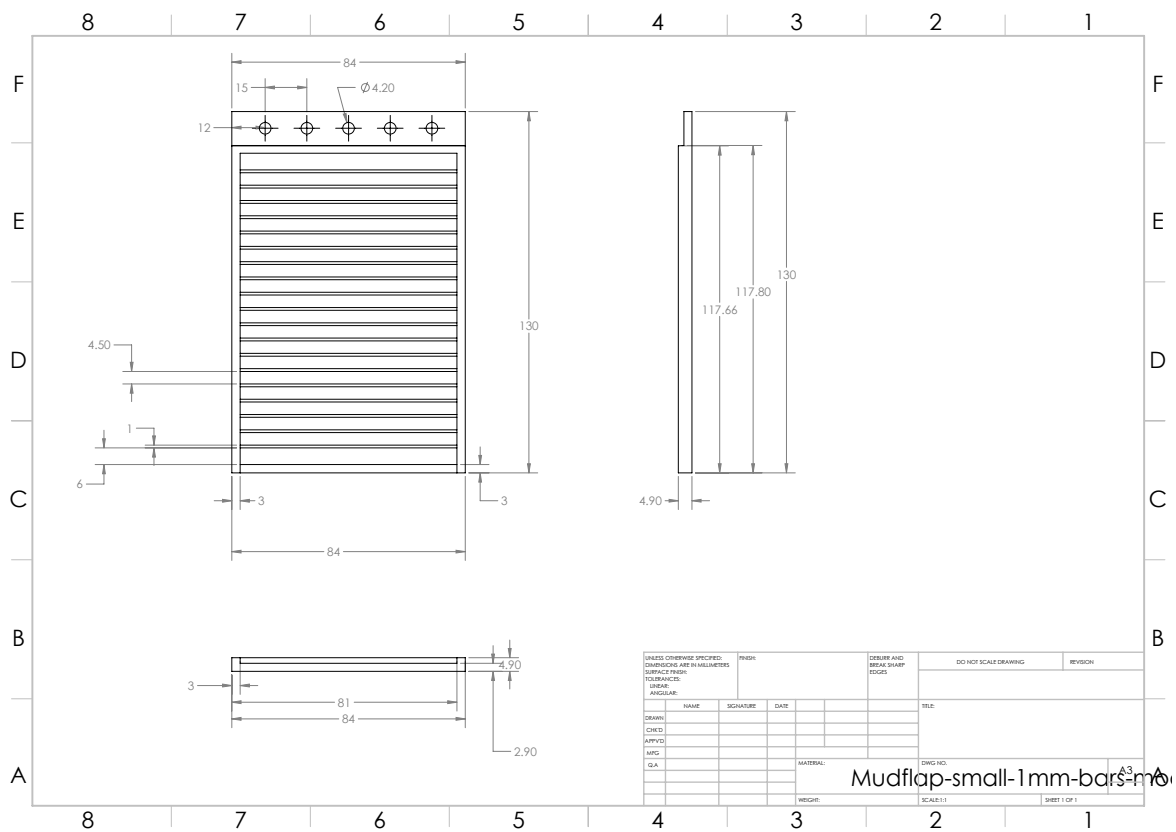


Figure B.9: Mudflap with 1 [mm] louvers CAD.

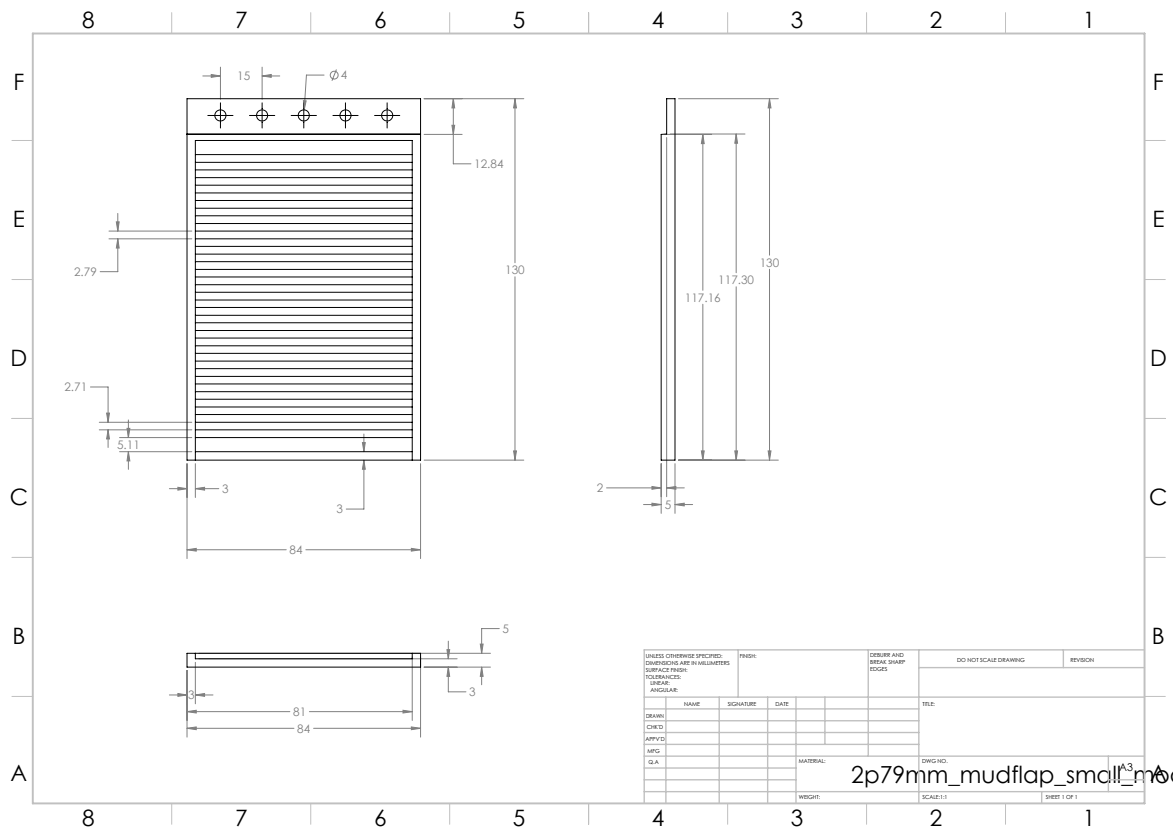
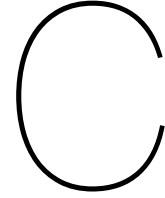


Figure B.10: Mudflap with 2.8 [mm] louvers CAD.



Velocity and Vorticity plots

This section provides the additional velocity and vorticity plots generated for data acquired during the experimental campaigns.

1. Isolated wheel - Planar

Figure C.1 and fig. C.2 shows the velocity plots for the right plane which is farthest from the axle.

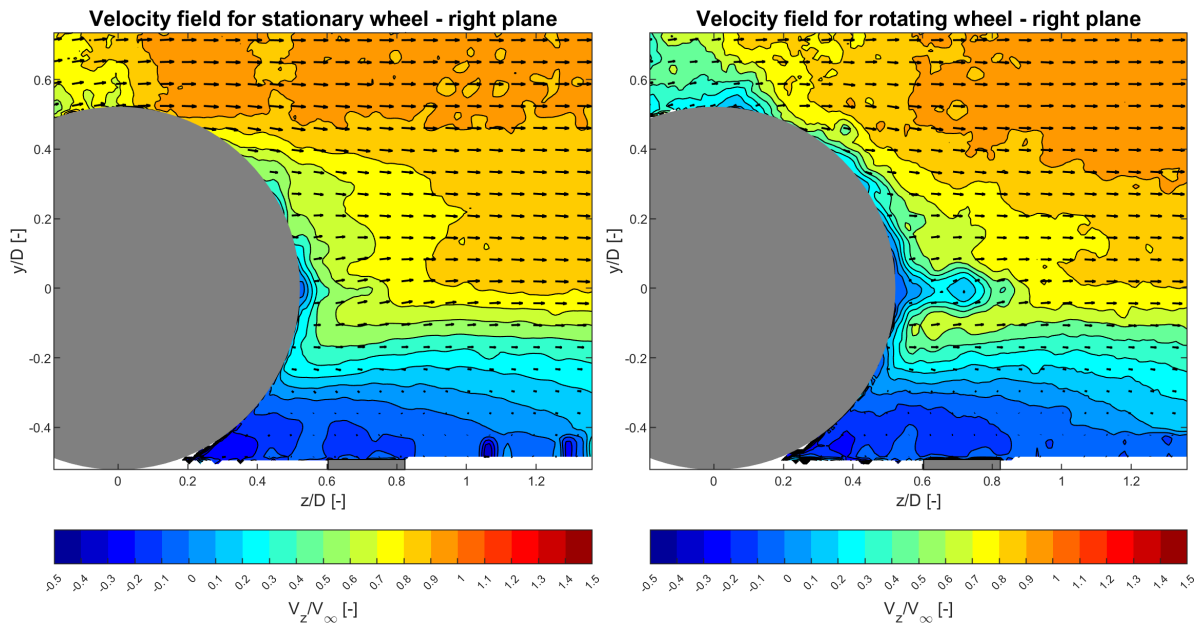


Figure C.1: Normalised streamwise velocity field (Y-Z plane) at the right-plane for the stationary isolated wheel. Wheel represented as grey circle and blower represented as grey rectangle.

Figure C.2: Normalised streamwise velocity field (Y-Z plane) at the right-plane for the rotating isolated wheel. Wheel represented as grey circle and blower represented as grey rectangle.

Figure C.3 and fig. C.4 shows the velocity plots for the right plane which is closest to the axle.

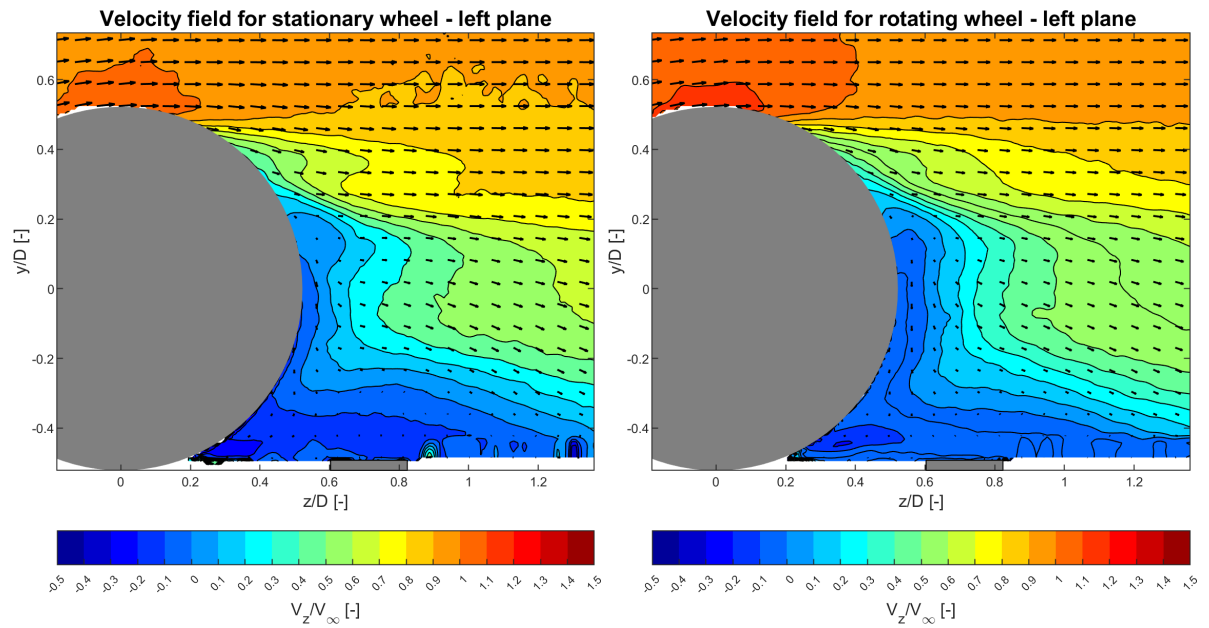


Figure C.3: Normalised streamwise velocity field (Y-Z plane) at the left-plane for the stationary isolated wheel. Wheel represented as grey circle and blower represented as grey rectangle.

Figure C.4: Normalised streamwise velocity field (Y-Z plane) at the left-plane for the rotating isolated wheel. Wheel represented as grey circle and blower represented as grey rectangle.

2. Isolated wheel - Stereoscopic

Figure C.5 to fig. C.13 shows the remaining velocity plots for the stationary, rotating and rotating with blowing isolated wheel case at different downstream planes.

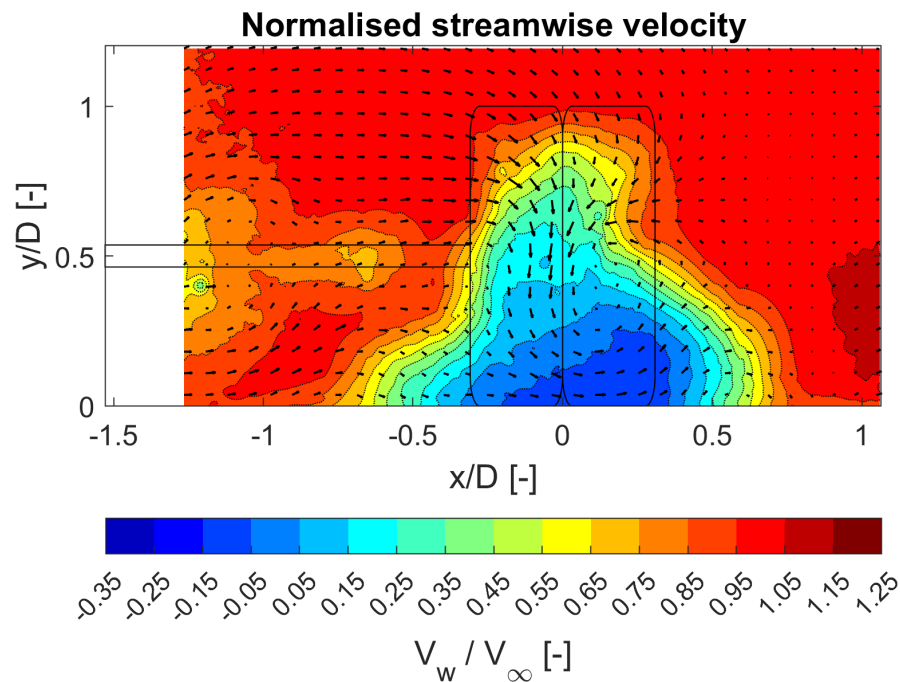


Figure C.5: Normalised streamwise velocity field (X-Y plane) for the rotating isolated wheel with blowing, at $z/D = 1$.

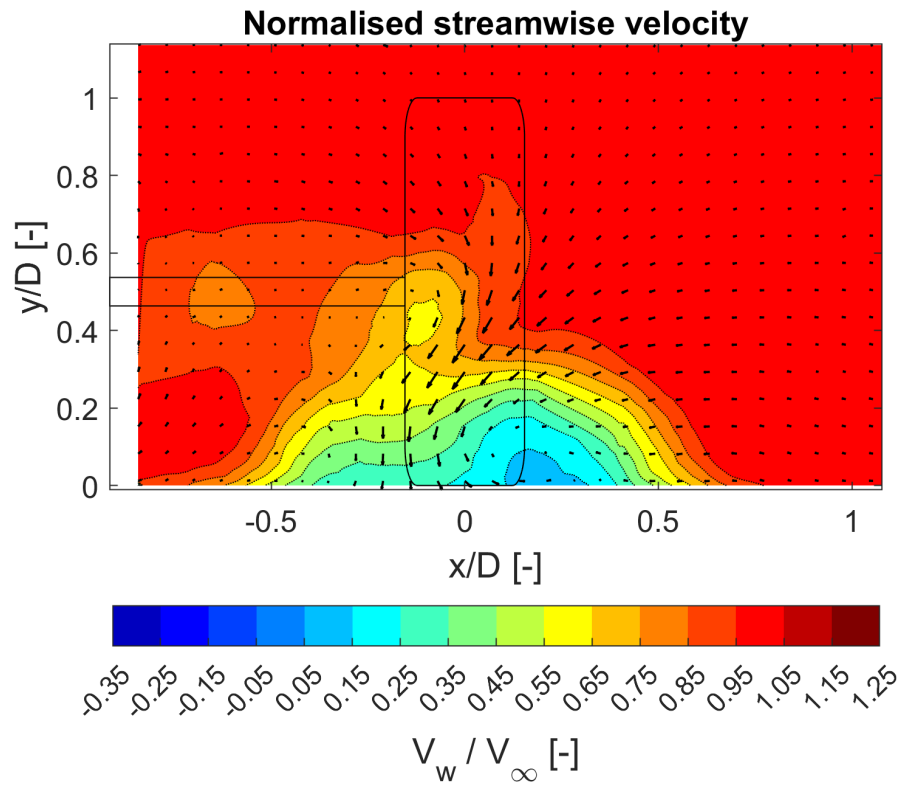


Figure C.6: Normalised streamwise velocity field (X-Y plane) for the stationary isolated wheel at $z/D = 1.5$.

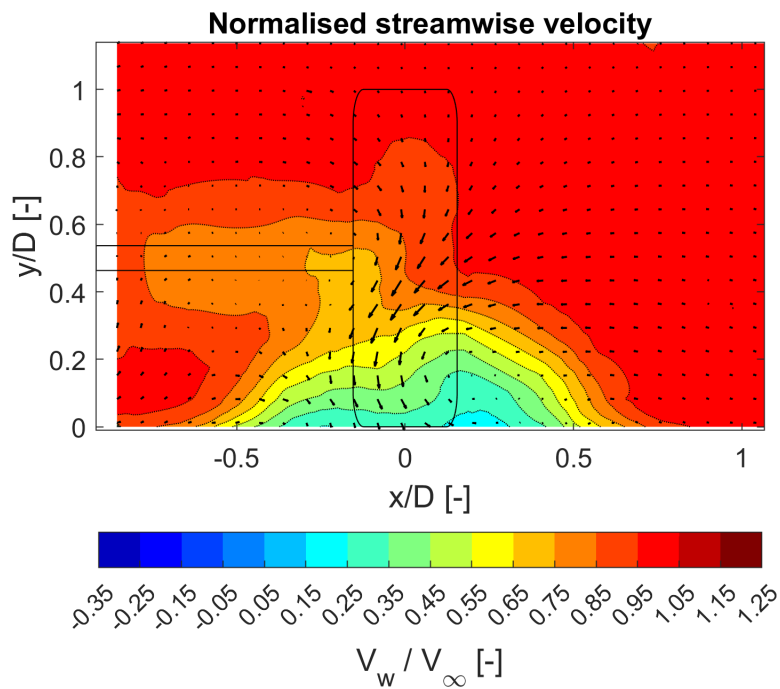


Figure C.7: Normalised streamwise velocity field (X-Y plane) for the rotating isolated wheel at $z/D = 1.5$.

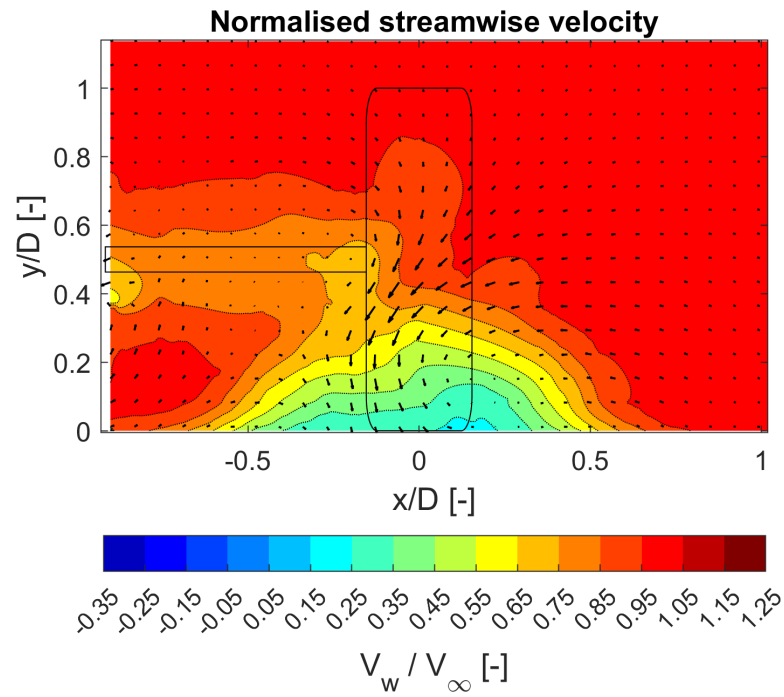


Figure C.8: Normalised streamwise velocity field (X-Y plane) for the rotating isolated wheel with blowing, at $z/D = 1.5$.

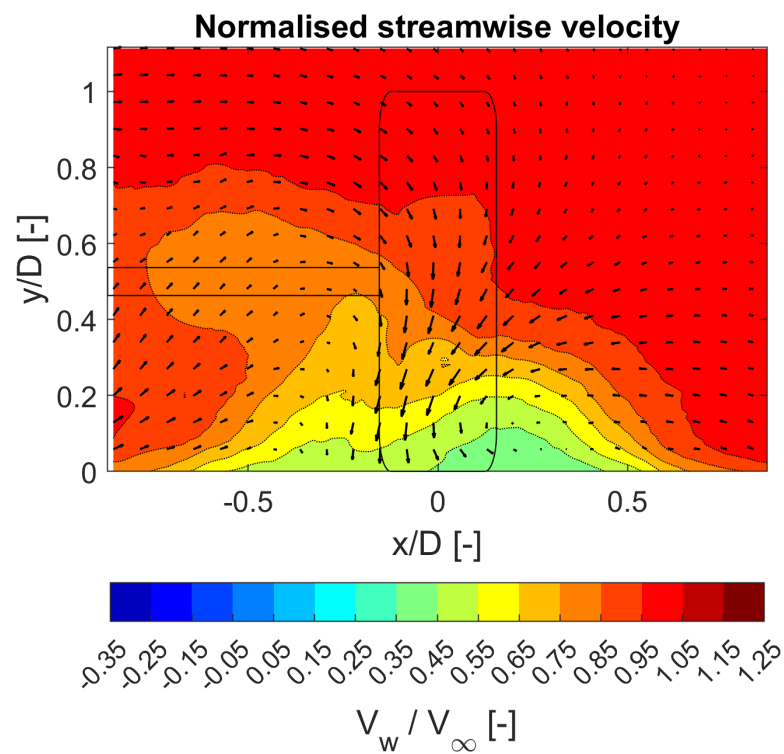


Figure C.9: Normalised streamwise velocity field (X-Y plane) for the stationary isolated wheel at $z/D = 2$.

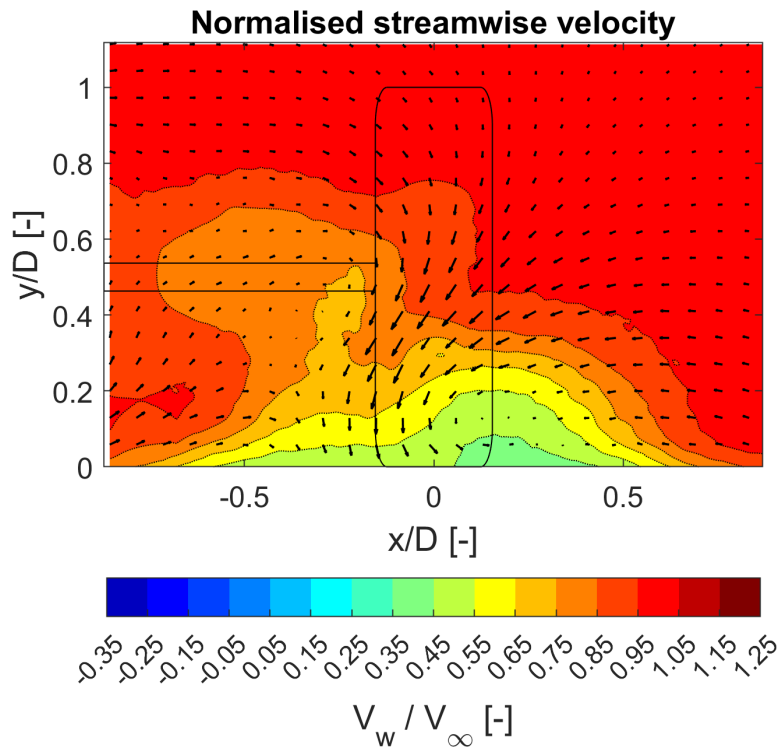


Figure C.10: Normalised streamwise velocity field (X-Y plane) for the rotating isolated wheel at $z/D = 2$.

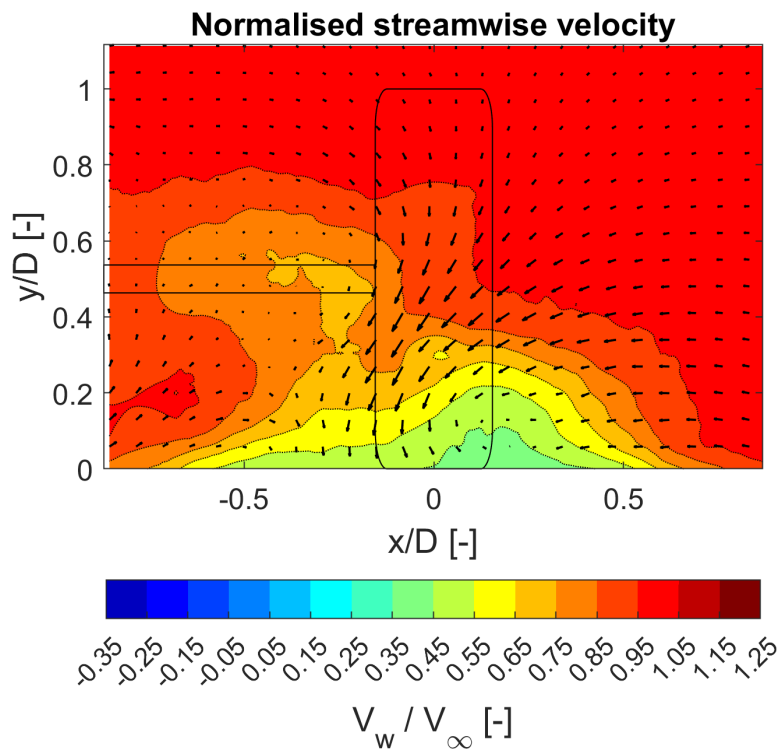


Figure C.11: Normalised streamwise velocity field (X-Y plane) for the rotating isolated wheel with blowing, at $z/D = 2$.

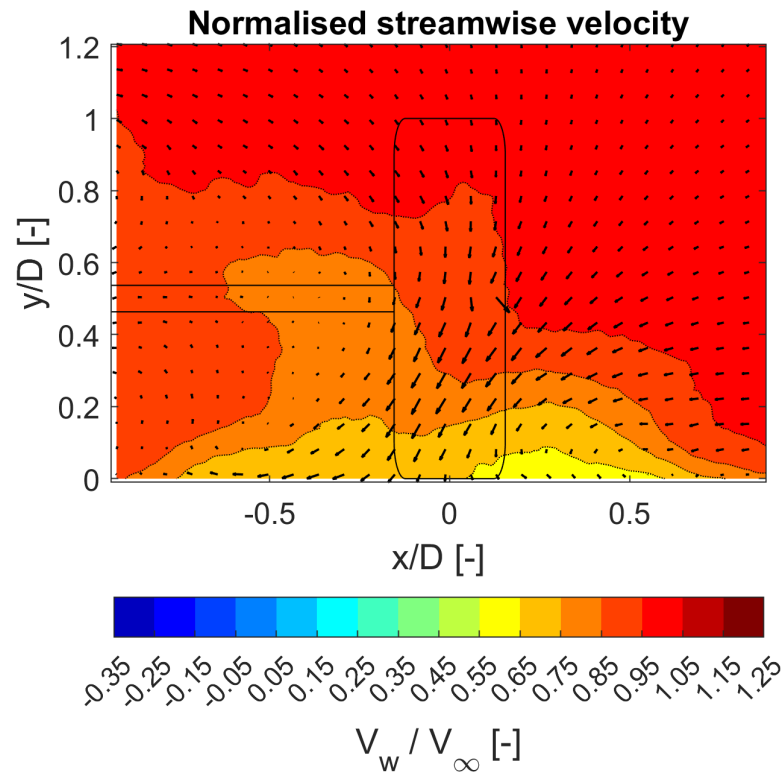


Figure C.12: Normalised streamwise velocity field (X-Y plane) for the stationary isolated wheel at $z/D = 3$.

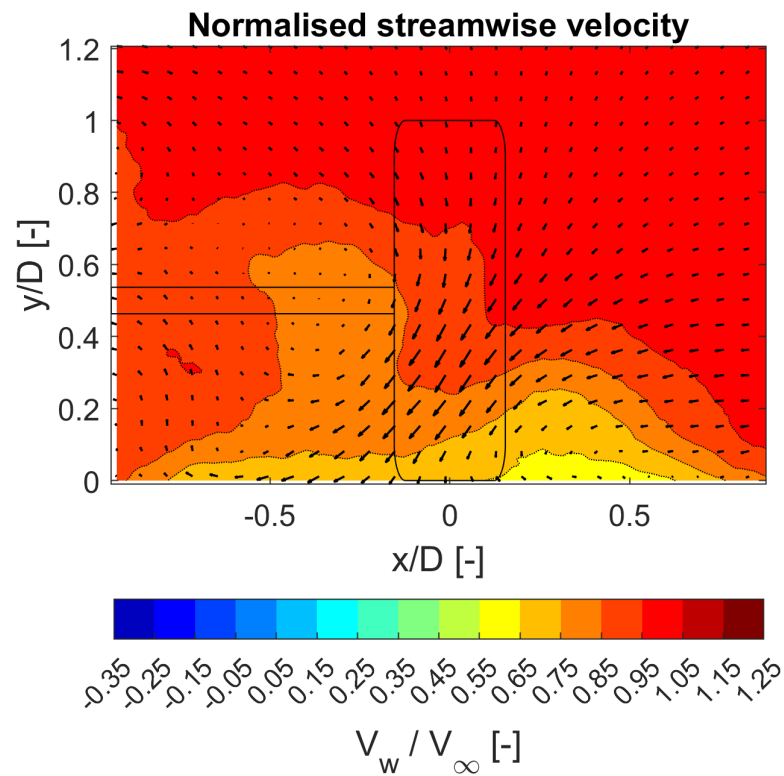


Figure C.13: Normalised streamwise velocity field (X-Y plane) for the rotating isolated wheel at $z/D = 3$.

3. Double wheel - Stereoscopic

Figure C.14 to fig. C.22 shows the remaining velocity plots for the stationary, rotating and rotating with blowing double wheel case at different downstream planes.

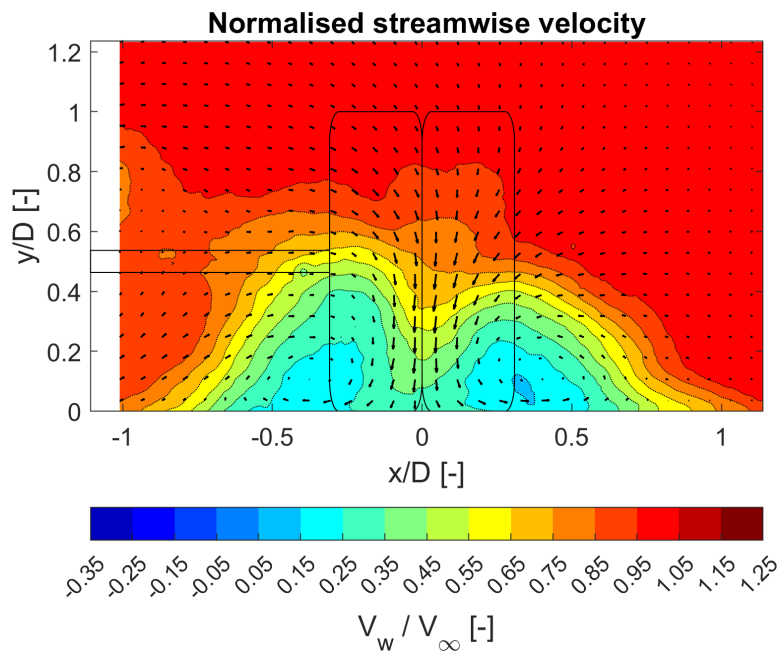


Figure C.14: Normalised streamwise velocity field (X-Y plane) for the stationary double wheel, at $z/D = 1.5$.

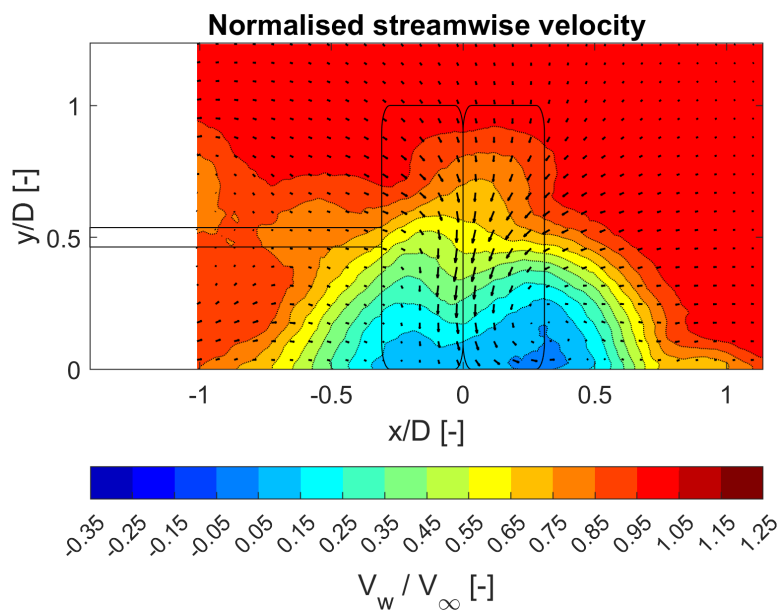


Figure C.15: Normalised streamwise velocity field (X-Y plane) for the rotating double wheel, at $z/D = 1.5$.

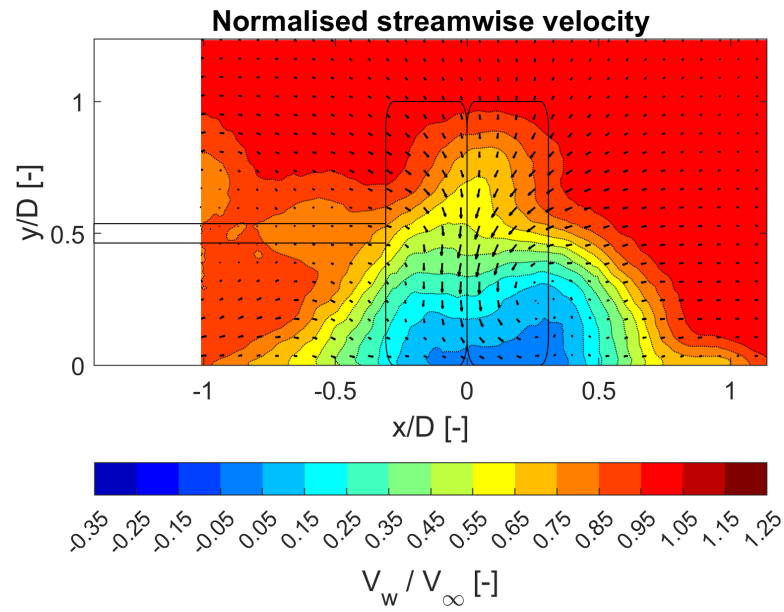


Figure C.16: Normalised streamwise velocity field (X-Y plane) for the rotating double wheel with blowing, at $z/D = 1.5$.

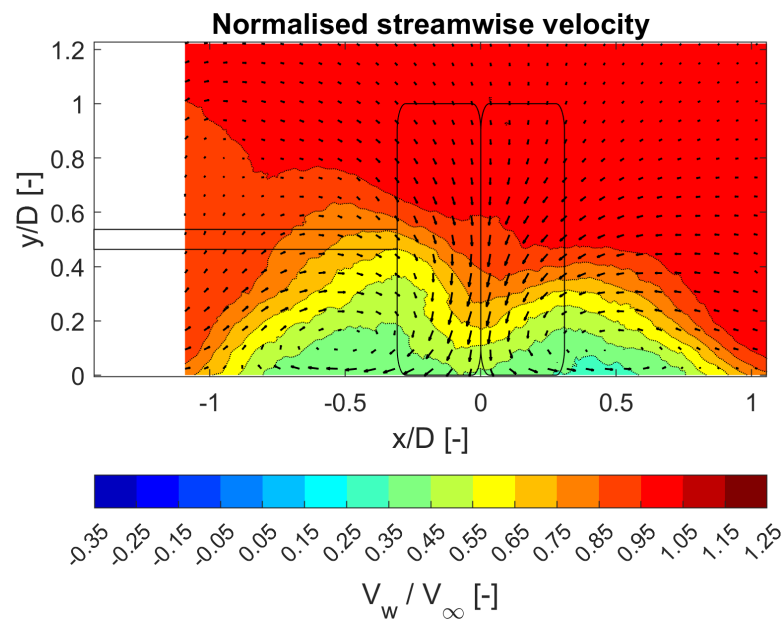


Figure C.17: Normalised streamwise velocity field (X-Y plane) for the stationary double wheel, at $z/D = 2$.

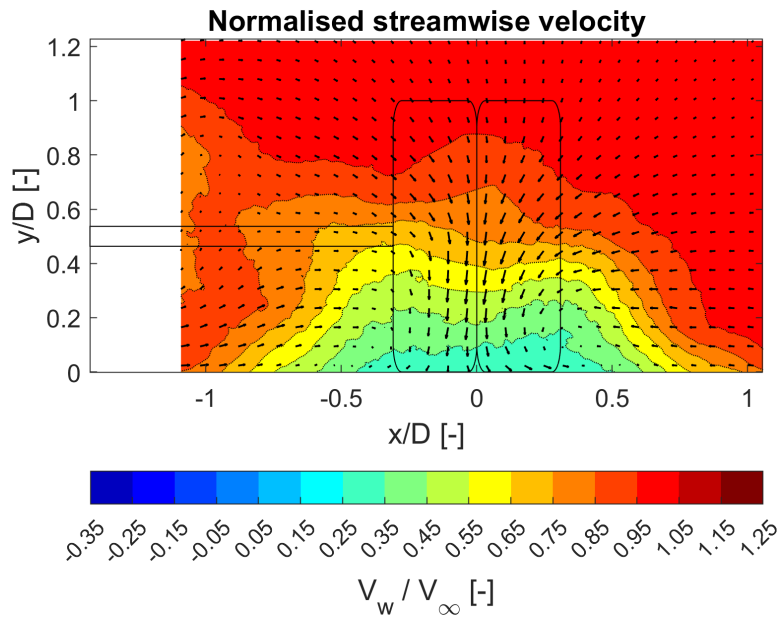


Figure C.18: Normalised streamwise velocity field (X-Y plane) for the rotating double wheel, at $z/D = 2$.

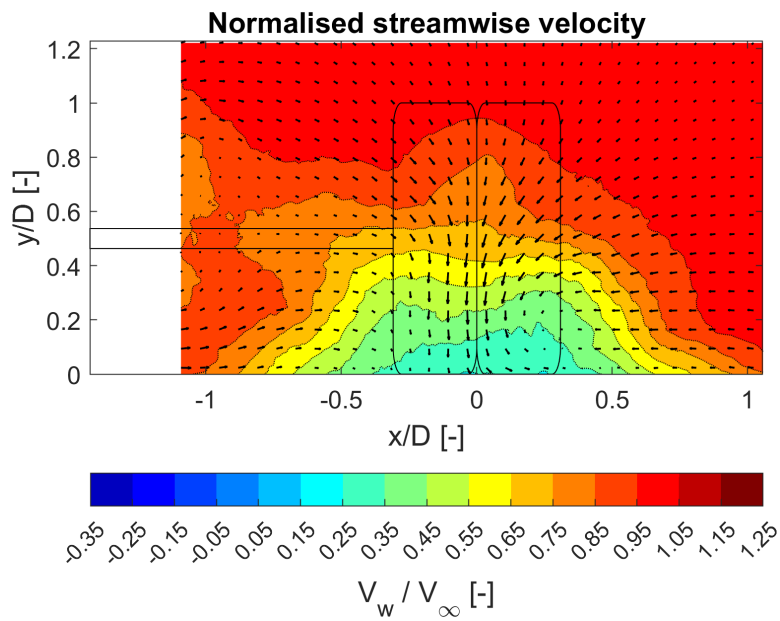


Figure C.19: Normalised streamwise velocity field (X-Y plane) for the rotating double wheel with blowing, at $z/D = 2$.

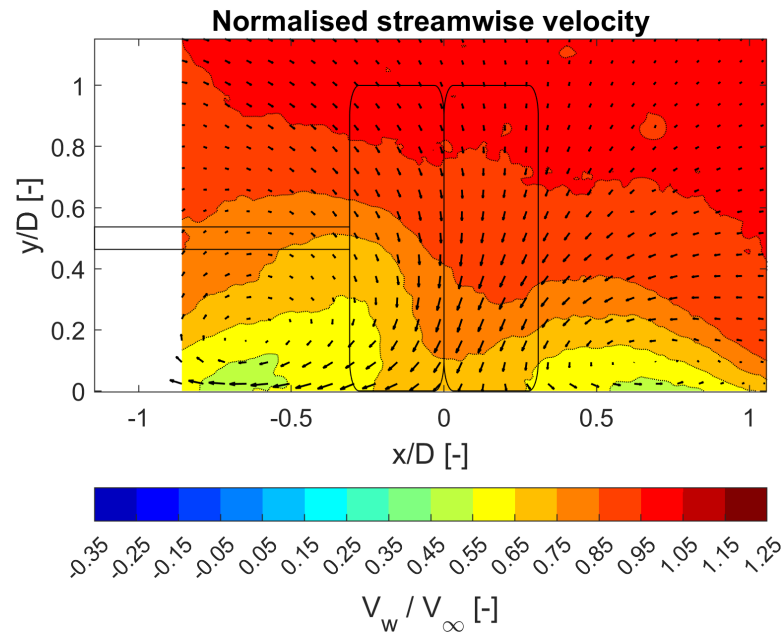


Figure C.20: Normalised streamwise velocity field (X-Y plane) for the stationary double wheel, at $z/D = 2$.

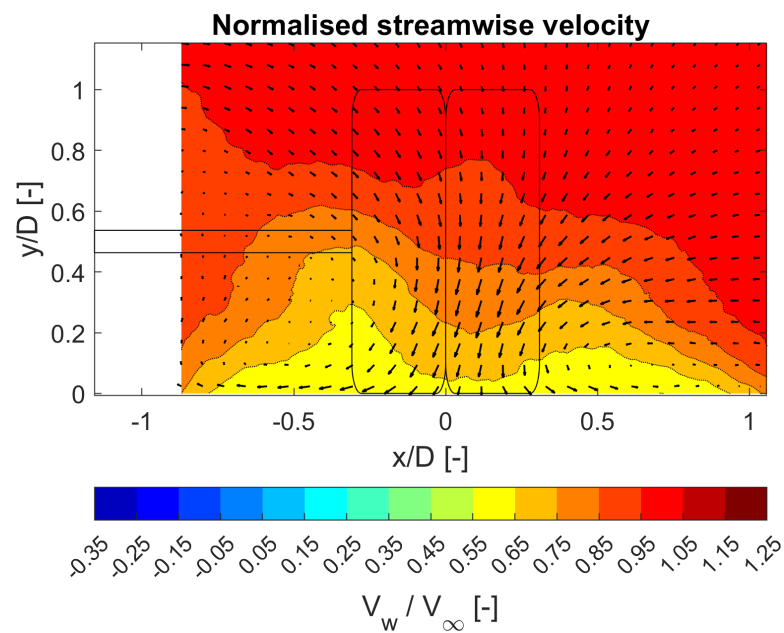


Figure C.21: Normalised streamwise velocity field (X-Y plane) for the rotating double wheel, at $z/D = 2$.

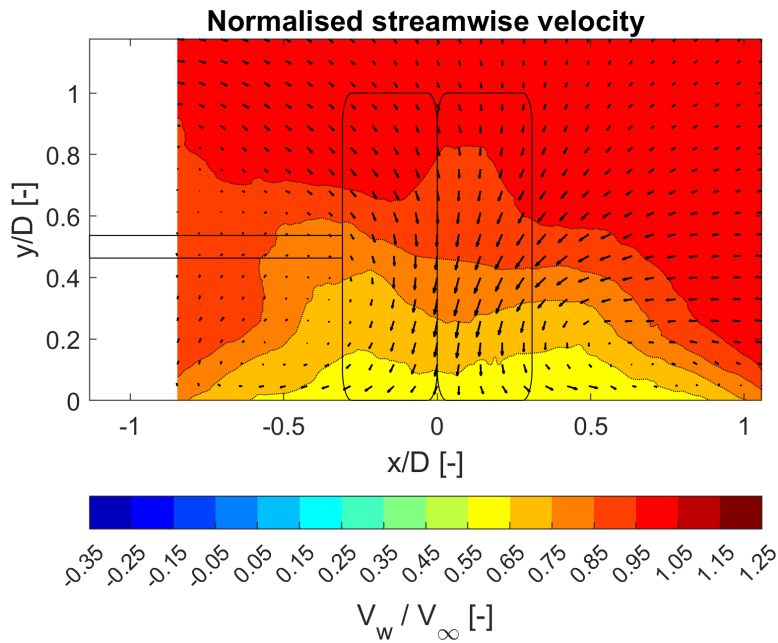


Figure C.22: Normalised streamwise velocity field (X-Y plane) for the rotating double wheel with blowing, at $z/D = 2$.

Figure C.23 to fig. C.29 shows the remaining vorticity plots for the stationary, rotating and rotating with blowing double wheel case at different downstream planes.

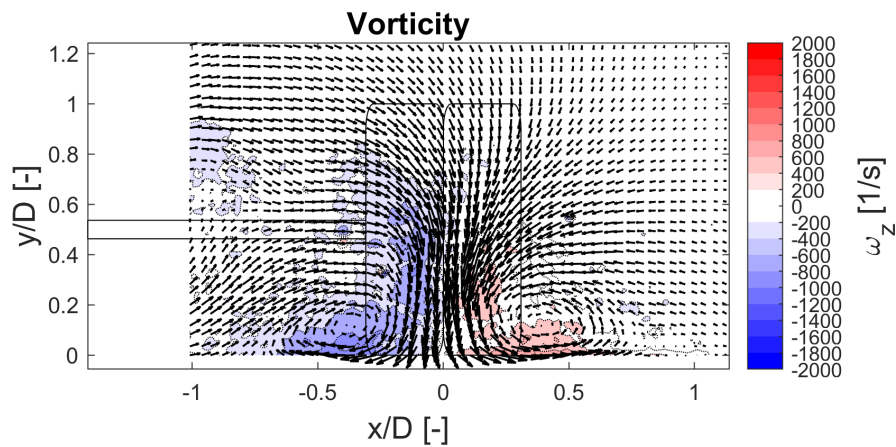


Figure C.23: Vorticity field (X-Y plane) for the stationary double wheel, at $z/D = 1.5$.

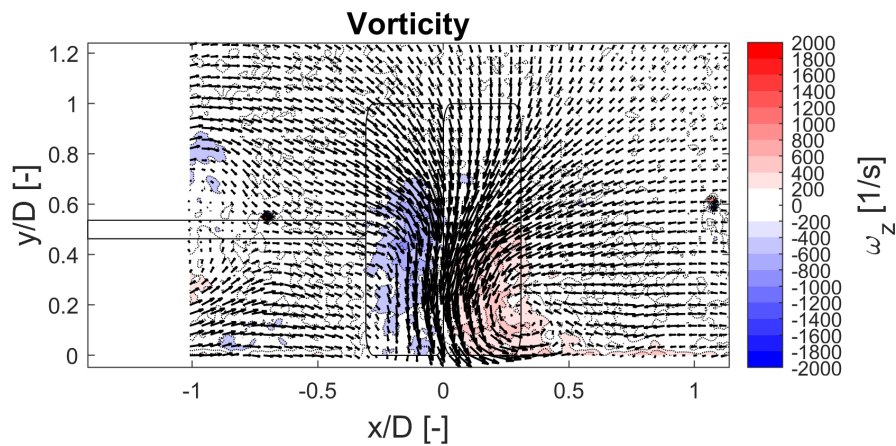


Figure C.24: Vorticity field (X-Y plane) for the rotating double wheel, at $z/D = 1.5$.

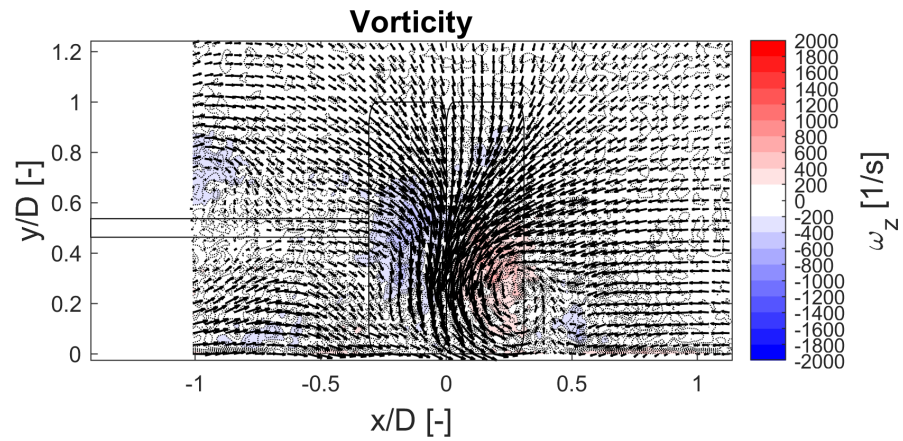


Figure C.25: Vorticity field (X-Y plane) for the rotating with blowing double wheel, at $z/D = 1.5$.

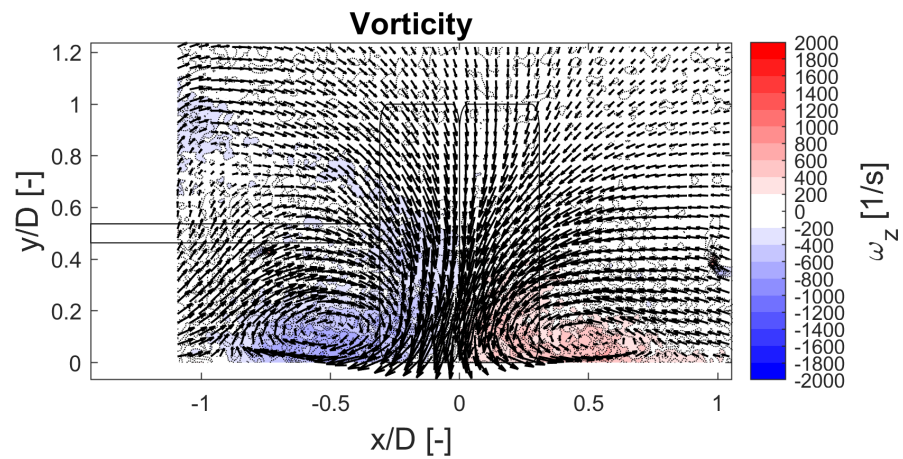


Figure C.26: Vorticity field (X-Y plane) for the stationary double wheel, at $z/D = 2$.

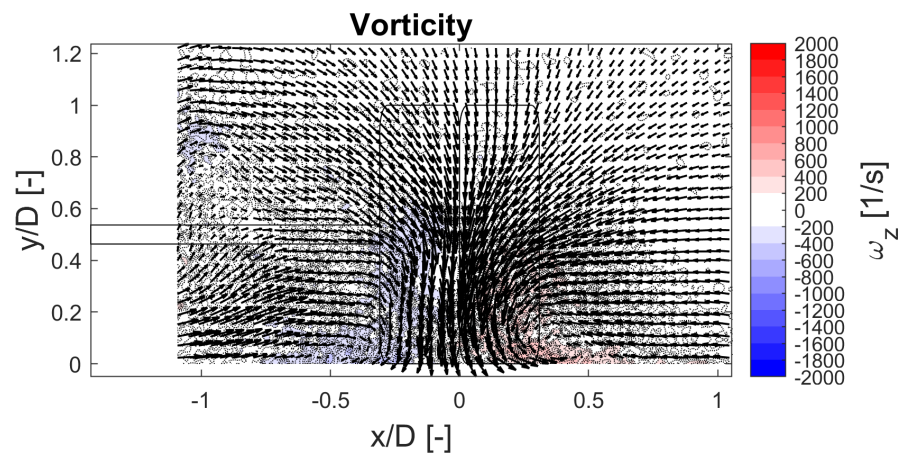


Figure C.27: Vorticity field (X-Y plane) for the rotating double wheel, at $z/D = 2$.

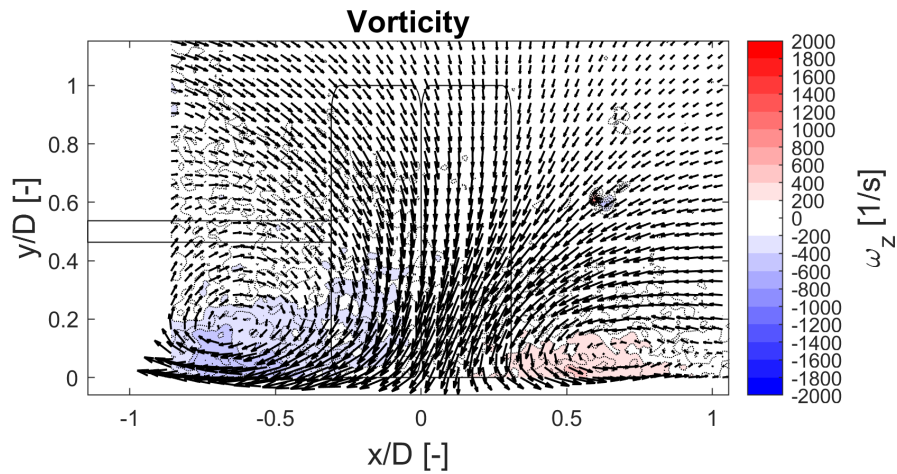


Figure C.28: Vorticity field (X-Y plane) for the stationary double wheel, at $z/D = 3$.

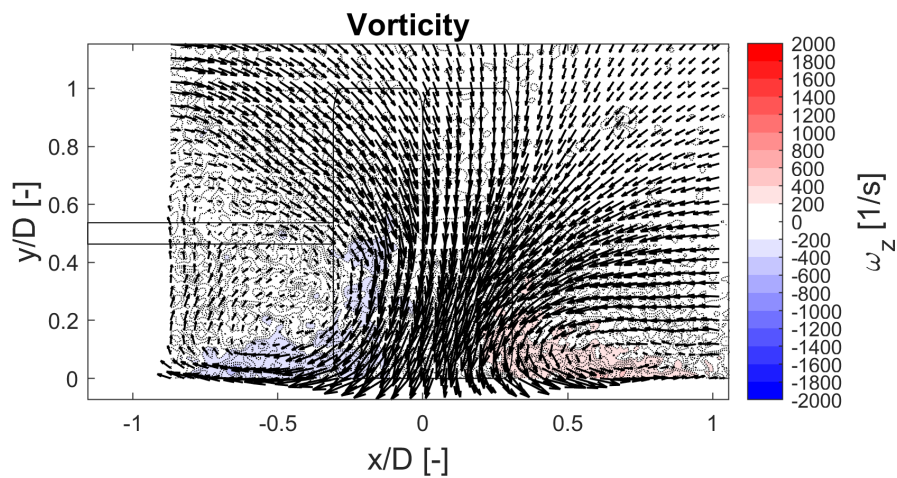


Figure C.29: Vorticity field (X-Y plane) for the rotating double wheel, at $z/D = 3$.

4. Underbody - Stereoscopic

Figure C.30 to fig. C.38 shows the remaining velocity plots for the stationary, rotating and rotating with blowing double wheel in the presence of the underbody case at different downstream planes.

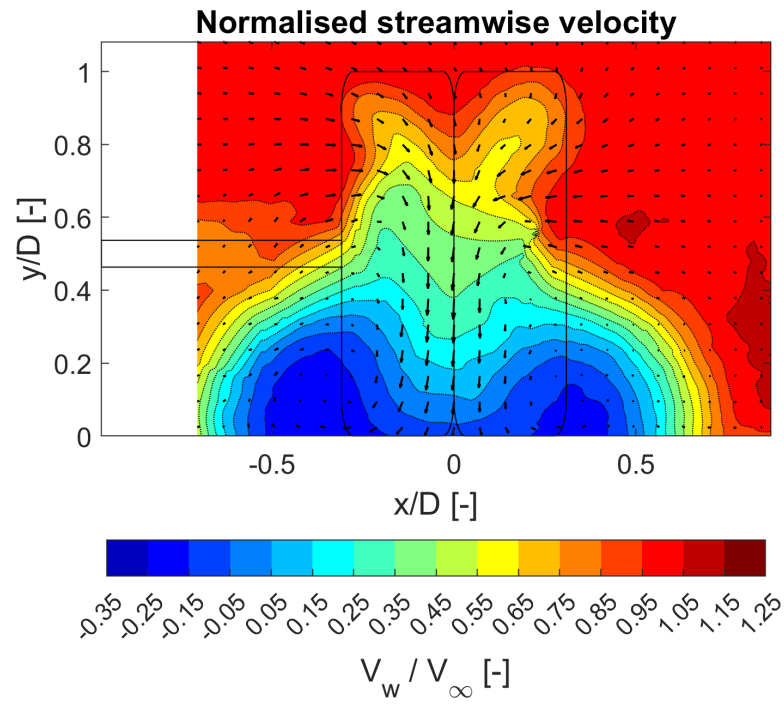


Figure C.30: Normalised streamwise velocity field (X-Y plane) for the stationary double wheel in the presence of underbody, at $z/D = 1$.

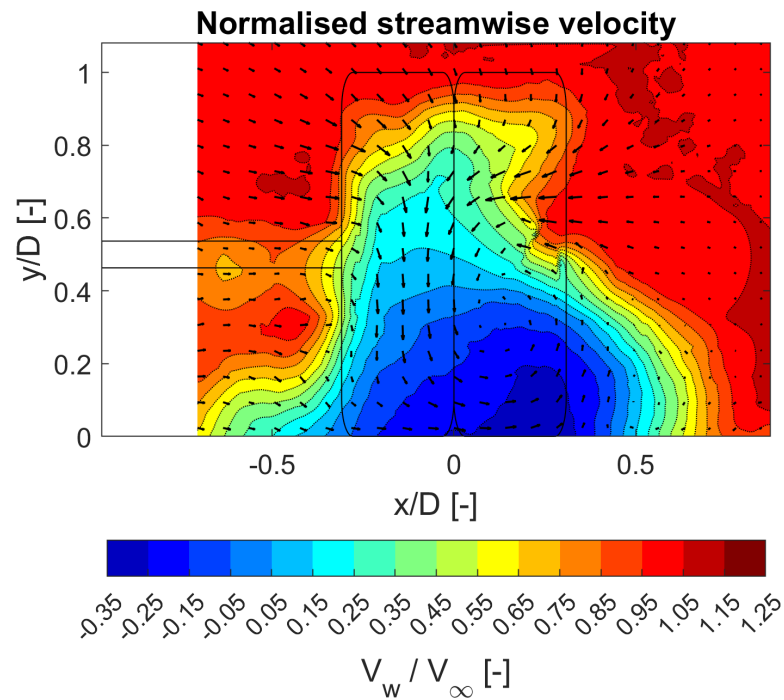


Figure C.31: Normalised streamwise velocity field (X-Y plane) for the rotating double wheel in the presence of underbody, at $z/D = 1$.

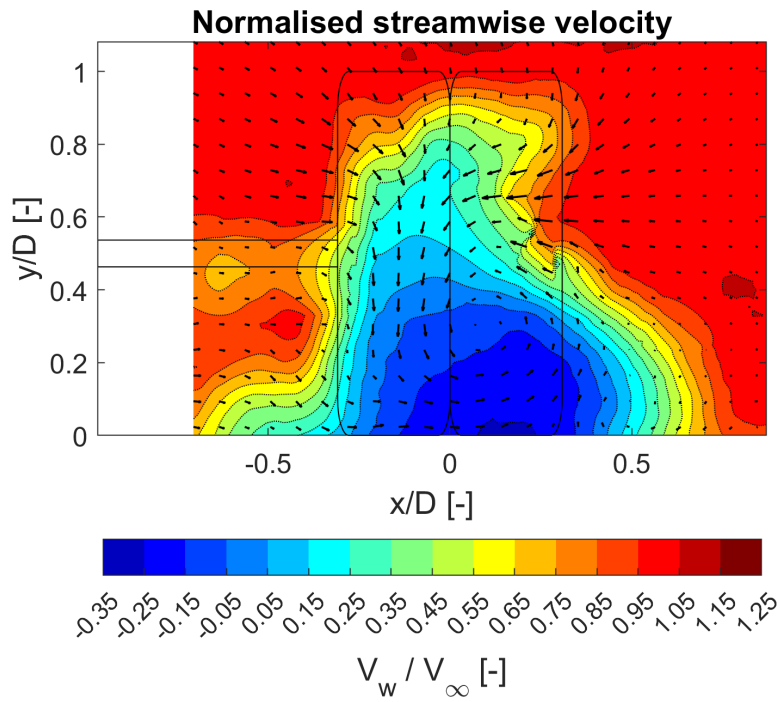


Figure C.32: Normalised streamwise velocity field (X-Y plane) for the rotating double wheel with blowing in the presence of underbody, at $z/D = 1$.

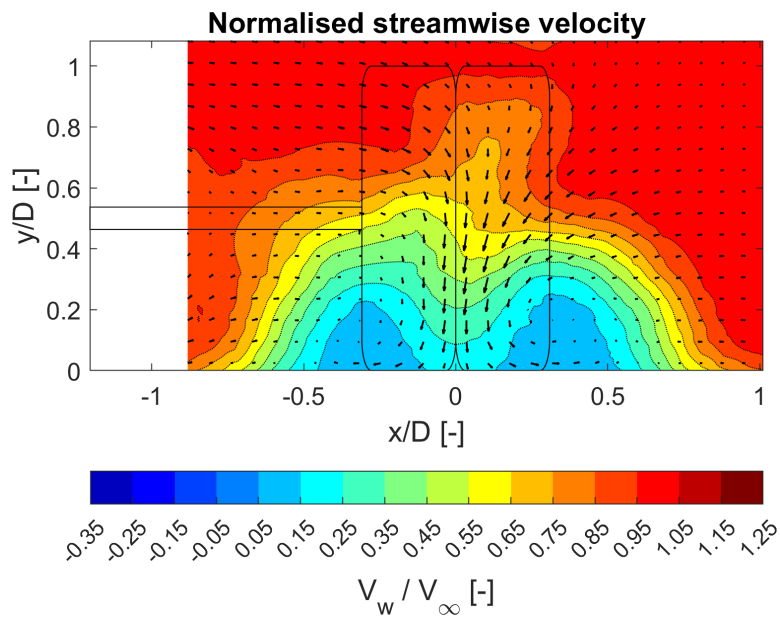


Figure C.33: Normalised streamwise velocity field (X-Y plane) for the stationary double wheel in the presence of underbody, at $z/D = 1.5$.

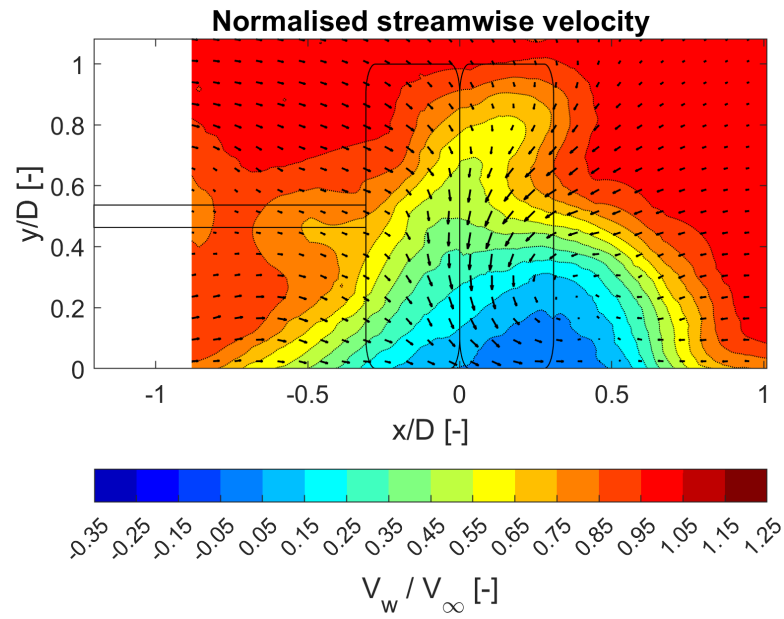


Figure C.34: Normalised streamwise velocity field (X-Y plane) for the rotating double wheel in the presence of underbody, at $z/D = 1.5$.

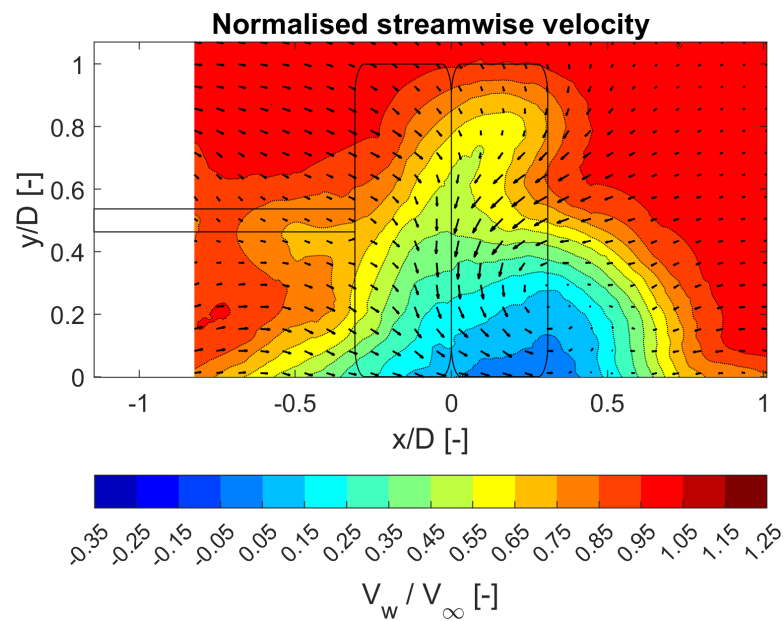


Figure C.35: Normalised streamwise velocity field (X-Y plane) for the rotating double wheel with blowing in the presence of underbody, at $z/D = 1.5$.

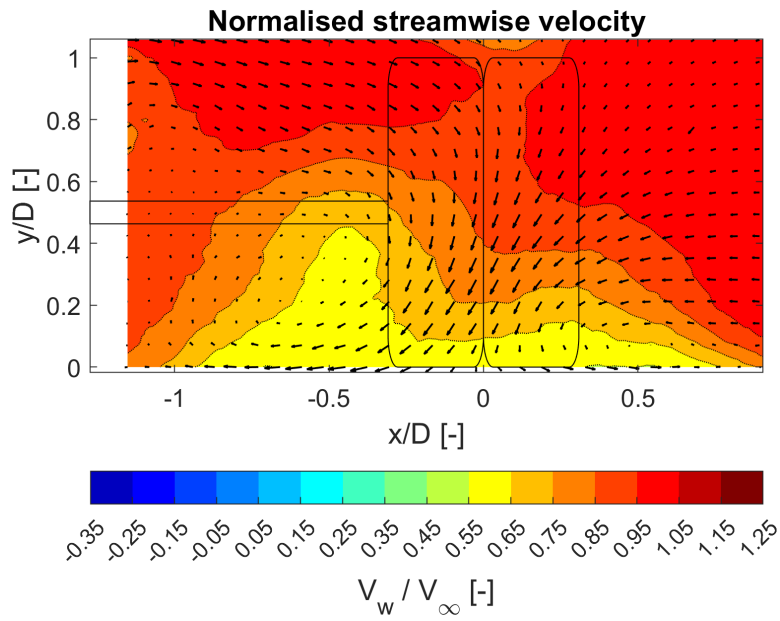


Figure C.36: Normalised streamwise velocity field (X-Y plane) for the stationary double wheel in the presence of underbody, at $z/D = 3$.

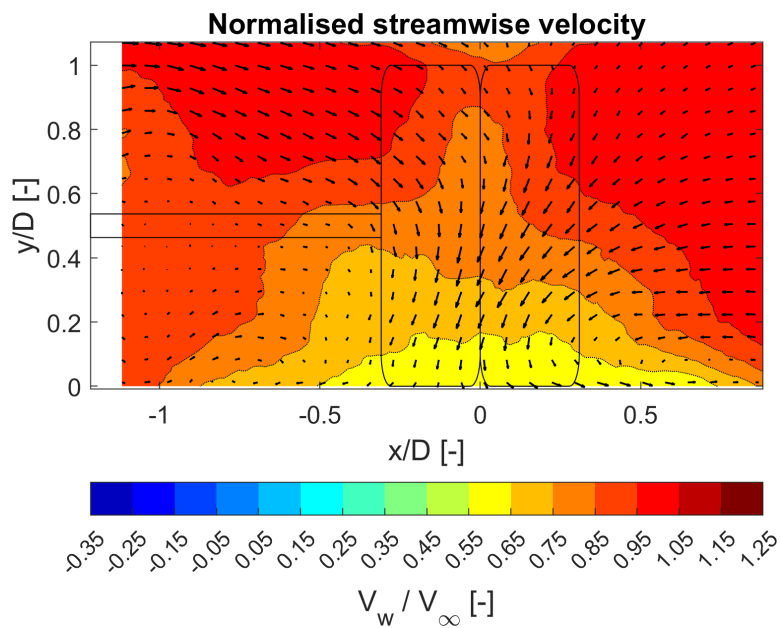


Figure C.37: Normalised streamwise velocity field (X-Y plane) for the rotating double wheel in the presence of underbody, at $z/D = 3$.

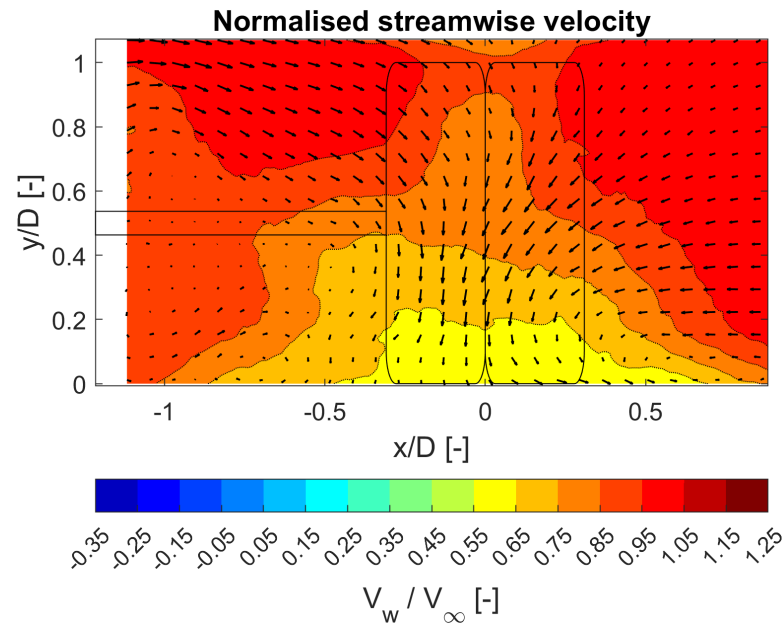


Figure C.38: Normalised streamwise velocity field (X-Y plane) for the rotating double wheel with blowing in the presence of underbody, at $z/D = 3$.

5. Mudflap holder - Stereoscopic

Figure C.39 to fig. C.41 shows the remaining velocity plots for the rotating with blowing double wheel equipped with mudflap holder case at different downstream planes.

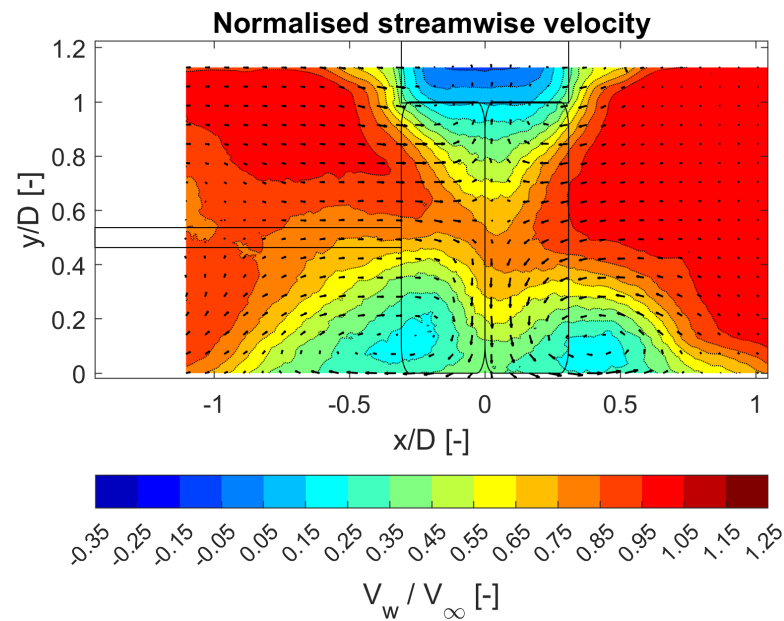


Figure C.39: Normalised streamwise velocity field (X-Y plane) for the rotating double wheel with blowing in the presence of mudflap holder, at $z/D = 1.5$.

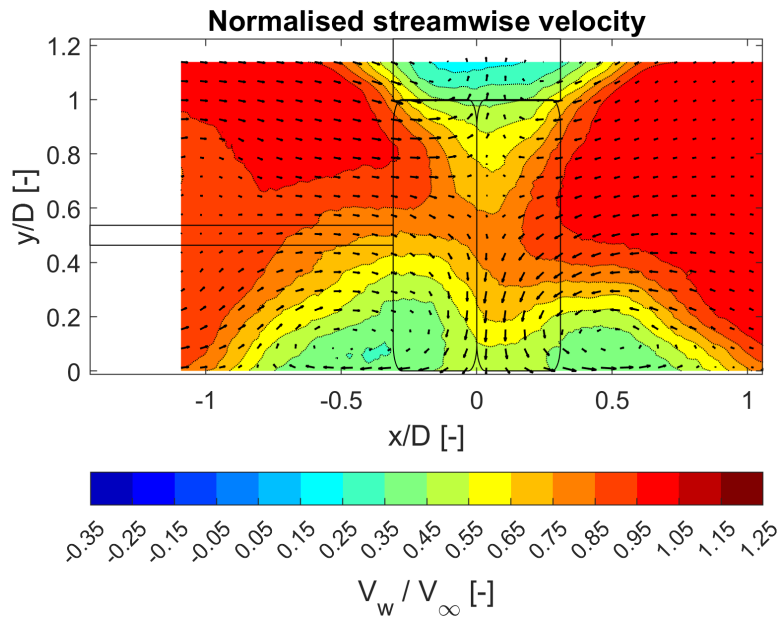


Figure C.40: Normalised streamwise velocity field (X-Y plane) for the rotating double wheel with blowing in the presence of mudflap holder, at $z/D = 2$.

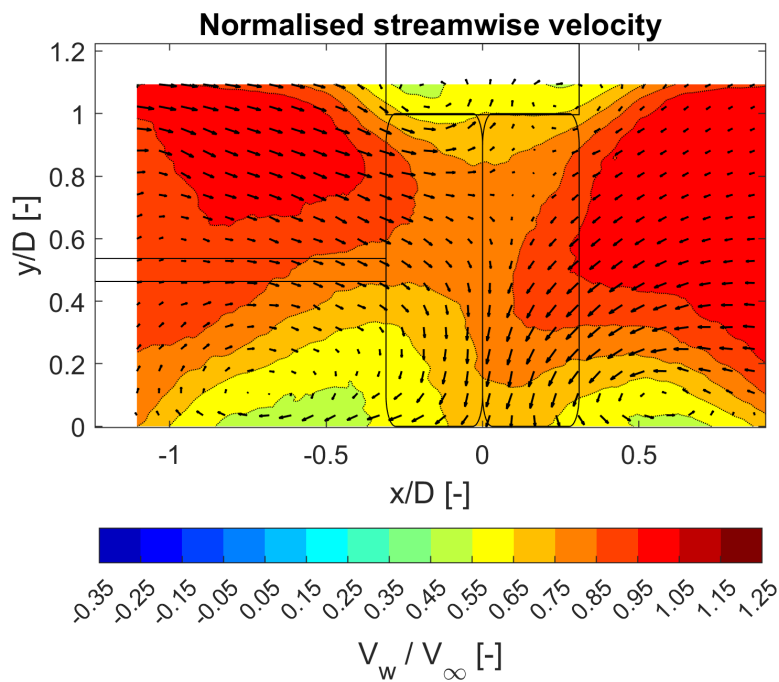


Figure C.41: Normalised streamwise velocity field (X-Y plane) for the rotating double wheel with blowing in the presence of mudflap holder, at $z/D = 3$.

6. Solid mudflap - Stereoscopic

Figure C.42 to fig. C.44 shows the remaining velocity plots for the rotating with blowing double wheel equipped with the solid mudflap case at different downstream planes.

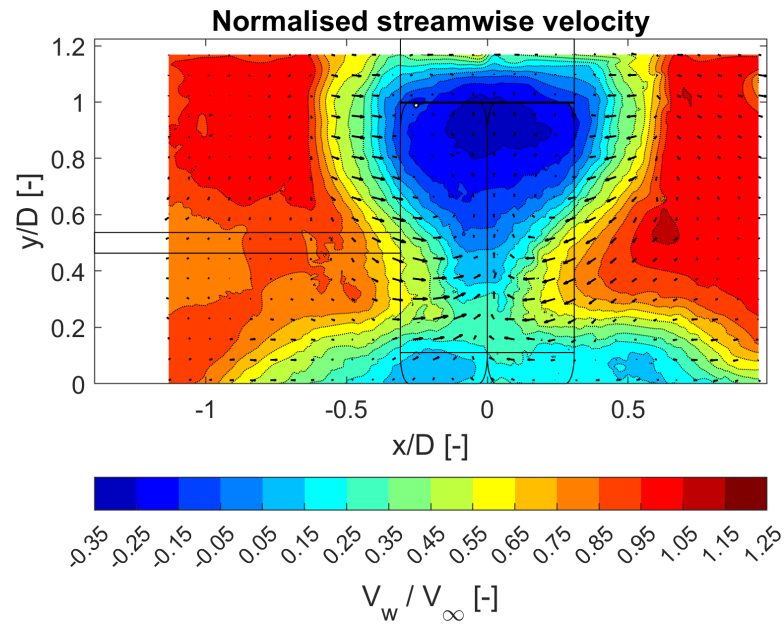


Figure C.42: Normalised streamwise velocity field (X-Y plane) for the rotating double wheel with blowing in the presence of solid mudflap, at $z/D = 1$.

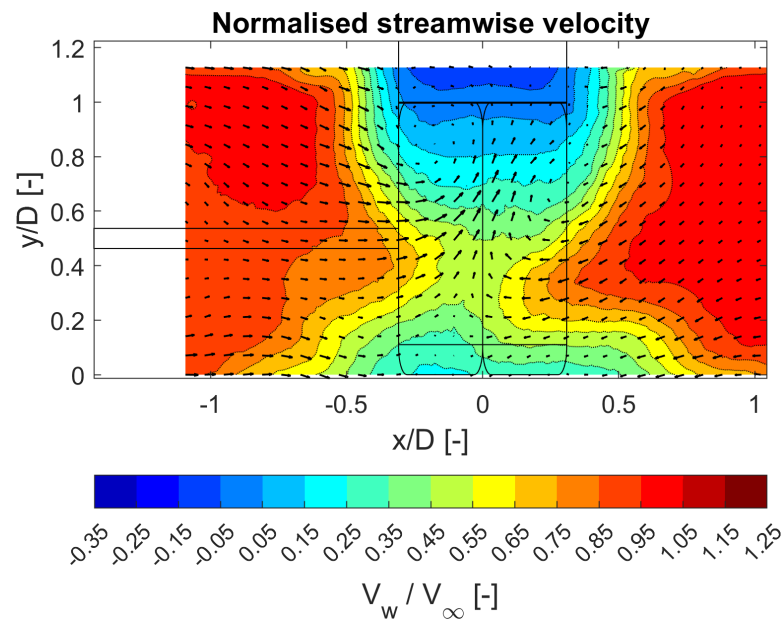


Figure C.43: Normalised streamwise velocity field (X-Y plane) for the rotating double wheel with blowing in the presence of solid mudflap, at $z/D = 2$.

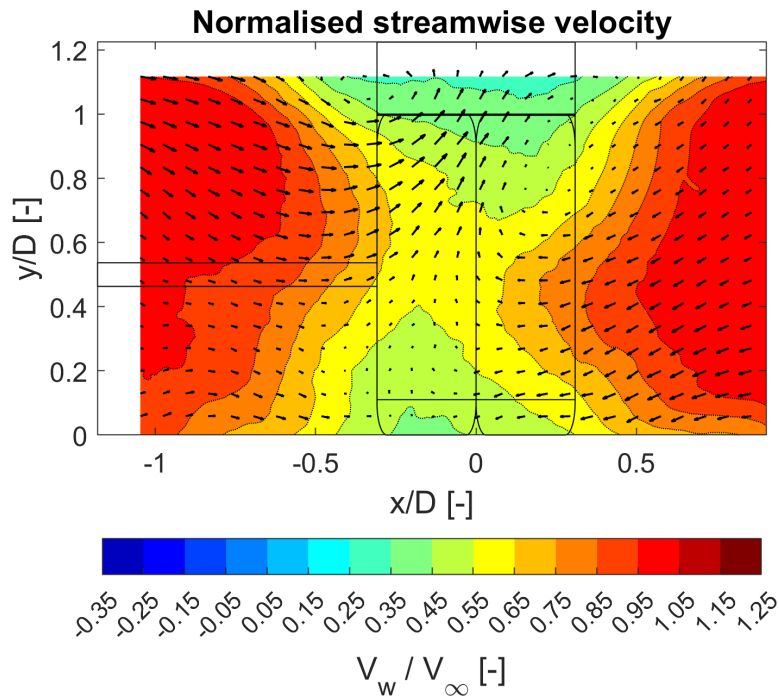


Figure C.44: Normalised streamwise velocity field (X-Y plane) for the rotating double wheel with blowing in the presence of solid mudflap, at $z/D = 3$.

7. Bottom hollow mudflap - Stereoscopic

Figure C.45 to fig. C.47 shows the remaining velocity plots for the rotating with blowing double wheel equipped with bottom hollow mudflap case at different downstream planes.

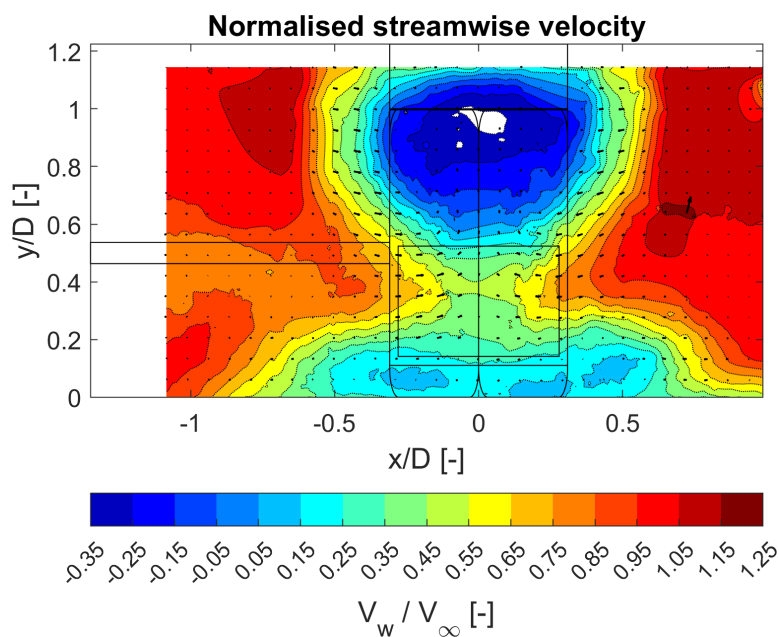


Figure C.45: Normalised streamwise velocity field (X-Y plane) for the rotating double wheel with blowing in the presence of hollow bottom mudflap, at $z/D = 1$.

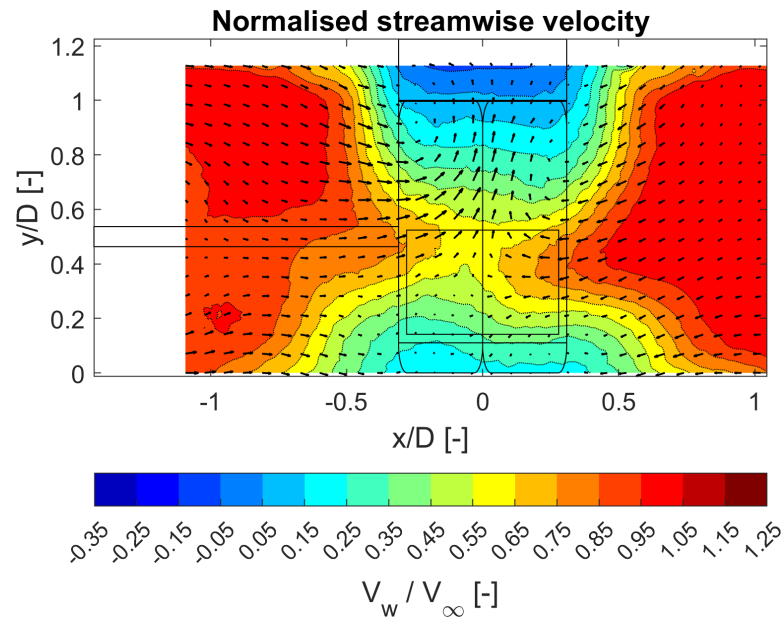


Figure C.46: Normalised streamwise velocity field (X-Y plane) for the rotating double wheel with blowing in the presence of hollow bottom mudflap, at $z/D = 2$.

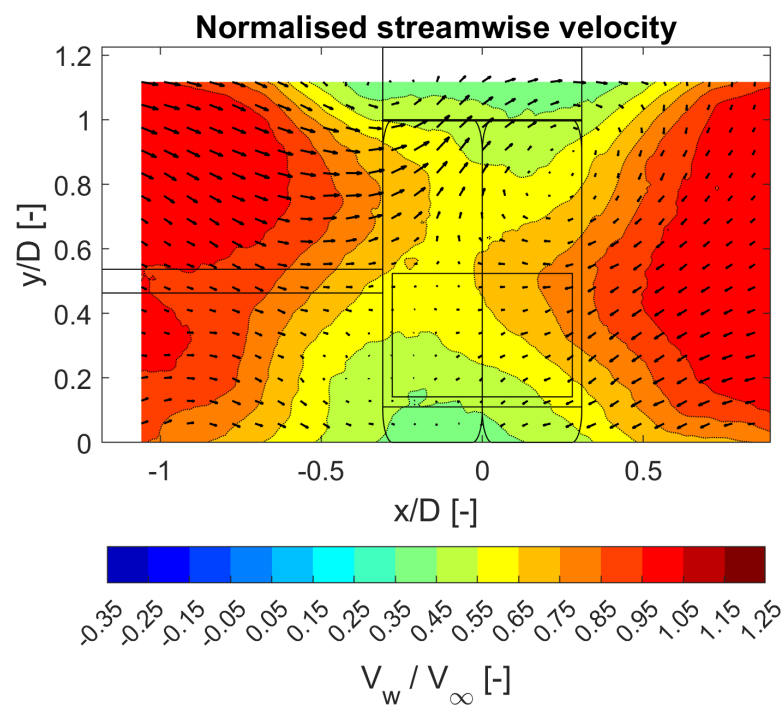


Figure C.47: Normalised streamwise velocity field (X-Y plane) for the rotating double wheel with blowing in the presence of hollow bottom mudflap, at $z/D = 3$.

8. Hollow top mudflap - Stereoscopic

Figure C.48 to fig. C.50 shows the remaining velocity plots for the rotating with blowing double wheel equipped with the hollow top mudflap case at different downstream planes.

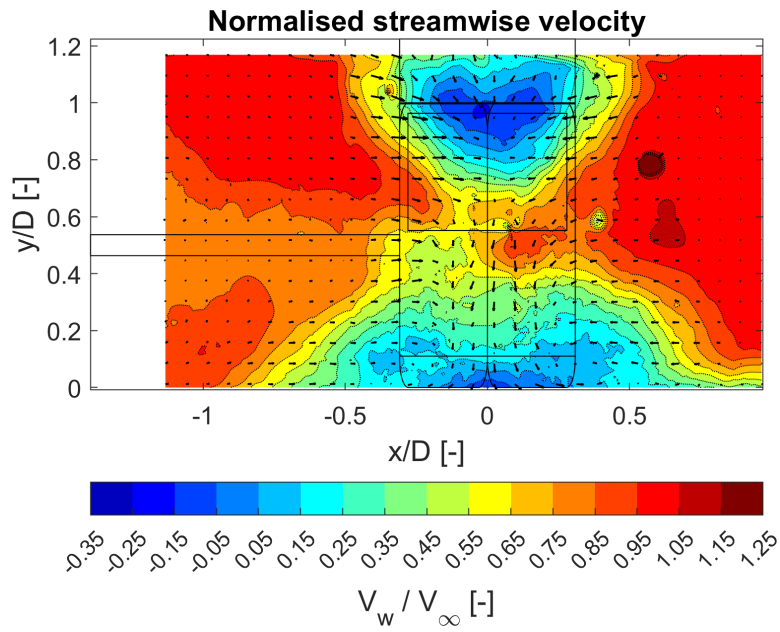


Figure C.48: Normalised streamwise velocity field (X-Y plane) for the rotating double wheel with blowing in the presence of hollow top mudflap, at $z/D = 1$.

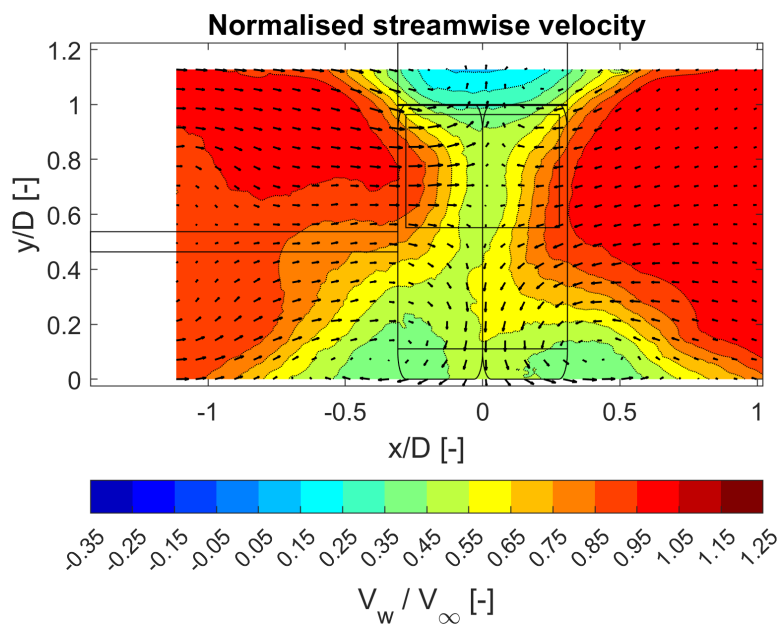


Figure C.49: Normalised streamwise velocity field (X-Y plane) for the rotating double wheel with blowing in the presence of hollow top mudflap, at $z/D = 2$.

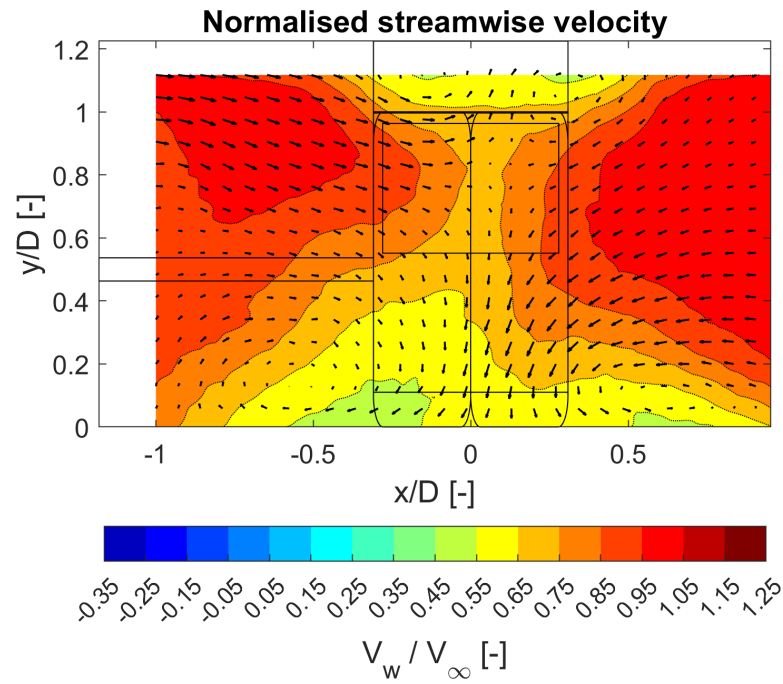


Figure C.50: Normalised streamwise velocity field (X-Y plane) for the rotating double wheel with blowing in the presence of hollow top mudflap, at $z/D = 3$.

9. 2.8mm mudflap - Stereoscopic

Figure C.51 to fig. C.53 shows the remaining velocity plots for the rotating with blowing double wheel equipped with mudflaps of 2.8 [mm] louvers case at different downstream planes.

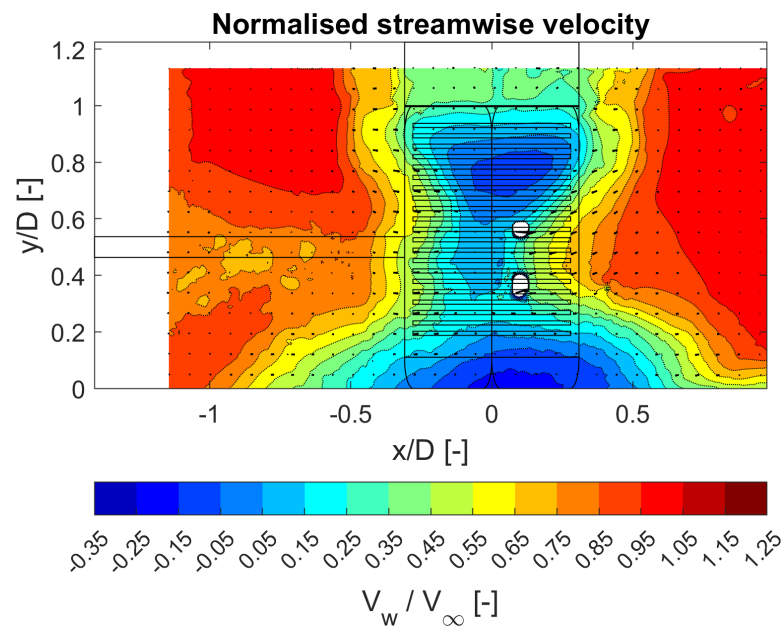


Figure C.51: Normalised streamwise velocity field (X-Y plane) for the rotating double wheel with blowing in the presence of 2.8mm louvered mudflap, at $z/D = 1$.

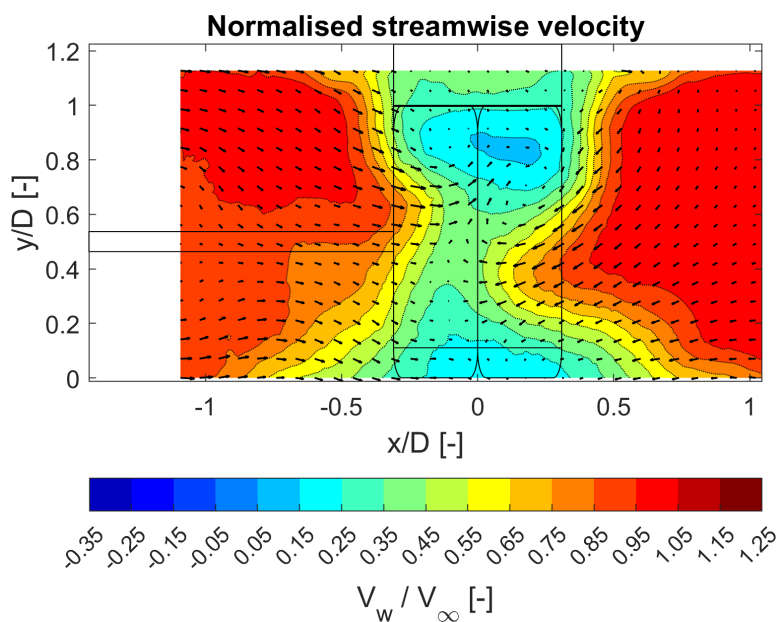


Figure C.52: Normalised streamwise velocity field (X-Y plane) for the rotating double wheel with blowing in the presence of 2.8mm louvered mudflap, at $z/D = 2$.

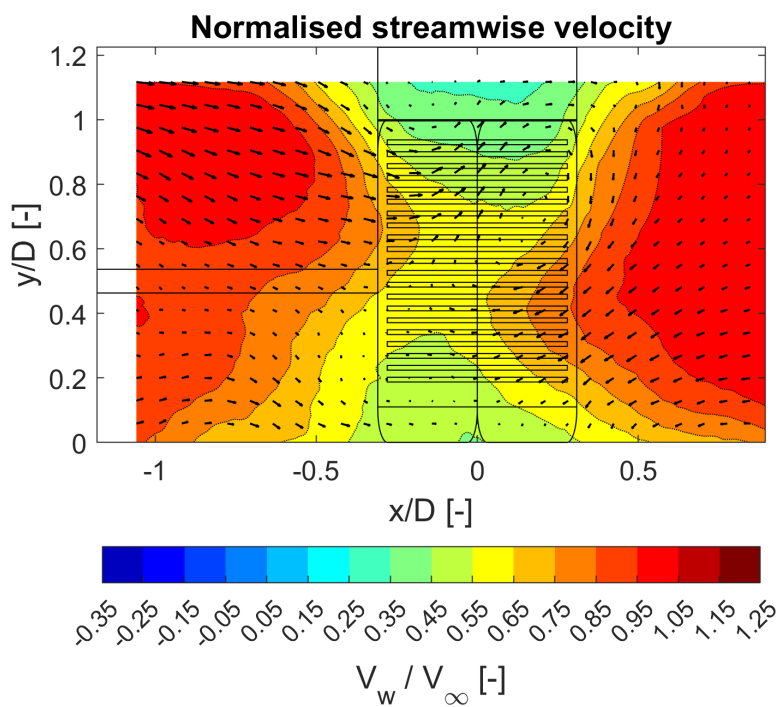


Figure C.53: Normalised streamwise velocity field (X-Y plane) for the rotating double wheel with blowing in the presence of 2.8mm louvered mudflap, at $z/D = 3$.

10. 1mm mudflap - Stereoscopic

Figure C.54 to fig. C.56 shows the remaining velocity plots for the rotating with blowing double wheel equipped with mudflaps of 1 [mm] louvers case at different downstream planes.

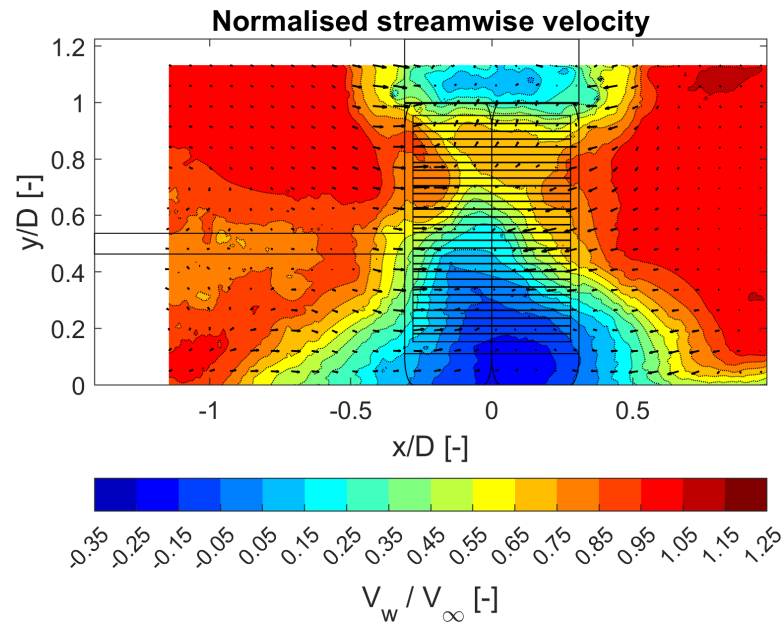


Figure C.54: Normalised streamwise velocity field (X-Y plane) for the rotating double wheel with blowing in the presence of 1mm louvered mudflap, at $z/D = 1$.

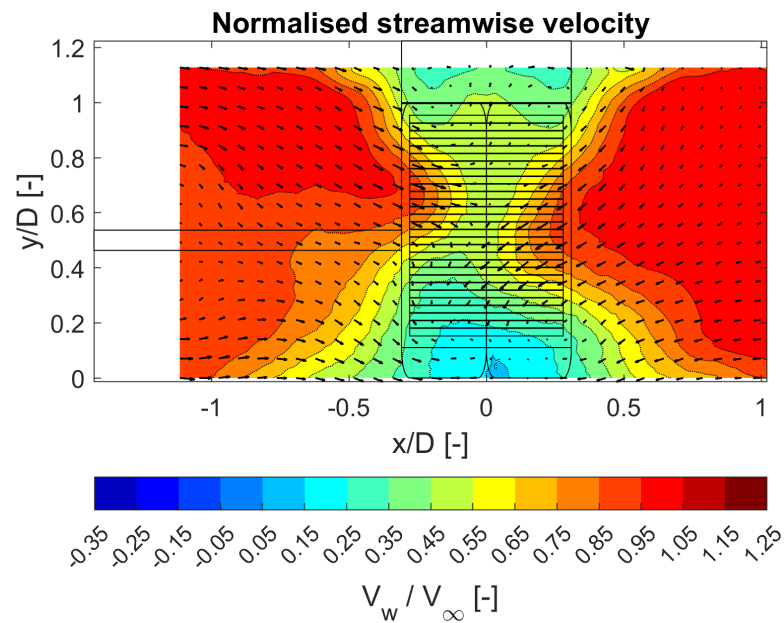


Figure C.55: Normalised streamwise velocity field (X-Y plane) for the rotating double wheel with blowing in the presence of 1mm louvered mudflap, at $z/D = 2$.

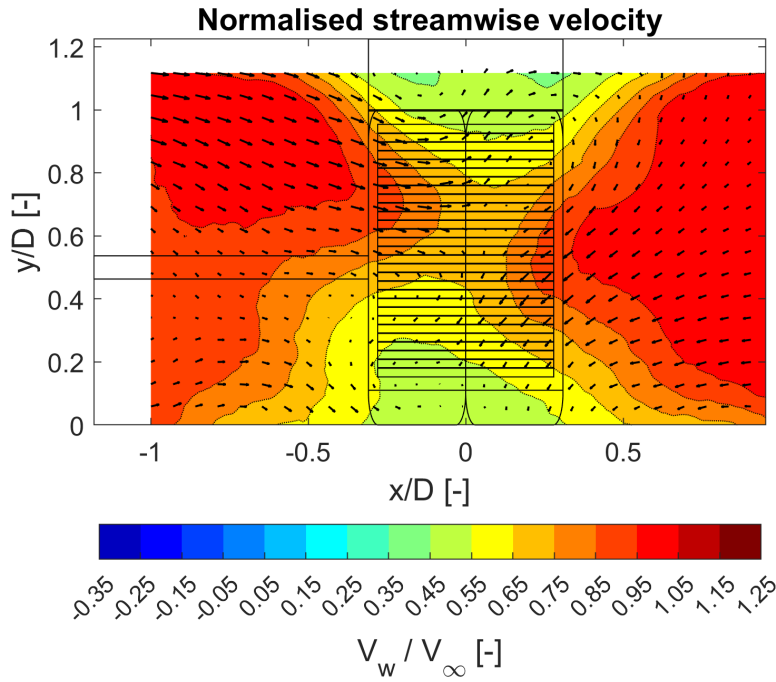


Figure C.56: Normalised streamwise velocity field (X-Y plane) for the rotating double wheel with blowing in the presence of 1mm louvered mudflap, at $z/D = 3$.

11. Drag analysis

The fig. C.57 provides the drag break down in terms of the momentum, pressure and fluctuation terms for the different cases tested.

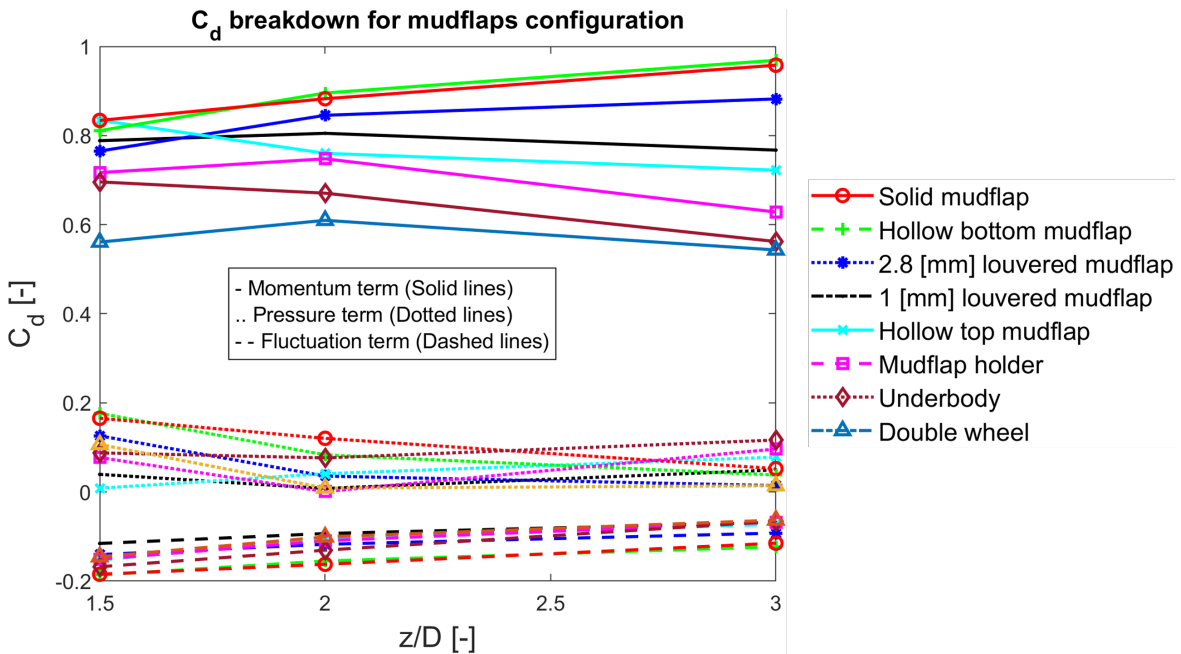


Figure C.57: Breakdown of the drag coefficient in terms of momentum, pressure and fluctuation terms for the various configurations at different wake planes (z/D).

The fig. C.58 provides the results of the ANOVA analysis of the different mudflaps designs tested. Note that for the P-values larger than 0.05, the hypothesis that two designs are statistically different cannot be proved true. Hence such P-values correspond to the designs providing similar drag values in future

tests.

Mudflap design 1	Mudflap design 2	Lower Limit	Design 1 -Design 2	Upper Limit	P-value
'Double wheel'	'Underbody'	-0.17729	-0.10392	-0.030556	0.0030777
'Double wheel'	'Mudflap holder'	-0.20877	-0.1354	-0.062034	0.00019045
'Double wheel'	'Hollow top mudflap'	-0.26758	-0.19421	-0.12084	2.0714e-06
'Double wheel'	'1mm louvered mudflap'	-0.28903	-0.21566	-0.14229	4.9453e-07
'Double wheel'	'2.8mm louvered mudflap'	-0.33503	-0.26166	-0.1883	3.1637e-08
'Double wheel'	'Hollow bottom mudflap'	-0.39865	-0.32528	-0.25191	1.231e-09
'Double wheel'	'Solid mudflap'	-0.41251	-0.33914	-0.26578	6.4478e-10
'Underbody'	'Mudflap holder'	-0.10485	-0.031478	0.04189	0.80429
'Underbody'	'Hollow top mudflap'	-0.16365	-0.090285	-0.016917	0.010775
'Underbody'	'1mm louvered mudflap'	-0.1851	-0.11173	-0.038367	0.0015142
'Underbody'	'2.8mm louvered mudflap'	-0.23111	-0.15774	-0.084372	3.0679e-05
'Underbody'	'Hollow bottom mudflap'	-0.29472	-0.22135	-0.14799	3.4395e-07
'Underbody'	'Solid mudflap'	-0.30859	-0.23522	-0.16185	1.4616e-07
'Mudflap holder'	'Hollow top mudflap'	-0.13218	-0.058807	0.014561	0.16968
'Mudflap holder'	'1mm louvered mudflap'	-0.15362	-0.080257	-0.0068889	0.026971
'Mudflap holder'	'2.8mm louvered mudflap'	-0.19963	-0.12626	-0.052894	0.0004176
'Mudflap holder'	'Hollow bottom mudflap'	-0.26324	-0.18988	-0.11651	2.803e-06
'Mudflap holder'	'Solid mudflap'	-0.27711	-0.20374	-0.13038	1.0816e-06
'Hollow top mudflap'	'1mm louvered mudflap'	-0.094817	-0.02145	0.051918	0.9657
'Hollow top mudflap'	'2.8mm louvered mudflap'	-0.14082	-0.067454	0.0059137	0.083575
'Hollow top mudflap'	'Hollow bottom mudflap'	-0.20444	-0.13107	-0.057701	0.00027559
'Hollow top mudflap'	'Solid mudflap'	-0.2183	-0.14494	-0.071568	8.5938e-05
'1mm louvered mudflap'	'2.8mm louvered mudflap'	-0.11937	-0.046005	0.027363	0.41555
'1mm louvered mudflap'	'Hollow bottom mudflap'	-0.18299	-0.10962	-0.036252	0.0018331
'1mm louvered mudflap'	'Solid mudflap'	-0.19685	-0.12349	-0.050119	0.00053216
'2.8mm louvered mudflap'	'Hollow bottom mudflap'	-0.13698	-0.063615	0.0097528	0.11532
'2.8mm louvered mudflap'	'Solid mudflap'	-0.15085	-0.077482	-0.004114	0.034648
'Hollow bottom mudflap'	'Solid mudflap'	-0.087235	-0.013867	0.059501	0.9972

Figure C.58: ANOVA results for different designs with their respective P-values.

